Wabash CarbonSAFE

The Geology of The Mt. Simon Sandstone
Storage Complex at the Wabash #1 Well,
Vigo Co., Indiana
Subtask 7.2
Technical Report

February 1, 2019 through March 31, 2022

**Jared T. Freiburg[1], Franck Delpomdor[1], John H. McBride[2],
Hannes E. Leetaru[1], Dave H. Malone[3], Nate Grigsby[1], Mansour Khosravi[1],
Scott Frailey[1], James R. Damico[1], Charles Monson[1], Zohreh Askari[1],
Yaghoob Lasemi[1], Donna Willette[1], Oladipupo Babarinde[1], Chris Korose[1],
Mingyue Yu[1], Lauren Gardiner[1]**

[1]Prairie Research Institute
University of Illinois
Urbana-Champaign, Illinois 61820

[2]Department of Geological Sciences
Brigham Young University
Provo, Utah

[3]Illinois State University
Normal, Illinois

Report Issued: April 25, 2022

DISCLAIMER

Contents

CHAPTER 3: GEOCHRONOLOGY OF THE MT. SIMON SANDSTONE AND BASALT FROM THE WABASH #1 WELL, WEST TERRE HAUTE, INDIANA 58

CHAPTER 4: PETROPHYSICS OF THE EAU CLAIRE FORMATION AND THE MT. SIMON SANDSTONE 85

INTRODUCTION

The Wabash CarbonSAFE project drilled the Wabash #1 stratigraphic test well (ID# 168045) at the Wabash Valley Resources (WVR) IGCC facility in Vigo County, Indiana, to characterize and evaluate the basal Cambrian Mt. Simon Sandstone for commercial-scale CO_2 storage near the site.

This report presents an extensive geologic characterization of the Mt. Simon storage complex and relevant data collected from the Wabash #1 well, such as lithologic data collected from cuttings and core, geophysical logging, geomechanical analysis of core samples, and well testing and fluid sampling within the Mt. Simon Sandstone.

The Mt. Simon storage complex comprises two major sections: the Mt. Simon Sandstone as the potential reservoir and the overlying Eau Claire Formation as its primary seal. Within the report, an extensive depositional, sedimentological, and geochronologic characterization of the Mt. Simon is included with supportive chapters on the regional geology and the geophysical, petrophysical, and petrologic data collected during the project. An overview of 2D seismic reflection data collected from and around the test well is presented. Also presented are chapters on the characterization of the sealing Eau Claire Formation, including a chapter on the capacity of the primary and secondary seals to the Mt. Simon as well as a chapter on geomechanical testing results of the Eau Claire Formation and Mt. Simon Sandstone.

Some of the information discussed in this report was used in the development of static and dynamic geologic models of the Mt. Simon Sandstone storage complex. The static and dynamic modeling of CO_2 injection in the Mt. Simon Sandstone are discussed in a separate report (Dessenberger et al., 2022) under the Wabash CarbonSAFE project.

Chapter 1
Sedimentology of the Mt. Simon Sandstone

By: Franck Delpomdor

Illinois State Geological Survey, Prairie Research Institute, University of Illinois at Urbana-Champaign

GEOLOGICAL SETTING

Located in the midwestern region of the United States, the Illinois Basin is a NNW-SSE-oriented, spoon-shaped structure, covering an area of approximately 110,039 mi^2 extending westward to eastward from Illinois to eastern Indiana and northward to southward from southern Wisconsin to northwestern Kentucky and northern Tennessee (Kolata and Nelson, 2010). The Paleozoic sedimentary fill of this basin was conditioned by at least four tectonic-eustatic cycles linked to the Precambrian and Paleozoic tectonic evolution of Laurentia continent (McBride et al., 2003). These cycles or supersequences include, from the oldest to the youngest, Sauk (Cambrian to early Ordovician), Tippecanoe (early Ordovician to early Devonian), Kaskaskia (early Devonian to late Mississippian), and Absaroka (early Pennsylvanian to early Permian) (Willman et al., 1975).

Three major tectonic structures crosscut the Illinois Basin that have been controlled by the deposition of the basin. They include the LaSalle Anticlinal Belt in eastern-central Illinois, the DuQuoin-Louden Anticlinal Belt in southern-central Illinois, and the Rough Creek-Shawneetown Fault Zone in extreme southwest Illinois (Willman et al., 1975; Treworgy et al., 1991). Other minor tectonic structures have been regionally controlled by the basin (e.g., Sandwich Fault Zone, etc.). The entire stratigraphic record of the Illinois Basin is up to 15,000 ft in thickness that thickens southward into the deep part located near the mouth of the Wabash River at the tri-state borders between Illinois, Indiana, and Kentucky (Willman et al., 1975). The Paleozoic system was deposited based on biostratigraphy, mainly trilobites and conodonts, and geochronology in a time interval between the Middle-Upper Cambrian to early Permian (Collinson et al., 1988; Norby, 1991; Thomas et al., 2020). Local consolidated sediments, Cretaceous in age, are found only in relatively small areas in southern and western Illinois (Willman et al., 1975). The bedrock is covered by late Cenozoic and Quaternary sediments that directly underlie the surface of almost the entire state (Willman et al., 1975).

The initial stage of pre-rifting has occurred in southeast-central Illinois and southwest-central Indiana by the strike-slip faulting of the 1.4-1.1 Ga Eastern Granite-Rhyolite Province (ages based on U-Pb geochronology; Heidlauf et al., 1986; Denison et al., 1987; Leighton and Kolata, 1991; Kolata and Nelson, 1991, 2010; Van der Pluijm and Catacosinos, 1996; Van Schmus et al., 1996, 2007) that initially formed the proto-Illinois Basin. Recently, borehole data from the Wabash #1 well in Vigo County, Indiana, have shown the deposition of sandstone with volcanic intrusions that overlies the Precambrian crystalline basement and underlies the Paleozoic system of the Illinois Basin. This new unit could be correlated with the pre-rifting Precambrian lacustrine-fluvial

late Middle Run Formation (Keweenawan in age) in Indiana and Ohio but ^{40}Ar/^{30}Ar age of the volcanics overlying these sands as well as U-Pb geochronology of the sands indicate an early Cambrian age (chapter 3). Seismic reflection data of the basement below these sands have revealed the occurrence of a layered sequence, considered as Centralia Sequence, that appears to thicken from east-central Illinois towards a north-east depocenter (chapter 2; Pratt et al., 1992; McBride and Kolata, 1999; McBride et al., 2003). Freiburg et al. (2014) have discussed the possible correlation of the layered Centralia Sequence with the occurrence of the Argenta sandstone, a unit underlying the lower Mt. Simon and discovered as a result of drilling for the Illinois Basin Decatur Project (IBDP) in Illinois. The Argenta appears to be related to rifting in east-central Illinois and west-central Indiana where there is general thickening from west-central Illinois to eastern-central and northern Illinois. This reflects the Mt. Simon (and Argenta) northern and east-central Illinois depocenter along the rift axis with a maximum deposition up to 2,500 ft (Freiburg et al., 2014). Since the Argenta is not a formally recognized formation and may be considered part of the Mt. Simon, "sandstone" is not capitalized. The Mt. Simon Sandstone is included in the Potsdam Group that is overlain by the Knox Dolomite Group, itself composed, from oldest to youngest, by the Eau Claire Formation, Ironton-Galesville Sandstone, Franconia Formation, Potosi Dolomite, and Eminence Formation on its lower part. Both the Potsdam and Knox Dolomite Groups are included in the Sauk supersequence in the Illinois Basin (Sloss, 1963). The Mt. Simon Sandstone is overlain by the Upper Cambrian Eau Claire Formation (Becker et al., 1978).

MATERIALS AND METHOD

In this report, data from the Argenta sandstone and the Mt. Simon Sandstone are investigated through detailed description of cores and high-resolution Fullbore Formation Micro-Imager (FMI) of the Wabash #1 well in Vigo County, Indiana. All cores are stored at the Sample and Core Library of the Illinois State Geological Survey (ISGS) in Champaign, Illinois. The core has been described with respect to units (A-E) used to describe depositional units in the Mt. Simon at the IBDP (Freiburg et al. 2014). Only 96 ft (located between 7,900.8 and 7,996.0 ft) of the arkose (unit A) of the Lower Mt. Simon Sandstone was cored. Other units were logged based on FMI that provide a high-resolution visualisation of the sedimentary structures in the borehole. FMI is an electric tool that measures the micro-resistivity of the rocks. The produced images have a vertical resolution of 5 mm and cover up to 80% of the borehole wall. The variation of brightness depends on the porosity. When the porosity is low, the FMI images are clear or white. Core and FMI logs are drawn based on descriptive observations and recognition of lithofacies codes from individual core segments, mosaics of core photographs, and FMI imaging that are digitally enhanced. Sedimentary facies were defined based on grain-size and sedimentary structures, following the methodology and lithofacies codes adapted from Miall (2006) for the fluvial deposits and Kocurek (1996) for the aeolian dune deposits.
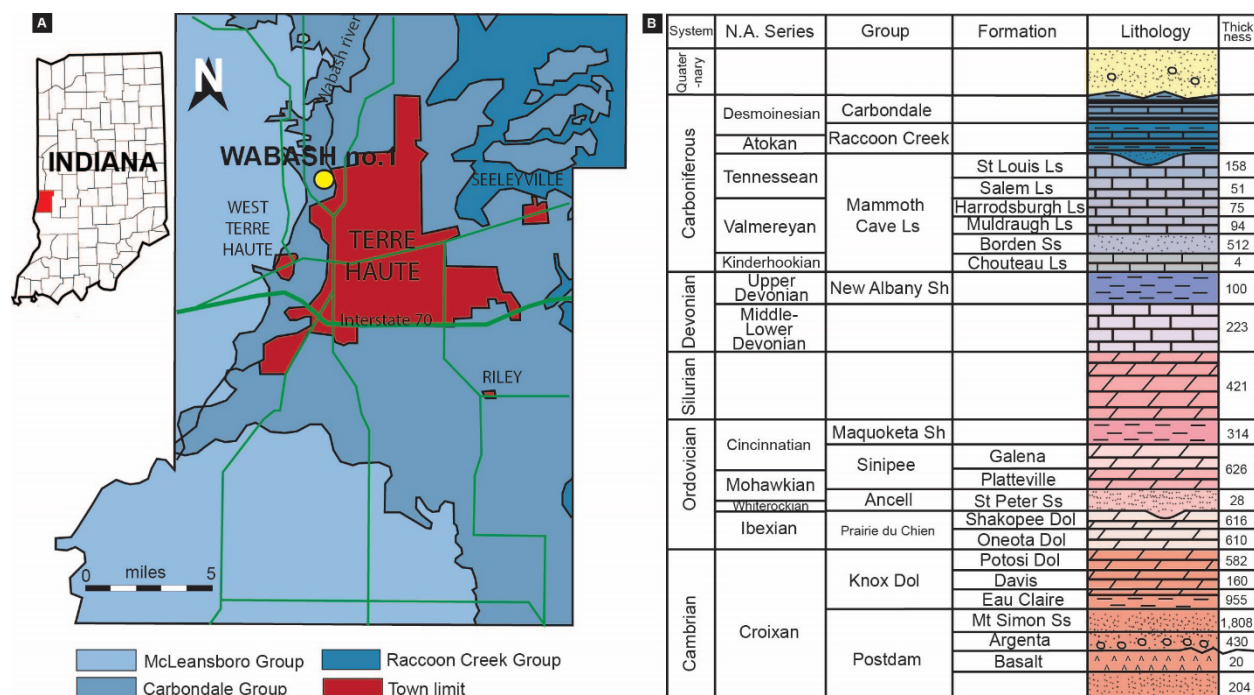
Figure 1: (A) Simplified geologic map of Vigo County, Indiana, with location of the Wabash #1 well (modified map from Indiana Geological Survey). (B) Stratigraphic column with the stratigraphic units that are crossed in the Wabash #1 well.

Lithofacies are grouped into five distinct lithofacies associations: alluvial-fluvial, fluvial, aeolian-fluvial, delta front-lagoon/lake, and open-marine offshore systems. A block diagram representing the paleoenvironmental evolution stages is proposed in Figure 8 for the deposition of the Argenta sandstone and Mt. Simon Sandstone. Grain size analysis is an analytical technique to determine the size of the different particles of sedimentary rocks and their distribution. The grain size analysis was performed using microscopy by point counting on thin section samples by Mingyue Yu and Jared Freiburg at ISGS. Weight percentage frequencies and cumulative weight percentage frequencies were calculated with the formulae of Folk and Ward (1957). The grain size parameters, including graphic mean, inclusive graphic standard deviation, inclusive graphic skewness, and graphic kurtosis, are presented in a graphical or statistical form. The stratigraphic framework was developed based on the assumptions of the sequence stratigraphy sensu Catuneanu (2006) and Catuneanu et al. (2009). A west-to-east correlation section between the referenced boreholes was constructed for the identification of key stratigraphic surfaces and system tracts.

RESULTS

Core Description

The near-surface bedrock geology of Vigo County, Indiana, mainly consists of Pennsylvanian sedimentary rocks that are composed to the west by the Raccoon Creek Group (Desmoinesian) and to the east by the Carbondale and McLeansboro Groups (Desmoinesian), in which the last cited units are crossed by the Wabash #1 well (Figure 1A). This borehole was drilled to a total depth of 8,739 ft (Figure 1B). The Mississippian-Pennsylvanian boundary is crossed at 748 ft in

depth. Below this boundary, the bedrock geology consists, from the top to the base, of Mississippian (Tennessean) St. Louis Limestone (748-906 ft), Salem Limestone (906-957 ft), the (Valmeyeran) Harrodsburgh Limestone (957-1,032 ft), Muldraugh Limestone (1,032-1,126 ft), Borden Sandstone (1,126-1,638 ft), and the (Kinderhookian) Chouteau/Rockford Limestone (1,638-1,642 ft). The Devonian System contains the Upper Devonian New Albany Shale (1,642-1,742 ft) and the Middle-Lower Devonian undifferentiated limestone (1,742-1,965 ft). The underlying units consists of the undifferentiated Silurian System (1,965-2,386 ft), the Upper Ordovician (Cincinnatian) Maquoketa Shale (2,386-2,700 ft), the Upper-Middle Ordovician (Cincinnatian-Mohawkian) Trenton Limestone (2,700-3,326 ft), the Middle Ordovician (Mohawkian-Whiterokian) St. Peter Sandstone (3,326-3,454 ft), the Lower Ordovician (Ibexian) Shakopee Dolomite (3,354-3,970 ft), and Oneota Dolomite (3,970-4,580 ft) (Knox Group). The Upper Cambrian units are composed, from the top to the base, by Potosi Dolomite (4,580-5,162 ft), Davis Sandstone (5,162-5,322 ft), Eau Claire Formation (5,322-6,277 ft), Mt. Simon Sandstone (6,277-8,085 ft), and the Argenta sandstone (8,085-8,515 ft). Basalt rocks are crossed between 8,515 and 8,535 ft, in which overlie an unidentified sandstone (8,535-8,739 ft). The Argenta sandstone-basalts boundary appears to be sharp and unconformable, as shown by the differential resistivity intensities in the FMI log.

The lithology of the unidentified sandstone (8,535-8,739 ft) is defined using the FMI log and plugs. This unit dominantly consists of fine- to coarse-grained sandstone. The lowermost unit is coarser than the uppermost unit, which consists of fine- to medium-grained sandstone with abundant mudstone layers. Massive and planar parallel sedimentary structures are dominant. A few low-angle cross-stratified layers are identified in the FMI log. No paleontological structures are recognized in the FMI images.

The Argenta sandstone (8,085-8,515 ft) mainly consists of medium- to very coarse-grained, locally pebbly or conglomeratic sandstone (Figure 3A). The lowermost unit, between 8,369 and 8,515 ft in depth, shows massive, planar parallel and low-angle cross-stratified, medium- to very coarse-grained sandstone, locally interbedded by 1 ft massive or planar parallel stratified, pebbly sandstone or conglomerate. The first 3 ft above the basalt contact shows a very fine-grained sandstone or clay. This level has been interpreted as a Skolithos "piperock" in the VW #1 well in Macon County, Illinois. Between 8,208 and 8,369 ft in depth, the unit shows coarser materials that are identified as a massive, planar parallel and low-angle cross-stratified, pebbly sandstone or conglomerate, in which they are interlayered by a 1 to 3-ft-thick, fine- to coarse-grained sandstone, often planar parallel and low-angle cross-stratified. A 24-ft-thick interval (8,184-8,208 ft in depth) displays medium- to coarse-grained sandstone, dominantly planar parallel, with local vertical and subvertical bioturbations. This interval (8,114-8,184 ft in depth) is overlain by discrete finning-upward sequence that is dominantly composed at the base by a massive, planar parallel and low-angle cross-stratified, pebbly sandstone or conglomerate, then a fine- to coarse-grained planar parallel and low-angle cross-stratified sandstone with local pebbly sandstone or conglomerate interlayers (av. ½ -1 ft thick). Between 8,085 and 8,114 ft in depth, fine- to medium-grained

sandstone and mudstone interlayers are the dominant rocks. Massive, planar parallel and low-angle crossed-stratification are common. Vertical to horizontal bioturbation is identified in the FMI log.
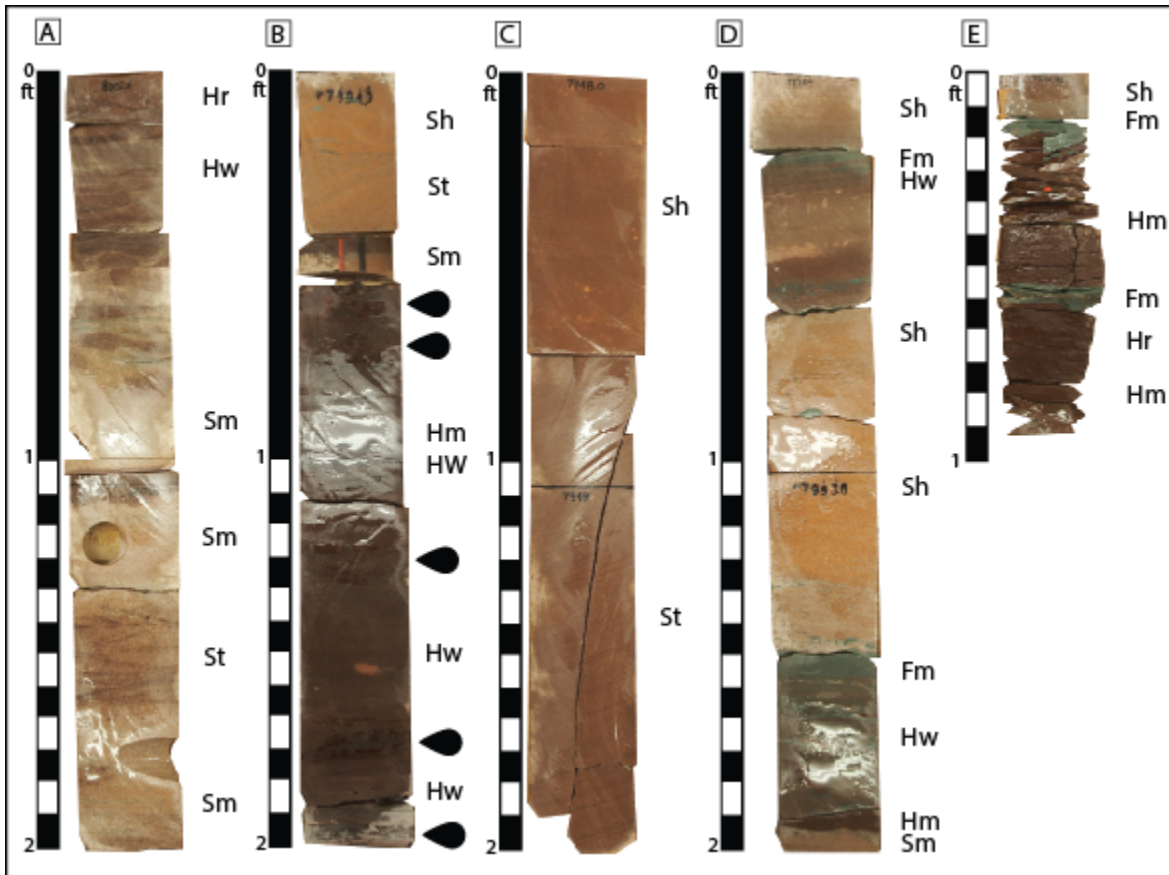
Figure 2: *(A) Distributary channel bars that composed massive (Sm) and trough cross-stratified (St) sandstone capped by mouth bar-type facies (Hw, Hr). Arkose (unit A), Lower Mt. Simon Sandstone, depth: 8,002-8,004 ft. (B) Bioturbated heterolithic mudstone (Hw, Hm) and sandstone forming a mouth bar facies. Arkose (unit A), Lower Mt. Simon Sandstone, depth: 7,994-7,996 ft. (C) Fluvial sand dunes that are composed of planar parallel (Sh) and trough cross-stratified (St) sandstone. Arkose (unit A), Lower Mt. Simon Sandstone, depth: 7,948-7,950 ft. (D) Floodplain mudstone at the base, followed by fluvial sandstone. Notice the presence of mud intraclasts in the planar parallel laminated sandstone (Sh). Arkose (unit A), Lower Mt. Simon Sandstone, depth: 7,951-7,953 ft. (E) Floodplain facies composed of heterolithic mudstone (Hr, Hm) and fine-grained mudstone (Fm). Arkose (unit A), Lower Mt. Simon Sandstone, depth: 7,914.8-7,915 ft.*
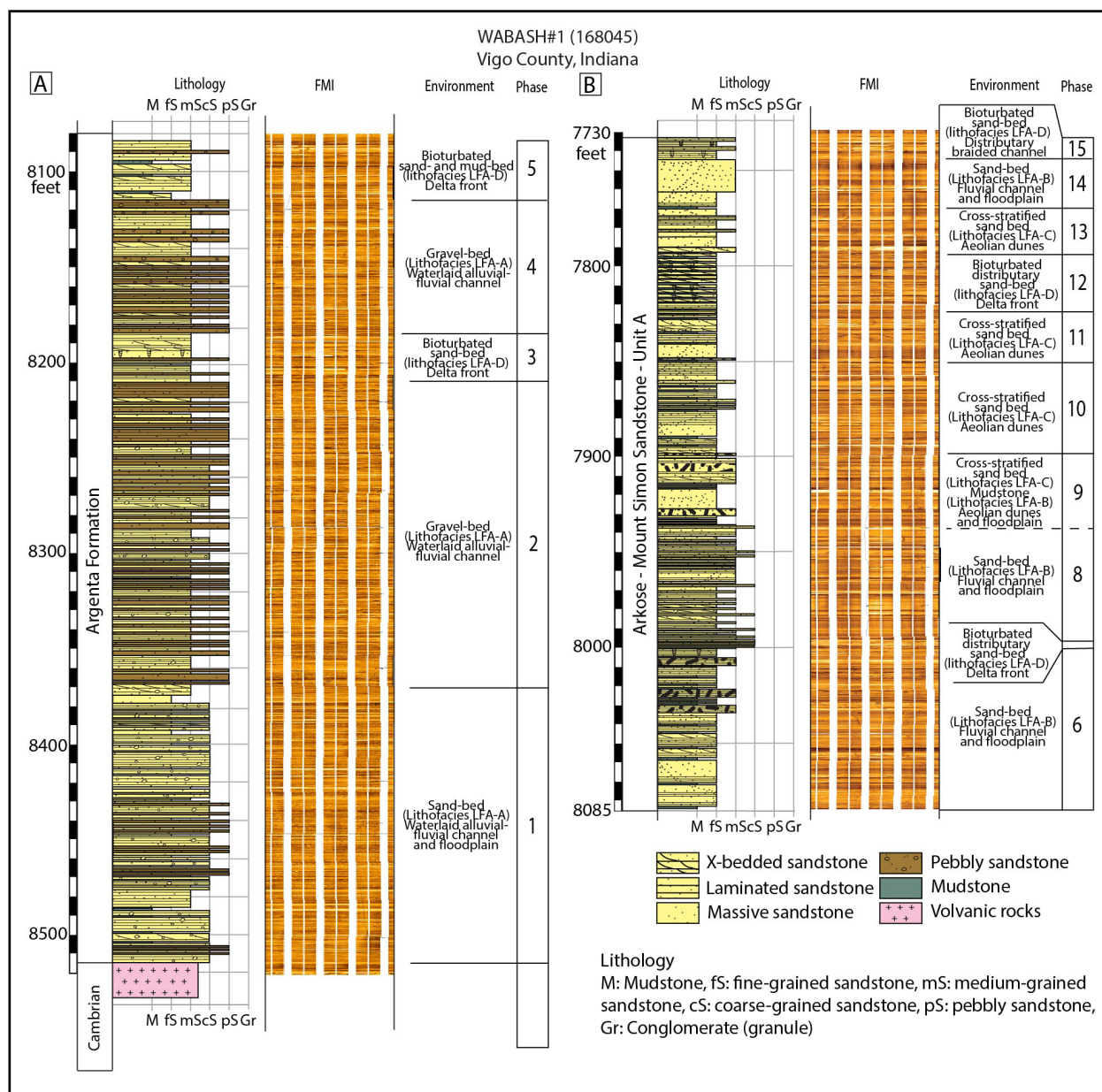
Figure 3: *Lithostratigraphic column, FMI log, and composition of the Argenta sandstone and arkose (unit A) of the Lower Mt. Simon Sandstone showing lithofacies associations and paleoenvironmental interpretation.*

In this report, the Mt. Simon Sandstone is divided into four subunits: (1) the arkose (unit A) of the Lower Mt. Simon Sandstone (7,733-8,085 ft), (2) the unit B of the Lower Mt. Simon Sandstone (7,418-7,733 ft), (3) the undifferentiated units C and D of the Middle Mt. Simon Sandstone (6,751-7,418 ft), and (4) the unit E of the Upper Mt. Simon Sandstone (6,277-6,751 ft). The base of the arkose (unit A) of the Lower Mt. Simon Sandstone shows 3-ft-thick, finely planar parallel, very fine- to medium-grained sandstone and mudstone; then the unit displays massive, planar parallel to cross-stratified, fine- to medium-grained sandstone and common mudstone layers (Figure 3B).

A few layers of coarser materials containing mud intraclasts, elongated following the bedding, are identified at depths of 7,996-8,001 ft, 8,013-8,016 ft, 8,024-8,025 ft, and 8,030-8,032 ft. The overlying rocks are cored between 7,900.8 and 7,996.0 ft in depth, and a description of their lithology follows (Figure 2). The lithology consists of light maroon to red (light tan to pink when altered), fine- to medium-grained, moderately to very well sorted sandstone and thin interlayers (av. ½ to 1 in thick) of greenish mudstone. Massive structures and large cross-stratification are common. Quartz is dominant and is subrounded to well-rounded and is consolidated in a dark maroon clay matrix. The rocks are overlain by massive to large cross-stratified, fine- to medium-grained sandstone, and thin layers of mudstone and local mud intraclasts within sandstone. Between 7,990 and 7,828 ft in depth, the unit consists of vertically to subvertically bioturbated, massive planar parallel and low-angle to large crossed-stratification, fine- to medium-grained sandstone and mudstone. Massive planar parallel to low-angle cross-stratified, fine- to medium-grained sandstone with common mudstone interlayers overlie the bioturbated facies between 7,744 and 7,990 ft in depth. The unit ends with an 11-ft-thick, vertically to subvertically bioturbated, massive planar parallel and low-angle crossed-stratification, fine- to medium-grained sandstone.

The unit B of the Lower Mt. Simon Sandstone mainly consists of medium- to coarse-grained sandstone, massive to planar parallel (Figure 4A). Sometimes, low-angle cross-stratification is identified in the uppermost unit. Between 7,700 and 7,708 ft in depth, a fine- to medium-grained sandstone with abundant vertical to subvertical bioturbation is recognized in the FMI images.

The undifferentiated units C and D of the Middle Mt. Simon Sandstone are dominantly a massive planar parallel and low-angle to trough cross-stratified, medium- to coarse-grained sandstone, locally associated with interlayers of fine materials (less than 1 ft thick) in the lower part (7,018-7,418 ft), and massive planar parallel and low-angle to trough cross-stratified, medium- to coarse-grained sandstone and abundant layers (½ to 4 ft thick) of very fine- to medium-grained sandstone and mudstone in the upper part (6,751-7,018 ft) (Figure 4B). This last part contains abundant massive structures, planar parallel, low angle to large and trough crossed-stratifications. A few layers of mud intraclasts, parallel to the bedding, are also identified in the FMI log (e.g., 7,070-7,071 ft, 7,084-7,092 ft, 7,098-7,100 ft, and 7,102-7,103 ft in depth). Bioturbation is common in the upper part.

The lithology of the unit E of the Upper Mt. Simon Sandstone shows a succession of 5- to 10-ft-thick fining-upward cycles that consist, from the base to the top, of massive to finely planar parallel, medium- to coarse-grained sandstone; low-angle cross-stratified, medium-grained sandstone; planar parallel to low-angle cross-stratified, very fine- to fine-grained sandstone; and massive to finely planar laminated mudstone (Figure 5). Associated with the mudstone, flaser and lenticular structures are locally identified in the FMI images. At 6,555-6,556 ft in depth, climbing ripples are also identified. A few layers of mud intraclasts are observed in the FMI log. In the uppermost unit, coarse-grained or gravelly sandstone with massive structure, planar parallel to low angle trough crossed-stratification is common. Vertical to subvertical bioturbation is locally identified in the FMI log through the unit E.
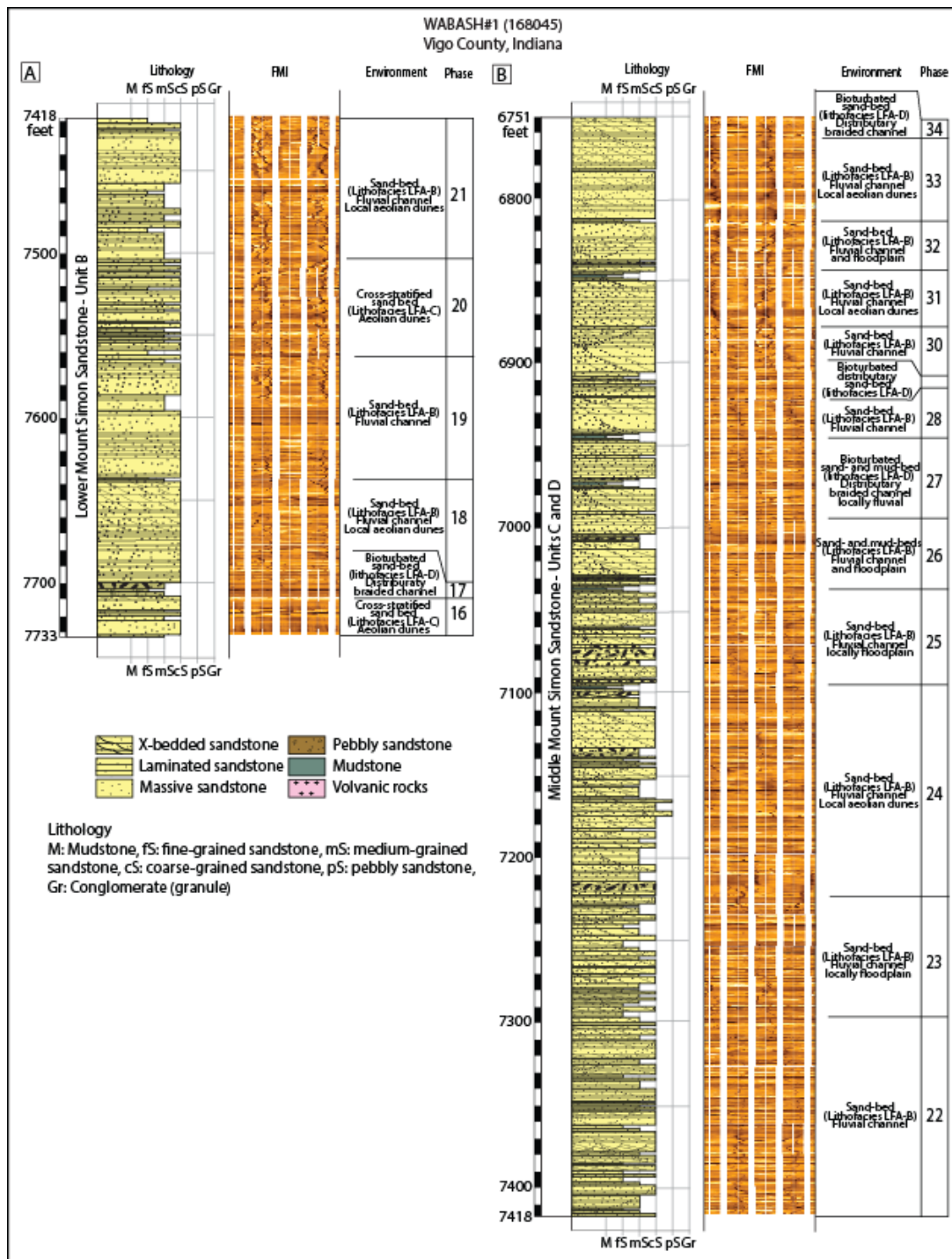
Figure 4: *Lithostratigraphic column, FMI log, and composition of the unit B and units C and D of the Lower and Middle Mt. Simon Sandstone respectively showing lithofacies associations and paleoenvironmental interpretation.*
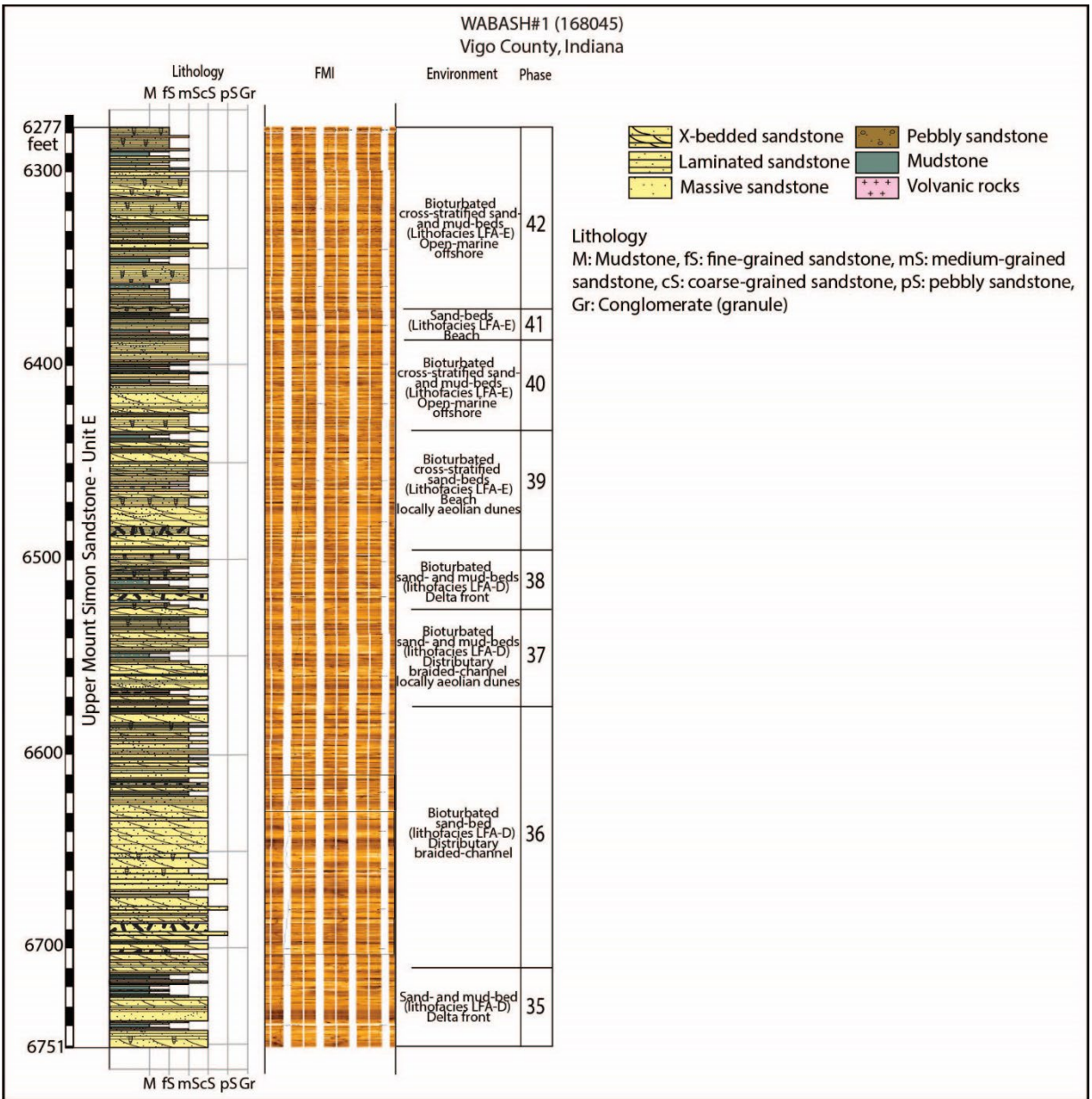
Figure 5: *Lithostratigraphic column, FMI log, and composition of the unit F Upper Mt. Simon Sandstone showing lithofacies associations and paleoenvironmental interpretation.*

PALEONTOLOGY

Trace fossils are the only fossils that are identified in the Argenta sandstone and Mt. Simon Sandstone through the Wabash #1 well. The identification of trace fossils is problematic because only the sedimentary structures and paleontology are identified from FMI logs. Most of the trace fossils display dominantly unbranched, vertical to subvertical burrows, with or without lining and passive fill. However, some of these tubes are horizontal to slightly inclined and cylindrical. Tube diameter is typically less than $^1/_{20}$ in, and tube length is from $^1/_{10}$ to a few inches. Morphology of some of these tubes is J-shaped, straight, or tortuous. *Planolites* is recognized at the base of the

arkose (unit A) of the Lower Mt. Simon Sandstone (Figure 6). It appears as elongated horizontal tubes, locally circular to elliptical sections, that actively fill sand fraction in mudstone. *Planolites* is reported as marine as well as non-marine. Other trace fossils have been identified in the unit E of the Upper Mt. Simon Sandstone. They appear as vertical to subvertical tubes, locally J-shaped, that can be interpreted as *Skolithos*-type ichnofacies, such as *Skolithos*, *Arenicolities* and *Cylindrichnus*. Those trace fossils are common in moderate to high-energy settings and episodic erosion or deposition in shallow to intertidal marine environments, as well as fluvial and other continental deposits (Droser, 1991; Melchor et al., 2012).
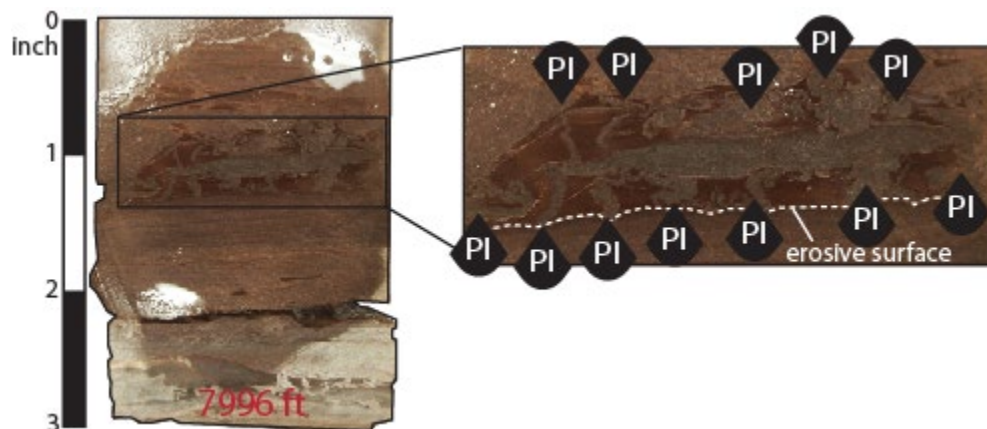
Figure 6: *Planolites-type burrows, formed by subvertical to horizontal tubes. Arkose (unit A), Lower Mt. Simon Sandstone, depth 7,995.9-7,996.0 ft.*

Samples from the arkose (unit A) of the Lower Mt. Simon Sandstone, which are collected for mineral separation for determination of conodont paleontology, are still in progress. The initial analytical process, hydrofluoric acid attack on the samples performed at the ISGS lab, was delayed several times, and the result is expected next fall.

COMPOSITION AND GRAIN SIZE ANALYSIS

Mineralogy

The Argenta sandstone displays a relatively high lithic content. As much as 78% of lithics are measured in the Argenta sandstone. The first 50 ft from contact with the basalt are significantly enriched in lithics, then their content decreases toward the top. The major lithic component is quartz, which ranges between 61.2 and 78.5% (av. 69.7%; n = 12). Monocrystalline quartz is dominant. Anorthite- and orthose-type feldspars are common, and their contents are up to 5.3% (av. 1.7% n = 12) and 4.3% (av. 1.8%; n = 12), respectively. Lithics such as magmatic-derived grains are abundant at the base of the formation. Authigenic quartz is abundant through the Argenta sandstone with a content of 8.5% (av. 5.0; n = 12). The illite is higher in the Argenta sandstone, and it ranges from 2.5 to 31.3% (av. = 13.8%; n = 12).

The overlying arkose unit of the Lower Mt. Simon Sandstone shows a similar content to the Argenta sandstone. The lithic quartz ranges from 16.5 to 75.8% (av. 54.5%; n = 9) with

monocrystalline quartz as dominant. The anorthite- and orthose-type feldspars range between 3.3 and 17.5% (av. 8.1% n = 9) and between 0 and 1.75% (av. 0.8%; n = 9), respectively. As authigenic contents, illite and quartz range up to 20% and from 0.5 to 26.3% (av. 14.3%; n = 9), respectively.

The lithics of the unit B of the Lower Mt. Simon Sandstone is only composed of monocrystalline quartz and anorthite- and orthose-type feldspars. The quartz content ranges between 64.8 and 82.5% (av. 74.7; n = 13). The anorthite- and orthose-type feldspars range between 0.5 and 7.5% (av. 3.1%; n = 13) and between 0 and 8.8% (av. 1.5%; n = 13), respectively. The authigenic quartz represents as much as 16.5% (av. 10.7%; n = 13) of total grains, while illite is nearly 5.8% (av. 2.9%; n = 13).

Table 1: *Descriptive statistical analysis for the grain size parameters from the unidentified sandstone, Argenta sandstone, and the Mt. Simon Sandstone. Data from Mingyue Yu and Jared Freiburg (ISGS).*

Grain size parameters

Formation/Member		Mean (Φ)	Sorting (σ)	Skewness (Ski)	Kurtosis (KG)
Precambrian Sandstone	Max.	2.23	1.48	0.29	0.88
	Min.	0.29	0.53	-0.21	0.47
	Ave.	1.43	0.83	0.03	0.64
Argenta Formation	Max.	1.85	1.77	0.22	0.98
	Min.	-0.29	0.58	-0.34	0.05
	Ave.	1.08	0.95	0.00	0.72
Mount Simon Sandstone					
Lower					
Unit A (Arkose)	Max.	3.75	1.74	0.52	0.70
	Min.	0.46	0.64	-0.24	0.50
	Ave.	2.40	0.89	0.09	0.62
Unit B	Max.	2.86	0.96	0.44	0.93
	Min.	0.82	0.41	-0.25	0.55
	Ave.	1.90	0.66	-0.02	0.67
Middle					
Units C and D	Max.	2.28	1.13	0.49	0.77
	Min.	1.57	0.56	-0.24	0.57
	Ave.	1.90	0.86	0.12	0.65
Upper					
Unit E	Max.	1.53	1.03	0.19	0.80
	Min.	3.43	0.44	-0.49	0.55
	Ave.	2.55	0.84	-0.01	0.66

The units C and D of the Middle Mt. Simon Sandstone are similar to the underlying unit B. The monocrystalline quartz and feldspars are dominant as lithics. The quartz content ranges from 66.3 to 75.3% (av. 71.3%; n = 7), while the volume of felspars is divided into anorthite (av. 2.6%; n = 7) and orthose (av. 0.3%; n = 7) grains. The average of authigenic quartz is 16.8% (n = 7), which has the same range as the unit B. The authigenic illite significantly decreases with an average of 1.8% (n = 7).

The unit E of the Upper Mt. Simon Sandstone shows an upward decreasing from 70.5% to 43.3% of quartz from the base to the top of the unit, while anorthite grains show a reverse trend from 2.0 to nearly 19%. The orthose-type feldspar is similar to the underlying units (av. 0.5%; n = 6). The authigenic contents are similar to the units C and D, but dolomite and illite are abundant to the top of the unit E.

GRAIN SIZE COMPOSITION

Grain size analyses are summarized in Table 1. The overall grain size of the analyzed samples ranges in sandstone. The cross-plot sorting (σ) vs mean (φ) shows that the unidentified sandstone vary between fine- to coarse-grained sandstone (Figure 7A). The sorting of these samples ranges between poorly and moderately sorted. The degree of symmetry or asymmetry of the grain-size distribution (skewness) ranges from fine-skewed and coarse-skewed (Figure 7B). The peakedness of the grain size distribution (kurtosis) is dominantly between platykurtic to very platykurtic (Figure 7C).
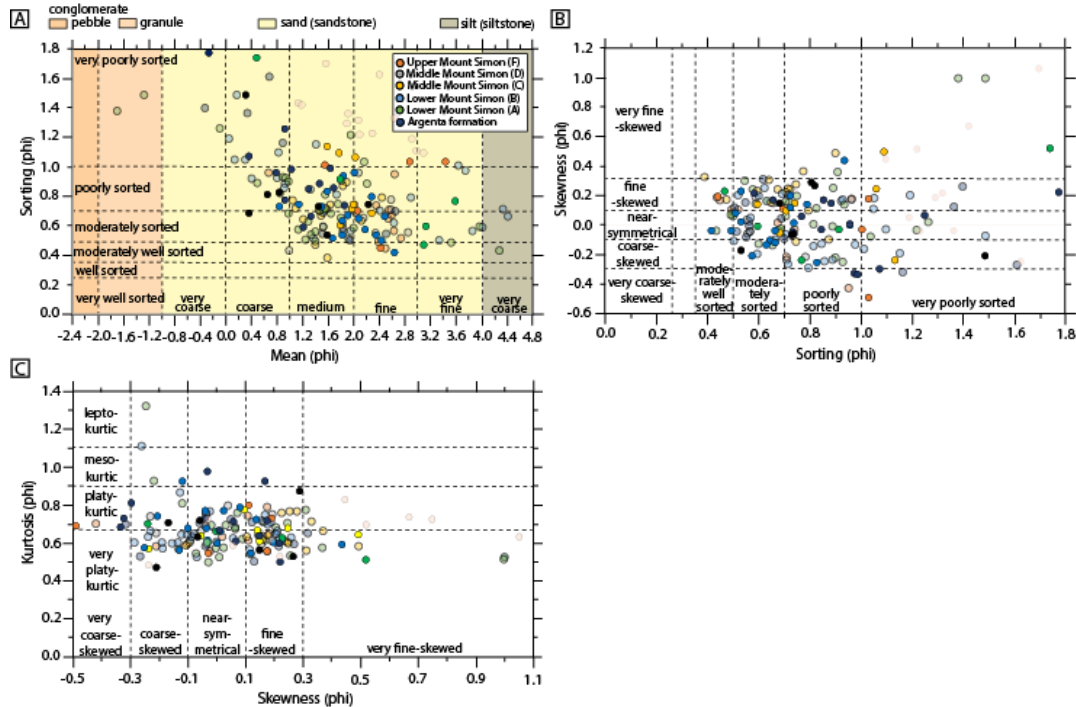
Figure 7: *Bivariate plots showing the grain size versus sorting, the sorting versus skewness, and the skewness versus kurtosis. In transparency, the data from T.R. McMillen #1 and VW #1 wells. The dashed lines show the descriptions of the grain size parameters.*

The grain size of the Argenta sandstone is coarser than the unidentified sandstone, and it shows dominantly medium- to very coarse-grained sandstone (Figure 7A). The sorting is dominantly poorly sorted (Figure 7B). The cross-plot skewness (Ski) vs kurtosis (KG) shows that the rock samples of the unidentified sandstone are dominantly fine- to very coarse-skewed and mesokurtic to very platykurtic (Figure 7C). The average of skewness is near symmetrical.

The arkose, unit A of the Lower Mt. Simon Sandstone, displays a grain size distribution and sorting that vary from very fine- to coarse-grained, very poorly to moderately sorted sandstone (Figures 7A-B). Their average is a medium-grained, poorly sorted sandstone. The cross-plot skewness vs kurtosis shows that the rock samples of the unit A are dominantly fine- to coarse-skewed and platykurtic to very platykurtic (Figure 7C). The average of skewness is near symmetrical.

The unit B of the Lower Mt. Simon Sandstone is coarser than the unit A, and the grain size distribution ranges between fine- to coarse-grained sandstone with an average of medium-grained sandstone (Figure 7A). The sorting is dominantly moderately sorted, but a few samples are poorly sorted. The skewness of the grain size distribution displays a range between very fine-skewed and coarse-skewed with an average of skewness near symmetrical (Figure 7B). The kurtosis is very platykurtic to platykurtic.

The grain size distribution and sorting of the Middle Mt. Simon Sandstone, which regroups the units C and D, dominantly displays a medium-grained, very poorly to moderately sorted sandstone (Figures 7A-B). The skewness and kurtosis range between fine-skewed and very coarse-skewed and between platykurtic and very platykurtic, respectively (Figure 7C).

The unit E of the Upper Mt. Simon Sandstone differs from previous rock samples because the grain size distribution is finer. The rock samples range from very fine- to medium-grained, very poorly to moderately sorted sandstone (Figures 7A-B). Most of the rock samples are fine-grained sandstone. The cross-plot skewness vs kurtosis shows that the rock samples of the unit A are dominantly fine- to very coarse-skewed and platykurtic to very platykurtic (Figure 7C). The average of skewness is fine-skewed.

SEDIMENTOLOGY

Lithofacies Associations

Five distinct lithofacies associations are identified in the Argenta sandstone and Mt. Simon Sandstone intervals of the Wabash #1 well: (1) gravelly braided river in waterlaid alluvial-fluvial deposits within incised valleys, (2) sandy braided river in a fluvial plain, (3) aeolian dunes in a fluvial plain, (4) sandy braided river delta deposits bordered by lagoon or lacustrine fine-grained deposits, and (5) open-marine coastal deposits. In total, fourteen lithofacies are identified and summarized in Tables 2 and 3. Detailed descriptions and interpretations are presented below.
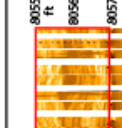
Lithofacies association LFA-A: waterlaid alluvial fan

Description: Lithofacies association LFA-A contains the lithofacies A1 and A2. The lithofacies A1 is the coarsest facies of the alluvial-fluvial plain. Lithofacies A1 comprises a few inches-thick, fining-upward sequences that are composed of massive (Gcm) or crudely stratified (Gh), clast-supported to sandy matrix-supported conglomerates in coarse-grained sandstone matrix. Basal scours are common. In the FMI log, the difference of resistivity appears massive and irregular with the recognition of coarse-grained sands, granules, and pebbles.

Lithofacies A2 is a faintly horizontal (GRm), low-angle (GRp) to trough (GRt) cross-stratified, pebbly-supported sandstone. The matrix is composed of a fine- to coarse-grained sandstone. The lithology of granules and pebbles is similar to the lithofacies A1. Individual beds eroded at the top and base contacts are 1 to 3 in thick (locally thicker). A normal grading at the bottom of beds is locally identified in the FMI log. In the FMI log, the difference of resistivity appears planar parallel and trough cross-stratified with the recognition of coarse-grained sands, granules, and pebbles.

Interpretation: The lithofacies association LFA-A represents the transition between a distal section of waterlain alluvial fans (lithofacies A1) and a proximal section of fluvial braided river plain (lithofacies A2), bordered by a floodplain (see lithofacies association LFA-B for description and interpretation). The lithofacies A1 records channel fill deposits in a waterlaid alluvial fan system, commonly characterized by relatively well sorted, sandy to gravelly lenses and sheets that were formed in high-energy water flow conditions in the absence of fine-grained suspension materials (Miall, 1977; Moscariello, 2018). The massive structure was developed in high-energy and persistent stream flows by traction currents and low-sinuosity channel systems (Miall, 2010). The lithofacies A2 represents fluvial channel bars formed by bedload-related traction currents by transport and saltation of grains (Maciaszek et al., 2019). The normal grading, forming locally gravel-sand couplets, was formed by unsteady sediment dumping under supercritical bedload currents (Moscariello, 1998). Proximal alluvial fan facies are associated with turbulent and supercritical flows of debris flow deposits.

Table 2: Description and interpretation of lithofacies and lithofacies associations based on high-resolution Fullbore Formation Micro-Imager (FMI) and gamma-ray logs of the Wabash#1 borehole, Vigo County (Indiana).

Lithofacies association	Lithology	Code	Sedimentology	FMI	Characteristics in FMI	Interpretation
LFA-A Waterlaid alluvial-fluvial system	A1: Massive sandy conglomerate	Gcm Gh	Massive or crudely stratified clast-supported to sandy matrix-supported conglomerates with a coarse-grained sandstone, composed of subangular to subrounded granules and pebbles of polymitic fragments (quartz, feldspar and lithic). Beds range from 1 to 5 inches in thickness. Local scour surfaces at the base.	8235 ft 8236 8237 8238	Massive, irregular appearance with granules and gravels.	Reworking of sediments in high hydro-dynamic conditions by strong subaqueous tractive current forming channel deposits.
	A2: Cross-stratified sandy conglomerate	GRm GRp GRt	Faintly horizontal stratified, low-angle to through cross-stratified clast-supported conglomerate to very coarse-grained sandstone, poorly sorted, composed of subangular to sub-rounded granules and pebbles of quartz, feldspar and lithic fragments. Beds range a few inches to 1-3 feet in thickness. Sharp erosive surfaces atop base and top.	8371 ft 8372 8373 8374	Planar parallel to through cross-stratified appearance with granules and gravels.	Reworking and transport of sediments in hyperconcentrated conditions by to tractional flows forming possible channel bars or channel deposits.
LFA-B Fluvial system	B1: Massive sandstone	Sm	Fine- to very coarse-grained, moderately to poorly-sorted massive sandstone, locally normal grading. Absence of sedimentary structures. Local dispersed subangular granules and pebbles of quartz, feldspar and lithic fragments, and mud intraclasts (<1/2 to 3 inches). Beds range a few inches to 1-3 feet in thickness. Local erosive surfaces at the base.	7234 ft 7235 7236 7237	Massive appearance.	Rapid deposition of hyperconcentrated to tractional flows in crevasse splay channels or channel deposits.
	B2: Horizontal to low-angle cross-stratified sandstone	Sh	Fine- to very coarse-grained, moderately to poorly-sorted sandstone with horizontal to low angle cross-stratification (less than 5°). Local dispersed subangular granules and pebbles of quartz, feldspar and lithic fragments. Beds range a few inches to 1-3 feet in thickness. Rare scour surfaces at the base.	8055 ft 8056 8057 8058	Sets of planar, straight or irregular appearance.	Predominantly tractional deposition from bedload transport in transition between lower and upper flow regime forming crevasse splay channels or channel deposits.
	B3: Trough cross-stratified sandstone	St St_d	Fine- to very coarse-grained, moderately to poorly-sorted sandstone with unidirectional trough crossed stratification (less than 20°). Local thin normal grading. Regular to irregular thin single mud drapes (1/10 to 1/2 inches in thickness). Local dispersed subangular granules and pebbles of quartz and lithic fragments. Beds range a few inches to 1-3 feet in thickness.	8055 ft 8056 8057 8058	Unidirectional sets of trough cross-stratified appearance.	Migration of subaqueous sandy dunes in unidirectional lower flow regime, and deposition by settling down of suspended load in standing water.
	B4: Heterolithic sandstone and siltstone	Hr Hr_d Hw	Heterolithic structures composed of very fine- to fine-grained, rarely coarse- to medium-grained, sandstone, fine to coarse-grained siltstone and mudstone with wavy, lenticular or flaser laminations. Locally thin parallel to wavy laminations of single muddy drapes (1/10 to 1/2 inches in thickness). Non- to weak normal grading occurs locally. Sharp or erosive surfaces at the base. Beds range from 1 to 5 inches in thickness.	8017 ft 8018 8019 8020	Planar parallel to wavy irregular appearance.	Alternating traction process with sub-aqueous ripples in unidirectional lower flow regime and deposition by decantation of suspended load deposited in a levee overbank (flood plain)
	B5: Mudstone	Fm Fl	Brick red to green mudstone, massive to thin parallel lamination. Beds range from 1/4 inches to 1-2 feet in thickness.	8017 ft 8018 8019 8020	Massive or planar appearance.	Floculation of clay, suspension settling deposited in a levee overbank (flood plain).

22

Lithofacies association LFA-B: fluvial braided river

Description: Lithofacies association LFA-B includes five distinct lithofacies: (1) massive sandstone (lithofacies B1), (2) horizontal to low-angle cross-stratified sandstone (lithofacies B2), (3) trough cross-stratified sandstone (lithofacies B3), (4) heterolytic sandstone, siltstone, and mudstone (lithofacies B4), and (5) mudstone (lithofacies B5). Lithofacies B1 is characterized by a few inches-thick, fining-upward sequences that are commonly composed of massive coarse- to pebble-grained, poorly to moderately sorted sandstone (Sm) at the bottom, overlain by fine- to medium-grained, moderately sorted sandstone. Dispersed coarse-grained, sand- to pebble-sized grain fraction of quartz, feldspar, lithic fragments, and abundant mud intraclasts are locally present in this lithofacies. Erosive surface contacts are common. In the FMI log, the difference of resistivity appears massive. The lithofacies B1 vertically grades and is fine- to very coarse-grained, faintly horizontal, low-angle cross-stratified sandstone (Sh), here attributed to the lithofacies B2. The angle of distinct stratification is lower than 5°. Rare scour surfaces are observed at the bottom of individual beds. In the FMI log, the difference of resistivity shows an appearance of planar parallel, straight and irregular sets.

Lithofacies B3 is marked by fine- to coarse-grained, moderately to poorly sorted, trough cross-stratified sandstone (St). The angle of distinct stratification is lower than 20°. Like the lithofacies B2, dispersed coarse-grained, sand- to pebble-sized grains are locally observed. Local ripples are observed. The individual beds vary from a few inches to a maximum 3-4 ft in thickness. Additionally, they can be marked by a scour surface at the bottom that is draped by regular to irregular single mud partings or layers. In the FMI log, the difference of resistivity shows unidirectional sets of trough cross-stratification.

Lithofacies B4 consists of very fine- to fine-grained, rarely coarse- to medium-grained, moderately to well sorted sandstone with flaser-type and wavy-type laminations. Flaser laminations (Hr) show small lenses of mud or silt within coarsely grained sands. They are concave upwards and fill the depressions between poorly visible ripples. The wavy laminations (Hw) form alternating, continuous, thick, sandy and thin, muddy layers within the channel-fill deposits. Locally, the depressions of wavy laminations (Hrd) are filled by single, thin mud drapes. When the amount of mud increases, lenticular laminations (Hr) are common in this lithofacies. Theses sedimentary structures are near-symmetrical, convex both upwards and downwards, lens-like, coarser-grained sands (e.g., muddy sand) in a matrix of finer-grained materials (e.g., mudstone). No grading is observed. The bottom contact can be marked by an erosive surface. In the FMI log, the difference of resistivity shows thin, alternating dark and light colors with planar parallel to wavy irregular appearance.

Lithofacies B5 is characterized by thin individual beds of pure mudstone (Fm) and finely planar, locally crinkly, laminated mudstone (Fl). Rare, small-scale, vertical to oblique bioturbation is preserved locally. In the FMI log, the difference of resistivity shows light-colored massive or planar appearances.
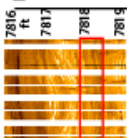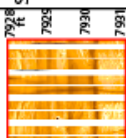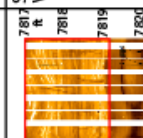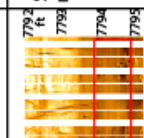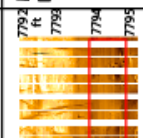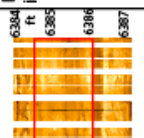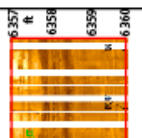
Interpretation: The lithofacies association LFA-B represents low-energy channel and floodplain deposits in a fluvial system. The finer materials than LFA-A indicate less kinetic energy. Lithofacies B1 to B3 may represent small-scale fluvial channels formed by low-energy traction flows. Thin mudstone layers within sandstones, which show a vertically normal grading, can be interpreted as crevasse splay channels on levee breaching or overbanking along channel bars or floodplains (Miall, 1996; Cain and Mountney, 2009). When the bedload-related transport is higher than the suspended-load transport, ripples can be formed on the top foreset of channel bars. Heterolithic structures were principally formed when low-energy water flow currents changed alternatively. Sandy materials were deposited under the highest flow regime (i.e., <0.5 m/s), while fine-grained materials were formed atop the ripples in intervals of slack to almost stagnant water. Erosive surfaces recorded the changes of flow regime (Maciaszek et al., 2019). The finest materials of the braided river system were deposited by suspension in a floodplain environment (Miall, 1996).

Lithofacies association LFA-C: aeolian dunes
Description: Lithofacies association LFA-C includes two lithofacies: planar stratified sandstone (lithofacies C1) and large cross-stratified sandstone (lithofacies C2). Lithofacies C1 comprises massive (Sm), faintly horizontal stratified (Sh), medium-grained, moderately sorted sandstone. The individual beds have a maximum thickness of a few feet. In the FMI log, the difference of resistivity appears planar or straight.

Lithofacies C1 normally grades to lithofacies C2, which is characterized by single to multiple bedsets of fine- to medium-grained, moderately to well sorted sandstone with uni- to bidirectional low-angle (Sp) and crossed (Sc) stratifications. Their angle is comprised between 5° and 15° and between 15° and 30°. In the FMI log, the difference of resistivity appears planar or straight. The cross-stratified bedsets are often eroded by an overlying single bedset. Rare climbing ripples (Src), which muddy materials can fill the depressions (Srcd), are observed. The individual beds are marked by an erosive surface at the bottom, and they range a few feet in thickness. In the FMI log, sets of crossed-stratification is visible by the difference of resistivity.

Interpretation: The lithofacies association LFA-C represents the migration of aeolian sandy dunes by mainly saltation transport on exposed channel bars, splay crevasses, or overbanks on floodplains (Lovell and Bowen, 2013). High windblown velocity caused sand deflation and accretion surfaces on the flat-related sand dunes. The deflation pattern is marked by the removal of finer sediments by wind activity, leaving coarse-grained sediments, such as coarse-grained sand, granule, and pebble, which cannot be moved in suspension or saltation (Reineck and Singh, 1986). The accretion surface is marked by the deposition of fine-grained sediments by migration of sand sheets forming a sand ridge or by sand avalanche if the slip face exceeded at least 34°. Normal grading is characterized by planar stratified sandstone at the base and small- to large-scale cross-stratified sandstone at the top.

Lithofacies association	Lithology	Code	FMI	Sedimentology	Characteristics in FMI	Interpretation
LFA-C Aeolian-fluvial system	C1: Planar stratified sandstone	Sm, Sh		Massive to faintly horizontal stratified medium-grained, moderately sorted, sandstone with local horizontally stratified dispersed subangular granules and coarse-grained sands of quartz (lag deposit). Beds range a few feet in thickness.	Planar, straight appearance.	High windblow velocities or grainfall deposition related to the zones of flow separation on horizontal surfaces (accretion stage).
	C2: Large cross-stratified sandstone	Sc, Sc_d, Sp, Scr		Fine- to medium-grained, well-sorted sandstone with bidirectional crossed stratification (15-30° in angle) and low-angle cross-stratification (5-15° in angle; pinstripe sets). Rare climbing ripples and mud drapes. Contacts are locally erosional and planar. Beds range a few feet in thickness.	Sets of crossed stratification in appearance.	Migration of aeolian sandy dunes in bimodal upper windblow regime by saltation and sand avalanche if slip face exceeds 34°.
LFA-D Meandering river delta-lacustrine/lagoon system	D1: Bioturbated cross-stratified sandstone	St, Sc, Sc_i		Fine- to medium-grained, moderately to poorly-sorted small-scale through cross-stratified sandstone, locally normal gradded and accumulation of siltstone and mudstone at the top. Bioturbation in muddy sandstone composed of fine sandstone and fine materials. Local layers of granules and pebbles. Beds range from a few inches to 1-2 feet in thickness.	Sets of crossed stratification in appearance. Vertical bioturbation.	Low flow regime and low current velocities caused by the interaction of river outflows and lacustrine/lagoon wave currents in a deltaic front environment forming mouth sand bars.
	D2: Bioturbated horizontal to planar stratified muddy sandstone and mudstone	Hr, Hr_d, Hw		Heterolithic structures composed of thin bedded of very fine- to medium-grained, medium-grained, sandstone and mudstone with wavy, lenticular or flaser laminations. Abundance of bioturbation. Beds range from 1 inch to 1 foot in thickness.	Sets of planar to wavy stratified in appearance. Vertical bioturbation.	Fall out and small-scale ripple migration in relative high energy flow regime and large input of braided river delta.
	D3: Bioturbated mudstone	Fm, Fl		Massive and finely stratified mudstone, strongly biotubated. Local thin layers of very fine- to medium-grained, moderately sorted sandstone. Rare deformation structures. Beds range from a few inches to 1-2 feet in thickness.	Massive appearance. Vertically crossed by bioturbation.	Floculation of clay by suspension settling. Possible turbidity currents formed in a delta-front slope of a lacustrine/lagoon environment.
LFA-E Beach and open marine offshore system	E1: Bioturbated cross-stratified gravelly sandstone	St, Sc, Sc_i		Fine- to medium-grained, locally coarse-grained or gravelly, moderately to poorly-sorted, sandstone. Massive stucture is minor, but low-angle through cross-stratification is dominant. Ripples and mud intraclasts are common. Bi-directional sets are locally observed in FMI. Bioturbation is abundant. Beds range from a few inches to 1-2 feet in thickness.	Bidirectional sets of crossed stratification in appearance. Vertical bioturbation.	Low to moderate flow regime caused by marine currents and/or waves.
	E2: Bioturbated heterolithic sandstone and mudstone	Hr, Hr_d, Hw, Fm, Fl		Heterolithic structures composed of thin bedded of very fine- to medium-grained, medium-grained, sandstone and mudstone with wavy, lenticular or flaser laminations. Ripples are common. Abundance of bioturbation. Beds range from 1 inch to 1 foot in thickness.	Sets of planar to wavy stratified, masive if mudstone, in appearance. Vertical bioturbation.	Fall out of fine-grained sediments in a marine environment.

Table 3: Description and interpretation of lithofacies and lithofacies associations based on high-resolution Fullbore Formation Micro-Imager (FMI) and gamma-ray logs of the Wabash#1 borehole, Vigo County (Indiana).

Lithofacies association LFA-D: breaded river delta

Description: Lithofacies association LFA-D includes three distinct lithofacies: (1) bioturbated cross-stratified sandstone (lithofacies D1), (2) bioturbated horizontal to planar stratified muddy sandstone and mudstone (lithofacies D2), and (3) bioturbated mudstone (lithofacies D3). Lithofacies D1 is characterized by fine- to medium-grained, poorly to moderately sorted sandstone with massive structure (Sm), planar parallel (Sh) to trough crossed-stratification (St). Additionally, graded bedding, erosional bases, and bottom mud drapes (Std) are locally observed. Interlayers of granules and pebbles are common. Apparent vertical to oblique bioturbation can be identified in the FMI log. In the FMI log, the difference of resistivity shows bidirectional sets of crossed-stratification.

Lithofacies D2 consists of thin-bedded, alternating mudstone and fine- to medium-grained, moderately sorted sandstone with heterolithic structures, (i.e., flaser, wavy, and lenticular structures). Occasionally, small-scale vertical and oblique bioturbation can be identified in the FMI log. In the FMI log, the difference of resistivity shows alternating sets of light and dark planar to wavy stratification.

Lithofacies D3 comprises strongly bioturbated mudstone with massive (Fm) or finely stratified (Fl) structures. Lithofacies D3 is often associated with the lithofacies D2. Local thin layers of very fine- to medium-grained, moderately sorted sandstone are present. Rare deformation structures can be identified in the FMI log. In the FMI log, the difference of resistivity appears massive.

Interpretation: The lithofacies association LFA-D represents a braided river delta fan system. The lithofacies D1 can be interpreted as distributary braided channels on delta-front lobes that are commonly characterized by clast debris, basal scour surfaces, and their thin bedding (Bhattacharya and Walker, 1991). The bidirectional trough crossed-stratification was produced by reversal currents and the direction of migration of the sand-sized sediments, which indicates a tidally influenced environment. The lithofacies D2 represents mouth bars deposited by alternating oscillatory and traction regimes, forming subaqueous ripples under lower flow regime and deposition of fine-grained suspended load (Dalrymple, 2010). The finer-grained materials of the lithofacies D3 were deposited in lagoon or lacustrine environments under flocculation of clay suspension or suspension settling from standing water (Miall, 2006). This lithofacies association LFA-D is marked by an intensive bioturbation.

Lithofacies association LFA-E: open-marine offshore and beach

Description: Lithofacies association LFA-E includes two distinct lithofacies: (1) bioturbated low-angle cross-stratified gravelly sandstone (lithofacies E1) and (2) bioturbated heterolithic sandstone and mudstone (lithofacies E2). Lithofacies E1 consists of fine- to medium-grained, locally coarse-grained or gravelly, with massive structure (Sm), planar parallel (Sh) to low-angle trough crossed-stratification (St). Current ripple, climbing ripple, and muddy intraclasts are common. Apparent (sub)vertical bioturbation is locally identified in the FMI log. Erosional bases and bottom mud drapes are commonly observed. The individual beds range from a few inches to several feet in

thickness. In the FMI log, the difference of resistivity shows unidirectional, locally bidirectional, sets of crossed-stratification.

Lithofacies E2 is commonly associated with lithofacies E1. It consists of thin-bedded, alternating mudstone and fine- to medium-grained, moderately sorted sandstone with heterolithic structures (i.e., flaser, wavy, and lenticular structures). Ripples are common. Vertical and oblique bioturbations are identified in the FMI log. The individual beds range from a few inches to 1 ft in thickness. In the FMI log, the difference of resistivity shows alternating sets of light and dark, planar to wavy stratification.

Interpretation: The lithofacies association LFA-E corresponds to an open-marine coastal environment that is composed of a beach and offshore system. The low-angle stratified, coarse- to gravelly-grained sandstone is interpreted as a sediment that is deposited in a beach environment. The bidirectional sets as identified in the FMI log are considered marine dunes that are tidally influenced. The lack of high-energy structures reflects a calm water surface. However, some ripples can indicate the action of marine currents and/or waves. The lenticular and flaser structures reflect alternating oscillatory and traction regimes, forming subaqueous ripples under lower flow regime and deposition of fine-grained suspended load (Dalrymple, 2010).

DEPOSITIONAL SEQUENCE

A framework of 42 depositional sequences is proposed for the Argenta sandstone and Mt. Simon Sandstone. All defined sequences are based on the variation of lithofacies associations that are defined by the variation of resistivity in the FMI log. The Argenta sandstone comprises 5 distinct depositional sequences (DS1 to DS5; Figure 3A). The first depositional sequence (DS1) comprises approximately 150 ft thick sandy deposits (lithofacies A2) that are overlain by approximately 160-ft-thick, gravelly sandstones and sandy conglomerates (lithofacies A1) deposited (DS2) in a distal waterlaid alluvial fan system. The waterlaid alluvial deposits vertically progress to nearly 25-ft-thick braided river delta facies (lithofacies association LFA-D; DS3) that are composed of braided channels and distributary braided rivers (lithofacies D1) (Figure 8A). The braided river delta facies are overlain by approximately 60 ft of alluvial gravelly sandstones and sandy conglomerates (lithofacies A1; DS4). The unit ends by approximately 40 ft of braided channels and distributary braided rivers (lithofacies D1; DS5).

The Lower Mt. Simon Sandstone contains 16 distinct depositional sequences (DS6 to DS21; Figures 3B and 4A). Ten depositional sequences (DS6 to DS15; Figure 3B) are defined in the arkose (unit A). At least ¾ of sediments of this unit are an aeolian origin, associated with deposits accumulated in a fluvial plain system (Figure 8B). The lower part of this unit contains approximately 160-ft-thick fluvial sandstone (DS6 and DS8) with thin layers of mudstone that are interpreted as deposited in a floodplain. A thin interval of delta front facies (lithofacies association LFA-D; DS7) separates the DS6 to DS8. The fluvial-aeolian transition is identified in DS9, which consists of approximately 45-ft-thick fluvial cross-stratified sandstone (lithofacies association LFA-B), draped atop by thin layers of mudstone and aeolian dunes (lithofacies association LFA-

C). The overlying depositional sequences (DS10, DS11, and DS13) show approximately 90-ft-thick of fine- to medium-grained trough cross-stratified sandstone that is accumulated in an aeolian-influenced fluvial plain. Locally, delta front facies (lithofacies association LFA-D; DS12 and DS15) occur in the upper part of the unit. The depositional sequences (DS16 to DS21; Figure 4A) of the unit B show similar environments (Figure 8C). The lowermost unit B displays approximately 95-ft-thick aeolian-influenced fluvial deposits (lithofacies association LFA-C; DS16 and DS18) that are associated with distributary braided river sandstones (lithofacies association LFA-D; DS17). These depositional sequences are overlain, from the base to the top, by approximately 75-ft-thick fluvial sand dunes (lithofacies association LFA-B; DS19), 60-ft-thick aeolian sand dunes (lithofacies association LFA-C; DS20), and a mixture between fluvial and aeolian sediments (DS21).

The Middle Mt. Simon Sandstone, which includes the units C and D, contains 13 distinct depositional sequences (DS22 to DS34; Figure 4B). The depositional sequences (DS22 to DS26 and DS28 to DS33) of the Middle Mt. Simon Sandstone dominantly contain fluvial sediments (lithofacies association LFA-B), which includes massive sandstone (lithofacies B1), horizontal to low-angle cross-stratified sandstone (lithofacies B2), and trough cross-stratified sandstone (lithofacies B3) at the base, that evolve to massive sandstone (lithofacies B1), horizontal to low-angle cross-stratified sandstone (lithofacies B2), heterolytic sandstone, siltstone, and mudstone (lithofacies B4) and mudstone (lithofacies B5). Most of these depositional sequences are associated with aeolian fine- to medium-grained cross-stratified sandstones (lithofacies association LFA-C). Two intervals (DS27 and DS34) of bioturbated planar and cross-stratified sandstone, which are interpreted as distributary channel sand dunes formed in a delta front system, are identified near the contact with the Upper Mt. Simon Sandstone (Figures 8D-E).

The unit E of the Upper Mt. Simon Sandstone is deltaic (DS35 to DS38) in the lower part, then marine (DS39 to DS42) in the upper part (Figures 5 and 8A). The base of the unit E is clearly marked by deltaic deposits. DS35 comprises approximately 30-ft-thick sandstone, heterolytic sandstone, and mudstone (lithofacies D1 to D3 of the lithofacies association LFA-D) that are accumulated in a mouth of a delta front system. This depositional sequence is overlain by a shift to fluvial-influenced distributary river sand dunes (lithofacies D1 of the lithofacies association LFA-D; DS36 and DS37), periodically under windblown regime as shown by the accumulation of aeolian-derived sandstones (DS37). DS38 marks the transition between delta front and marine coastal systems. Approximately 30-ft-thick sandstone, heterolytic sandstone, and mudstone (lithofacies D1 to D3 of the lithofacies association LFA-D) precede bioturbated, tidally influenced, cross-stratified sandstone that is considered as deposits in a beach (lithofacies E1; DS39). Bioturbated sandstone and mudstone of the DS40 and DS42 are interpreted as offshore deposits. A 20-ft-thick interval of beach facies is identified in DS41.
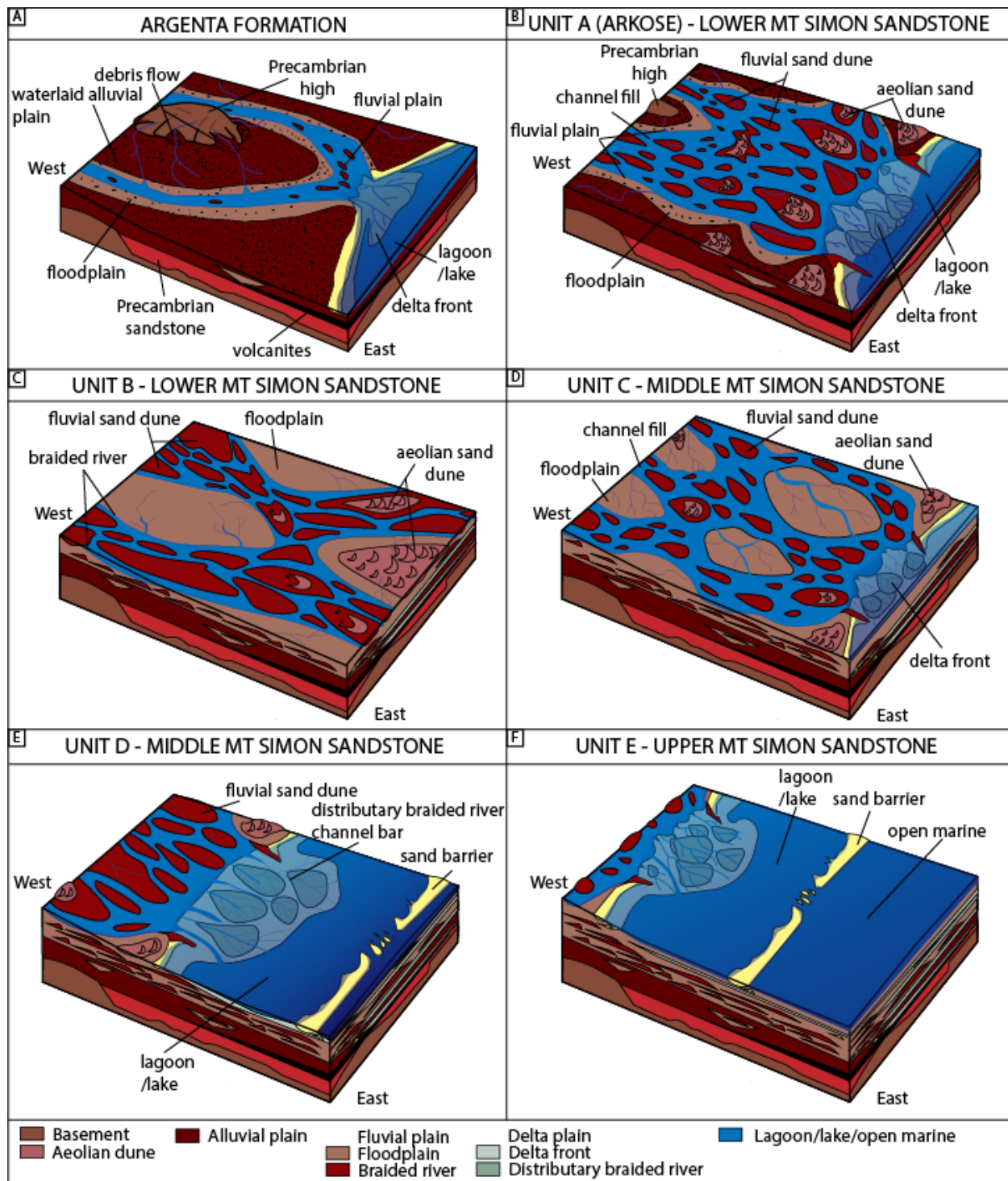
Figure 8: *3D depositional models for the Wabash #1 well showing the paleoenvironmental evolution of the Argenta sandstone and Mt. Simon Sandstone. (A) Waterlaid alluvial-fluvial fan system, (B) Eolian-influenced fluvial plain bordered by delta fan system, (C) Eolian-influenced fluvial plain, (D) Fluvial plain bordered by delta fan system, (E) Delta fan system opened on a lagoon/lake and beach, (F) Open-marine offshore system.*

29

INTERPRETATION

Composition and Grain Size Interpretation

The mineral composition of the Argenta sandstone shows a high lithic content likely from eroded Precambrian crystalline sources (e.g., paleohigh, paleomountain, etc.), in which coarse-grained sediments have been transported under high-energy regime. The occurrence of magmatic-volcanic fragments suggests a regional source, such as from the Eastern Granite-Rhyolite Province. The major mineral is a monocrystalline quartz, while feldspars (e.g., anorthite, orthose) are minor. A few polycrystalline quartzes are identified, which confirm an igneous source of the mineral content. Authigenic quartz (e.g., overgrowth cement) was formed during deep burial. The determination of authigenic clay such as illite was probably formed by illitization of K-feldspars and the early-formed kaolinite during deep burial. Traces of kaolinite are identified in the T.R. McMillen #2 well. Such kaolinite was probably formed under warm climate with alternating humid and dry seasons.

The igneous content in the arkose (unit A) of the Lower Mt. Simon Sandstone significantly decreases, which corresponds to a partial denudation of the Precambrian crystalline paleoreliefs. The complete erosion of paleoreliefs is highlighted by the absence of igneous content in the overlying units of the Mt. Simon Sandstone. The content of feldspars slightly decreases in the arkose and overlying units. The grain size differs between the Wabash #1 well and the T.R. McMillen #2 and VW #1 wells. The sorting is better organized in the Wabash #1 well than the other wells, which indicates a long transport of grains from sources. However, the grain sizes in the T.R. McMillen #2 and VW #1 wells are finer due to the high volume of aeolian deposits. Kaolinite is measured in trace in the arkose within the T.R. McMillen #2 well, while illite is well represented in the Wabash #1 well. The other units do not contain kaolinite, which could indicate that (1) all kaolinite was transformed into illite by illitization during deep burial, or (2) the kaolinite was absent, while the smectite was dominant, and the smectite was transformed into illite. Smectite is commonly considered as a paleoclimatic indicator of arid, semi-arid, or temperate climates with contrasting seasons and a pronounced dry season. The unit E of the Upper Mt. Simon Sandstone shows an upward-increase of illite near the boundary with the Eau Claire Formation, which could be the result of a high content of marine smectite that has be transformed into illite during the deep burial.

The depositional environment of sediments could be reconstructed using the grain size parameters (i.e., mean, sorting, skewness, and kurtosis) that reflect differences in the fluid-flow mechanisms of sediment transportation and deposition (Sutherland and Lee, 1994). The Argenta sandstone and Lower Mt. Simon Sandstone (Unit A/arkose and unit B) show significant shifts from positive to negative skewness. This negative shift of skewness can be interpreted as the result of a selective erosion from Precambrian crystalline basement paleohighs, which finer materials are preferentially transported. The Middle and Upper Mt. Simon Sandstone display a positive skewness, which is therefore interpreted as the relatively high proportion of coarse grains in the fluvial sand dunes

(Folk, 1966). In some case, the skewness can positively increase because of the decrease in the amount of fines that can be removed as the grain size increases (Flemming, 2007).
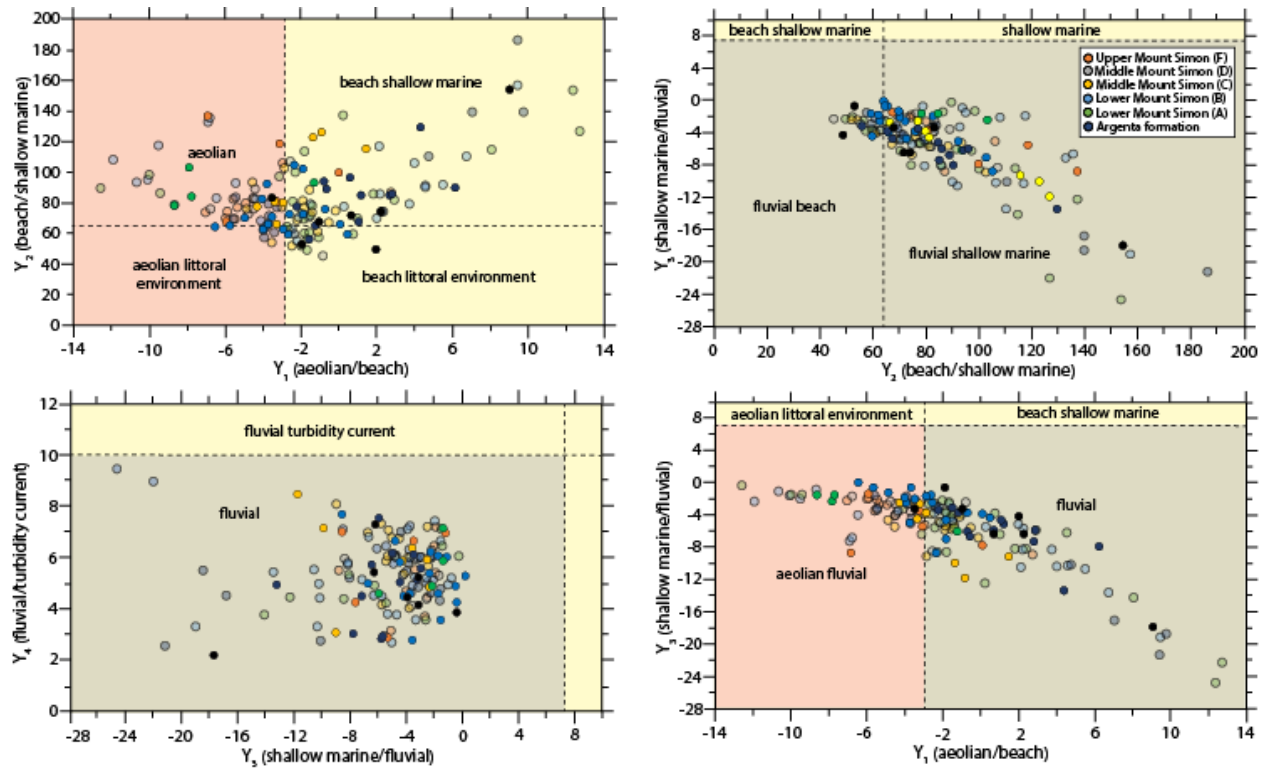
Figure 9: *Plots of statistical method of linear discriminate function analysis from the formulae of Sahu (1964). The plots show the discrimination of paleoenvironments for the unidentified sandstone, Argenta sandstone, and Mt. Simon Sandstone. Most of the samples have fluvial and aeolian origins. In transparency, the data from the T.R. McMillen #1 and VW #1 wells.*

Skewness associated with kurtosis can interpret the genesis of sediment by quantifying the degree of normality of its size distribution (Folk, 1966). The cross-plot skewness vs. kurtosis shows that all rock samples of the Argenta sandstone and Mt. Simon Sandstone lie within the very platykurtic to platykurtic range. Variation in the kurtosis values reflects the flow characteristic of the depositing medium grain size population, and the subordinate of finer size of platykurtic nature of sediments reflects the maturity of the sand. Generally, dune sands have positive skewness and are mesokurtic, while aeolian sands have positive skewness and are leptokurtic (Martins, 1965). Beach sands are normal or negative skew and leptokurtic (Martins, 1965). The grain size distribution shows that when sediment is removed by a unidirectional river or wind, the grains that can be transported in suspension or by saltation vary with the competency of the transport of medium-sized materials, without changes in fine materials, which can explain the positive skewness. In beach environments, transported material is submitted to bidirectional tidal currents, which coarser materials may be carried inward and deposited on the beach and fine material may be carried out to the deeper water.

The determination of paleoenvironments can be revealed using grain size parameters (i.e., mean, sorting, skewness, and kurtosis). Statistical method of linear discriminate function (LDF) analysis, developed by Sahu (1964), can distinguish the nature of sediment deposition. The analysis was carried out using the following equations: (1) Aeolian/beach: $Y1 = -3.5688\,\varphi + 3.7016\,\sigma2 - 2.0766$ Ski $+ 3.1135$ KG. If Y is > -2.7411, the environment is "Beach", but if Y is < -2.7411, the environment is "Aeolian"; (2) Beach/shallow agitated water: $Y2 = 15.6534\,\varphi + 65.7091\,\sigma2 + 18.1071$ Ski $+ 18.5043$ KG. If Y is < 63.3650, the environment is "Beach", but if Y is > 63.3650, the environment is "Shallow marine"; (3) Shallow marine/fluvial environment: $Y3 = 0.2852\,\varphi - 8.7604\,\sigma2 - 4.8932$ Ski $+ 0.0482$ KG. If Y is > -7.4190, the environment is "Shallow marine", but if Y is < -7.4190, the environment is "Fluvial"; (4) Fluvial/turbidity: $Y4 = 0.7215\,\varphi + 0.403\,\sigma2 + 6.7322$ Ski $+ 5.2927$ KG. If Y is > 10.000, the environment is "Turbidity", but if Y is < 10.000, the environment is "Fluvial".

Figure 9 shows a significant amount of coastal sands for the overall rock samples. However, a few amounts of these sands have an aeolian source, as shown by the distribution of the Lower Mt. Simon Sandstone (units A and B) samples. None of these sands have a source from aeolian littoral environment. The overall sands from a source of shallow marine/beach environments fall in the fluvial process, and none of these samples have a marine source (Figure 9). The cross-plot Y1 vs. Y3 differentiates the fluvial process to aeolian sediments. All sands from the unidentified sandstone and Argenta sandstone show a fluvial source, while the sands from the Mt. Simon Sandstone vary from fluvial to aeolian fluvial sources. Figure 9 confirms a non-marine aeolian source for the arkose (unit A) of the Lower Mt. Simon Sandstone, while the unit B of the Lower Mt. Simon Sandstone shows fluvial to aeolian fluvial sources. The Middle (units C and D) and Upper (unit F) Mt. Simon Sandstone are dominantly fluvial. In conclusion, the unidentified sandstone, Argenta sandstone, and Mt. Simon Sandstone were deposited in a dominant fluvial system with periodic deposition of aeolian dunes.

Overall data from the Wabash #1, T.R. McMillen #2, and VW #1 wells show a dominant fluvial origin for the sediments. The range of data from the Wabash #1 well is narrower than other wells that show a wider range of data. This could be interpreted by the better sorting and longer transport of sediments. The aeolian sediments are better represented in the T.R. McMillen #2 and VW #1 wells, while the sediments from the Wabash #1 well are fluvial. The LDF analyses, associated with lithofacies analysis and sequence stratigraphy, show distinct lateral variation of grain size from west to east of the Illinois Basin.

DEPOSITIONAL MODEL AND PALEOENVIRONMENTAL EVOLUTION
Unidentified Sandstone
The grain size analyses of the unidentified sandstone highlight a fluvial origin. However, this unit was not fully investigated in this report. In Ohio and southwest Indiana, a late Precambrian-aged sandstone of the Middle Run Formation beneath the Cambrian-aged Mt. Simon Sandstone has been identified (Shrake et al., 1991). This sandstone has been interpreted as rift-related clastic

materials recycled from the Grenville orogenic belt to the east and from the erosion of the Eastern Granite-Rhyolite Province to the west (Shrake et al., 1991). This formation has been constrained using U-Pb dating on detrital zircon grains that gave a depositional age between 1.2 and 0.9 Ga (Santos et al., 2002). In the Wabash #1 well, the unidentified sandstone is overlain by 20 ft thick basalts that are recently dated as early Cambrian in age (chapter 3). Consequently, the unidentified sandstone is not considered as strata, equivalent with the Middle Run Formation, that were deposited in the early phase of the proto-Illinois Basin during the continental-scale rifting of the North American cratonic interior basins.
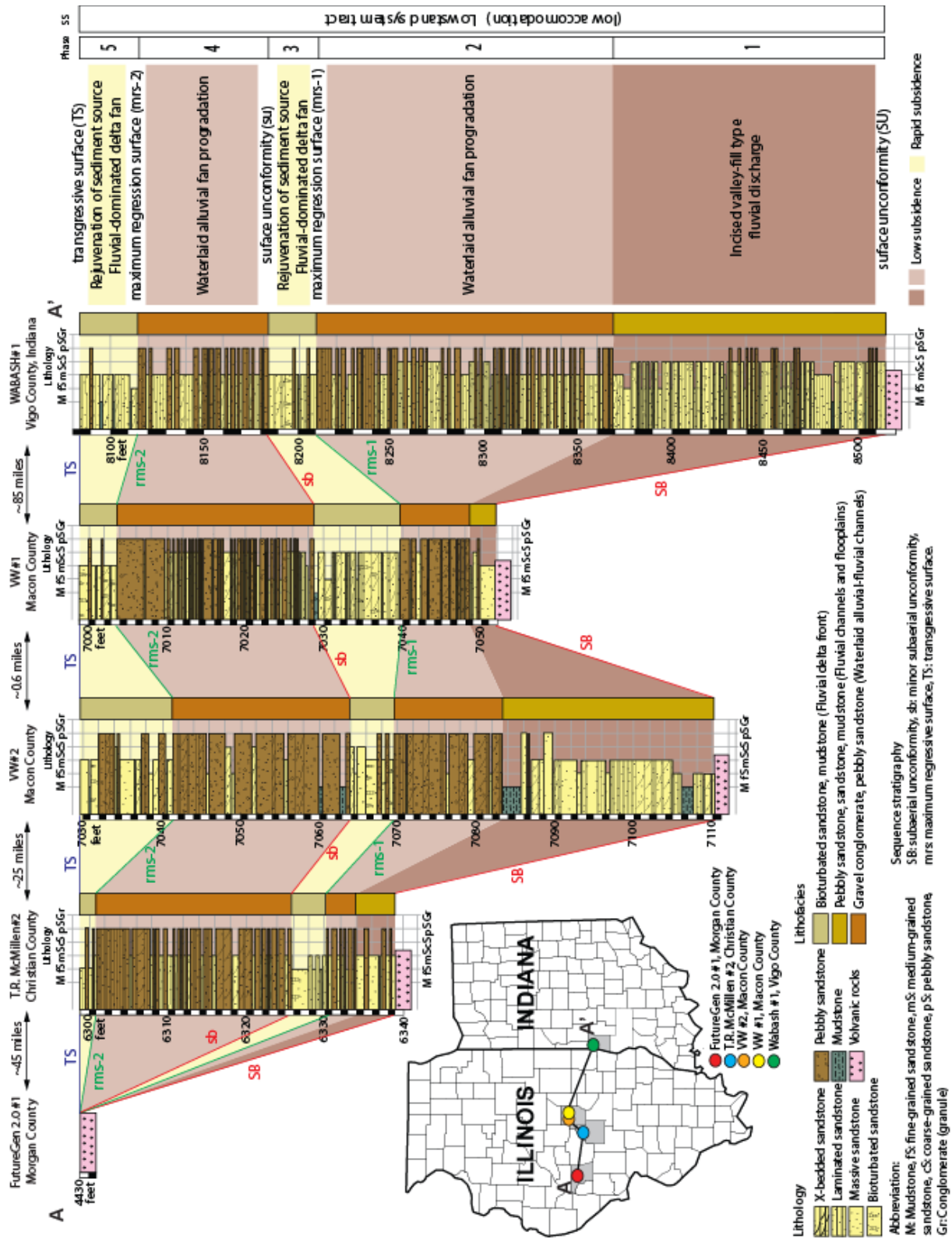
Argenta sandstone

The Argenta sandstone overlies a boundary surface at the contact with the Precambrian crystalline basement (Figure 10). SB represents a fluvial incision during a base-level fall, in which fluvial increases or sediment load decreases (Miall, 2002). The overlying sediments record dominantly fluvial depositional sequences (DS1 to DS5) that were deposited during low accommodation system tracts (Figure 11). This system tracts are controlled by the upstream flow within fluvial sequences that are independent of sea-level fluctuations. As the fluvial system of the Argenta sandstone and Mt. Simon Sandstone are often associated with shoreline shift of sea-level, the sequence stratigraphy of these strata responds to downstream controls, where the standard hierarchy of lowstand-transgressive-highstand system tracts could be applied (Boyd and Leckie, 2003). In this report, the Argenta sandstone is delimited at the base by SB and at the top by a transgressive surface (TS) (Figure 10). This normal regression developed in the Argenta sandstone forms a coarsening-up succession that is divided into two cycles composed of sandy conglomerates and pebbly sandstones (lithofacies LFA-A) separated by a distinctive muddy sandstone unit (lithofacies LFA-D). The lithofacies are interpreted as the vertical evolution from waterlaid alluvial fan deposits to delta distributary channel rivers at the transition between a fluvial plain and a possible ephemeral lake. The variation of lithology at the base of the formation indicates rapid and prolonged changes in the ratio between sediment supply and the rate of accommodation space. The finer-grained sandy materials (lithofacies A2) at the base of the formation can be interpreted as the activation of the depositional system, which the coarser-grained materials were delayed from the source. Sandy sediments were driven by high-energy traction flow regime, which developed the migration of a low-relief sheet or dune elongated downstream as interpreted as longitudinal channel fills and bars (Miall, 2006). These channel bars amalgamated in the fluvial plain under conditions of low accommodation that is usually the case with the lowstand system tracts (Catuneanu, 2008). With the increase of sediment supply (coarser materials composed of very coarse-grained sands, granules, and pebbles), the accommodation space progressively decreased, developing initial alluvial fan surface incision during the expansion of the drainage basin. Channel-lag pebble fill deposits (lithofacies A1) were accumulated under high-energy subaqueous traction regime in a waterlaid alluvial-fluvial fan system complex (Figure 11). Due to widening of the flow into a braided river, flood flows spreading out from the channels, which develop the deposition of sheet flood sediments such as gravel- to sand-sized dunes and antidunes (Reinech and Singh, 1986). Multiple waterlaid flows occurred in the alluvial fan system that produced the truncation

(e.g., scour- and fill-structures) of dunes and antidunes. The top of this coarser material unit (DS2) is inferred to a minor maximum regressive surface (mrs-1) that marked a phase of retrogradation before the progradation of the overlapping of a fluvio-deltaic system complex (lithofacies association LFA-D) (Figure 10).

A rapid differential subsidence occurred through the basin with the progradation of delta front facies (lithofacies association LFA-D), which eastward evolved into lacustrine sediments. Rare wave-related reversal currents created bidirectional trough crossed-stratification by the migration of distributary channel dunes (lithofacies D1) in a transition between a fluvial and delta-front lobe system complexes (DS3). Tidal influences could be interpreted as the result of transgressive systems tracts. The distributary channel dunes generated during this stage vertically graded to mouth bar deposits. However, no mouth bar deposits are identified in the Argenta sandstone within the Wabash #1 well. The top of the sequence DS3 is inferred to a local or regional minor erosive surface or maximum flooding surface (mfs) that marked the beginning of regressive highstand/lowstand system tracts for the second cycle (D4 to D5). Because the drainage of the basin became more dominant, a probable proximal source of sediments (e.g., paleohigh) nourished the alluvial plain system by the deposition of the second coarsening-up cycle (lithofacies association LFA-A). This phase can be inferred as a minor retrogradation that is marked by a minor maximum regressive surface (mrs-2) at the top of D4. The source area denudation significantly decreases with the decrease of coarser-grained material supply and the transition of a new transgressive episode of progradation of fluvial-delta front sediments (lithofacies association LFA-D). The top of D5 is inferred as a TS.

Figure 10: *Tectono-stratigraphic correlation between Wabash #1, VW #1 and #2, T.R. McMillen #1, and FutureGen #1 wells. The Argenta sandstone shows two alluvial cycles marked by low and rapid subsidence under low accommodation system tracts that are related to synrift extensional regime.*

Stratigraphic correlation of the Argenta sandstone is here discussed in the area that is covered by the FutureGen #1 and T.R. McMillen #2 wells to the west, the VW #1 and #2 wells to the center, and the Wabash #1 well to the east (Figure 12). Such a profile corresponds to significant variations of thickness and deposition that thicken north-northeastwards. Coarsening-up cycles, previously identified in the T.R. McMillen #2 well (Delpomdor, 2020) are recognized in all wells (Figure 10). Both coarsening-up phases recorded periods of increasing sediment flux to subsidence rate ratios that developed in basinward growth of the alluvial fan system complex. The relatively high feldspars, volcanic, and lithic fragments are typical properties of sediment derived from juvenile basement in valley subsidence in extensional regimes or source uplift in compressional regimes (Dickinson, 1985; Piper et al., 1996). The lateral variation of thickness within the Argenta sandstone reflects evidence for local tilting of the alluvial fan surface in deeply incised valleys. The newly formed strata were intensely incised by hyperconcentrated water flows that marked minor regression surfaces. The transition with the finer-grained sediments reflected the progradation of delta lobe systems (lithofacies association LFA-D) through the basin that resulted from the rapid subsidence during a relative tectonic quietness. A second tectonic pulse generated a new phase of sediment supply from local source areas (e.g., paleohigh). The differential vertical movements occurred subaerial unconformity that initiated the erosion of the crystalline Precambrian palaeohighs and the increases of alluvial fan supply (lithofacies association LFA-A). A decrease of this supply turned on the progradation of delta lobe system complex (lithofacies association LFA-D) that was predominant in the north-northeastern part of the proto-Illinois Basin. The bottom of the proto-Illinois Basin deepened north-northeastwards, which is confirmed with the location of the depocenter in the eastern central part of the Illinois Basin.

Mt. Simon Sandstone

The switch from alluvial fan (lithofacies association LFA-A) to fluvial braided stream (lithofacies association LFA-B) systems began with the deposition of the arkose (unit A) of the Mt. Simon Sandstone (Figures 8B and 12). This transition marked an early stage of transgressive system tract (TST) through the basin (Figure 12). The mode of deposition highlights an increase of fluvial style of sedimentation, when the rate of sediment supply exceeds that of accommodation space creation in which the sediments recorded a passive tectonic phase where the hinterland erosion was weak and the drainage basin expanded (Soegaard, 1990). Periodic increase of coarser-grained lithic sediment supply in the fluvial braided river system is interpreted as the reactivation of proximal source area denudation from crystalline basement paleoreliefs. In the Wabash #1 well, coarser-grained lithics are less abundant than in the T.R. McMillen #1 well, in which seismic reflection has showed a partially denudated paleohigh that pinchs out with the Lower Mt. Simon Sandstone. The arkose (unit A) of the Lower Mt. Simon Sandstone accumulated extensive, vertically and laterally amalgamated channel-fill and channel bar complexes (lithofacies association LFA-C) that were formed by the bedload-related migration of sand dunes under high-energy flow regime (Figure 11). The fluvial braided river system spread widely with the vertical and lateral deposition of aeolian dunes (lithofacies association LFA-C) (Figure 11). Near the depocenter, a narrow

braided river delta system, mainly composed of amalgamated distributary braided channels (lithofacies association LFA-D), deposited (Figures 8B and 11). These sediments were formed during a high discharge of river supply in a relatively high energy delta fan system that was influenced by microtidal conditions. Such delta facies laterally correspond to the fluvial braided river system that are recognized in the VW #1 and #2 and T.R. McMillen #2 wells. The switches from braided stream to delta front sedimentation correspond to minor continental-scale marine transgression stages through the proto-Illinois basin. Near the depocenter, a low rate of subsidence, a tectonic quietness, and a high rate of accommodation space facilitated the accumulation of prograding delta front deposits through the proto-Illinois Basin (Figure 11). The lowermost arkose was periodically flooded, as shown by the deposition of mudstone that indicates a significant highstand sea-level in the depocenter. However, the few contents of floodplain deposits indicate that the high mobility of the fluvial braided river system does not preserve the floodplain muds. The overlying strata of the Lower Mt. Simon Sandstone show aeolian sand dunes (lithofacies association LFA-C) that vertically and laterally spread on the fluvial braided river system (Figures 8C and 12). These aeolian deposits mark an expansion of basin drainage and a large sediment supply, in which the accommodation space creation was able to exceed the subsidence, where the strata were marked by subaerial unconformities. The Lower-Middle Mt. Simon Sandstone boundary is interpreted as a minor TS that precedes a second stage of TST (Figure 12).

The Middle (units C and D) of the Mt. Simon Sandstone highlights a significant decrease of lithic contents, particularly igneous-derived supply. Such a decrease is recognized through the basin and, consequently, indicates the paleo-topography of the Precambrian crystalline basement was completely denudated. The fluvial mode of deposition in the units C and D suggests a rate of sediment supply that exceeded the accommodation space. Due to the moderate to rapid subsidence, fluvial river sediments developed a wide area of fluvial plain system (Figures 8D-E). Sometimes the rate of subsidence decreased and the rate of accommodation increased, which facilitated the deposition of aeolian sand dunes and distally delta facies when the system prograded landward. The Middle and Upper Mt. Simon Sandstone is here interpreted as late TST (Figure 12).
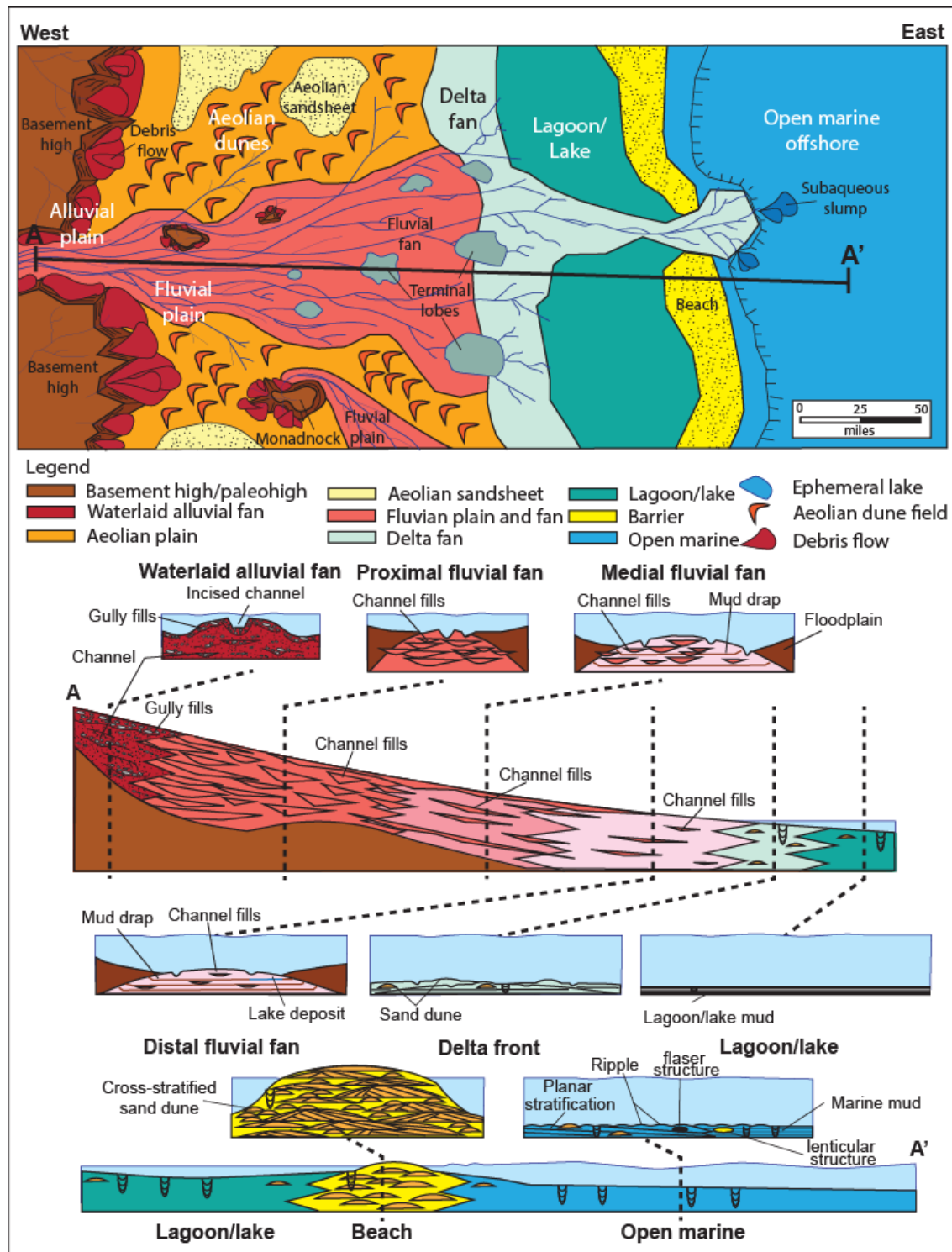
Figure 11: *Large-scale depositional model for the Argenta sandstone and Mt. Simon Sandstone showing the interaction from alluvial fan to open-marine environments. Fluvial plain is bordered by a floodplain that accumulated aeolian dune field. Cross-sections of the alluvial and fluvial plains with details of the waterlaid alluvial fan, fluvial plain, delta fan, and open-marine environments (modified from Moscariello, 2018).*
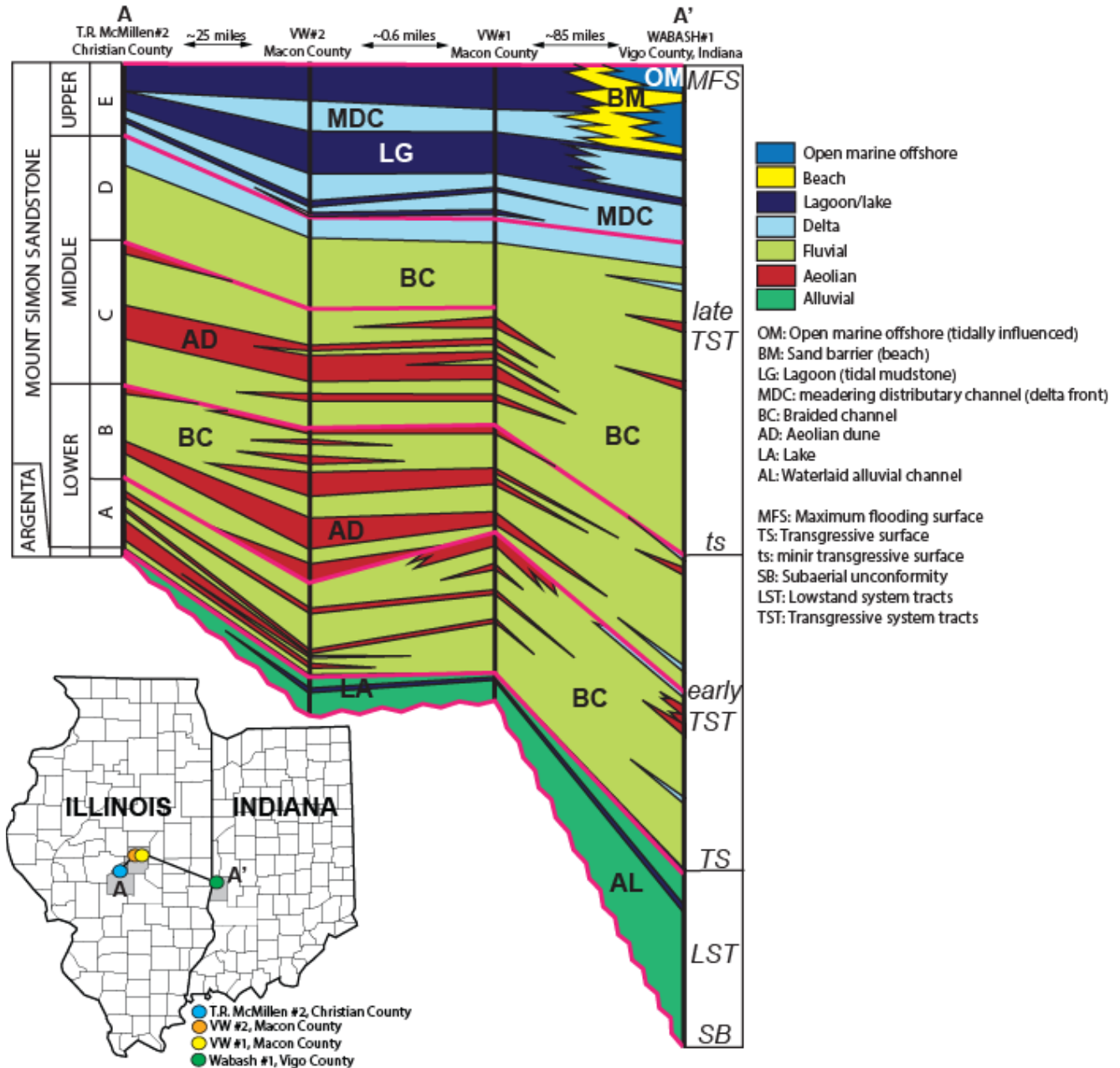
Figure 12: *Profile of lithostratigraphic correlation from central Illinois to central-west Indiana. Sequence stratigraphy shows that the sedimentary succession of the Argenta sandstone and Mt. Simon Sandstone begins by a (low accommodation) lowstand system tract (LST) over a subaerial unconformity (SB) over the crystalline Precambrian basement. LST is bounded by a transgressive surface (TS) that marked the progradation of the fluvial system through the basin. Two phases produced a fluvial-dominated and delta-dominated to open-marine deposition for the Lower-Middle and Middle-Upper Mt. Simon Sandstone, respectively. The boundary with the Eau Claire Formation is marked by a maximum flooding surface (MFS).*

The latest phase of this marine transgression is marked by the progradation of a braided river delta system that passes eastward to an open-marine offshore system (Figures 8F and 11). In the T.R. McMillen #1 well, the deposition shows a transition between fluvial-dominated to delta front-dominated systems, mostly amalgamated distributary braided channels (lithofacies D1 of the lithofacies association LFA-D) (Figure 12). These distributary braided channels gradually progressed with lagoonal muds (lithofacies D3 of the lithofacies association LFA-D) (Figure 8F). In the Wabash #1 well, the facies display dominantly amalgamated distributary braided channels and mouth bar deposits (lithofacies D1 to D3 of the lithofacies association LFA-D) that are overlain by beach barrier sands and marine sand dunes and muds (lithofacies association LFA-E) (Figure 12). Such variation of facies is common during a transgressive stage. The marine influence is marked by the deposition of microtidal structures (e.g., current and wave ripples) that were formed under alternating oscillatory and traction regimes (Dalrymple, 2010). The maximum of marine flooding occurred at the boundary between the Upper Mt. Simon Sandstone and Eau Claire Formation (Ostrom, 1970; Runkel et al., 2007) (Figure 12).

CONCLUSION

The Middle-Upper Cambrian Argenta sandstone and Mt. Simon Sandstone of the Postdam Group, Illinois Basin, comprise 2,462-ft-thick, dominantly fluvial sandstone strata that contain thinner floodplain muds and aeolian sandstone. The fluvial sandstone extends from west-central to east-central Illinois for delta front and open-marine offshore fine-grained materials. The fluvial sandstone is principally composed of massive, horizontal to low-angle and trough cross-stratified sandstone and a few thin strata of heterolytic sandstone, siltstone, and mudstone. This sandstone represents single to amalgamated channel bars in a braided river system, bordered by crevasse splays, levees, and floodplain channels that were reduced due to the high velocity of the river. Mudstone that is often bioturbated represents mainly floodplain and lagoon/lacustrine deposition.

Underlying this sandstone, a coarse-grained, locally pebbly or conglomeratic formation is identified as the Argenta sandstone, which was considered the oldest Cambrian unit in Illinois. The discovery of the early Cambrian basalt and underlying early Cambrian sandstones changes this. The Argenta represents channel fill deposits in a waterlaid alluvial fan system that was formed in high-energy water flow conditions during low accommodation or lowstand system tracts. Finer-grained sandstone rests on an incised basalt layer, which in the Wabash #1 well pinches out with a fluvial-considered unidentified sandstone. This finer-grained material can be interpreted as the activation of a fluvial depositional system, in which the coarser-grained materials were delayed from the source. Lithics are relatively high in the Argenta sandstone; these grains were derived from denudation of a juvenile Precambrian crystalline basement in valley subsidence in extensional regimes or source uplift in compressional regimes. The overlying strata shows the vertical evolution from waterlaid alluvial fan deposits to delta distributary channel rivers at the transition between a fluvial plain and a possible ephemeral lake. Differential subsidence movements occurred through the basin with the progradation of delta front facies such as

distributary channel dunes, which evolved eastward into possibly tidally influenced lagoon/lacustrine sediments.

The Mt. Simon Sandstone has a greater proportion of sandstone strata that marks the switch from alluvial fan to fluvial braided stream systems. This transition marks an early stage of transgressive system tracts through the basin, tectonically inactive, in which the hinterland erosion was low and the drainage basin expanded. Periodic increase of coarser-grained lithic sediment supply in the fluvial braided river system, particularly in the Lower Mt. Simon Sandstone, is interpreted as the reactivation of proximal source area denudation from crystalline Precambrian paleoreliefs. The Lower and Middle Mt. Simon Sandstone accumulated extensive, vertically and laterally braided river amalgamated channel-fill and channel bar complexes that evolved vertically and laterally by aeolian dunes when the accommodation space exceeded the rate of subsidence. The basin drainage expanded during regional transgression or highstand stages, and the fluvial plain was flooded, accumulating floodplain muds and eastward delta front facies.

The Upper Mt. Simon Sandstone recorded the latest phase of a marine transgression before the onset of the sea-level highstand stages initiated during deposition of the Eau Claire Formation. In central-west Indiana, the open-marine offshore system prograded westward to a lagoon that was bordered by braided river delta and fluvial systems.

Climate during deposition of the Argenta sandstone and Mt. Simon Sandstone was warm, alternating humid and dry seasons. Kaolinite was probably the dominant clay during deposition of the Argenta sandstone and the Lower Mt. Simon Sandstone, while smectite occurred in the Middle and Upper Mt. Simon Sandstone. Smectite is an indicator of arid, semi-arid, or temperate climates with contrasting seasons and a pronounced dry season. The high content in authigenic illite could be the result of illitization of K-feldspars and the early-formed kaolinite during deep burial.

The Middle-Upper Cambrian fluvial-dominated Argenta sandstone and Mt. Simon Sandstone are some of the best examples where the deposition responds to a number of allogenic controls on sedimentation, which include eustasy, climate, source area tectonism, and basin subsidence. The Argenta sandstone recorded local synrift tilting of the Precambrian crystalline basement that drove the style of deposition, paleocurrent directions, and late diagenetic clay minerals in the alluvial fan system. This tectonic phase extended to the Lower Mt. Simon Sandstone, which recorded differential subsidence movements. With the quietness of the basin, only the climate and basin subsidence controlled the style of deposition.

REFERENCES

Becker, L.E., Hreha, A.J., and Dawson, T.A., 1978. Pre-Knox (Cambrian) stratigraphy in Indiana. State of Indiana Department of Natural Resources Geological Survey, 72 p.

Bhattacharya, J. and Walker, R.G., 1991. River- and wave-dominated depositional systems of the Upper Cretaceous Dunvegan Formation, northwestern Alberta. *Bulletin of Canadian Petroleum Geology, 39* (2), 165-191.

Cain, S.A. and Mountney, N.P., 2009. Spatial and temporal evolution of a terminal fluvial fan system: the Permian Organ Rock Formation, South-east Utah, USA. *Sedimentology 56* (6), 1774-1800.

Catuneanu, O., 2006. *Principles of Sequence Stratigraphy*. Elsevier, 374 p.

Catuneanu, O., Abreu, V., Bhattacharya, J.P., Blum, M.D., Dalrymple, R.W., Eriksson, P.G., Fielding, C.R., Fisher, W.L., Galloway, W.E., Gibling, M.R., Giles, K.A., Holbrook, J.M., Jordan, R., Kendall, C.G.St.C., Macurda, B., Martinsen, O.J., Miall, A.D., Neal, J.E., Nummedal, D., Pomar, L., Posamentier, H.W., Pratt, B.R., Sarg, J.F., Shanley, K.W., Steel, R.J., Strasser, A., Tucker, M.E., and Winker, C., 2009. Towards the standardization of sequence stratigraphy. *Earth-Science Reviews 92*, 1-33.

Collinson, C., Sargent, M.L., and Jennings, J.R., 1988. Illinois basin region. Sedimentary Cover—North American Craton, US: Geological Society of America, *The Geology of North America 2*, 383-426.

Dalrymple, R.W., 2010. Tidal depositional systems. In: James, N.P., Dalrymple, R.W., Eds., Facies Models 4. Geological Association of Canada, St. John′s, 201–232.

Delpomdor, F., 2020. Report: SLB Podolsky Oil Company T.R. McMillen2 borehole: Sedimentology and sequence stratigraphy. Illinois State Geological Survey, internal report, October 2020, 45 p.

Denison, R.E., Bickford, M.E., Lidiak, E.G., and Kisvarsanyi, E.B., 1987. Geology and Geochronology of Precambrian Rocks in the Central Interior Region of the United States. U.S. Geological Survey, Reston, Virginia, Professional Paper 1241-C.

Dickinson, W.R., 1985. Interpreting provenance relations from detrital modes of sandstones. In: Zuffa, G.G., ed., Provenance of Arenites. D. Reidel, The Netherlands, 333–361.

Droser, M.L., 1991. Ichnofabric of the Paleozoic *Skolithos* ichnofacies and the nature and distribution of the Skolithos Piperock. *Palaios 6*, 316-325.

Flemming, B.W., 2007. The influence of grain-size analysis methods and sediment mixing on curve shapes and textural parameters: implications for sediment trend analysis. *Sedimentary Geology 202*, 425–435.

Folk, R.L., 1966. A review of the grain size parameters. *Sedimentology 6*, 73–93.

Folk, R.L. and Ward, M.C., 1957. Brazos River bars: a study in the significance of grain size parameters. *Journal of Sedimentary Petrology 27*, 3–27.

Freiburg, J.T., Morse, D.G., Leetaru, H.E., Hoss, R.P., and Yan, Q., 2014. A Depositional and Diagenetic Characterization of the Mt. Simon Sandstone at the Illinois Basin–Decatur Project Carbon Capture and Storage Site, Decatur, Illinois, USA. *Circular 583*, Illinois State Geological Survey, Champaign, 42 p.

Freiburg, J.T., McBride, J.H., Malone, D.H., and Leetaru, H.E., 2020. Petrology, geochronology, and geophysical characterization of Mesoproterozoic rocks in central Illinois, USA. *Geoscience Frontiers 11* (2), 581-596.

Heidlauf, D.T., Hsui, A.T., and Klein, G.W., 1986. Tectonic subsidence analysis of the Illinois basin. *Journal of Geology 94*, 779-794.

Kocurek, G., 1996. Desert Aeolian systems. In: Reading, H.G., ed., *Sedimentary environments processes facies and stratigraphy*, 3rd ed. Blackwell Science, Oxford, pp. 125-153.

Kolata, D.R. and Nelson, W.J., 1991.Tectonic history of the Illinois basin. In: Leighton, M.W., Kolata, D.R., Oltz, D.E, Eidel, J.J., eds., *Interior Cratonic Basins*. American Association of Petroleum Geologists, Memoir 51, pp. 263-285.

Kolata, D.R. and Nelson, W.J., 2010. Tectonic history. In: Kolata, D.R., Nimz, C.K., eds., *Geology of Illinois*. Illinois State Geological Survey, University of Illinois, Champaign, pp. 77– 89.

Boyd, R.K. and Leckie, D.A., 2003. Comparison of the Cretaceous Paddy Estuary, Canada and the Modern Hervey Bay, Australia—Insights from analog modeling. AAPG Annual Meeting 2004.

Leighton, M.W. and Kolata, D.R., 1991. Selected Interior Cratonic Basins and Their Place in the Scheme of Global Tectonics. In: Leighton, M.W., Kolata, D.R., Oltz, D.E, Eidel, J.J., eds., *Interior Cratonic Basins*. American Association of Petroleum Geologists, Memoir 51, pp. 729-797.

Lovell, T.R. and Bowen, B.B., 2013. Fluctuations in Sedimentary Provenance of the Upper Cambrian Mt. Simon Sandstone, Illinois Basin, United States. *Journal of Geology 121*, 129-154.

Maciaszek, P., Chomiak, L., and Wachocki, R.M., 2019. The interpretative significance of ripple-derived sedimentary structures within an upper Neogene fluvial succession of central Poland. *Geologos 25* (1), 1-13.

Martins, L.R., 1965. Significance of Skewness and Kutosis in environmental interpretation. *Journal of Sedimentary Petrology 35*(3), 768–770.

McBride, J.H. and Kolata, D.R., 1999. Upper crust beneath the central Illinois Basin, United States: *Geological Society of America Bulletin 111*, 375–394.

McBride, J.H., Kolata, D.R., and Hildenbrand, T.G., 2003. Geophysical constraints on understanding the origin of the Illinois basin and its underlying crust. *Tectonophysics 363*, 45-78.

Melchor, R.N., Genise, J.F., Buatois, L.A., and Umazano, A.M., 2012. Fluvial environments. In: Knaust, D., Bromley, R.G., (Eds.), *Trace fossils as indicators of sedimentary environments. Developments in Sedimentology 64*, 329-378.

Miall, A.D., 1977. A review of the braided-river depositional environment. *Earth-Science Reviews 13*, 1–62.

Miall, A.D., 1996. *The Geology of Fluvial Deposits*. Springer, New York.

Miall, A.D., 2002. Architecture and sequence stratigraphy of Pleistocene fluvial systems in the Malay Basin, based on seismic time-slice analysis. *AAPG Bulletin 86* (7), 1201-1216.

Miall, A.D., 2006. *The Geology of Fluvial Deposits: Sedimentary Facies, Basin Analysis, and Petroleum Geology*. Springer-Verlag, Berlin, New York, 582 p.

Miall, A.D., 2010. Alluvial deposits. In: James, N.P., Dalrymple, R.W., eds., *Facies Model Revisited*. SEPM, Special Publication 90, pp. 105-137.

Moscariello, A., 2018. Alluvial fans and fluvial fans at the margins of continental sedimentary basins: geomorphic and sedimentological distinction for geo-energy exploration and development. In: Ventra, D., Clarke, L.E., eds., *Geology and Geomorphology of Alluvial and Fluvial Fans: Terrestrial and Planetary Perspectives*. Geological Society, London, Special Publications, 440, pp. 215–243.

Norby, R.D., 1991. Biostratigraphy Zones in the Illinois Basin. In: Leighton, M.W., Kolata, D.R., Oltz, D.F., Eidel, J.J., eds., *Interior cratonic basins, American Association of Petroleum Geologists Memoir 51*, pp. 179-194.

Ostrom, M.E., 1970. Sedimentation cycles in the Lower Paleozoic rocks of western Wisconsin, in Field Trip Guidebook for Cambrian-Ordovician geology of western Wisconsin: Wisconsin Geological and Natural History Survey, *Information Circular 11*, 10-34.

Piper, J.D.A., Elliot, M.T., and Kneller, B.C., 1996. Anisotropy of magnetic susceptibility in a Palaeozoic flysch basin: the Windermere Supergroup, northern England. *Sedimentary Geology 106*, 235–258.

Pratt, T.L., Hauser, E.C., and Nelson, K.D., 1992. Widespread buried Precambrian layered sequences in the US Mid-Continent: evidence for large Proterozoic depositional basins. AAPG *Am. Assoc. Pet. Geol. Bulletin 76*, 1384-1401.

Reineck, H.E. and Singh, I.B., 1986. *Depositional Sedimentary Environments* (2nd. Ed.). Springer-Verlag, Berlin, Heidelberg, New York, 551 p.

Runkel, A.C., Miller, J.F., McKay, R.M., Palmer, A.R., and Taylor, J.F., 2007. High-resolution sequence stratigraphy of lower Paleozoic sheet sandstones in central North America: The role of special conditions of cratonic interiors in development of stratal architecture: *Geological Society of America Bulletin 119* (7–8), 860–881.

Sahu, B.K., 1964. Depositional mechanisms from the size analysis of clastic sediments. *Journal of Sedimentary Petrology 34*, 73–83.

Santos, J.O.S., Hartmann, L.A., McNaughton, N. J., Easton, R.M., Rea, R.G., and Potter, P.E., 2002. Sensitive high resolution ion microprobe (SHRIMP) detrital zircon geochronology provides new evidence for a hidden Neoproterozoic foreland basin to the Grenville Orogen in the eastern Midwest U.S.A. *Canadian Journal of Earth Sciences 39*, 1505–1515.

Shrake, D.L., Carlton, R.W., Wickstrom, L.H. Potter, P.E., Richard, B.H., Wolfe, P.J., and Sitler, G.W., 1991. *Pre-Mt. Simon Basin under the Cincinnati Arch. Geology 19*, 139-142.

Sloss, L.L., 1963. Sequences in the cratonic interior of North America. *Geological Society of America Bulletin 74* (2), 93-114.

Soegaard, K., 1990. Fan-delta and braid-delta systems in Pennsylvanian Sandia Formation, Taos Trough, Northern New Mexico: depositional and tectonic implications. *Bulletin of the Geological Society of America 102*, 1325–1343.

Sutherland, R.A. and Lee, C.T., 1994. Discrimination between coastal sub environments using textural characteristics. *Sedimentology 41*, 1133–1143.

Thomas, W.A., Gehrels, G.E., Sundell, K.E., Greb, S.F., Finzel, E.S., Clark, R.J., Malone, D.H., Hampton, B.R., and Romero, M.C., 2020. Detrital zircons and sediment dispersal in the eastern Midcontinent of North America. *Geosphere 16* (3), 817-843.

Treworgy, J.D., Sargent, M.L., and Kolata, D.R., 1991. Tectonic subsidence history of the Illinois Basin (extended abstract). In: Program with Abstracts for the Louis Unfer, Jr. Conference on the Geology of the Mid-Mississippi Valley, Cape Girardeau, MO.

Van der Pluijm, B.A. and Catacosinos, P.A., 1996. Basement and basins of eastern North America. Geological Society of America, Special Paper 308, p. 14.

Van Schmus, W.R., Schneider, D.A., Holm, D.K., Dodson, S., and Nelson, B.K., 2007. New insights into the southern margin of the Archean–Proterozoic boundary in the north-central United States based on U-Pb, Sm-Nd, and Ar-Ar geochronology. *Precambrian Research 157*, 80–105.

Van Schmus, W.R., Bickford, M.E., and Turek, A., 1996. Proterozoic geology of the east-central midcontinent basement. In: van der Pluijm, B.A., Catacosinos, P.A., eds., Basement and basins of eastern North America: Geological Society of America Special Paper 308, 7–32.

Willman, H.B., Atherton, E., Buschbach, T.C., Collinson, C., and Frye, J.C., 1975. Handbook of Illinois stratigraphy. *Illinois State Geological Survey Bulletin 95*, 1-261.

Chapter 2

Geophysical Acquisition, Data Processing, and Geological Interpretation for Wabash CarbonSAFE Project (Illinois Basin)

By: John H. McBride[1], Hannes E. Leetaru[2], and Jared T. Freiburg[2]

[1]Department of Geological Sciences, Brigham Young University, Provo, Utah

[2]Illinois State Geological Survey, Prairie Research Institute, University of Illinois at Urbana-Champaign

SUMMARY

The Illinois Basin now has a multitude of seismic reflection profiles and 3D volumes as a result of several years of Carbon Capture and Storage (CCS) projects. One of the most recent CCS projects, Wabash CarbonSAFE, has produced two new seismic common mid-point (CMP) profiles in Edgar County, Illinois and Vigo County, Indiana. These profiles provide high-resolution images of Paleozoic stratigraphy in the Basin, including the CCS target zone, and the underlying Precambrian basement, which is locally strongly layered. The purpose of this report is to present the new seismic profiles (Figure 1), including acquisition and processing parameters, and describe the Paleozoic stratigraphy and basement structure in the context of previously acquired CCS seismic CMP data and the regional geology. We also compare and contrast results from a third seismic profile recently acquired in Richland County, Illinois, under a previous program supported by the United States Department of Energy (U.S. DOE.)

INTRODUCTION AND REGIONAL GEOLOGIC SETTING

Long-record seismic reflection data (0-5 s) acquired for CCS over the Illinois Basin have become a resource for studying Paleozoic and Precambrian stratigraphy and structure, crustal structure, and magmatic history. A better understanding of the Precambrian below the Basin can constrain interpretations of deep CCS sites by, for example, understanding how injection in the Mt. Simon Sandstone is influenced by the structure of the Precambrian rocks that immediately underlie it. The profiles presented herein (Figure 2) were acquired as part of an ongoing program of evaluation of potential reservoirs for CCS (Greenberg, 2013) by the Illinois State Geological Survey, supported by the U.S. DOE through their Wabash CarbonSAFE program. The profiles, which were purposefully recorded to upper crustal traveltimes (5 s), lie south of a major Precambrian terrane boundary that cuts diagonally across the central Illinois Basin (Figure 1). The boundary (or suture) is defined by neodymium model ages that divide the Mazatzal province (1.69-1.65 Ga old) to the north from the Granite-Rhyolite province (1.55-1.35 Ga old) to the south (Van Schmus et al., 1996; Whitmeyer and Karlstrom, 2007). The new seismic profiles were surveyed over the northeastern flank of the Illinois Basin, as defined by Paleozoic isopach maps (Buschbach and Kolata, 1991) (Figure 1).
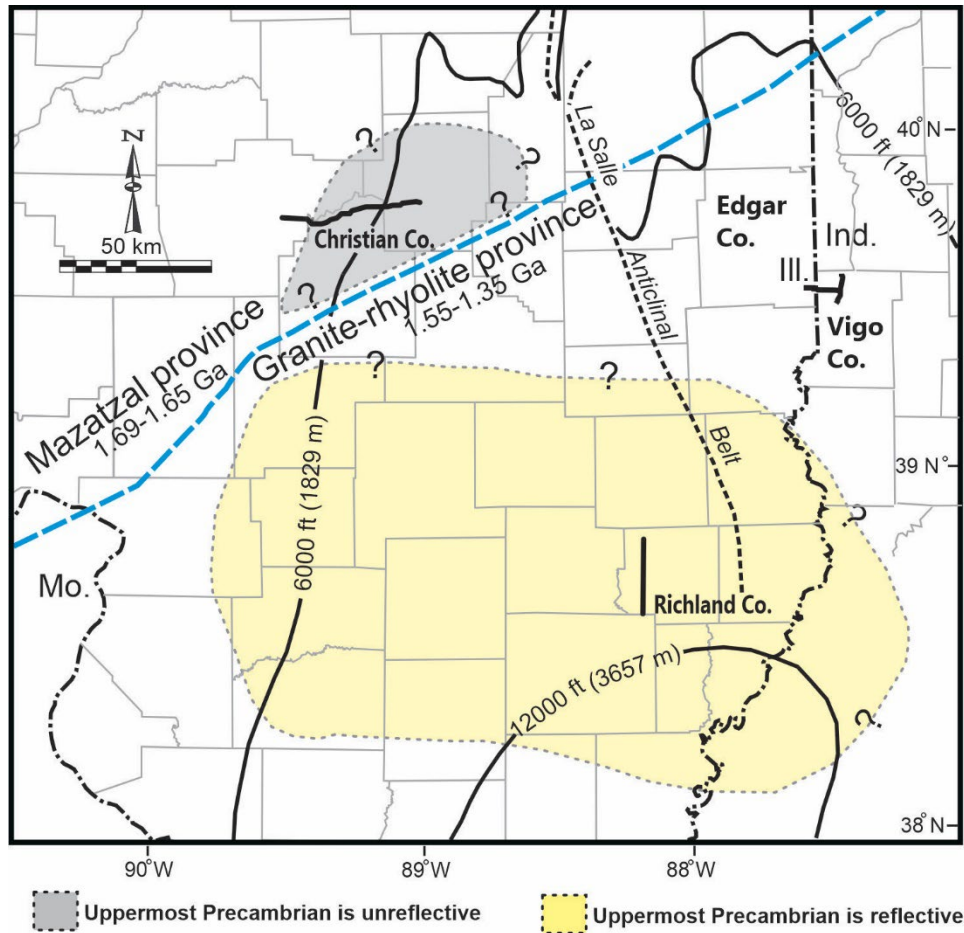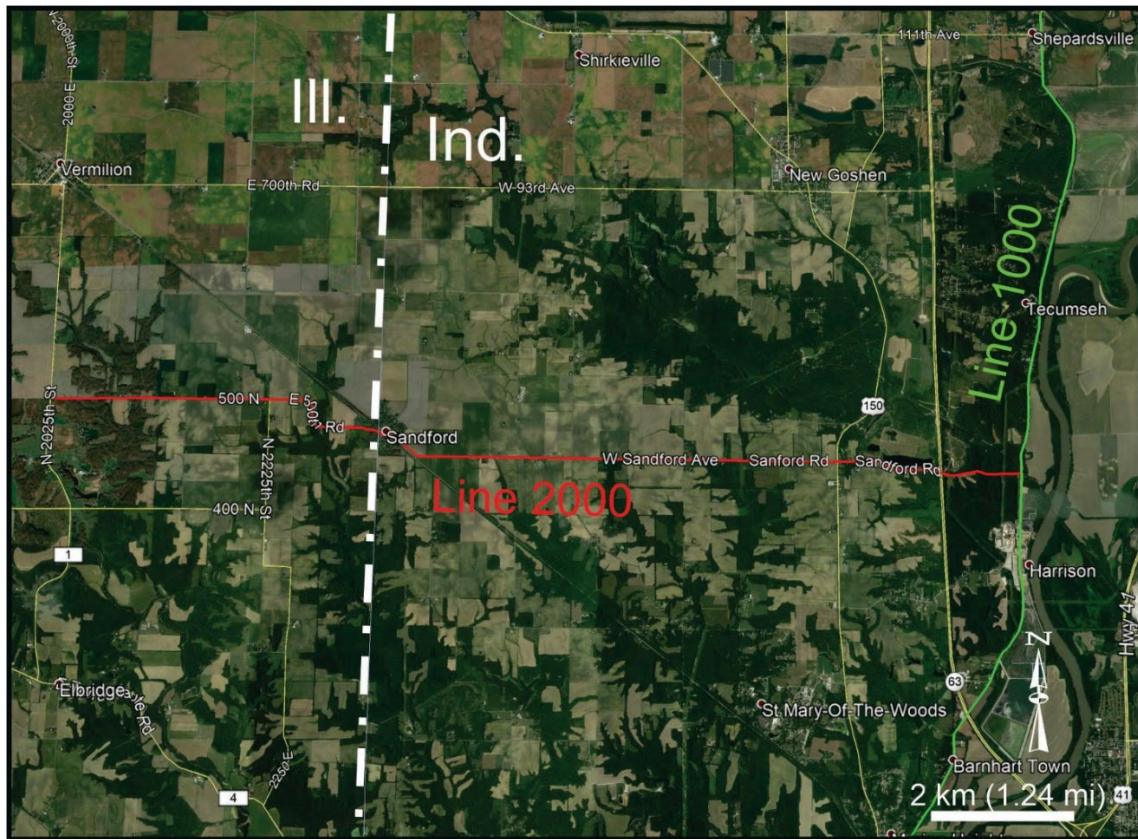
Figure 1*: Location map for seismic profiles used in this study in Christian, Edgar, and Richland Counties, Illinois, and Vigo County, Indiana. Two structural contours for top of Precambrian (Buschbach and Kolata, 1991) are selected for reference. The blue dashed line is a geochemically defined terrane boundary (Van Schmus et al., 1996). The shaded areas show reflection character of uppermost Precambrian, based on the present study and on previous compilations of long-record seismic data (Pratt et al., 1992; Bear et al., 1997; Drahovzal, 1997; Potter et al., 1997; McBride et al., 2013; McBride et al., 2016; Freiburg et al., 2020; McBride et al., 2020).*

NEW SEISMIC REFLECTION PROFILES

Locations

The new seismic data were collected as two approximately north-south and east-west intersecting profiles, respectively Lines 1000 and 2000 in Figure 2. Line 1000 is 42,735 ft (13,025.6 m) long (CMP distance) and was surveyed in western Vigo County, Indiana. Line 2000 is 59,510 ft (18,138.6 m) long (CMP distance) and was surveyed in southeastern Edgar County, Illinois, and western Vigo County, Indiana.

Figure 2: *Location map on Google Earth base map for the new Wabash seismic CMP profiles.*

ACQUISITION AND PROCESSING PARAMETERS

Field acquisition was conducted by Echo Seismic in 2019. The acquisition parameters for both profiles were identical. Both used a Vibroseis source (two 60,000-lb trucks, four sweeps per station), a geophone group and source interval of 110 ft (33.5 m) with a CMP bin size half of that, and a recording sample rate of 1 ms. The surveys used 220 recording channels with 10-Hz vertical geophones. An 8-s source sweep produced a correlated record of 5 s. The sweep frequency range was 2-100 Hz. The profiles were shot with a split spread using 0-12,100 ft (0-3,688.1 m) offsets centered on the flag, which yielded a CMP fold of cover of 6-67 for Line 1000 and 3-60 for Line 2000. Final data processing was performed by Sterling Seismic Services and included a frequency filter of 6-100 Hz, an automatic gain control (AGC) (1000-ms window), true amplitude gain recovery, noise burst editing, elevation, refraction, and floating datum static corrections, surface consistent amplitude equalization, surface consistent deconvolution (180-ms operator length), normal move-out (NMO) and muting of first arrivals analysis, surface consistent residual static corrections, linear noise attenuation and trace equalization, application of NMO, mute, and residual statics corrections, offset Kirchhoff prestack time migration (PSTM), CMP stack, frequency spectrum whitening, and frequency-space domain (FX) deconvolution. Elevation datum is 800 ft (243.8 m) with a replacement velocity 10,000 ft/s (3,048 m/s). The profiles are shown as traveltime sections since the seismic velocity for the Paleozoic section and especially for Precambrian rocks is not well-constrained.
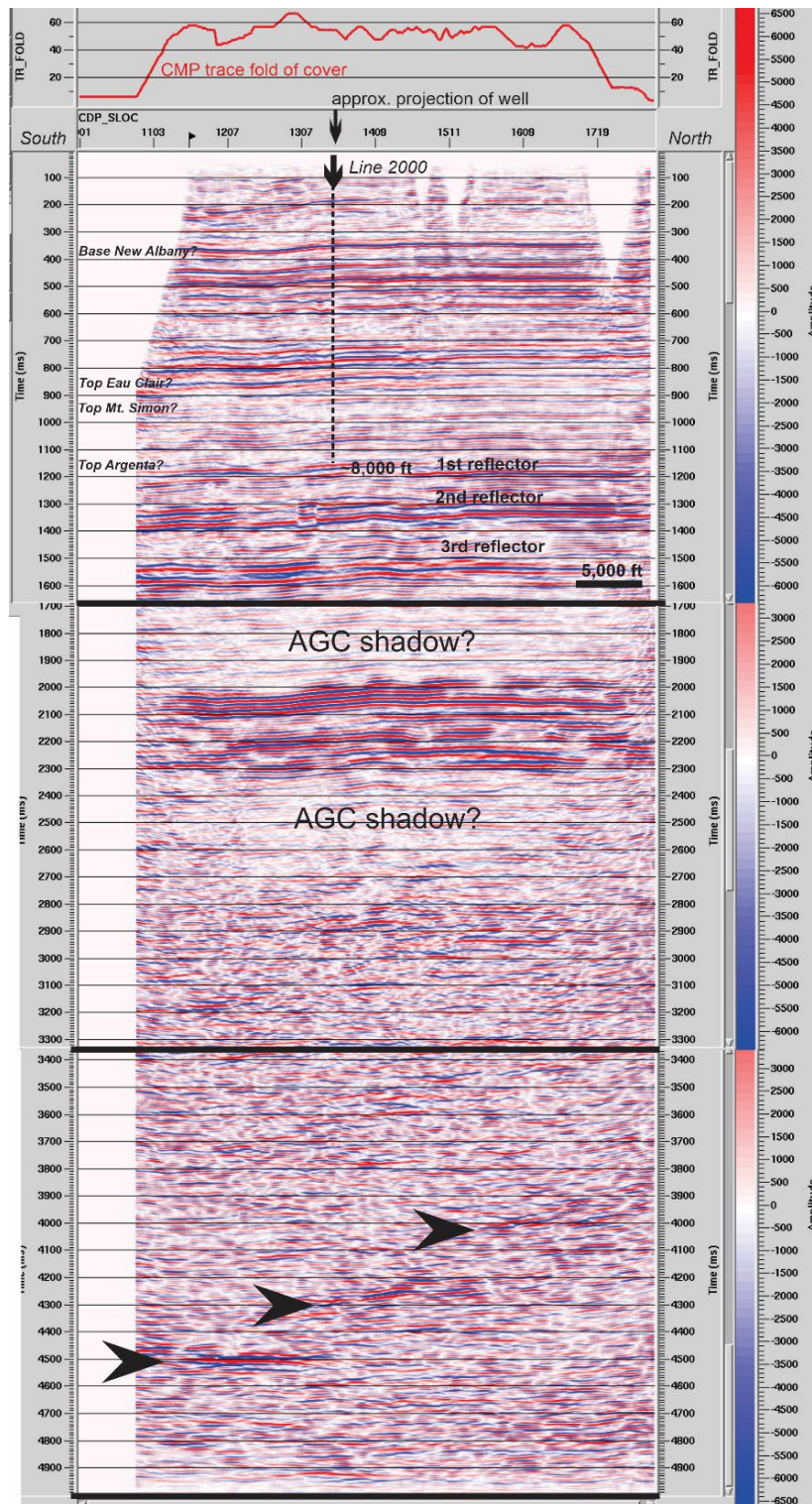
Figure 3a*: Line 1000 CMP seismic profile (Figure 2). The formation picks are only approximate since reliable well control is unavailable. The Wabash #1 well is projected.*
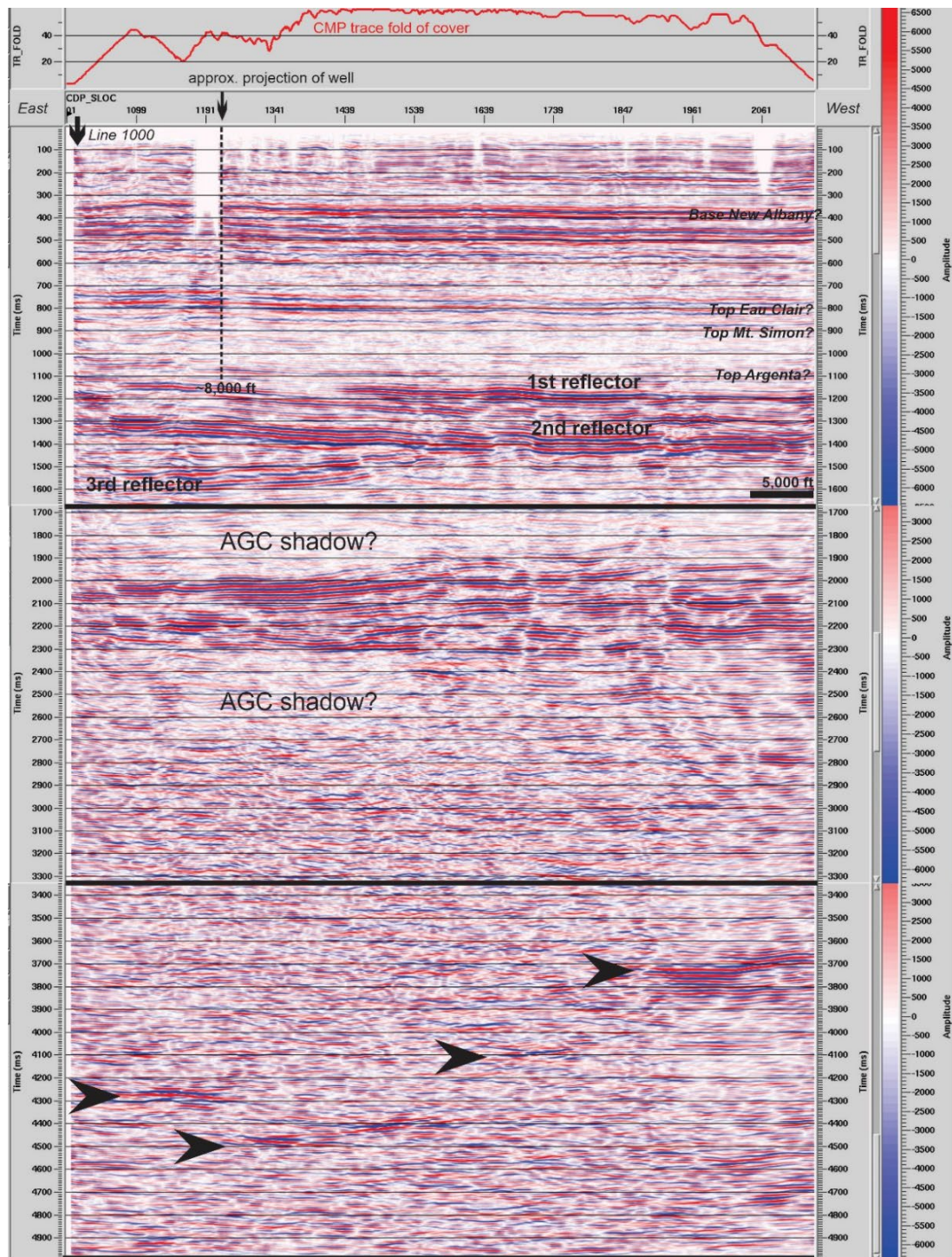
Figure 3b*: Line 2000 CMP seismic profile (Figure 2). The formation picks are only approximate since reliable well control is unavailable. The Wabash #1 well is projected. Aspect ratio same as for Figure 3a.*

RESULTS AND OBSERVATIONS

Line 1000

The Line 1000 CMP section is described in three time-intervals: 0-1,667 ms (Paleozoic and uppermost Precambrian panel), 1,667-3,333 ms (middle Precambrian panel), and 3,333-5,000 ms (lower Precambrian panel) (Figure 3a). The Paleozoic strata are very reflective, as usual for this part of the Basin; the target CCS interval is denoted on the upper panel between the provisionally picked top of the Eau Clair and top of the Mt. Simon underlain by the Argenta, or perhaps the basalt penetrated at approximately 8,500 ft (2,591 m) in the Wabash #1 well (Figure 3a). The basalt is approximately 30 ft (9.1 m) thick and is underlain by a tight micaceous siltstone about 100 ft (30.5 m) thick. The juxtaposition of these two rock types would produce significant impedance contrast. Assuming a range of interval velocities 13, 123-19,685 ft/s (4,000-6,000 m/s) and a dominant frequency of 60 Hz yields a vertical resolution (1/4 wavelength criterion) of about 54.7-82.0 ft (16.7-25.0 m). These calculations suggest that the top and bottom of the basalt layer cannot be resolved; however, a bright reflection is nonetheless expected and could correlate to the "1st reflector" labeled on the Wabash seismic sections (Figures 3a and 3b). If this correlation is correct, the later-arriving strong basement reflections ("2nd and 3rd reflectors" in Figures 3a and 3b) could also be basalt layers.

A possible monocline, verging to the south in the plane of the section, is expressed throughout the Paleozoic section (for example, see the flexure on the Base New Albany marker immediately south of approximate well location [Figure 3a]). A series of similarly folded reflectors has been previously mapped from seismic profiles further south, along the La Salle anticlinal belt (Figure 1) (McBride, 1997). Between 1,300 and 1,400 ms, a prominent series of reflectors appears. This is underlain by a similar series from 1,500 to 1,650 ms. The most prominent reflector interval appears on the middle panel, between 1,980 and 2,350 ms (Figure 3a). The multi-cyclic character may be an effect of short-period multiple reflection ("reverberation") and require further data processing. Between 2,350 and about 2,800 ms, the section has apparent suppressed relative amplitude; however, this may be an effect of an AGC "shadow" induced by strong overlying reflectivity (see McBride et al. [2020] for discussion of a similar effect on Illinois Basin seismic data). Below 2,808 ms occur only a few short reflector segments and/or diffractions (recognized on unmigrated versions of the profile, not shown in this report). The most noticeable deeper Precambrian reflectivity appears on the lower panel, which shows three horizontal or gently south-dipping (in the plane of the section) segments, each roughly 20,000 ft (6,096 m) long (at 4,000; 4,250; and 4,500 ms) (Figure 3a). This pattern suggests a stepping-down to the south (in the plane of the section) of intra-basement reflectors.

Line 2000

The Line 2000 CMP section (Figure 3b) is also described in three time-intervals, as in Figure 3a. The top panel shows the same general reflection character for the Paleozoic section as Line 1000 (Figure 3a). The stratal reflectors dip very gently to the west, toward the deeper part of the Basin. A monoclinal structure is not recognized as on Line 1000 (Figure 3a) except for a possible folded

structure expressed on the Base New Albany near the east end of the profile. In this sense, Line 2000 is mostly structurally a strike profile. On the lower part of the upper panel, a west-dipping 200-ms time-thick interval appears just beneath the top of the Argenta or perhaps basalt (uppermost Precambrian, just below the bottom of the well total depth on Figure 3b). This interval correlates to that on Line 1000 arriving at 1,200-1,400 ms (Figure 3a); however, the mostly horizontal third reflector series on the upper panel of Line 1000 (1,500-1,600 ms, Figure 3a) correlates to a reflector-defined wedge on Line 2000 that thins westward and pinches out beneath the second reflector in an angular uniformity beneath CDP_SLOC 1540 (Figure 3b). The upper part of the middle panel for Line 2000 (Figure 3b) shows a reflector series similar and correlating to the upper part of the middle panel for Line 1000 (Figure 3a). This series is significantly more structured on Line 2000 and includes several reflector disruptions and possible offsets on the western half of the profile. The lower panel for Line 2000 (Figure 3b) displays a pattern of isolated reflector segments very similar to that observed on the lower panel of Line 1000 (Figure 3a). The easternmost reflector segment on Line 2000 (4,280 ms) appears to correlate to a reflector segment arriving at the same time (Figure 3a) where the two profiles intersect.

Richland County Profile

To provide a broader context for interpreting Lines 1000 and 2000, we compare their results with a profile (Figure 4) collected in 2019 in Richland County, Illinois, located about 62 mi (100 km) southwest of the intersection of the two profiles in Vigo County, Indiana (Figure 1). The Paleozoic stratigraphy is basically similar but with thicker intervals owing to the profile being in a deeper part of the Illinois Basin. Below the center of the profile, the top of the Precambrian arrives at about 1,625 ms (Figure 4), much deeper than on the Wabash profiles (Figures 3a and 3b), is one to two cycles, and is similar to the Paleozoic markers above it. The top-Precambrian reflector is much more coherent. A relatively thin interval appears further down the section (60-200 ms time-thick), characterized by segmented reflections and abundant diffractions at its base (observed on the unmigrated version, not shown), very different from the overlying top-Precambrian reflection. Deeper, a well-developed series of flat-lying and north-dipping (apparent) reflections appears at the southern end of the profile, one at 2,370 ms, a second at 2,680 ms, and a third basal reflector at 3,170 ms. None of these events mimic overlying reflections and are unlikely to be multiples. The lowermost reflection of this series is the most continuous and coherent with the highest relative amplitude. Its north-dip increases abruptly across a hinge (CDP 2500), beyond which it dips more steeply. (Note that no such dip changes appear in the overlying Paleozoic section). Further down, below the prominent basal reflector, reflectivity is sporadic with occasional short reflection segments and diffractions, similar to the pattern that appears on the lower panels for Lines 1000 and 2000 (Figures 3a and 3b).
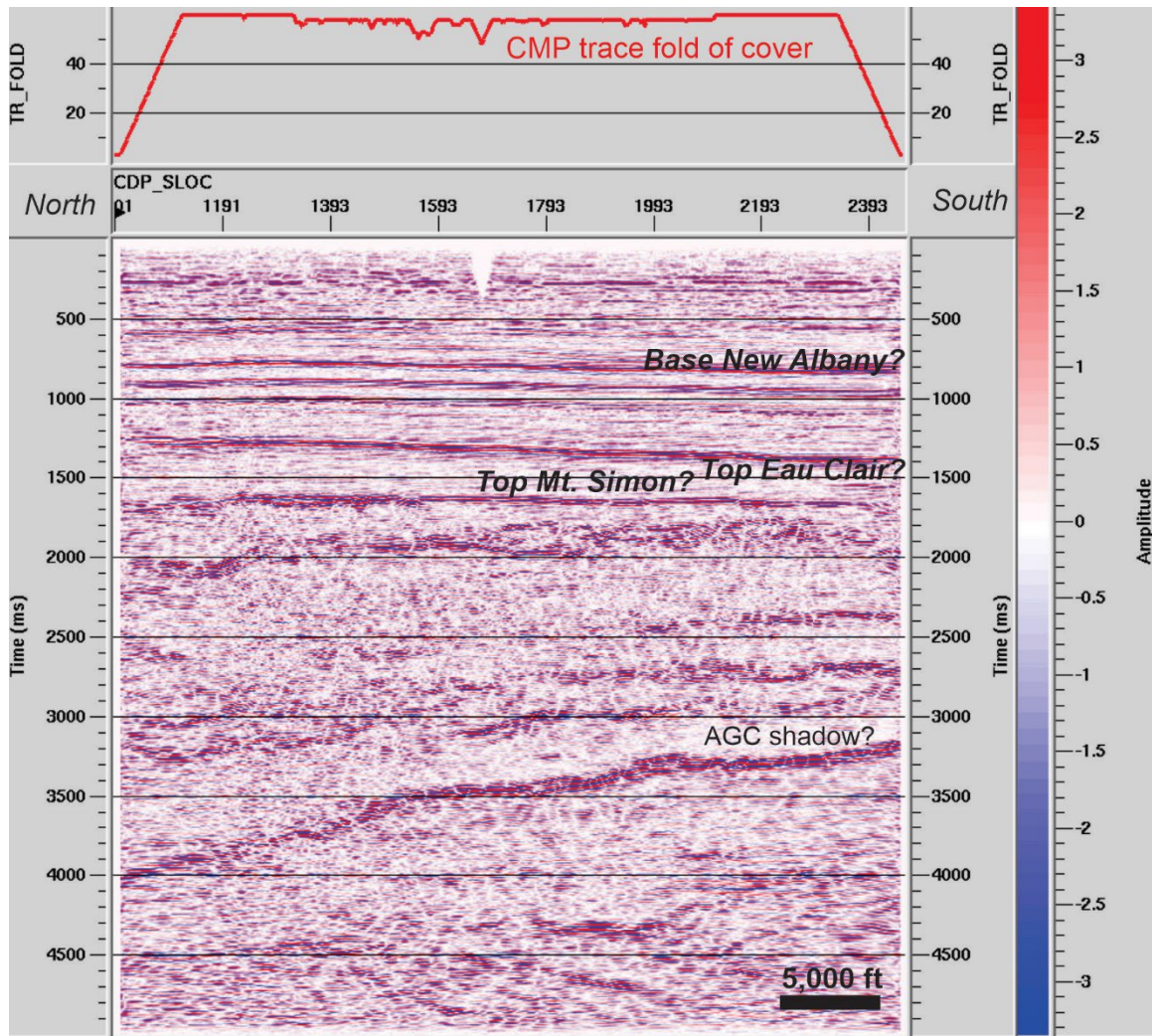
Figure 4: *Richland County CMP seismic profile (Figure 1). The stratigraphic markers are based on regional correlations. See McBride et al. (2020) for more information.*

SUMMARY AND CONCLUSIONS

The two new seismic profiles show a readily interpretable Paleozoic section, although reflectivity around the target CCS zone is relatively poorly developed. As typically observed on other long-record seismic CMP sections in the Illinois Basin (e.g., Pratt et al., 1992; McBride et al., 2020), extraordinarily bright and continuous Precambrian reflectors appear on the new profiles. For both seismic profiles, a bright reflector series occurs (middle panels, Figures 3a and 3b) that includes stratigraphic features, such as pinch-outs and angular unconformities. On the lower panels for the Wabash profiles, a distinct fabric of diffractions and short offset reflector segments marks the deeper basement. However, the Precambrian reflectivity on the new profiles is otherwise distinct from that on the Richland County profile, located about 62 mi (100 km) to the southwest. The shallow basement in Richland County shows a highly reflective and layered series resting over the bright dipping reflector. The shallow basement observed on the Wabash profiles is mostly sub-

horizontal and less strongly layered. Locating the Wabash profiles in the context of regional Precambrian reflectivity (Figure 1) suggests that they are at the edge of a vast but poorly understood depocenter of igneous and/or sedimentary material.

Shallow basement reflectivity on the Richland County profile can be interpreted as part of the Centralia sequence as first recognized by Pratt et al. (1992) from older regional deep seismic profiles. These and other workers (e.g., McBride et al. [2003]; Freiburg et al. [2020]) have suggested a range of geological interpretations, including Precambrian sedimentary strata and layered felsic igneous rocks along with mafic igneous sills, which are exposed in the St. Francois mountains in southeastern Missouri (Kisvarsanyi and Kisvarsanyi, 1990). Other areas beneath the Basin do not show this extraordinary layering. For example, the CCS seismic CMP profile in Christian County (Figure 1; McBride et al., 2020) does not show a Centralia-like uppermost basement, but only the single strong dipping reflector and underlying diffractive zone. Other profiles north of the terrane boundary and east of the current profile show the same pattern (McBride et al., 2016).

ACKNOWLEDGMENTS

REFERENCES

Bear, G.W., Rupp, J.A., and Rudman, A.J., 1997, Seismic interpretation of the deep structure of the Wabash Valley Fault System: *Seismological Research Letters 68*, 624-640.

Buschbach, T.C., and Kolata, D.R., 1991, Regional setting of Illinois Basin, in Leighton, M.W., Kolata, D.R., Oltz, D.F., and Eidel, J.J., eds., *Interior Cratonic Basins: AAPG Memoir 51*, 29-55.

Drahovzal, J.A., 1997, Proterozoic sequences and their implications for Precambrian and Cambrian geologic evolution of western Kentucky: Evidence from seismic-reflection data: *Seismological Research Letters 68*, 553–566.

Freiburg, J. T., McBride, J. H., Malone, D. H., and Leetaru, H. E., 2020, Petrology, geochronology, and geophysical characterization of Mesoproterozoic rocks in central Illinois, USA, *Geoscience Frontiers 11*, 581-596, doi.org/10.1016/j.gsf.2019.07.004.

Greenberg, S. E., 2013, Creating a sequestration capacity building and knowledge sharing program: *Energy Procedia 37*, 7291–7298.

Kisvarsanyi, E.B., and Kisvarsanyi, G. 1990, Alkaline granite ring complexes and metallogeny in the Middle Proterozoic St. Francois Terrane, southeastern Missouri, U.S.A., *in* Gower, C., Rivers, T., Ryan, B., eds., Mid-Proterozoic Laurentia-Baltica, Geological Association of Canada Special Paper 38, 433–446.

McBride, J. H., 1997, Variable deep structure of a midcontinent fault and fold zone from seismic reflection: La Salle deformation belt, Illinois basin. *Geological Society of America Bulletin 108*, 1502-1513.

McBride, J.H., Kolata, D.R., and Hildenbrand, T.G., 2003, Geophysical constraints on understanding the origin of the Paleozoic Illinois basin and the Proterozoic eastern granite-rhyolite province, USA: *Tectonophysics 363*, 45-78.

McBride, J. H., Leetaru, H. E., Keach, R. W., II, and McBride, E. I., 2016, Fine-Scale Structure of the Precambrian beneath the Illinois Basin, *Geosphere 12* (2), 585-606, doi:10.1130/GES01286.1.

McBride, J. H., Leetaru, H. E., Freiburg, F. T., and Whittaker, S. G., 2020, Precambrian structure revealed by CCS seismic profiles from the Illinois Basin, SEG Technical Program Expanded Abstracts 2020, https://doi.org/10.1190/segam2020-3425742.1.

Potter, C.J., Drahovzal, J.A., Sargent, M.L., and McBride, J.H., 1997, Proterozoic structure, Cambrian rifting, and younger faulting as revealed by a regional seismic reflection network in the Southern Illinois Basin: Seismological Research Letters 68, 537-552.

Pratt, T.L., Hauser, E.C., and Nelson, K.D., 1992, Widespread buried Precambrian layered sequences in the U.S. Mid-continent: Evidence for large Proterozoic depositional basins: *AAPG Bulletin 76*, 1384-1401.

Van Schmus, W.R., Bickford, M. E., and Turek, A., 1996, Proterozoic geology of the east-central Midcontinent basement, *in* van der Pluijm, B.A., Catacosinos, P.A., eds., Basement and basins of eastern North America: Geological Society of America Special Paper 308, 7-32.

Whitmeyer, S. J., and Karlstrom, K. E., 2007, Tectonic model for the Proterozoic growth of North America, *Geosphere 3*, 220–259. doi: 10.1130/GES00055.1

Chapter 3

Geochronology of the Mt. Simon Sandstone and Basalt from the Wabash #1 Well, West Terre Haute, Indiana

By: Jared T. Freiburg[1] and Dave H. Malone[2]

[1]Illinois State Geological Survey, Prairie Research Institute, University of Illinois at Urbana-Champaign

[2]Illinois State University, Normal, Illinois

INTRODUCTION

The Wabash #1 well, drilled for the Wabash CarbonSAFE Project and located in West Terre Haute, Vigo County, Indiana, was drilled in early 2020 as a stratigraphic test well to characterize and evaluate the basal Cambrian Mt. Simon Sandstone for carbon dioxide storage. With a limited number of wells drilled into the basal Cambrian strata throughout the Illinois Basin, the distribution of the anomalously high porosity and permeability Lower Mt. Simon Sandstone, commonly referred to as the "arkose", is poorly understood. Previous research has proposed the Precambrian basement exerts controls on the distribution of the arkose. These controls include Precambrian topography (Leetaru and McBride, 2009), basement heterogeneity (Freiburg et al., 2020a), for example the age and extent of the Granite-Rhyolite Province (Van Scmus et al., 1996), a proximal sediment source (Freiburg et al., 2020b), and the extent of Neoproterozoic rift basins (Keller et al., 1983; Stein et al., 2015; Malone et al., 2016). The Wabash #1 well is located along the eastern axis of a suspected ancient rift valley and approximately 100 miles southeast from the Illinois Basin Decatur Project wells, 120 miles southeast from the CarbonSAFE Macon County T.R. McMillen #2 well, and 165 miles southeast from the FutureGen Alliance #1 well; all of which lie on the western flacks of the suspected rift zone (Figures 1 and 2).

In this report, we present 905 new detrital zircon ages from five samples of the Mt. Simon and a sandstone unit currently referred to as the pre-Mt. Simon due to its stratigraphic position underlying a basalt flow within the Cambrian succession. These new data are compared with detrital zircon age spectra from the Mt. Simon strata located along the western flank of the interpreted rift zone and provide valuable insight to sediment pathways from source to sink and allow a greater understanding of the arkose reservoir distribution. We also present new ^{40}Ar/^{39}Ar isotopic age data of mineral separates from the basalt encountered at the Wabash #1 well as well as from a gabbro from the Illinois Basin Decatur Project Verification #2 well encountered in the Precambrian basement and previously reported as Midcontinent Rift age based on zircon age data (Freiburg et al., 2020a).

BACKGROUND

The Illinois Basin is an intracratonic basin formed within the North American Craton or Laurentia. The core of Laurentia is formed by a series of Paleoproterozoic collisional events between Archean continental fragments. Progressive addition of volcanic arc and oceanic terranes accreted onto this core and formed the lithosphere of Laurentia (Whitmeyer and Karlstrom, 2007). Of these are the basement rocks of the Illinois Basin that consist of a voluminous Mesoproterozoic magmatic province (ca. 1.45 Ga) referred to as the Eastern Granite-Rhyolite province (EGRP; Thomas et al. 1984; Van Schmus et al. 1993), and areas overlain by younger magmatic rocks (ca. 1.35 Ga), often referred to as the southern granite-rhyolite province (SGRP; Bickford and Van Schmus et al., 1987. For simplicity, together they will be referred to herein as the Granite-Rhyolite Province (GRP). The EGRP is bisected by a southwest–northeast trending isotopic discontinuity dubbed the "Nd line" (Figure 1; Van Schmus et al. 1996). The Nd line separates Mesoproterozoic igneous rocks with Nd model ages > 1.55 Ga to the northwest from those with <1.55 Ga model ages to the southeast and is interpreted to be a continental-scale Proterozoic terrane boundary. Mesoproterozoic rocks to the south-east are thought to represent 1.55–1.35 Ga juvenile crust that accreted as part of a long-lived arc system, whereas rocks to the northwest were derived from melting of Paleoproterozoic crust during Granite-Rhyolite magmatism (Van Schmus et al. 1996; Whitmeyer and Karlstrom 2007; Bickford et al. 2015). EGRP rocks are bound by the Yavapai (1.8-1.70 Ga) and Mazatzal Province (1.70 -1.60 Ga) juvenile crust to the northwest and are overprinted by rocks related to Grenville-age tectonism to the east. The Illinois Basin located along the southern margin of Laurentian crust likely had early origins as intra-continental transverse rift structure (i.e., Reelfoot, Wabash, LaSalle) that initiated in response to Midcontinent rifting and rifting along the Laurentian margin and may be part of the greater East Continent Rift Basin (ECRB; Drahovzal et al., 1992). Previous studies have proposed two phases of rifting based on igneous magmatism along the Laurentian margin: 1) the first and older rifting event occurred from 765 to 650 Ma; 2) the second event spanned from 539 to 530 Ma and is associated with the continental breakup of Rodinia and the opening of Iapetus (Thomas, 2014; Freiburg et al., 2020b). Rifting, synrift volcanism, and sediment fill formed what has previously been referred to as the proto-Illinois Basin (Freiburg et al., 2020a), with later subsequence occurring to the south along the Reelfoot Rift and forming the Illinois Basin.

Pre-Mt. Simon sandstones were noted by others throughout the Illinois Basin (Pratt et al., 1989; McBride and Kolata, 1999; McBride et al., 2003; Freiburg et al., 2014) and further east into the older ECRB (Denison et al., 1984; Lidiak et al., 1985; Shrake et al, 1990). Regionally, pre-Mt. Simon units are referred to as the Middle Run Formation in Ohio (Shrake 1991; Wickstrom et al., 1992), Indiana, and Kentucky (Drahovzal et al., 1992; Moecher et al., 2017) and have been differentiated from the Mt. Simon based on the unconformable contact, compositional and diagenetic differences, and sometimes separated by basalt (Shrake, 1991; Drahovzal et al, 1992). Basalts separating the Mt. Simon Sandstone from the Middle Run Formation and sometimes interbedded within the Middle Run are identified in wells in Ohio, Kentucky, and Indiana (Drahovzal et al, 1992). Age data of the basalts are scarce and all located in Ohio closer to the areas of the Midcontinent Rift, Fort Wayne Rift, and Grenville

front. Igneous rocks (including basalts) beneath the Mt. Simon have yielded dates slightly older than the 1.1 Ga Midcontinent rift (Drahovzal et al, 1992), suggesting that rifting and synrift sediment fill is Proterozoic and not Cambrian. Furthermore, detrital zircon ages from a pre-Mt. Simon litharenite in western Kentucky is proposed to be the distal correlative of the Middle Run Formation in Kentucky and yields a maximum depositional age of 1,020 Ma with synrift sediments capped by basalt hypothesized to be older (~1,100 Ma) and correlative with Midcontinent Rifting (Moecher et al., 2017). Freiburg et al. (2020b) presented Cambrian detrital zircon ages in Lower Mt. Simon and pre-Mt. Simon sandstones in central Illinois, suggesting Cambrian igneous activity associated with regional rifting events. Herein, we present further evidence of Cambrian rifting in the Illinois Basin.
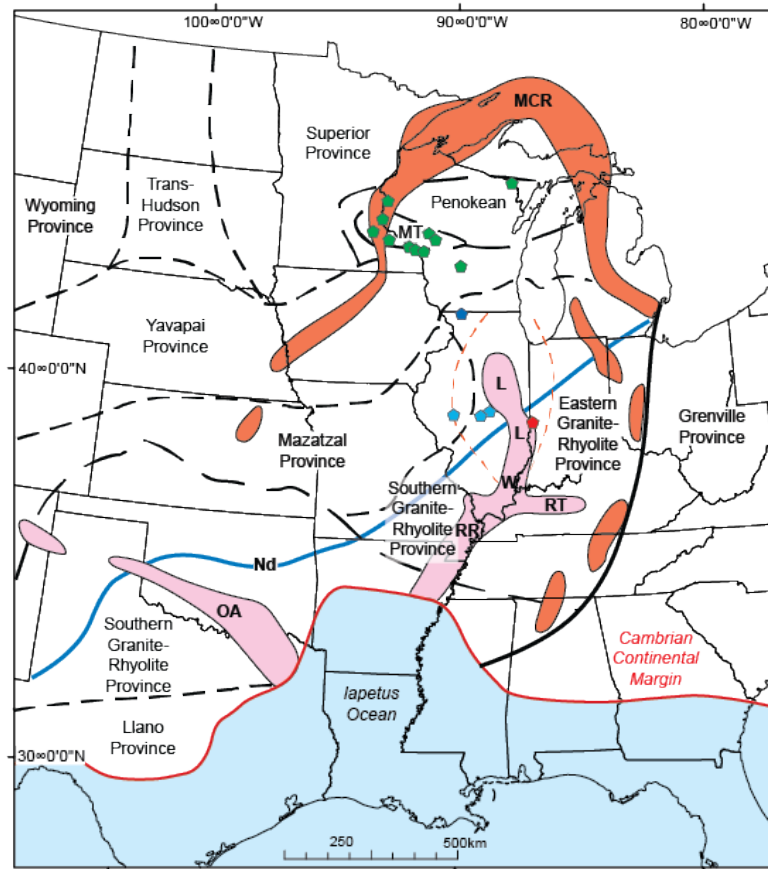
Figure 2: *Map of basement terranes of the Laurentian midcontinent (modified from Bickford et al., 2015; Freiburg et al., 2020b). The locations of the Oklahoma Aulocogen (OA), Reelfoot Rift (RR), Rome Trough (RT), and Wabash (W) and LaSalle (L) deformational belts are indicated in pink. The 1.1 Ga Midcontinent rift (MCR) is indicated in orange. Light blue pentagons = Illinois Basin Decatur Project and CarbonSAFE Macon Co. Project samples. Green pentagons = sampling sites for late Cambrian arenites reported in Konstantinou et al. (2014). Dark blue pentagons = Mt. Simon drill core sampling locality reported in Lovell and Bowen (2013). Red pentagons = Mt. Simon and pre-Mt. Simon samples from the Wabash #1 well. Blue line is the "Nd line" of Bickford et al. (2015), which separates crust yielding Nd model ages greater than 1.55 Ga to the north and less than 1.55 Ga to the south. Modified from Bickford et al., 2015 and Stein et al., 2018.*
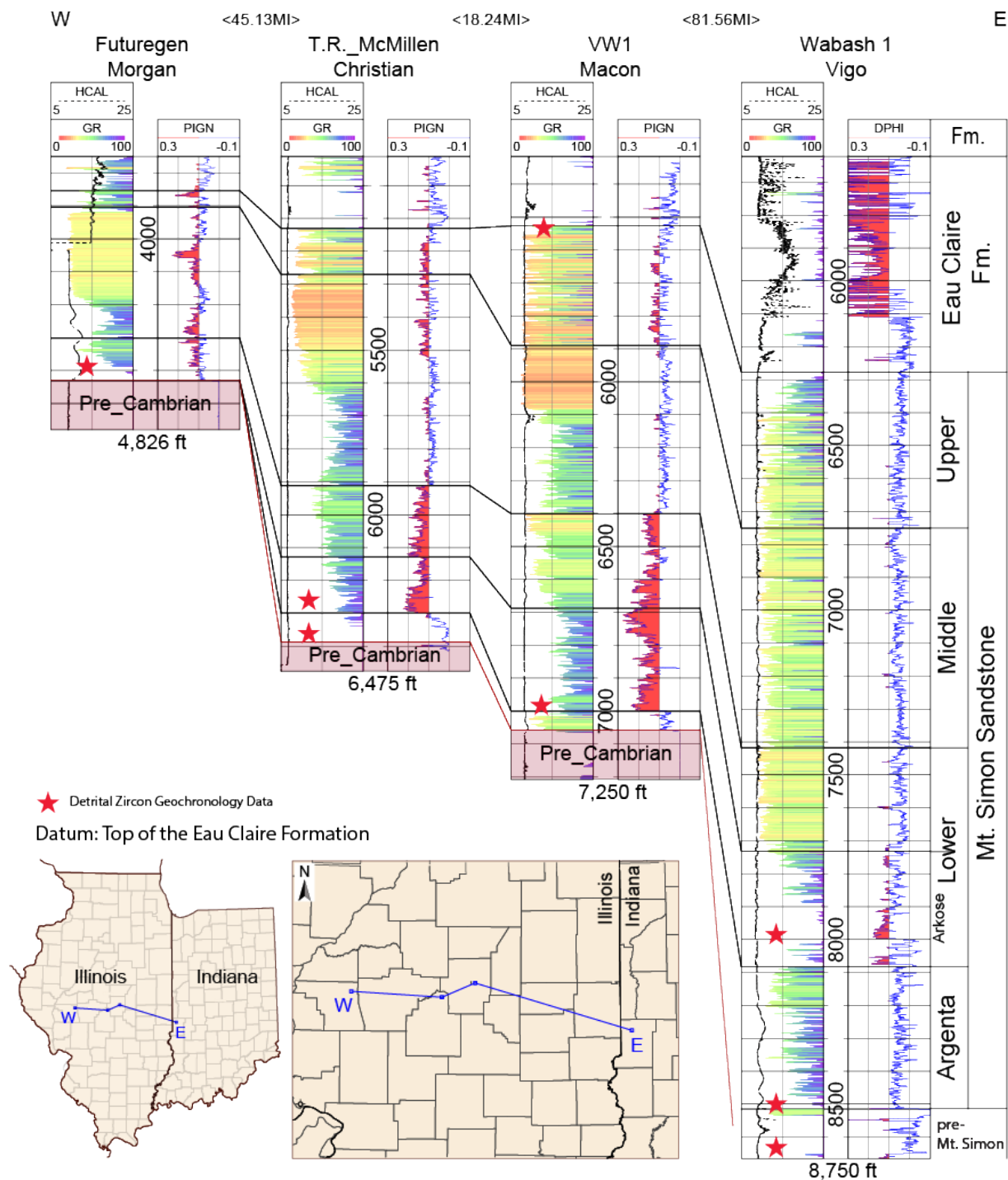
Figure 3: *Geophysical log cross-section of the Mt. Simon Sandstone in the (right to left) Wabash #1 well, Vigo Co., Indiana; Verification #1 well (VW1), Macon Co., Illinois; T.R. McMillen #2 well, Christian Co., Illinois; and the FutureGen Alliance #1 well, Morgan Co., Illinois. Red stars represent detrital zircon geochronology data from core samples presented herein. Figure provided by Z. Askari (ISGS).*

METHODS

Detrital Zircon U-Pb Geochronology

A total of five samples were taken for detrital zircon U/Pb geochronology from core samples cut in the Wabash Valley Resources #1 well (Indiana Geological Survey #168045; Indiana Natural Resource Division of Oil and Gas Permit #55855). One sample is from the Mt. Simon Sandstone from 3.5-in or full diameter core in what is considered the Lower Mt. Simon Sandstone (Figure 3). Four 1-in diameter rotary sidewall cores were sampled; one from what is considered Mt. Simon (or perhaps Argenta) and occurs stratigraphically above a basalt and three samples from what is considered pre-Mt. Simon Sandstone and occur stratigraphically below the basalt (Figure 3 and Figure 4). Zircon crystals were extracted from core samples by traditional methods of crushing and grinding, followed by separation by panning, heavy liquids, and a Frantz magnetic separator. Approximately 6 in (length) of sample was prepared for the full diameter core sample while all the 2-in (length) rotary sidewall core sample was processed after sub-sampling for preparation of thin sections other reports.

Extracted zircons were set in mounts and grided down to a depth of ~20μm, polished, imaged, and cleaned before isotopic analysis. U-Pb geochronology of zircons was conducted by laser ablation-inductively coupled plasma mass spectrometry at the Arizona LaserChron Center. The analysis involved ablation of zircon with a Photon Machines Analyte G2 excimer laser equipped with Helx ablation cell using a spot diameter of 20~μm. The ablated material was carried in helium into the plasma source of an Element2 HR inductively coupled plasma mass spectrometer, which sequences rapidly through U, Th, and Pb isotopes.

The ages are shown on relative age-probability diagrams using the routines in Isoplot (Figures 5-8). Composite age probability plots were made from an in-house excel program that normalizes each curve according to the number of constituent analyses, such that each curve contains the same area, and then stacks the probability curves. The maximum depositional age (MDA) for each sample was calculated by taking the weighted mean of the youngest subset of grains (at least four) with overlapping age errors.

$^{40}Ar/^{30}Ar$ Geochronology

Two samples were selected for $^{40}Ar/^{39}Ar$ dating: the basalt from the Wabash #1 well and a gabbro encountered in the Verification #2 well in Decatur, Illinois. Trim from rotary sidewall core samples were used for thin section preparation for petrographic analysis and mineral characterization. The remaining core samples were crushed, sieved, washed, dried, and sieved between 250-150 μm to using standard mineral separation techniques. Groundmass and mineral separates were cleaned by rinsing each sample with cold water, then washing in an ultrasonic cleaner for 15 minutes using triple distilled water (Milli-Q Water), then dried in a drying oven at 55°C. Special care was taken to remove any alteration material for the groundmass and plagioclase for the basalt sample by using an intensive acid leaching procedure that involved a combination of HCl and HNO_3 at different acid strengths and drying the samples in a drying oven at 55°C (Koppers et al., 2000).

Once the samples were dried, they were again sieved between 250-150 μm to remove finer fractions produced from the ultrasonic cleaning. Final groundmass and mineral separates were obtained using a binocular microscope to obtain purities of >99%. Finally, any visible alteration or adhering crystal phases that were still present after leaching were carefully removed prior to packaging and irradiation of the samples.

^{40}Ar/^{39}Ar ages (Table 1) were obtained by incremental heating methods using the ThermoFisher Scientific ARGUS-VI mass spectrometer and data collection using internal lab software ArArExperiments version 4.5.7. The samples were irradiated for 6 Megawatt hours (Irradiation 21-OSU-01) in the CLICIT position in the Oregon State University's TRIGA nuclear reactor. Sample were irradiated with the Fish Canyon Tuff sanidine (FCT-2-NM sanidine) with an age of 28.201 ± 0.023 Ma, 1σ flux monitor (Kuiper et al. 2008). Individual J-values for each sample were calculated by polynomial extrapolation of the measured flux gradient against irradiation height and typically give 0.06-0.12% uncertainties (1σ). The ^{40}Ar/^{39}Ar incremental heating age determinations were performed on a multi-collector ARGUS-VI mass spectrometer at Oregon State University that has five Faraday collectors (all fitted with two 10^{12} Ohm resistors for masses ^{41}Ar and ^{40}Ar and three 10^{13} Ohm resistors for argon masses ^{39}Ar, ^{38}Ar, and ^{37}Ar). Measurement of mass ^{36}Ar was obtained using an ion-counting CuBe electron multiplier (located in a position next to the lowest mass Faraday collector). This allows us to measure simultaneously all argon isotopes, with mass 36 on the multiplier and masses 37 through 40 on the four adjacent Faradays. This configuration provides the advantages of running in a full multi-collector mode while measuring the lowest peak (on mass 36) on the highly sensitive electron multiplier (which has an extremely low dark-noise and a very high peak/noise ratio). Irradiated samples were loaded into Cu-planchettes in an ultra-high vacuum sample chamber and incrementally heated by scanning a Synrad Firestar 20Watt defocused 30 W CO_2 laser beam in pre-set patterns across the sample in order to release the argon evenly. Each heating step is 62 seconds. After heating, reactive gases were cleaned up using four SAES Zr-Al AP10 getters for three minutes; two operated at 450°C and two operated at room temperature (21°C). All ages were calculated using the corrected Steiger and Jäger (1977) decay constant of 5.530 ± 0.097 x 10^{-10} 1/yr (2σ) as reported by Min et al. (2000). For all other constants used in the age calculations, we refer to Table 2 in Koppers et al. (2003). Incremental heating plateau ages and isochron ages were calculated as weighted means with $1/\sigma^2$ as weighting factor (Taylor, 1997) and as YORK2 least-square fits with correlated errors (York, 1969) using the ArArCALC v2.6.2 software from Koppers (2002) available from the http://earthref.org/ArArCALC/ website. Argon isotopic results are corrected for system blanks, radioactive decay, mass discrimination, reactor-induced interference reactions, and atmospheric argon contamination. Decay constants reported by Min et al. (2000) are utilized for age calculation. Isotope interference corrections as determined using the ARGUS VI are: $(^{36}$Ar/^{37}Ar$)_{Ca}$ = 0.0002703 ± 0.0000005; $(^{39}$Ar/^{37}Ar$)_{Ca}$ = 0.0006425 ± 0.0000059; $(^{40}$Ar/^{39}Ar$)_K$ = 0.000607 ± 0.000059; $(^{38}$Ar/^{39}Ar$)_K$ = 0.012077 ± 0.000011. Ages were calculated assuming an atmospheric ^{40}Ar/^{36}Ar ratio of 298.56 ± 0.113 (Lee et al., 2006). Data reduction and age calculation were processed using Ar-Ar Calc 2.7.0 (Koppers, 2002). Plateau ages are defined as including

>50% of the total ^{39}Ar released with at least three consecutive steps, where the ^{40}Ar/^{39}Ar ratio for each step is in agreement with the mean at the 95% confidence level. In many cases, only a mini-plateau age is given, where a mini-plateau <50% of the ^{39}Ar released.
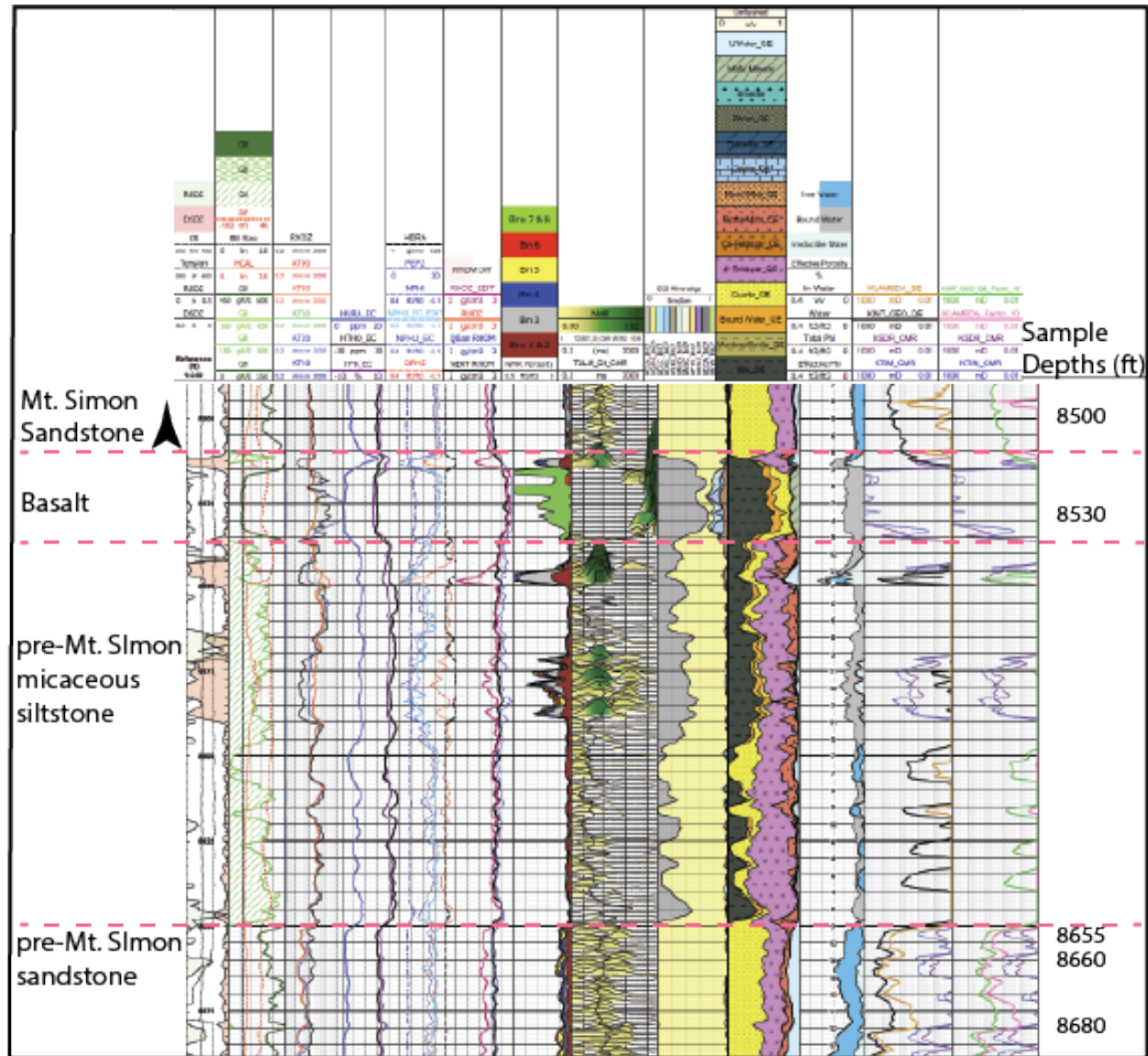
Figure 4*: Elemental Capture Spectroscopy Quanti-Elemental Analysis log (ELAN) near the TD section of the Wabash #1 well. Sample depths (rotary sidewall core) with detrital zircon (8,500 ft, 8,655 ft, 8,660 ft, 8,680 ft) and Ar/Ar dating (8,530 ft) analysis presented herein.*

Figure 5: *Photographs of Wabash #1 well Mt. Simon Sandstone full diameter (3.5 inch) core sample from 7,972-7,973 and rotary sidewall core samples (1-inch diameter) from the Wabash #1 well and Verification #2 well. Samples depths (ft) 8,500; 8,655; 8,660; 8,680 are sandstone and were disaggregated for detrital zircon extraction and U/Pb dating. Sample depths (ft) 8,530 is a basalt from Wabash #1 well and 7,184.9 is a gabbro from Verification #2 were prepared for Ar/Ar dating.*

RESULTS

Sandstone Detrital Zircon Ages

The probability density plots and the MDAs for each sample are provided in Figures 5-8. The Mt. Simon Sandstone full diameter core was sampled from a depth of 7,972-7,972.5 ft (Figure 5). During drilling operations, this coring run was cut as it was suspected to be closest in correlation to the arkose observed to the west in wells such as those at IBDP and CarbonSAFE Macon County. A total of 295 detrital zircon ages are presented. The dominant age peak is ~1,367 Ma, with lesser peaks at 1,460; 1,179; 1,643; 522; 2,678, and 1,807 Ma.

The Mt. Simon or Argenta sandstone at a depth of 8,500 ft (Figure 5) is located approximately 14 ft above the top of the basalt (Figure 4). A total of 342 zircon ages are presented. The dominant age peak is at ~2,696 Ma, with lesser peaks at 1,461; 1,789; 1,122; and 541 Ma.

Three samples below the basalt were logged as the pre-Mt. Simon at the time of drilling and occur at depths 8,655; 8,660; and 8,680 ft. The 8,655 and 8,660 ft samples are reported together due to the low number of zircons retrieved and the similarities in age. A total of 19 detrital zircon ages are presented. The dominant age peak is ~1,474 Ma. A major difference compared to shallower samples is the absence of detrital zircon ages older than ~1,900 Ma. Cambrian-age zircons are still present.

The deepest sample in the pre-Mt. Simon (below basalt) is from a depth of 8,680 ft with a total of 290 detrital zircon ages presented. The dominant age peak is ~1,477 Ma, with lesser peaks at 1,203 Ma and 541 Ma.

When treated as a whole (i.e., all 905 grains), the youngest age group (~1.5% of the total) ranges in age from 508 to 562 Ma and has a peak age of 540 Ma. The bulk of these Cambrian zircons are found in the shallower Mt. Simon sample (7,972 ft) which may relate to the quantity of sample processed (full diameter compared to rotary sidewall core) rather than fertility bias. Mesoproterozoic zircons represent the largest age peak of 1,477 Ma, with a secondary age peak of 1,367 Ma, and account for ~50% of age spectrum (1,300-1,600 Ma). Grenville-age zircons (900-1,300 Ma) with age peaks of 1,122 Ma (8,500 ft), 1,179 Ma (7,972 ft), and 1,203 Ma (8,680 ft) account for ~20% of age spectrum. Paleoproterozoic zircons (1,600-2,500 Ma) with age peaks of 1,643 Ma (7,972 ft), 1,789 Ma (8,500 ft), 1,807 Ma (7,972 ft) account for ~15% of the age spectrum with nearly all concentrated in samples above basalt (8,500 ft; 7,972 ft). Archean zircons (2,500-3,000 Ma) with an age peak of 2,696 Ma (8,500 ft) and 2,678 (7,972 ft) account for ~12% of the age spectrum with nearly all concentrated in samples above the basalt (8,500 ft; 7,972 ft). The
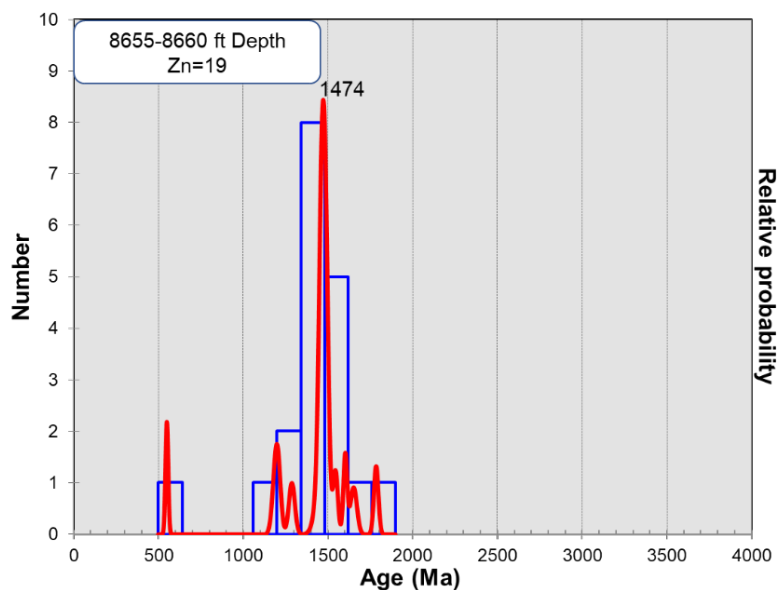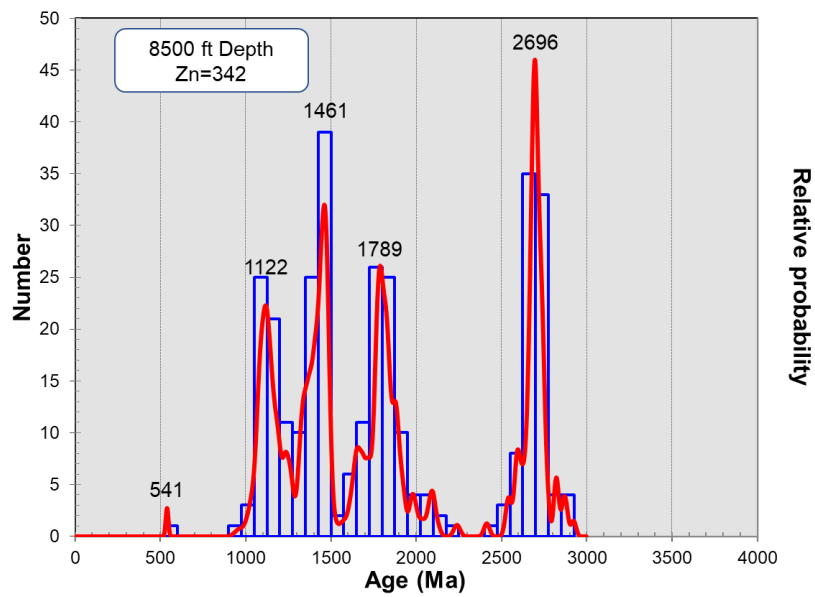

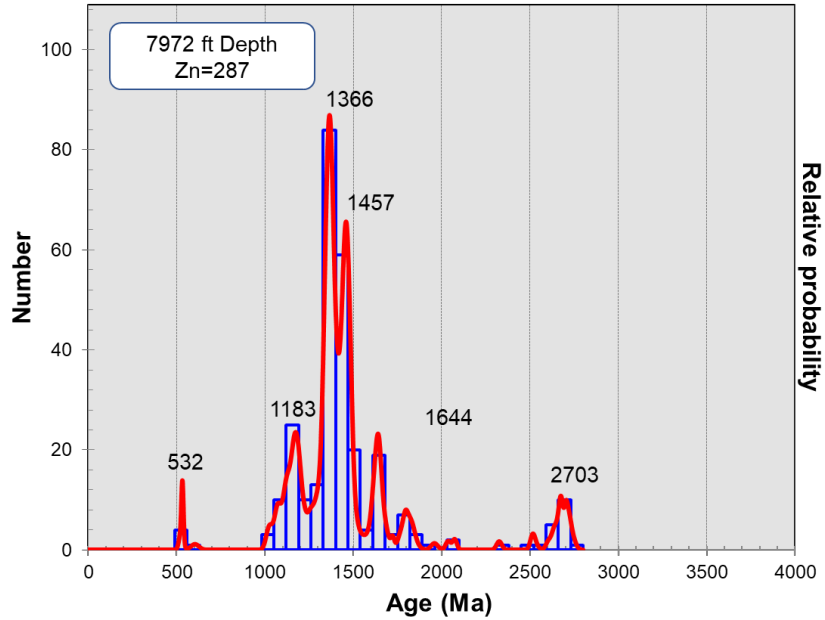majority (nearly 85%) of Archean zircons are found in sample 8,500 ft.

Figure 6: Probability density plot of the pre-Mt. Simon Sandstone (below basalt) from the Wabash #1 well.
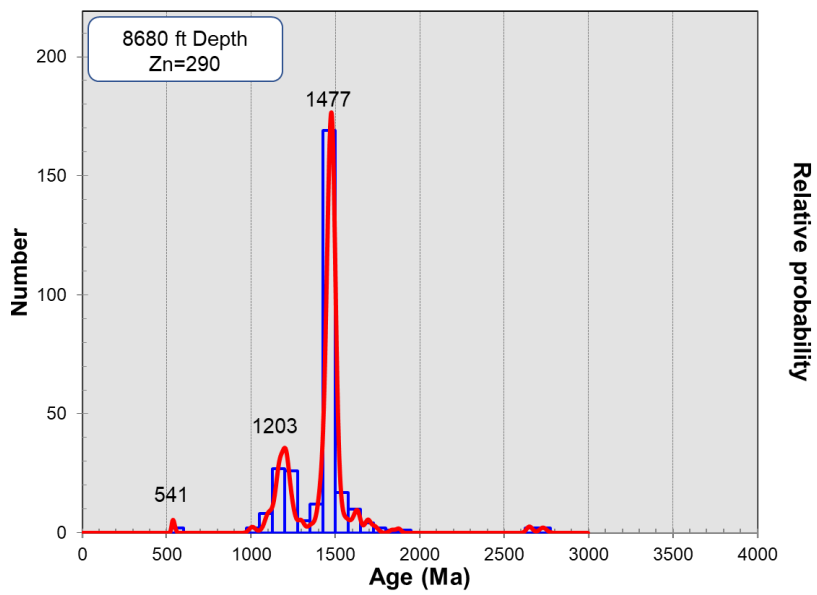
Figure 7: Probability density plot of pre-Mt. Simon Sandstone (below basalt) from the Wabash #1 well.

Figure 8: Probability density plot of Mt. Simon Sandstone (above basalt) from the Wabash #1 well.

Figure 9: *Probability density plot of Mt. Simon Sandstone (above basalt) from the Wabash #1 well.*

Volcanic Ages

The ^{40}Ar/^{39}Ar dating results (plateau ages with 2σ uncertainties) for the basalt Wabash-8530) and the gabbro (VW2-7155) are summarized in Table 1.

Table 1: *Summary of ^{40}Ar/^{39}Ar dating results for the Wabash #1 well basalt in Terre Haute, Indiana, and the Verification #2 well gabbro in Decatur, Illinois.*

Sample			Results			
Sample Name	Location	Material	Age Type	Age Interpretation	Age ± 2σ (i)	± 2σ (f)
Wabash-8530	Terre Haute, Indiana	Groundmass	Plateau	Crystallization Age	525.79 ± 1.10 Ma	± 25.62 Ma
VW2-7155	Decatur, Illinois	Plagioclase	Plateau	Crystallization Age	725.26 ± 13.99 Ma	± 37.27 Ma
Wabash-8530	Terre Haute, Indiana	Plagioclase	Mini Plateau	Crystallization Age	na na	na
VW2-7155	Decatur, Illinois	Biotite	Plateau	Crystallization Age	1.332 ± 0.003 Ga	± 0.060 Ga
VW2-7155	Decatur, Illinois	Hornblende	Plateau	Crystallization Age	1.335 ± 0.019 Ga	± 0.063 Ga
VW2-7155	Decatur, Illinois	Pyroxene	Plateau	Crystallization Age	1.311 ± 0.003 Ga	± 0.059 Ga

68
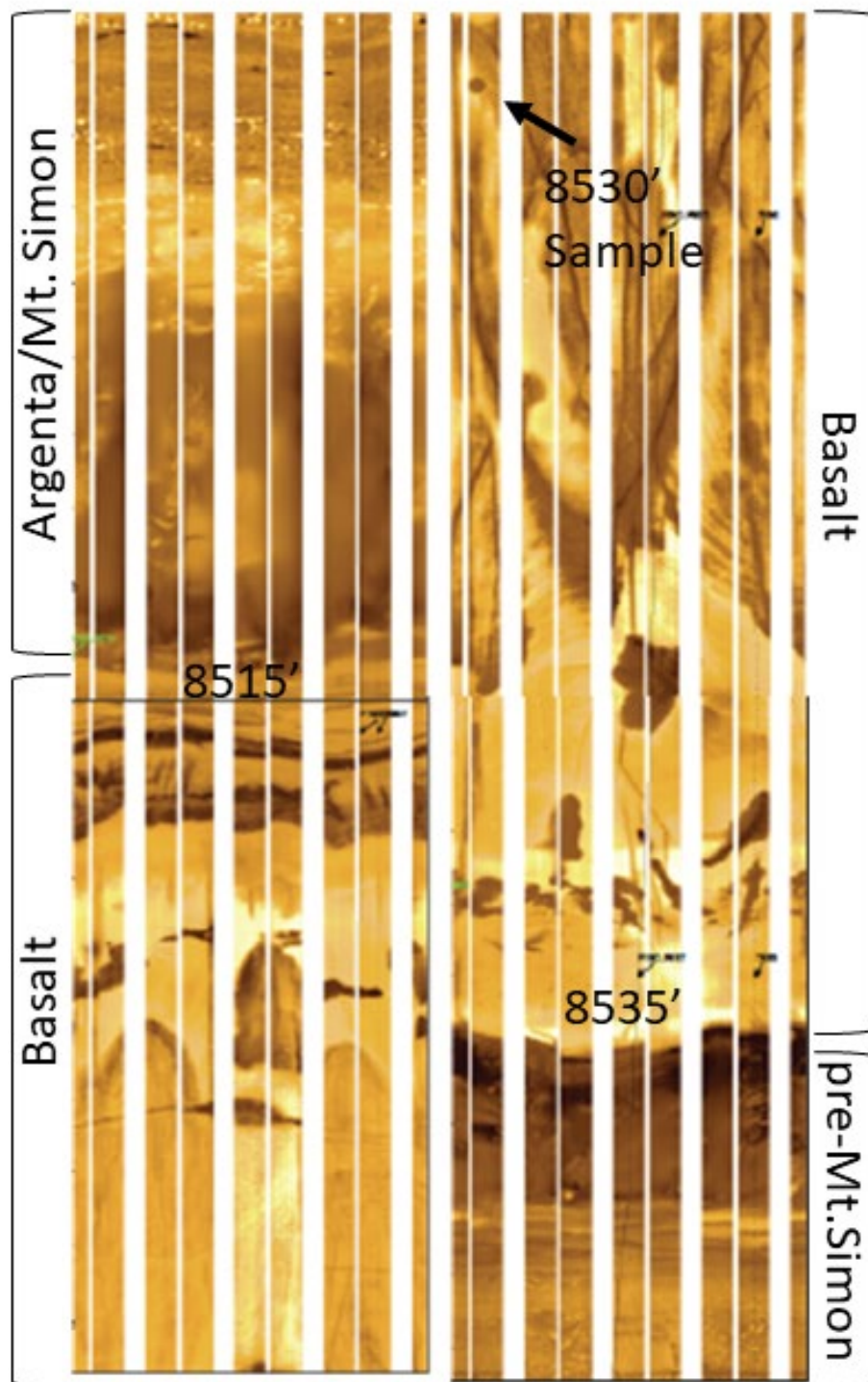
Figure 10: *Fullbore formation micro-imager log photos showing the top contact of the basalt with the Mt. Simon or Argenta sandstone at 8,515 ft and the basal contact with the pre-Mt. Simon sediments at 8,535 ft. Rotary sidewall core sample (figure) location of basalt is shown at 8,530 ft. The sediments on top of the basalt are comprised of muddy siltstone that grades upward to fine-grained sandstone. The sediments below the basalt are comprised of muddy siltstone that is highly micaceous.*
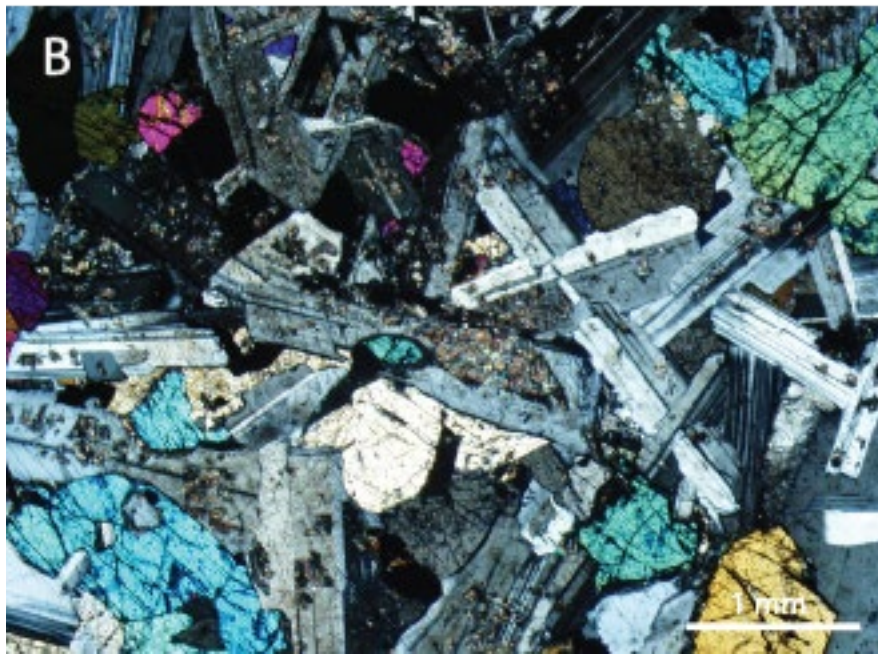
Figure 11: Thin section cross-polarized light photomicrographs of (A) the basalt from the Wabash #1 well at a depth of 8,530 ft and (B) the gabbro from the Verification #2 well, Decatur, Illinois, at a depth of 7,184.9 ft. Both samples are dominantly composed of plagioclase with a fine-grained groundmass of pyroxene, amphibole, and magnetite in the basalt and coarse crystals of pyroxene, olivine, and magnetite in the gabbro.

DISCUSSION

Age and Provenance of the Lower Mt. Simon and pre-Mt. Simon Sandstones

Cambrian strata, particularly the Upper Mt. Simon and overlying Eau Claire Formation in Missouri and Wisconsin are interpreted to be late Cambrian in age (Ojakangas 1963; Houseknecht and Ethridge, 1978) based on biostratigraphic markers. As previously noted (Freiburg et al., 2020b), cores in the Lower Mt. Simon and Argenta as well as new core recovered in pre-Mt. Simon sediments (beneath basalt) do not provide biostratigraphic control for the age of the Lower Mt. Simon (or earlier deposits), although they are likely middle Cambrian in age. This middle Cambrian age is supported by the presence of a roughly 1,000-m demonstrably late Cambrian strata overlying the Mt. Simon as well as the middle to early Cambrian MDAs presented herein (Figures 5-8). The identification of Cambrian-age detrital zircon in the Mt. Simon Sandstone was the first verifiable indication of Cambrian vulcanism in or around the Illinois Basin and allowed for precise middle Cambrian MDA constraints for the Lower Mt. Simon Sandstone (Freiburg et al., 2020b).

Detrital zircon geochronologic data indicate that the Mt. Simon and pre-Mt. Simon Sandstones sampled in this study area have a provenance similar to the Mt. Simon Sandstone west of the well location (Figure 1 and Figures 11-15) and distinct from the overlying ubiquitous late Cambrian arenites present across the Laurentian midcontinent as well as the enigmatic pre-Mt. Simon or Middle Run sediments filling the ECRB east of the study location (Moecher et al., 2018). Following is a summary of the major detrital zircon populations present in the Mt. Simon and pre-Mt. Simon Sandstones in the Wabash #1 and their possible sources. This summary has important implications for the exploration of the Lower Mt. Simon arkose and, more broadly, implications for the Archean to Cambrian evolution of the Laurentian midcontinent.

Archean Ages

The oldest detrital zircon population present in the samples have peak ages of 2,696 Ma and 2,678 Ma (Figures 13 and 14). This age is characteristic of the Archean Superior Province, which is a unique age in the Lower Mt. Simon as it is typically only observed in the uppermost Mt. Simon. This age corresponds to the cratonic shield that forms the core of Laurentia north of the Illinois Basin exposed on the Canadian shield (Figure 16). Samples below the basalt have a nearly complete absence of Archean zircons, implying accommodation space from early rifting was closed to a distal Archean shield source to the north and these sediments were locally derived (Figure 17). This influx of distal shield sediments may mark a eustatic event forcing depositional changes from local braid-plaint to marine-delta sediment transport. Alternatively, this influx of northern originating Archean detritus may reflect the development of a larger but less developed rift complex extending to the north. As northern accommodation space fills, the Archean source is essentially cut-off. This hypothesis is plausible with an overall diminishing Archean zircon account up section in the shallower Mt. Simon sample. Outside of the rift interior, on the western shoulder at a higher paleotopography, Archean sediments are rare in Lower Mt. Simon and Argenta sandstones (Freiburg et al., 2020b). Out on this flank, away from the depocenter, Archean

sediments don't appear until the Upper Mt. Simon (Lovell and Bowen, 2013; Konstantinou et al., 2014), marking a major eustatic event (i.e., Sauk II), as indicated by widespread correlative black shales.

Paleoproterozoic Ages

Nearly all Paleoproterozoic age zircons are observed exclusively in the samples above the basalt, with a variety of sources observed with peaks of 1,807 Ma (7,972 ft), 1,789 Ma (8,500 ft), and 1,643 Ma (7,972 ft). The 1,807 Ma peak correlates to a late Penokean Province that extends north of the Illinois Basin from central Minnesota across northern Michigan (Van Wyck and Johnson, 1997; Van Wyck and Norman, 2004; Whitmeyer and Karlstrom, 2007; Craddock et al., 2018). The 1,789 Ma peak correlates to the Yavapai Province that extends southwest from southern Wisconsin to Arizona. Sediment transport likely followed pathways like those of Archean origin. The 1,643 Ma peak age is characteristic of the Mazatzal Province. Mazatzal Province is known to occur in the subsurface of the Illinois Basin, particularly western Illinois. Mazatzal-age zircons are also found in Lower Mt. Simon and Argenta sandstones on the western shoulder of the rift and likely reflect a relative proximal source input (Figures 11-13).

GRP Ages

All samples reported herein contain GRP zircons with prominent age peaks of 1,366 Ma and 1,457 (7,972 ft; Mt. Simon), 1,461 Ma (8,500 ft; Mt. Simon), 1,474 Ma and 1,477 Ma (8,680 ft, 8,655 ft, 8,660 ft; pre-Mt. Simon). EGRP ages (1,457-1,477 Ma) are dominantly represented in the deeper samples, whereas both an EGRP and SGRP source is prominent in the 7,972 ft Mt. Simon sample with the SGRP representing the most dominant source in this sample. An EGRP source is likely more proximal while an SGRP source is more distal (to the west) during early rift fill. This is also reflected in Mt. Simon samples on the west flank of the rift where an SGRP source is prominent (Figures 11-13) and proximal to the deposits on the rift shoulder until burial of this proximal source and a distal Archean terrane dominates as the main sediment source (Figures 14-16).

Grenville Ages

Distinct age peaks correlating most closely with the Grenville Provenance are found in nearly all the samples. The deepest sample in the pre-Mt. Simon has a distinct age peak of 1,203 Ma (Figure 5). This age peak predates the Midcontinent rift event (~1,115-1,085 Ma; Davis and Paces, 1990; Paces and Miller, 1993; Vervoort et al., 2007) and more closely corresponds to Grenville magmatism and more specifically the late Elzevirian event in the Appalachians, Adirondacks, and Central Metasedimentary Belt (McLelland et al., 1996). Younger age peaks occur above the basalt in the Mt. Simon samples and include a 1,183 Ma peak (Figure 8) and a 1,122 Ma peak (Figure 7). Both age peaks broadly represent "Grenvillian" provenance (Yonkee et al., 2014) and may be closely related to the Shawinigan magmatic event (1,120-1,180 Ma; McLelland et al. 2013). Sandstones of late Mesoproterozoic and late Paleozoic age in west Texas exhibit a similar

dominant detrital zircon age of 1,120 Ma and are interpreted as a general southwest Grenville and Midcontinent provenance (Spencer et al. 2014). Although there is some agreement with ages presented here and Texas clastic sequences, and such a distal provenance cannot be ruled out, major sediment input would be expected from the more proximal Grenville highlands in the Midcontinent. In the Middle Run Formation of western Kentucky, the greatest number of detrital zircon ages reported fell in between the range of 1,080-1,180 Ma and are reported as being derived from a Grenville highland or recycled Midcontinent Rift volcanic rocks or synrift sediments (Moecher et al., 2018). The relatively low concentration of "Grenvillian" age detrital zircons of the pre-Mt. Simon at the Wabash #1 well compared to those reported in the Middle Run of Kentucky imply these are different clastic sequences, in different basins, with relatively different sediment source rocks. To the west of the well site, on the western shoulder of the basin depocenter, Grenville age zircons occur in all Mt. Simon Sandstone samples observed with one age peak closer to a possible Midcontinent Rift source at 1,107 Ma (Figures 11-14).

Cambrian Ages

An early Cambrian MDA is supported in our results at age peak and MDA of 532 Ma (7,972 ft). All samples analyzed in the Mt. Simon and the pre-Mt. Simon (above and below basalt) contained Cambrian detrital zircons (Figures 11-14) with similar ages to the basalt age reported here. Others analyzed detrital zircons in sandstones considered pre-Mt. Simon or commonly referred to as Middle Run Formation in Ohio (Schneider Santose et al., 2002) and western Kentucky (Moecher et al., 2018) and found an MDA of ~1.0 Ga, younger than the Midcontinent Rift, more consistent with deposition in a Grenville foreland basin, and no Cambrian-aged zircons. Cambrian-aged detrital zircons have been found by others in western Indiana (Lovell, 2017) and central Illinois (Freiburg et al., 2020b). Lovell (2017) found one Cambrian-aged detrital zircon in the Mt. Simon located in southwestern Indiana and stratigraphically shallower than the Mt. Simon detrital zircons in west-central Indiana presented herein. This Cambrian zircon was dismissed as erroneous data since only one was found. Freiburg et al. (2020b) found that the Lower Mt. Simon and underlying Argenta sandstones in central Illinois contain an abundance of Cambrian-aged detrital zircons. The central Illinois location is proposed as the western flank of a rift that is proposed as a northern arm of the northeast-southwest striking Reelfoot Rift in southern Illinois and Kentucky that cuts northward, striking slightly northwest-southeast into western Indiana and eastern Illinois. The MDA presented herein are consistent with other Cambrian zircons found in the Mt. Simon and suggest a regional Cambrian source rock associated with localized continental rift activation. The sediments below the basalt at the Wabash #1 well location differ from the Middle Run Formation with the inclusion of Cambrian zircons. These previously termed pre-Mt. Simon sediments (below basalt) are favored to be Mt. Simon or similar to the Argenta observed in central Illinois (Freiburg et al., 2020b). Alternatively, a Cambrian source rock such as the basalt may have been confined to the Reelfoot Rift and its extension up into central Illinois depositing sediments along the rift axis and along extensional features west. To the east, the Middle Run had a dominant Grenville and perhaps an MCR and reflects older events of the Rodinian breakup.

Age of Rift-related Volcanism

The basalt underlying the Mt. Simon and overlying sediments that have previously been referred to as the pre-Mt. Simon is reported herein as early Cambrian with an ^{40}Ar/^{39}Ar plateau age date of 525.79 ± 1.10 Ma (Table 1). This date is consistent with late events of rifting along the Laurentian margin and similar to other synrift igneous rocks reported along the margin (Badger and Sinha, 1988; Aleinikoff et al., 1995; Thomas et al., 2012; Hanson et al., 2013; Thomas, 2014) and marks the end of the break-up of Rodinia (Li et al., 2008). Image logs of this early Cambrian basalt show a sharp horizontal contact with sedimentary rocks at both the top and bottom, implying the basalt was deposited as a flood or perhaps a horizontal sill (Figure 9). A flow is favored as there are major sedimentological and depositional breaks with the sediments directly below the basalt compared to sediments directly above the basalt, implying a brief hiatus separated by this volcanic event. A thick succession of micaceous silt occurs directly below the basalt and may be interpreted as lacustrine deposits within the rift arm. Sandstone occurs directly above the basalt with no gradation observed from the below siltstones. A flood basalt is also supported by the numerous other wells that have encountered a basalt cap over pre-Mt. Simon or Middle Run sediments in Indiana, Kentucky, and Ohio deposited in the ECRB (Drahovzal et al., 1992). Despite a stratigraphic similarity, basalts on the eastern margin of the ECRB date at 1.325 Ga (Lucius and Von Frese, 1988), which are older than the Midcontinent Rift or Keweenawan (~1.1Ga; Van Schmus and Hinze, 1985) and may be associated with a faulted eastern margin of GRP and thus not associated with the basalt in the Wabash #1 well in western Indiana. Other basalts are confirmed to be of continental affinity based on chemistry and were assumed to be correlative with basaltic volcanism of the Midcontinent Rift system (Wickstrom et al., 1992), although no modern geochronology exists to test this assumption.

The gabbro from the Verification #2 well in Decatur, Illinois was included in this study as it was initially suspected to have an MCR age based on minimal zircon data (Freiburg et al, 2020a). The gabbro located on the western flank of this Reelfoot Rift arm has an ^{40}Ar/^{39}Ar plateau age date of approximately 1.33 Ga with slight variations in pyroxene, hornblende, and biotite, likely a result of argon variation. This age is consistent (though slightly younger) with the pervasive GRP basement in the region and particularly the younger SGRP (Bickford and Van Schmus et al., 1987) volcanism. This highly magnetic gabbro is thought to be associated with the magnetic high observed in Decatur (Freiburg et al. 2020a) and may be related to volcanism associated with the rhyolite basement penetrated on the southwest flank of this anomaly that is also highly magnetic with zircons yielding a U/Pb age of approximately 1.37 Ga (Freiburg and Malone, unpublished). These anomalies are common throughout the GRP because of the common magnetite-series granite and rhyolite (Zietz and Godson, 1982; Yarger, 1985). Despite the gabbro not showing a genetic relationship to the Wabash #1 gabbro, it does show a potential thermal reset stage in the plagioclase with a ^{40}Ar/^{39}Ar plateau age date of 725.26 +/- 13.99 Ma. This date is consistent with and may relate to the early event of rifting along the continental margin as proposed by the many synrift igneous rocks along

the Laurentian margin (references within Thomas, 2014) and implies an earlier origin to the development of the proto-Illinois rift basin.
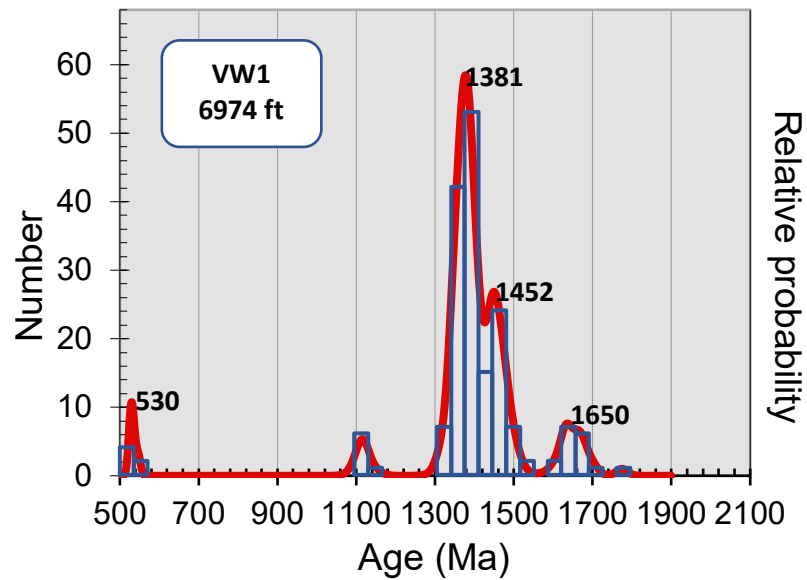
Figure 12: *Probability density plot of the Lower Mt. Simon Sandstone from the Verification #1 well, Macon Co., Illinois.*
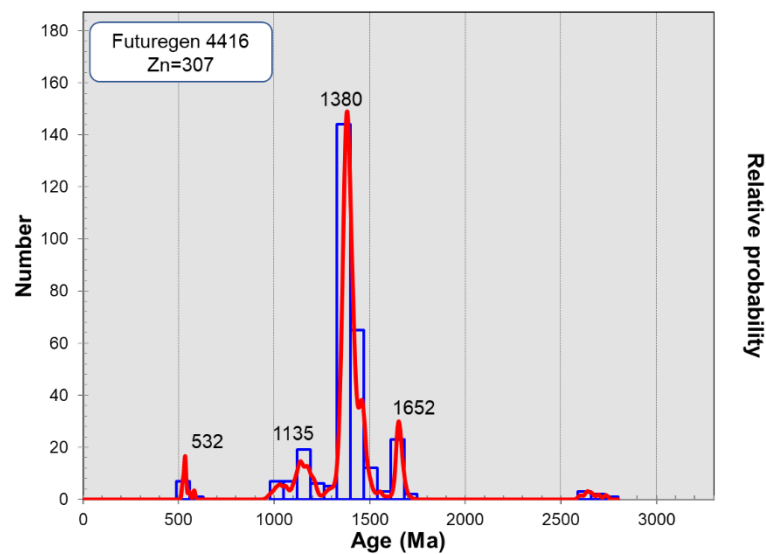
Figure 13: *Probability density plot of the Mt. Simon Sandstone from the FutureGen Alliance #1 well, Morgan Co., Illinois.*
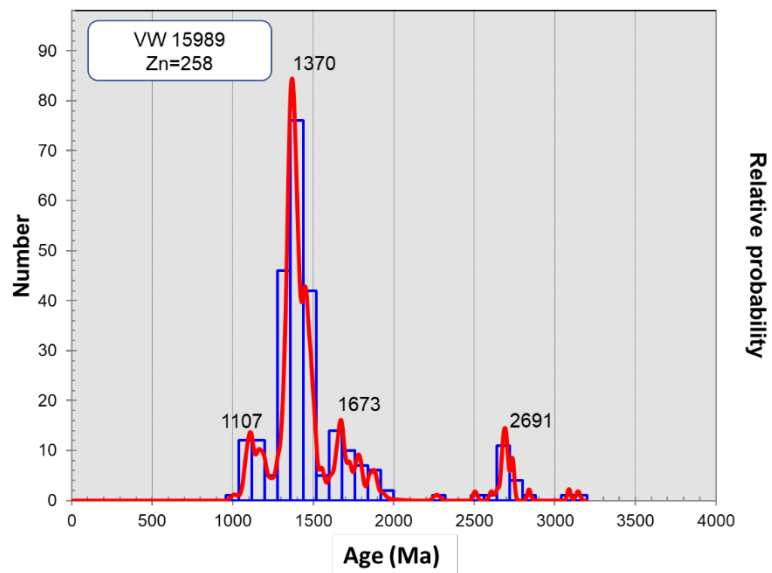
Figure 14*: Probability density plot of the middle Mt. Simon Sandstone from the Verification #1 well, Macon Co., Illinois.*
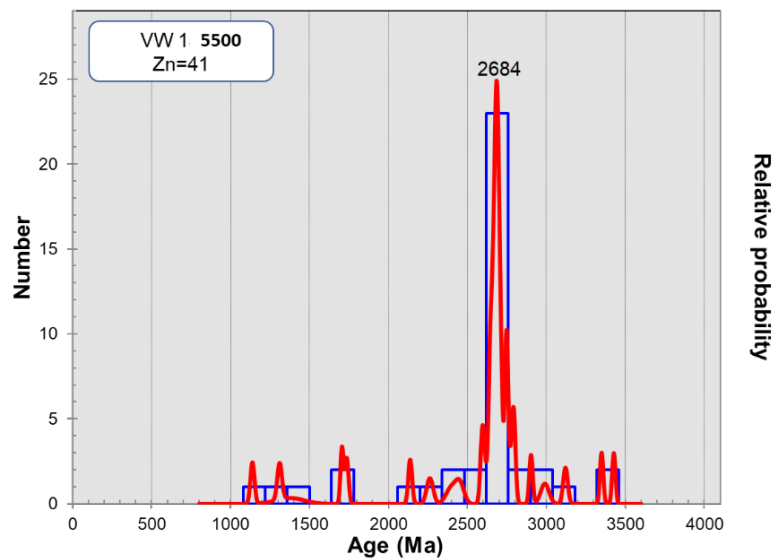
Figure 15*: Probability density plot of the Upper Mt. Simon sandstone from the Verification #1 well, Macon Co., Illinois.*
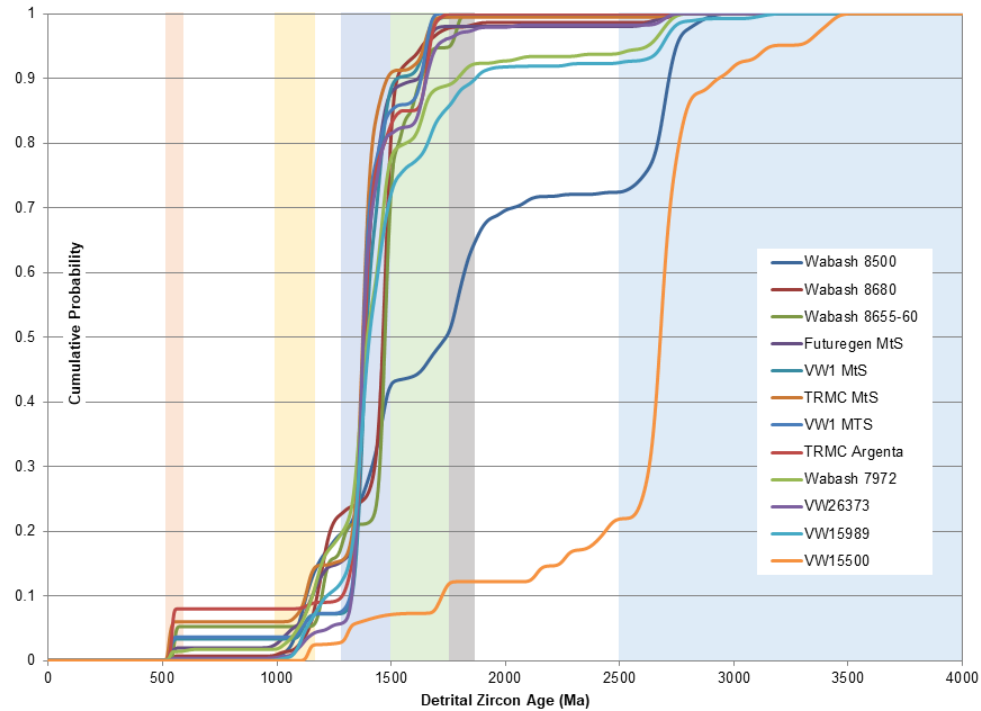
Figure 16: *Stacked probability plots comparing the Mt. Simon and pre-Mt. Simon Sandstones detrital zircon ages analyzed from the Wabash #1 well to Mt. Simon detrital zircon ages from core samples in the Verification #1l (VW1) and T.R. McMillen #2 wells (TRMC) in central Illinois and the FutureGen Alliance #1 well (FutureGen) in western Illinois.*
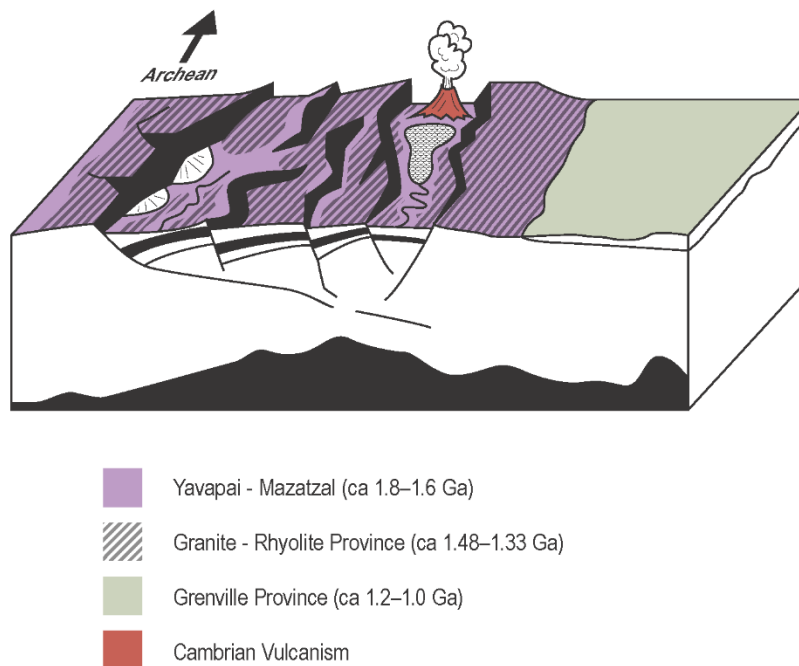
Figure 17: *Hypothetical rift model and Precambrian terrains for east central Illinois and western Indiana. Arrow indicates north direction and the paleo-direction of Archean terranes.*
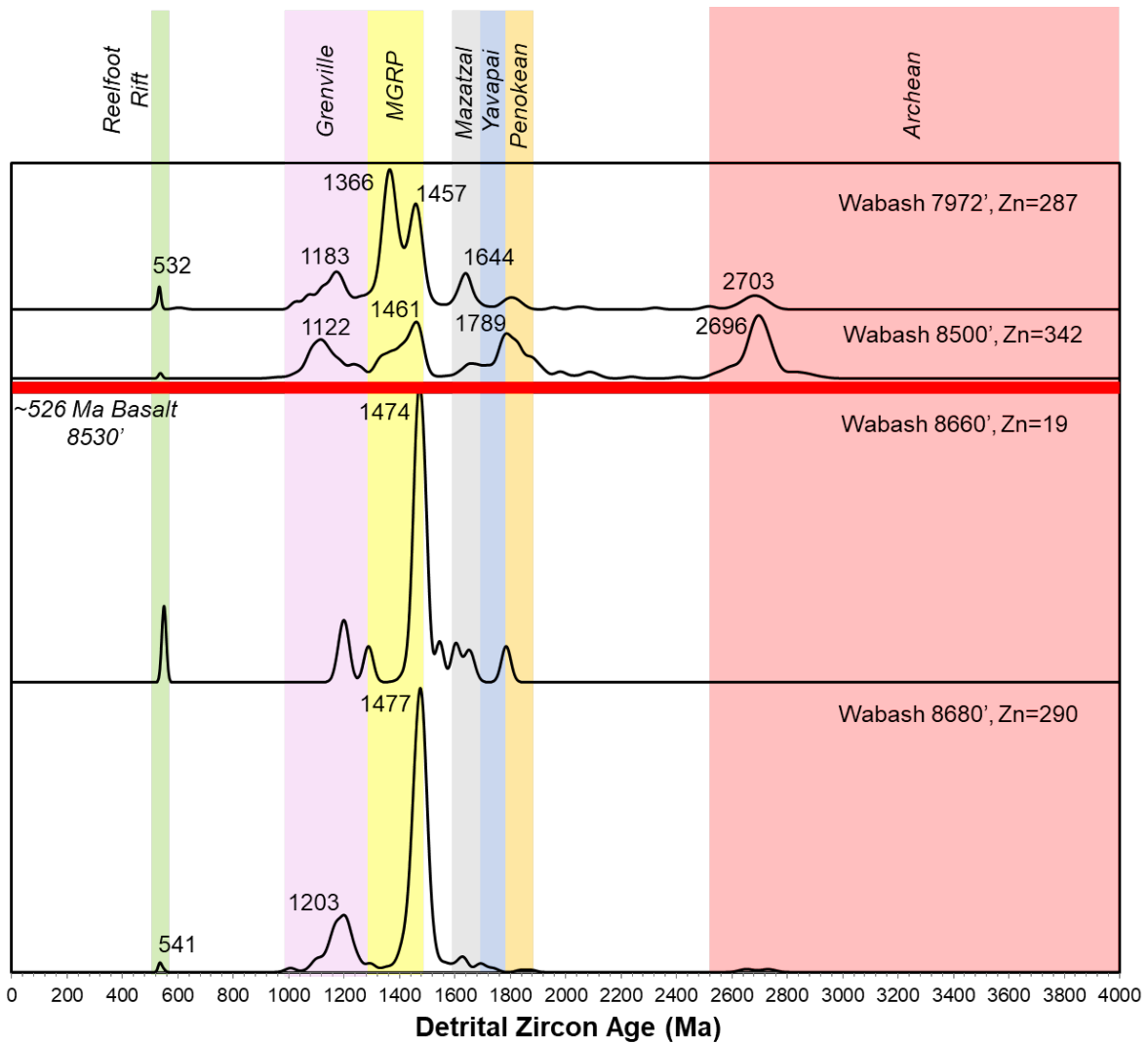
Figure 18: *Stacked probability plot of all samples with detrital zircon geochronology analysis from the Wabash #1 well.*

CONCLUSION

The detrital zircon geochronology data of the Mt. Simon and sediments previously known as the pre-Mt. Simon in the Wabash #1 well, Vigo County, Indiana, show a unique provenance that has numerous implications for the origin to the Mt. Simon depocenter or proto-Illinois Basin. These sediments along with the interlayered basalt represent the final stages of rifting in the continental interior and originating from the southern Laurentian margin. The following conclusions are made from this research:

- The Mt. Simon at the Wabash #1 well closely reflects a source similar to that of the Mt. Simon in central Illinois (Freiburg et al., 2020b). The exception is the influx of Archean and early Paleoproterozoic sediments represented as zircons found within Mt. Simon in the Wabash #1. In central Illinois, this age zircons, particularly the Archaean, are not found

in the Argenta or Lower Mt. Simon, but rather begin to appear in the Middle Mt. Simon and represent the main sediment source in the widely distributed Upper Mt. Simon. At Wabash, Archean sediments are largely absent below the basalt (Figure 17), with those sediments more closely reflecting a source similar to the Lower Mt. Simon and Argenta in central Illinois (Figure 15). Thus, the sediments below the basalt at the Wabash #1 are unlike the Middle Run described in Indiana, Kentucky, and Ohio and will be referred to as the Mt. Simon. This conclusion would suggest that the arkose reported in central Illinois may not have been penetrated in the Wabash #1 well and the Mt. Simon may be thicker than previously reported.

- The basalt penetrated in the Wabash #1 well is interpreted as a flood overlying lacustrine deposits in a continental rift setting. The early Cambrian age of the basalt represents late synrift volcanism that marks the end of the break-up of Rodinia.

- A new $^{40}Ar/^{39}Ar$ age for the gabbro interlayered between EGRP rhyolite has been dated at approximately 1.33 Ga, consistent with SGRP most notably found in Missouri and south towards Texas (Van Schmus et al., 1996). This occurrence extends the area of known SGRP plutonism and is further confirmed by detrital zircon data in the Mt. Simon. This late GRP event was largely eroded and a major source of sediment along this rift arm. Early indications of rifting are suggested by thermal resetting of plagioclase ca 725 Ma. This is consistent with many synrift igneous bodies of this age along the southern Laurentian margin.

- The zircons reflect a largely proximal sediment source that was deposited in a continental rift environment extending up from the Reelfoot rift.

REFERENCES

Aleinikoff, J.N., Zartman, R.E., Walters, M., Rankin, D.W., Lyttle, P.T. and Burton, W.C., 1995. U-Pb ages of metarhyolites of the Catoctin and Mount Rogers Formations, central and southern Appalachians: Evidence for two pulses of Iapetan rifting. *American Journal of Science 295*(4), 428-454.

Badger, R. and Sinha, A.K., 1988. Age and Sr isotopic signature of the Catoctin volcanic province: Implications for subcrustal mantle evolution. *Geology 16*(8), 692-695.

Craddock, J.P., Malone, D.H., Schmitz, M.D. and Gifford, J.N., 2018. Strain variations across the Proterozoic Penokean orogen, USA and Canada. *Precambrian Research 318*, 25-69.

Davis, D.W. and Paces, J.B., 1990. Time resolution of geologic events on the Keweenaw Peninsula and implications for development of the Midcontinent Rift system. *Earth and Planetary Science Letters 97*(1-2), 54-64.

Denison, R.E., Bickford, M.E., Lidiak, E.G. and Kisvarsanyi, E.B., 1987. Geology and geochronology of Precambrian rocks in the central interior region of the United States.

Drahovzal, J.A., Harris, D.C., Wickstrom, L.H., Walker, D., Baranoski, M.T., Keith, B. and Furer, L.C., 1992. *The east continent rift basin: a new discovery*. Ohio. Division of Geological Survey.

Freiburg, J.T., Morse, D.G., Leetaru, H.E., Hoss, R.P. and Yan, Q., 2014. *A depositional and diagenetic characterization of the Mt. Simon Sandstone at the Illinois Basin-Decatur Project carbon capture and storage site, Decatur, Illinois, USA*. Illinois State Geological Survey, Prairie Research Institute, University of Illinois.

Freiburg, J.T., McBride, J.H., Malone, D.H. and Leetaru, H.E., 2020a. Petrology, geochronology, and geophysical characterization of Mesoproterozoic rocks in central Illinois, USA. *Geoscience Frontiers 11*(2), 581-596.

Freiburg, J.T., Holland, M.E., Malone, D.H. and Malone, S.J., 2020b. Detrital Zircon Geochronology of Basal Cambrian Strata in the Deep Illinois Basin, USA: Evidence for the Paleoproterozoic-Cambrian Tectonic and Sedimentary Evolution of Central Laurentia. *The Journal of Geology 128*(3), 303-317.

Keller, G.R., Lidiak, E.G., Hinze, W.J. and Braile, L.W., 1983. The role of rifting in the tectonic development of the midcontinent, USA. In *Developments in Geotectonics 19*, 391-412. Elsevier.

Konstantinou, A., Wirth, K.R., Vervoort, J.D., Malone, D.H., Davidson, C. and Craddock, J.P., 2014. Provenance of quartz arenites of the early Paleozoic midcontinent region, USA. *The Journal of Geology 122*(2), 201-216.

Koppers, A.A.P., Staudigel, H., and Wijbrans, J.R., 2000, Dating crystalline groundmass separates of altered Cretaceous seamount basalts by the 40Ar/39Ar incremental heating technique, *Chemical Geology 166*, 139-158.

Koppers, A. A. P., ArArCALC—Software for 40Ar/39Ar age calculations, *Comput. Geosci. 28*, 605–619, 2002. (Available at http://earthref.org/tools/ararcalc.htm.)

Koppers, A., H. Staudigel, J. R. Wijbrans, and M. Pringle, 2003, Short-lived and discontinuous intraplate volcanism in the South Pacific: Hot spots or extensional volcanism, *Geochem. Geophys. Geosyst. 4,* 10. doi:10.1029/2003GC000533.

Kuiper, K. F., Deino, A., Hilgen, F. J., Krijgsman, W., Renne, P. R., Wijbrans, J. R., 2008, Synchronizing Rock Clocks of Earth History, Science 320, 500 (2008); DOI: 10.1126/science.1154339.

Lee, J.Y., Marti, K., Severinghaus, J.P., Kawamura, K., Yoo, H.S., Lee, J.B. and Kim, J.S., 2006. A redetermination of the isotopic abundances of atmospheric Ar. *Geochimica et Cosmochimica Acta*, *70*(17), 4507-4512.

Leetaru, H.E. and McBride, J.H., 2009. Reservoir uncertainty, Precambrian topography, and carbon sequestration in the Mt. Simon Sandstone, Illinois Basin. *Environmental Geosciences 16*(4), 235-243.

Lidiak, E.G., Bickford, M.E. and Kisvarsanyi, E.B., 1993. Proterozoic geology of the eastern Midcontinent region. *Geological Society of America, Decade of North American Geology (DNAG) 100*, 259-270.

Li, Z.X., Bogdanova, S., Collins, A.S., Davidson, A., De Waele, B., Ernst, R.E., Fitzsimons, I.C.W., Fuck, R.A., Gladkochub, D.P., Jacobs, J. and Karlstrom, K.E., 2008. Assembly, configuration, and break-up history of Rodinia: a synthesis. *Precambrian research 160*(1-2), 179-210.

Lovell, T.R. and Bowen, B.B., 2013. Fluctuations in sedimentary provenance of the Upper Cambrian Mount Simon Sandstone, Illinois Basin, United States. *The Journal of Geology 121*(2), 129-154.

Lovell, T.R., 2017. *An Intracratonic Record of North American Tectonics* (Doctoral dissertation, Purdue University).

Lucius, J.E. and von Frese, R.R., 1988. Aeromagnetic and gravity anomaly constraints on the crustal geology of Ohio. *Geological Society of America Bulletin 100*(1), 104-116.

Malone, D.H., Stein, C.A., Craddock, J.P., Kley, J., Stein, S. and Malone, J.E., 2016. Maximum depositional age of the Neoproterozoic Jacobsville Sandstone, Michigan: Implications for the evolution of the Midcontinent Rift. *Geosphere 12*(4), 1271-1282.

McBride, J.H., Kolata, D.R. and Hildenbrand, T.G., 2003. Geophysical constraints on understanding the origin of the Illinois basin and its underlying crust. *Tectonophysics 363*(1-2), 45-78.

McBride, J.H. and Kolata, D.R., 1999. Upper crust beneath the central Illinois basin, United States. *Geological Society of America Bulletin 111*(3), 375-394.

McLelland, J., Daly, J.S. and McLelland, J.M., 1996. The Grenville orogenic cycle (ca. 1350-1000 Ma): an Adirondack perspective. *Tectonophysics 265*(1-2), 1-28.

McLelland, J.M., Selleck, B.W. and Bickford, M.E., 2013. Tectonic evolution of the Adirondack Mountains and Grenville orogen inliers within the USA. *Geoscience Canada*, 318-352.

Min, K., R. Mundil, P. R. Renne, and K. R. Ludwig, A test for systematic errors in 40Ar/39Ar geochronology through comparison with U/Pb analysis of a 1.1-Ga rhyolite, *Geochim. Cosmochim. Acta 64*, 73–98, 2000.

Moecher, D.P., Bowersox, J.R. and Hickman, J.B., 2018. Zircon U-Pb geochronology of two basement cores (Kentucky, USA): Implications for late Mesoproterozoic sedimentation and tectonics in the eastern Midcontinent. *The Journal of Geology 126*(1), 25-39.

Paces, J.B. and Miller Jr, J.D., 1993. Precise U-Pb ages of Duluth complex and related mafic intrusions, northeastern Minnesota: Geochronological insights to physical, petrogenetic, paleomagnetic, and tectonomagmatic processes associated with the 1.1 Ga midcontinent rift system. *Journal of Geophysical Research: Solid Earth 98*(B8), 13997-14013.

Pratt, T., Culotta, R., Hauser, E., Nelson, D., Brown, L., Kaufman, S., Oliver, J. and Hinze, W., 1989. Major Proterozoic basement features of the eastern midcontinent of North America revealed by recent COCORP profiling. *Geology 17*(6), 505-509.

Schneider Santos, J.O., Hartmann, L.A., McNaughton, N.J., Easton, R.M., Rea, R.G. and Potter, P.E., 2002. Sensitive high-resolution ion microprobe (SHRIMP) detrital zircon geochronology provides new evidence for a hidden Neoproterozoic foreland basin to the Grenville Orogen in the eastern Midwest, USA. *Canadian Journal of Earth Sciences 39*(10), 1505-1515.

Shrake, D.L., 1990. *Lithologic and geophysical description of a continuously cored hole in Warren County, Ohio: including description of the middle run formation (Precambrian?) and a seismic profile across the core site*. Ohio. Division of Geological Survey.

Shrake, D.L., 1991. The Middle Run Formation: a subsurface stratigraphic unit in southwestern Ohio.

Spencer, C.J., Prave, A.R., Cawood, P.A. and Roberts, N.M., 2014. Detrital zircon geochronology of the Grenville/Llano foreland and basal Sauk Sequence in west Texas, USA. *Bulletin 126*(7-8), 1117-1128.

Stein, C.A., Kley, J., Stein, S., Hindle, D. and Keller, G.R., 2015. North America's Midcontinent Rift: when rift met LIP. *Geosphere 11*(5), 1607-1616.

Steiger, R. H., and E. Ja¨ger, Subcommission on geochronology: Convention on the use of decay constant in geo- and cosmochronology, *Earth Planet. Sci. Lett. 36,* 359–362, 1977.

Taylor, J. R., An Introduction to Error Analysis: The Study of Uncertainties in Physical Measurements, 1997. Univ. Sci. Books, Mill Valley, Calif., 327 pp.

Thomas, J.J., Shuster, R.D., and Bickford, M.E., 1984. A terrane of 1,350-to 1,400-my-old silicic volcanic and plutonic rocks in the buried Proterozoic of the mid-continent and in the Wet Mountains, Colorado. *Geological Society of America Bulletin 95*(10), 1150-1157.

Thomas, W.A., Tucker, R.D., Astini, R.A. and Denison, R.E., 2012. Ages of pre-rift basement and synrift rocks along the conjugate rift and transform margins of the Argentine Precordillera and Laurentia. *Geosphere 8*(6), 1366-1383.

Thomas, W.A., 2014. A mechanism for tectonic inheritance at transform faults of the Iapetan margin of Laurentia. *Geoscience Canada*, 321-344.

Van Schmus, W.R. and Hinze, W.J., 1985. The midcontinent rift system. *Annual Review of Earth and Planetary Sciences 13*(1), 345-383.

Van Schmus, W.R., Bickford, M.E., Sims, P.K., Anderson, R.R., Shearer, C.K. and Treves, S.B., 1993. Proterozoic geology of the western midcontinent basement. *Precambrian: Conterminous USA Geological Society of America, Boulder, Colo., Geology of North America 2*, 239-258.

Van Schmus, W.R., Bickford, M.E., Turek, A., Van der Pluijm, B.A. and Catacosinos, P.A., 1996. Proterozoic geology of the east-central Midcontinent basement. *SPECIAL PAPERS-GEOLOGICAL SOCIETY OF AMERICA*, pp.7-32.

Van Wyck, N. and Johnson, C.M., 1997. Common lead, Sm-Nd, and U-Pb constraints on petrogenesis, crustal architecture, and tectonic setting of the Penokean orogeny (Paleoproterozoic) in Wisconsin. *Geological Society of America Bulletin 109*(7), 799-808.

Van Wyck, N. and Norman, M., 2004. Detrital zircon ages from early Proterozoic quartzites, Wisconsin, support rapid weathering and deposition of mature quartz arenites. *The Journal of Geology 112*(3), 305-315.

Vervoort, J.D., Wirth, K., Kennedy, B., Sandland, T. and Harpp, K.S., 2007. The magmatic evolution of the Midcontinent rift: New geochronologic and geochemical evidence from felsic magmatism. *Precambrian Research 157*(1-4), 235-268.

Whitmeyer, S.J. and Karlstrom, K.E., 2007. Tectonic model for the Proterozoic growth of North America. *Geosphere 3*(4), 220-259.

Wickstrom, L.H., Drahovzal, J.A. and Keith, B.D., 1992. The geology and geophysics of the East Continent Rift Basin: report of Cincinnati Arch Consortium. *Indiana Geol. Surv. Open-File Study*, 92-04.

Yarger, H.L., 1985. Kansas basement study using spectrally filtered aeromagnetic data. In *The utility of regional gravity and magnetic anomaly maps*, 213-232. Society of Exploration Geophysicists.

Yonkee, W.A., Dehler, C.D., Link, P.K., Balgord, E.A., Keeley, J.A., Hayes, D.S., Wells, M.L., Fanning, C.M. and Johnston, S.M., 2014. Tectono-stratigraphic framework of Neoproterozoic to Cambrian strata, west-central US: Protracted rifting, glaciation, and evolution of the North American Cordilleran margin. *Earth-Science Reviews 136*, 59-95.

York, D., Least squares fitting of a straight line with correlated errors, 1969. *Earth Planet. Sci. Lett. 5*, 320–324.

Zietz, I. and Godson, R.H., 1982. *Composite magnetic anomaly map of the United States*. The Geological Survey (US).

Chapter 4

Petrophysics of the Eau Claire Formation and the Mt. Simon Sandstone

By: Nate Grigsby, Mansour Khosravi, Scott Frailey, and James Damico

Illinois State Geological Survey, Prairie Research Institute, University of Illinois at Urbana-Champaign

INTRODUCTION

The Wabash CarbonSAFE project drilled the Wabash #1 stratigraphic test well (ID# 168045) at the Wabash Valley Resources gasification facility in Vigo County, Indiana, to characterize and evaluate the basal Cambrian Mt. Simon Sandstone for commercial-scale CO_2 storage near the site. The petrophysics of the Mt. Simon Sandstone and Eau Claire Formation were evaluated based on petrophysical wireline logs and core recovered from the Wabash #1 well.

Petrophysical analysis of well logs is one of the primary methods to characterize the reservoir properties of the formations evaluated for CO_2 injection and their associated confining zones. A full suite of modern well logs, including a standard triple combo (Gamma ray [GR], resistivity, neutron-density porosity), spectral Gamma ray (SGR), photoelectric (Pe), Nuclear Magnetic Resonance (NMR) and interpreted Combinable Magnetic Resonance (CMR), and Elemental Capture Spectroscopy (ECS) logs were acquired at the Wabash #1 well used for interpretation of the Mt. Simon Sandstone storage complex. Rotary sidewall cores taken for all the intervals evaluated and whole core taken from the Arkose unit (the suspected target interval) were also used to calibrate the log data and better understand the petrophysical properties.

Lithologic properties of the confining units were determined using standard geophysical log analysis techniques. Bulk density (RHOZ), porosity, Pe, NMR, and SGR logs were utilized to estimate the total porosity, lithologic variability, and clay minerals of the units. Pe was plotted against RHOZ for each zone to identify the lithology and estimate the porosity ranges. Neutron (TNPH) and Density (DPHZ) porosities were averaged to determine an estimate of total porosity (PHIT). Furthermore, cross plots of apparent limestone neutron porosity against RHOZ were prepared to estimate the corrected porosity regarding to main lithology types of each zone (see Asquith and Krygowski, 2004; Schlumberger, 1998). The porosity range statistical parameters were calculated using the histograms of each unit. Cross plots of thorium-potassium derived from the SGR log were used to identify clay mineral type and to distinguish shale and clay-rich intervals from the pure sandstone, limestone, and dolomite (Schlumberger, 1998). The NMR logs were used to assess the presence of the clay mineral and fine grain sediments and determine the bound water and free water in the pore spaces quantitively.

Geocellular modeling requires porosity and permeability vs. depth for individual wells. Generally, porosity logs (e.g., neutron and/or density) provide porosity vs. depth directly every 0.5 ft, but permeability vs. depth must be estimated from correlations with well log properties. In some instances, published correlations (e.g., Timur, 1968) are used. When core and/or well test data are

available, porosity and permeability estimated from correlations are calibrated to core porosity and permeability and to well test permeability.

PHIT was used for porosity for the Wabash #1 well. In addition to published correlations, ISGS developed a permeability transform from porosity for the Illinois Basin Decatur Project (IBDP) based on resistivity and porosity logs and core porosity and permeability. This ISGS method was used to estimate permeability for the Mt. Simon Sandstone for the Wabash #1 well.

Interval Definition

The primary seal for the Mt. Simon Sandstone, the Eau Claire Formation, can be lithologically separated into two sections: an upper, carbonate-rich section and a lower, silty-shale section often referred to as the Eau Claire shale. The Eau Claire shale is considered a "true" shale, while the upper part of the Eau Claire fluctuates in lithology. The logs captured only the lowest <100 ft of the 256 ft thick Upper Eau Claire at the Wabash #1 well, so the upper portion could not be properly characterized. However, the logs did fully capture the 699 ft thick Lower Eau Claire shale.

For this study and to correlate this well to other wells, the Mt. Simon Sandstone is divided into three major subunits (Upper, Middle, and Lower) that are observable amongst most Mt. Simon wells. An additional portion of the Mt. Simon, called the Arkose, is located below the Lower Mt. Simon, generally has good reservoir qualities, and is also identifiable in other wells. A porous interval below the Arkose is defined here as the Argenta, but more work is required to determine if this unit is truly the Argenta or a sub-Arkose member of the Mt. Simon. A 20-ft thick Cambrian age-dated basalt (interpreted to be a flood basalt) is found at the base of the Argenta. A sedimentary formation below the basalt was tentatively correlated during drilling and well testing as Precambrian, but later analyses have identified the basalt and unit below it as Cambrian in age; the sandstone below the basalt is labelled here as unidentified sandstone due to the lack of a full characterization. The Mt. Simon extends from a depth of 6,277 ft to 8,085 ft, for a thickness of 1,808 ft. The thickness of the Upper is 473 ft, the Middle is 668 ft, the Lower is 315 ft, and the Arkose is 352 ft (Table 1). The Argenta is 430 ft. The unidentified sandstone was not fully penetrated but is at least 204 ft thick.

Table 2: *Formation tops used for this evaluation*

Formation	Top (measured depth [ft])
Upper Eau Claire	5,322
Eau Claire shale	5,578
Upper Mt. Simon	6,277
Middle Mt. Simon	6,751
Lower Mt. Simon	7,418
Arkose	7,733

Argenta	8,085
Basalt	8,515
Unidentified sandstone	8,535
Total Depth	8,739

LITHOLOGY

Eau Claire Formation

Based on lithology the Eau Claire Formation can be divided into two parts: 1) the Upper Eau Claire from depths of 5,322 to 5,578 ft; 2) the Lower Eau Claire shale from 5,578 to 6,277 ft.

The NMR log was only acquired below ~5,520 ft (~70 ft above the base of the Upper Eau Claire), so it was not available for interpretation of the Upper Eau Claire. The Upper Eau Claire shows a GR range of 10 to 25 API and PHIT generally under 3%. The cross plot of Pe against RHOZ indicates the interval is predominately composed of pure limestone (Figure 1). The interval between the depths of 5,387 to 5,448 ft is believed to be argillaceous due to its elevated GR (25-60 API) and Pe (4-5 b/e) relative to pure limestones. The cross plot of thorium against potassium displays the clay contents are primary chlorite and illite (Figure 2).
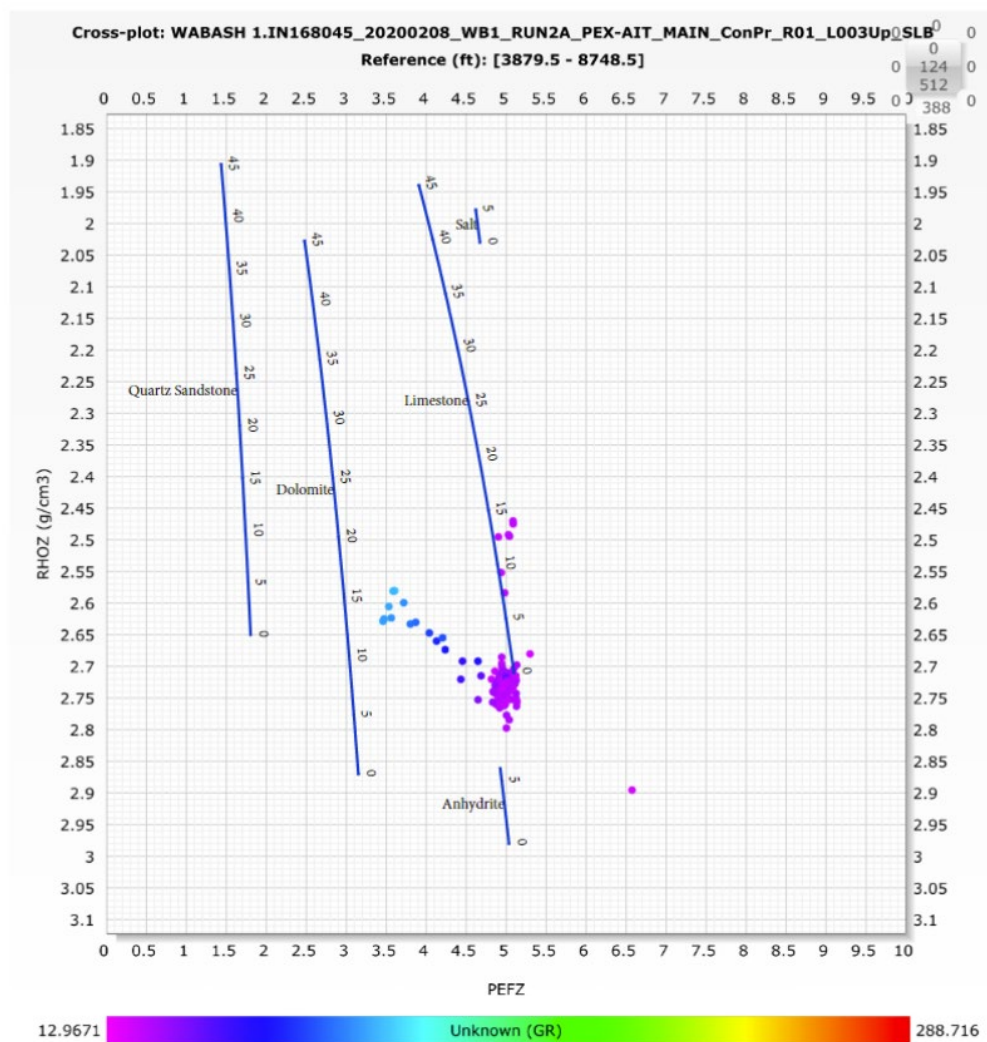
Figure 19*: Cross plot of the Pe and RHOZ data from the Upper Eau Claire. Data is colored by GR value. Most of the data suggests a pure limestone.*
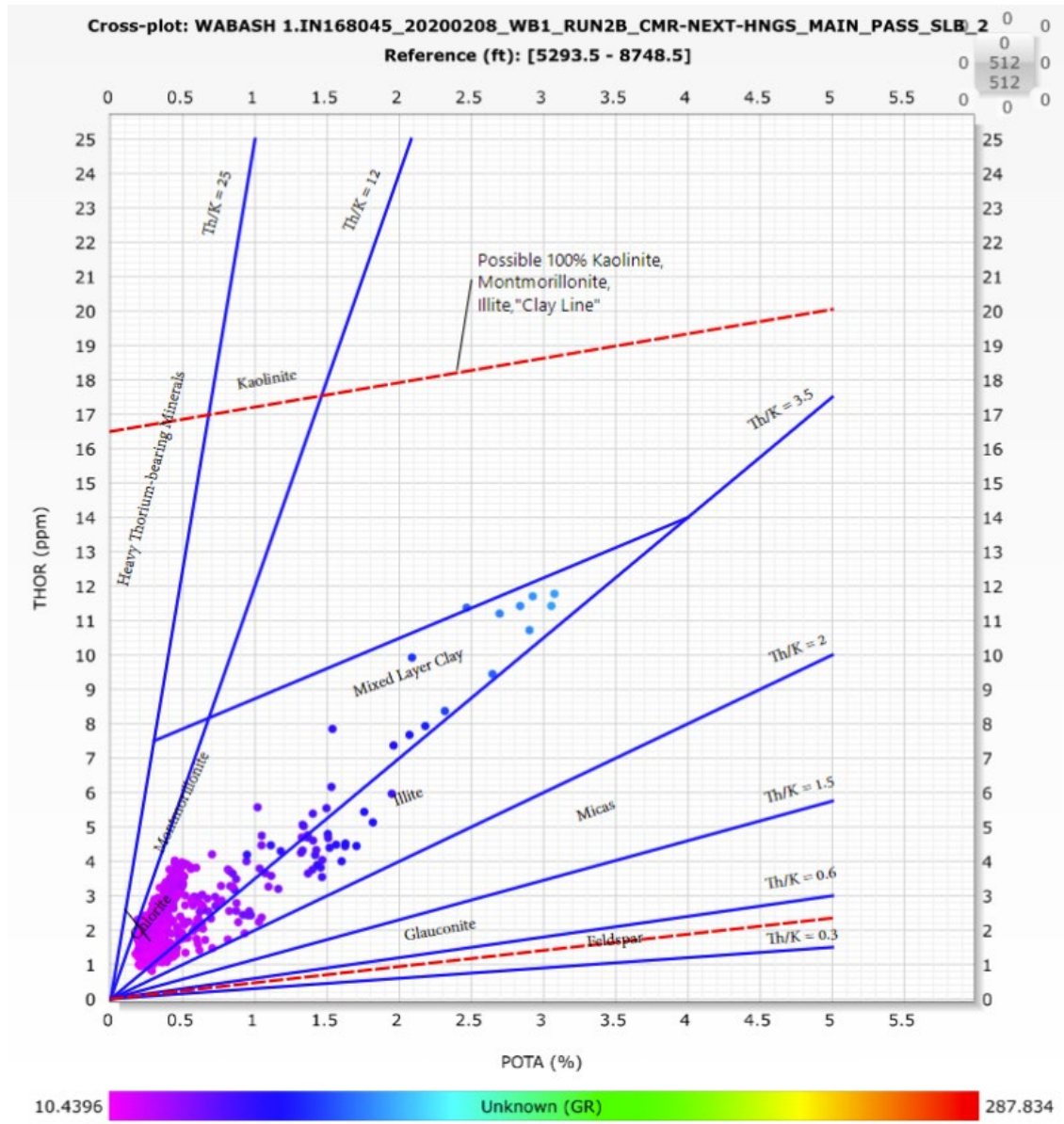
Figure 20: *Potassium/Thorium cross plot for the Upper Eau Claire from SGR log showing that the clays are mostly illite and chlorite. Data points are colored by GR value.*

The prepared thin sections from the Eau Claire shale indicated the interval mainly consists of heavily bioturbated dolomitic shale, siltstone, and very fine sandstone (Lasemi and Askari, see chapter 6 of this report). The GR range of 70 to 150 API and high concentration of bounded water indicates that most parts of the Eau Claire shale consist of thick intervals of shale (Figure 3). The lower part of the Eau Claire shale (from 6,153 to 6,202 ft) consists of interlayers of very fine-grained sandstone, siltstone, and shaly sandstone based on thin section studies (Lasemi and Askari, see chapter 6 of this report), GR values of less than 70 API, and lower concentration of bounded water (Figure 3).
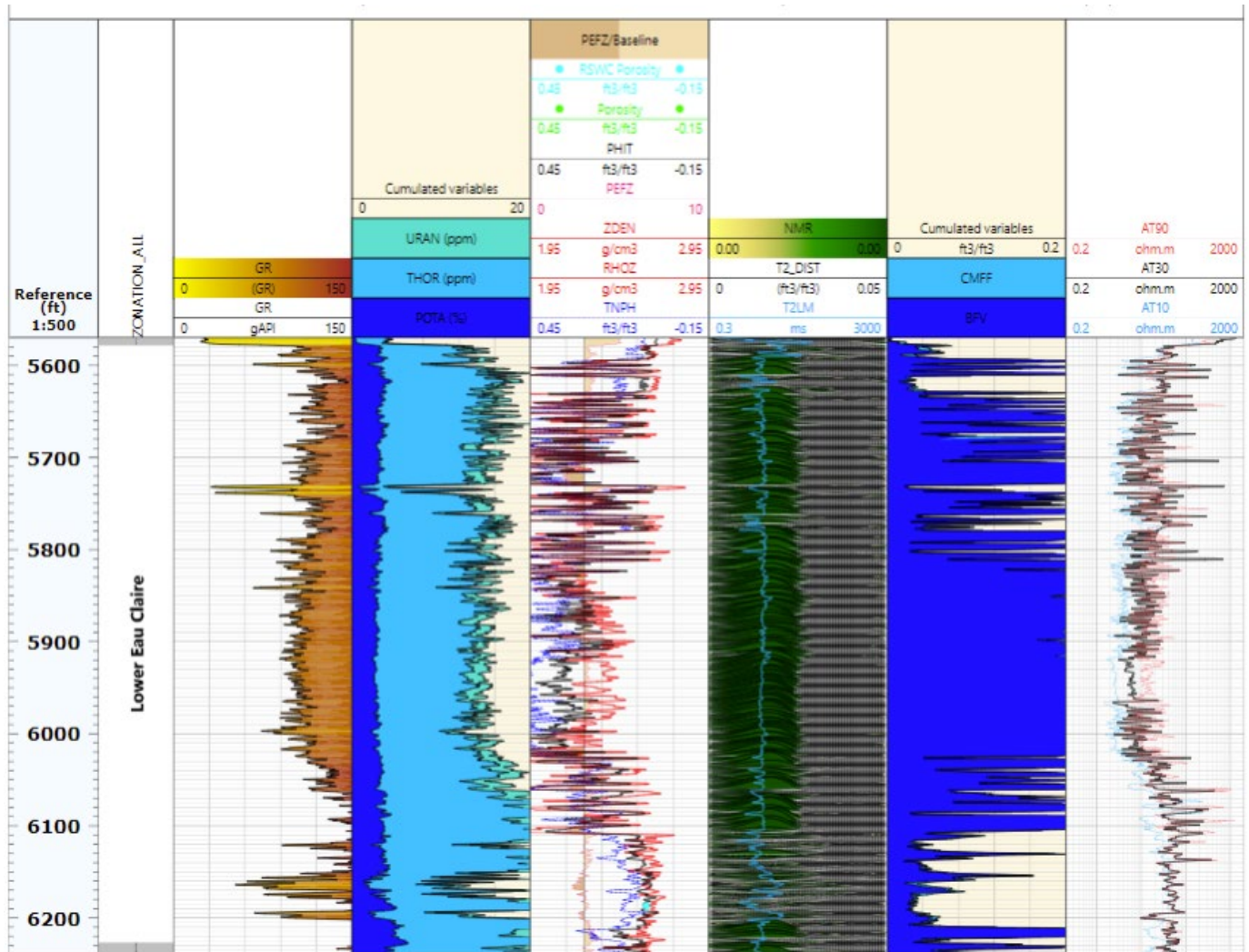
Figure 21: *Geophysical logs vs. depth in the Eau Claire shale formation.*

Upper Mt. Simon

The sedimentology study and image log analyses indicated that the Upper Mt. Simon consists of planner fine- to coarse-grained sandstones, interbedded with massive to finely planar laminated mudstone (see Delpomdor, Chapter 1 of this report). The Upper Mt. Simon contains both pure sandstone (where GR is between 20 to 40 API) and muddy sandstones and mudstone intervals (where GR is 40 to over 100 API). The cross plot of thorium against potassium shows that the clay contents are predominately illite and mica (Figure 4). The cross plot of Pe and RHOZ displays that the unit is predominately composed of pure sandstone, and intervals with higher Pe indicate the presence of mudstone and muddy sandstones (Figure 5).

PHIT is 1-13% for the entire interval of the Upper Mt. Simon (Figure 6). The porosity ranges do not significantly change from the top to the bottom of the unit, but the lower part of the Upper Mt. Simon (below ~6,548 ft) is believed to have a higher reservoir quality than the upper part. This

90

conclusion is supported by the T2 distribution, CMFF, and BFV from the NMR log, which show that the lower part of the Upper Mt. Simon contains larger pore sizes and more free water relative to the upper part (Figure 6). The SGR also shows a higher concentration of potassium (3-5%) in the upper part (from 6,226 to 6,468 ft) relative to the lower part of the Upper Mt. Simon (Figure 6). The higher concentration of potassium corresponds to higher overall GR and is most likely an indication of feldspar sandstones and fine mica as clay mineral between intervals.
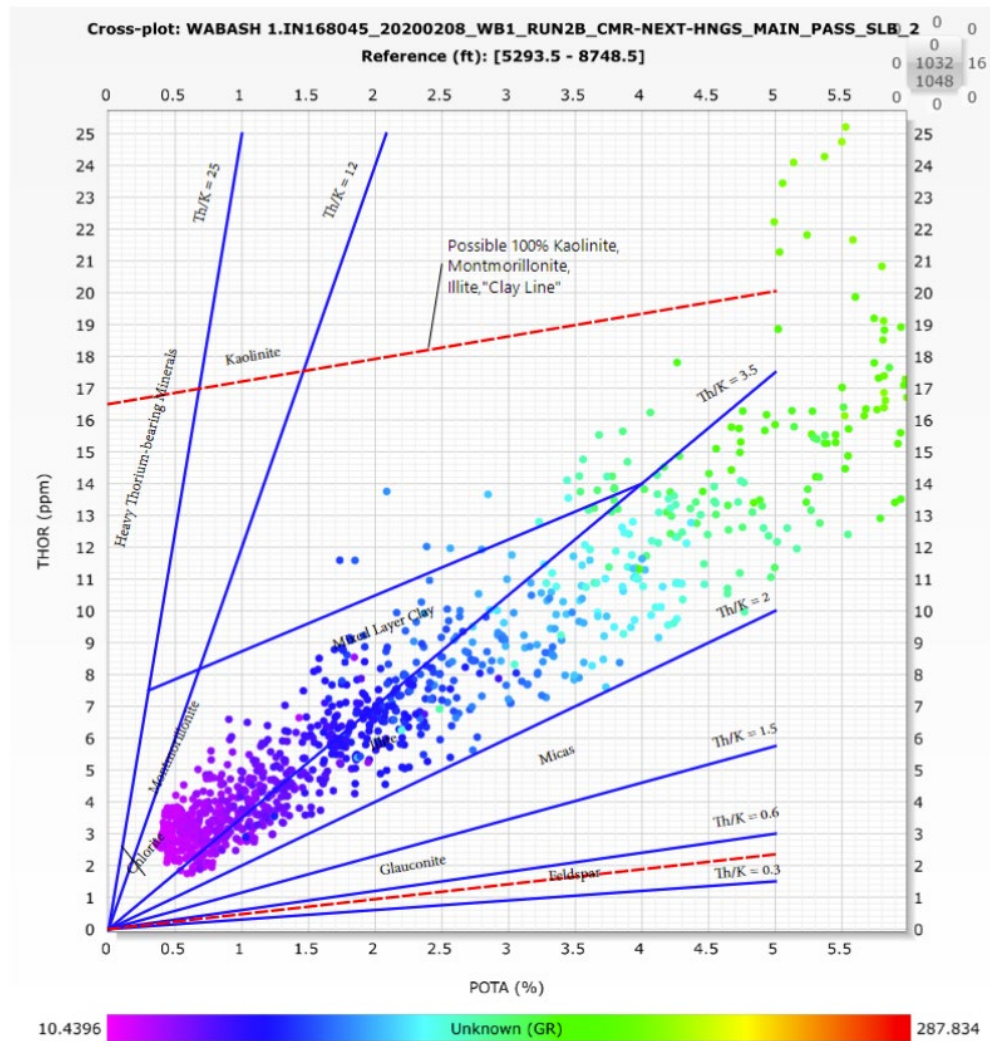
***Figure 22**: Potassium/Thorium cross plot for the Upper Mt. Simon from spectral gamma ray log. Data is colored by GR value.*
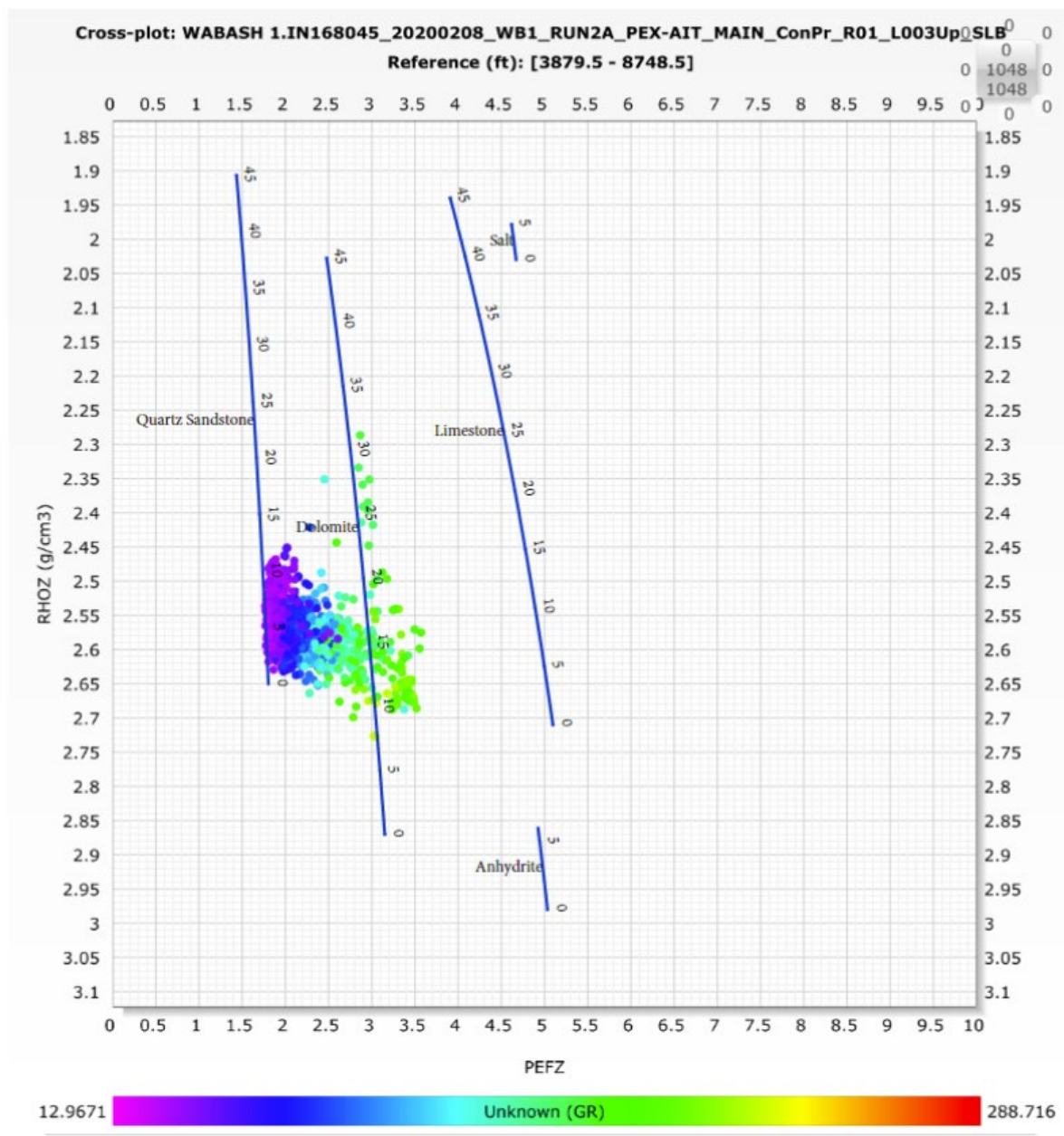
Figure 23*: Cross plot of the Pe and RHOZ data from the Upper Mt. Simon. Data is colored by GR value. Most of the data suggests a sandstone, but intervals of mudstone and muddy sandstone occur with high GR.*
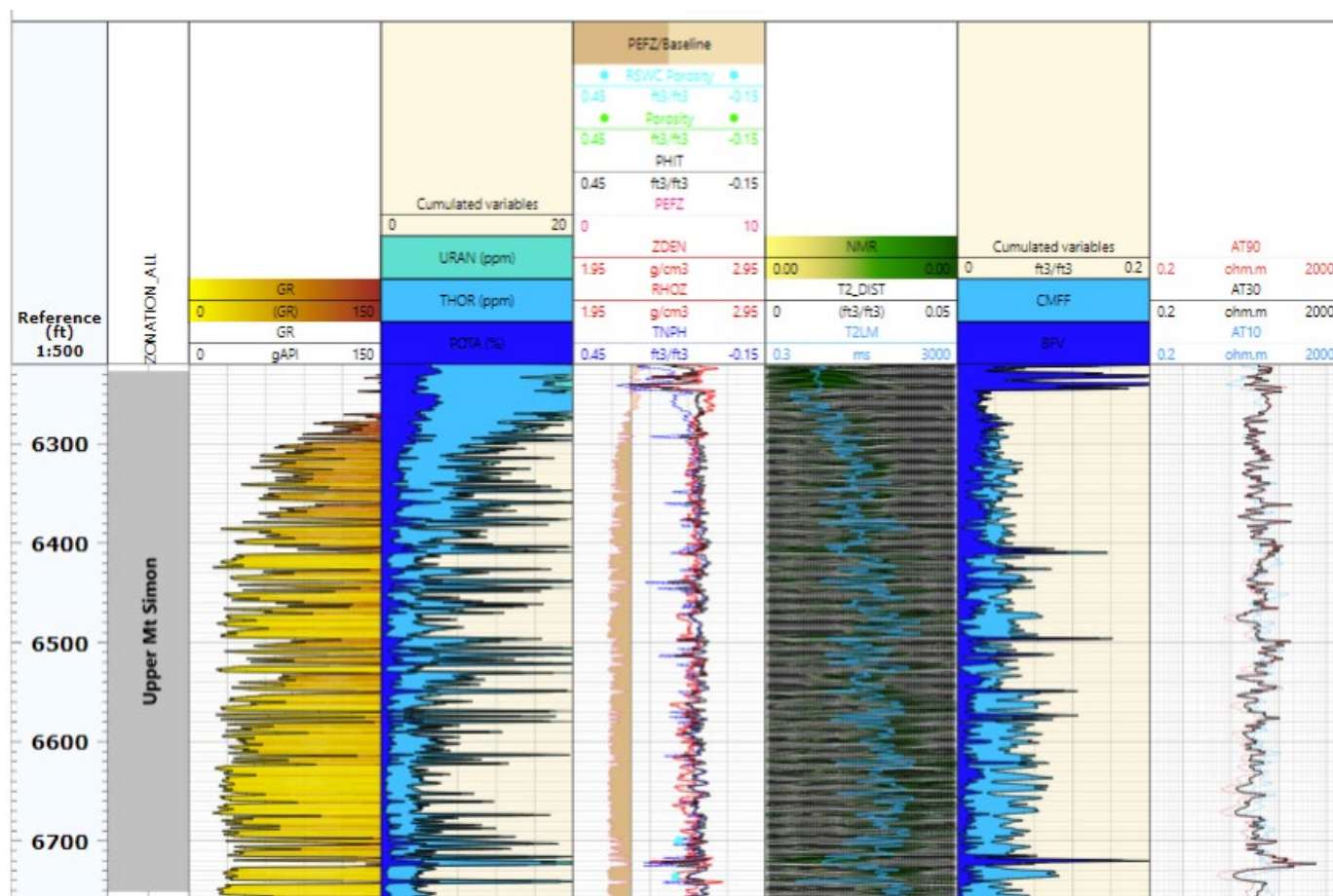
Figure 24: *Geophysical logs vs. depth in the Upper Mt. Simon.*

Middle Mt. Simon

The Middle Mt. Simon predominantly consists of massive planar parallel and low-angle to trough cross-stratified, medium- to coarse-grained sandstone, interbedded with thin intervals of mudstone (see Delpomdor, Chapter 1). The cross plot of Pe against RHOZ shows that the unit consists of pure sandstone with only a few data points with higher Pe (2.5 to 3.2 b/e) and GR values (40-150 API) that are indicative of fine muddy sandstone and mudstone (Figure 7). The cross plot of thorium and potassium indicates most of the clay contents are chlorite and illite (Figure 8).

The low concentration of potassium (less than 1%), low GR responses, and T2 distribution, CMFF, and BFV are all indicative of clean quartz sandstones with larger pore sizes and higher concentration of free fluid relative to the Upper Mt. Simon (Figure 9). Furthermore, the thickness of muddy sandstone and mudstone intervals are less than those in the Upper Mt. Simon.
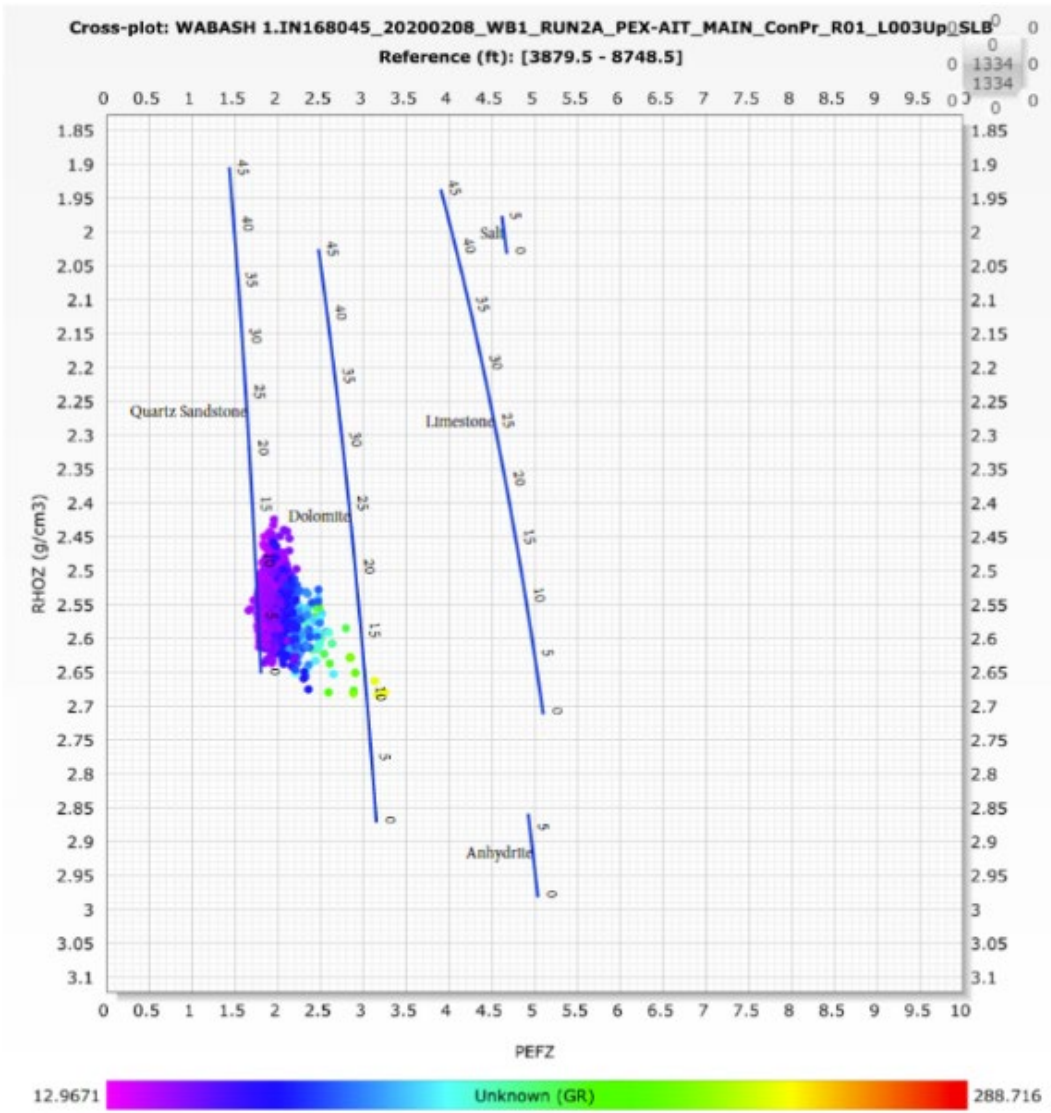
Figure 25*: Cross plot of the Pe and RHOZ data from the Middle Mt. Simon. Data is colored by GR value. Low GR data align with the clean sandstone line and migrate towards dolomite as GR increases.*
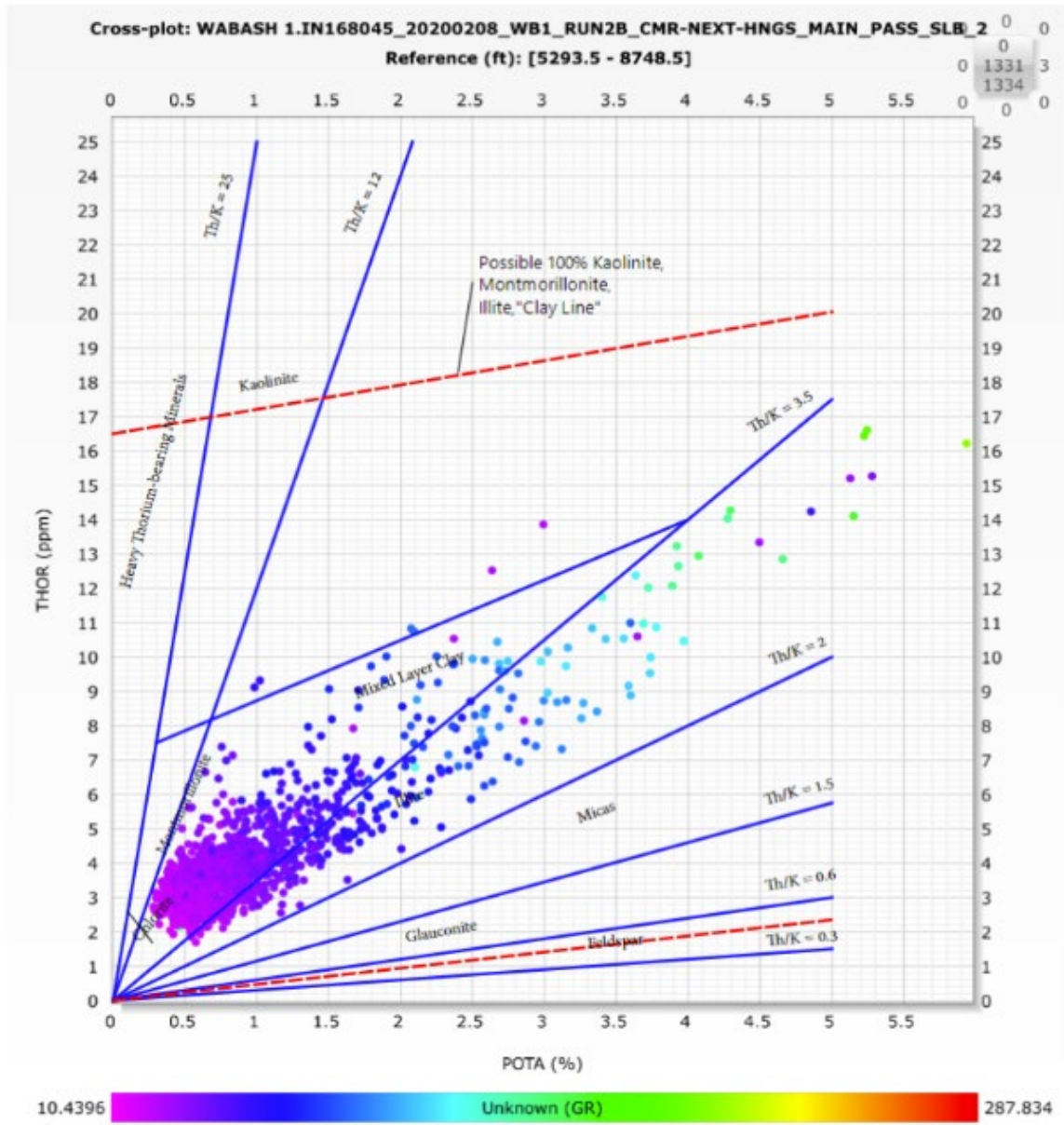
Figure 26: *Potassium/Thorium cross plot for the Middle Mt. Simon from spectral gamma ray log. Data points are colored by GR value.*
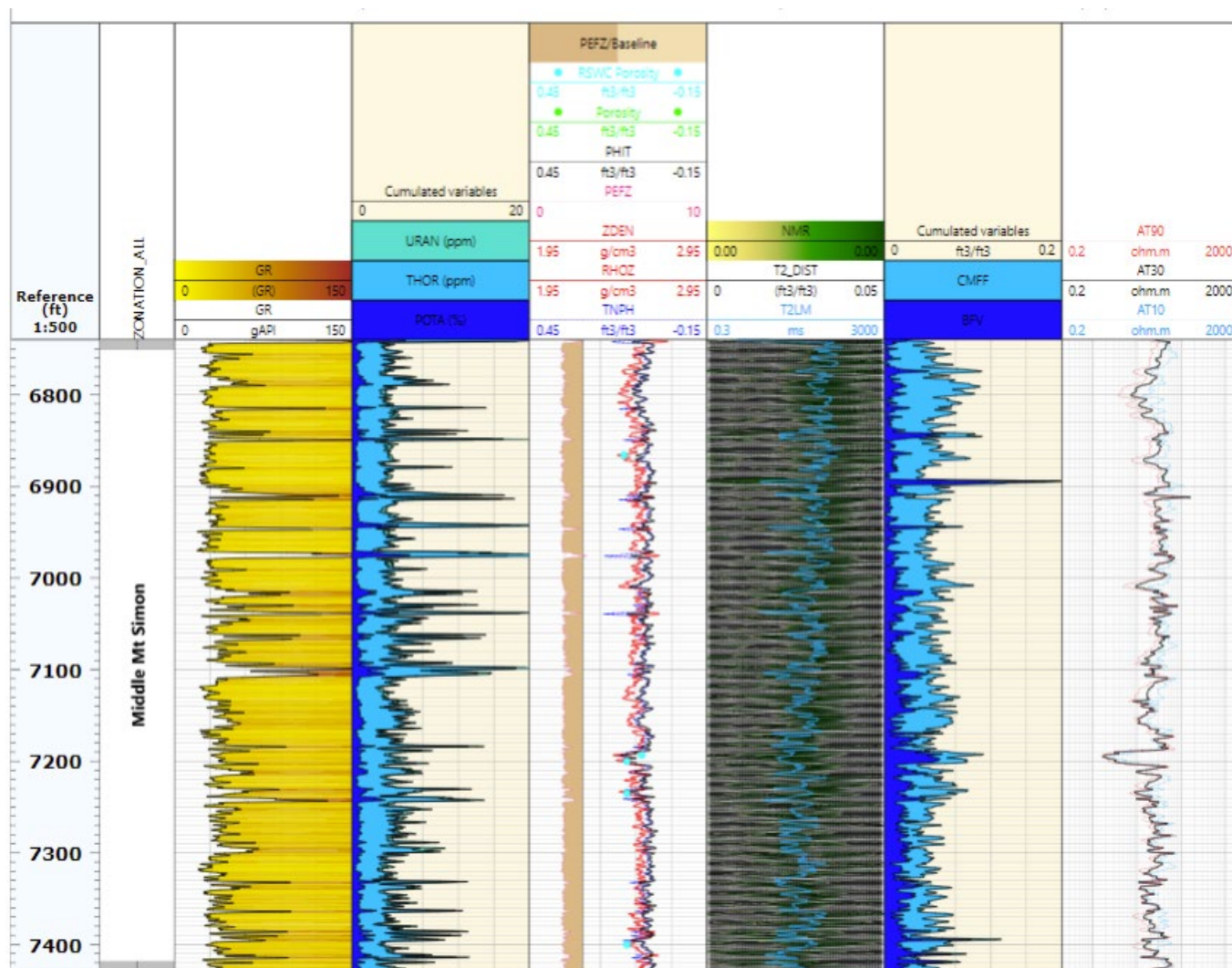
Figure 27: *Geophysical logs vs. depth in the Middle Mt. Simon.*

Lower Mt. Simon

The Lower Mt. Simon consists of pure sandstone with GR ranges from 20 to 40 API. The thickness of mudstone and shale intervals with higher range of GR are dramatically lower than Upper and Middle Mt. Simon. The low concentration of potassium observed by the SGR log and Pe below 2.4 b/e indicate the sandstone grains are composed primarily of quartz and that the Lower Mt. Simon has less feldspars than the upper units (Figure 10). The thorium/potassium cross plot displays the clay contents are mainly chlorite and illite (Figure 11). The PHIT of the Lower Mt. Simon is generally less than 10%, and the T2 distribution, BFV, and CMFF logs represent a low percentage of water between grains (Figure 12).
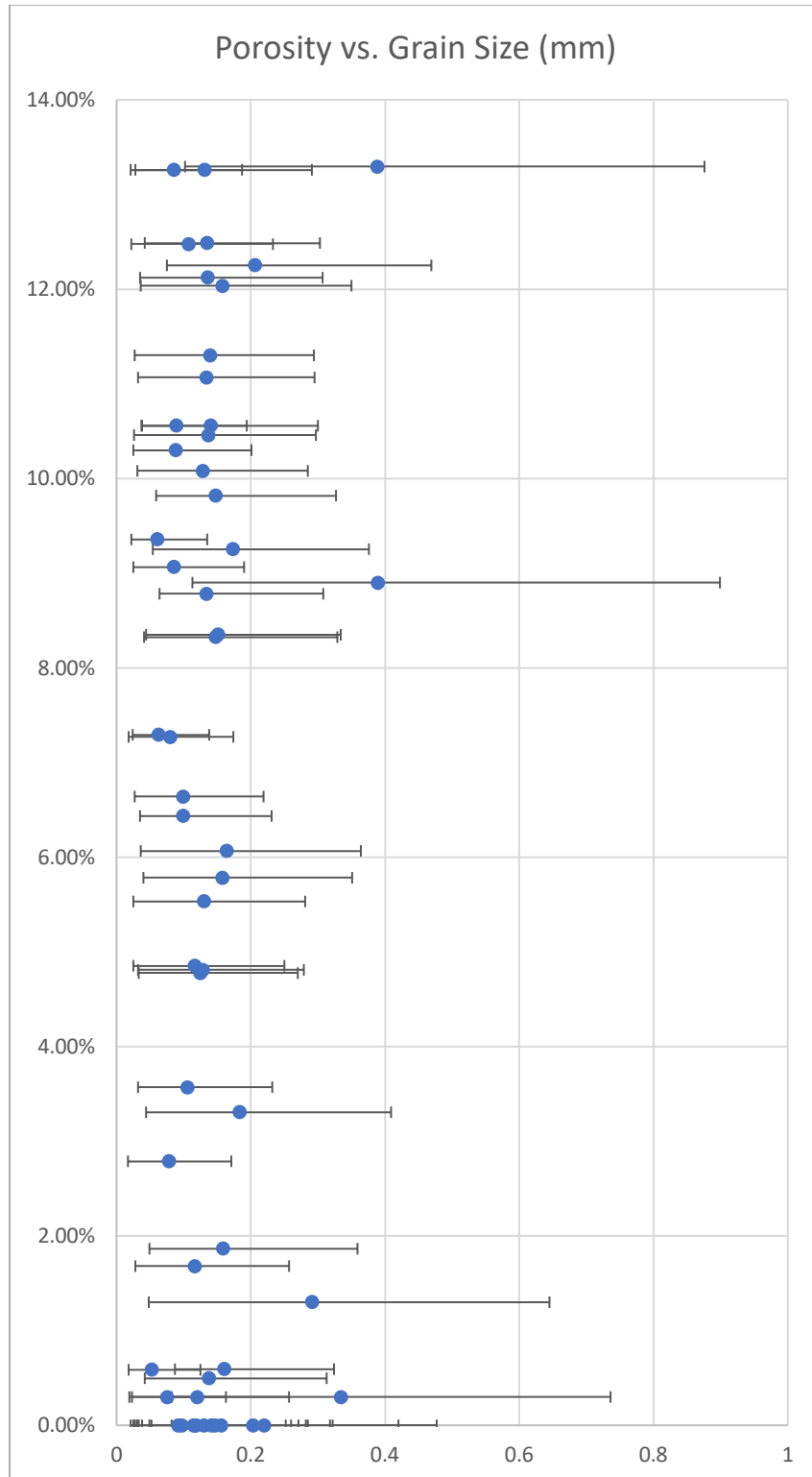
Figure 45: *Graph showing porosity and grain size (average and range). Note there is little correlation between grain size and total porosity.*
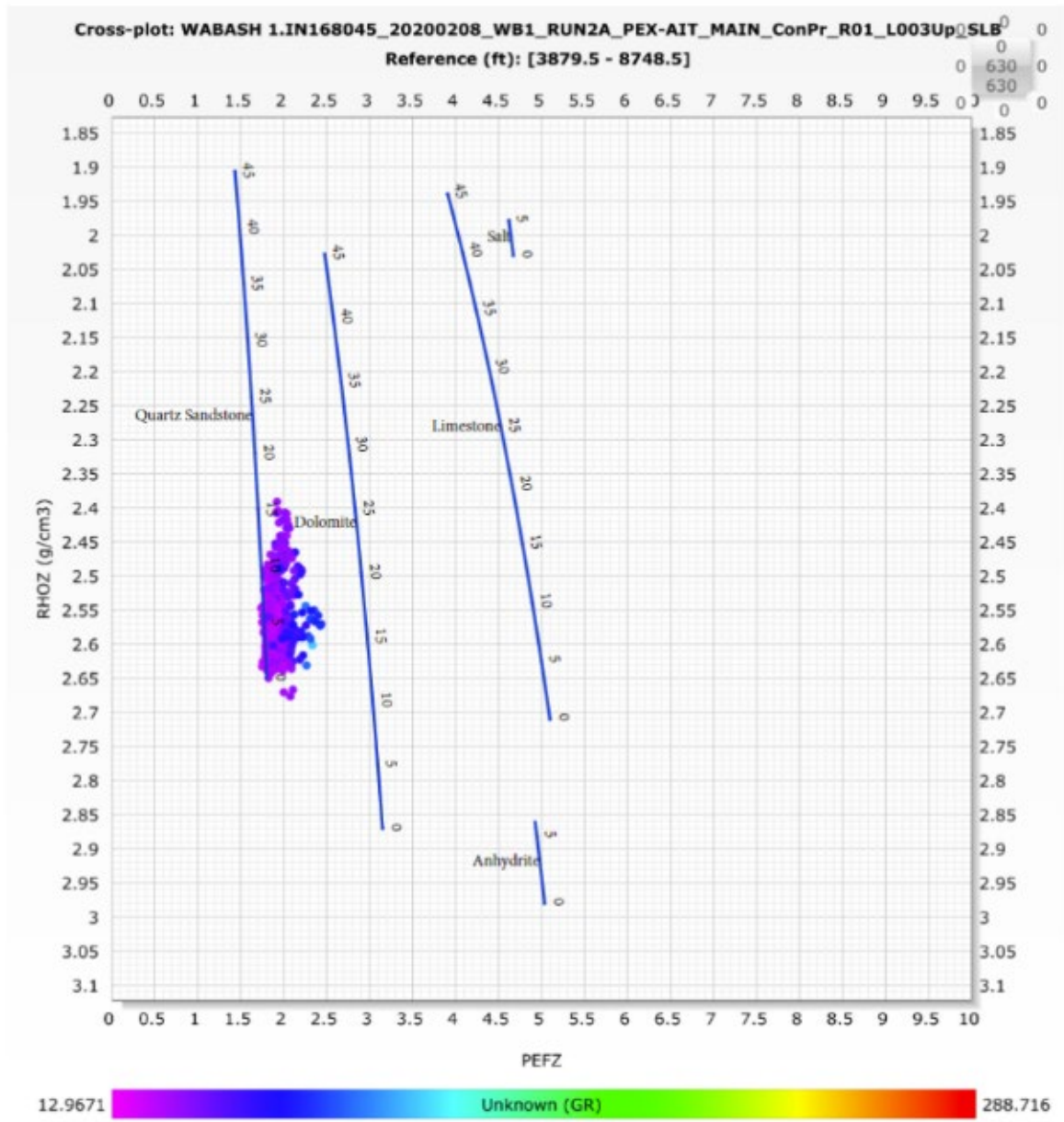
Figure 28*: Cross plot of the Pe and RHOZ data from the Lower Mt. Simon. Data is colored by GR value. All the data align with the clean sandstone line, which suggests that the interval contains very little clay or feldspar.*
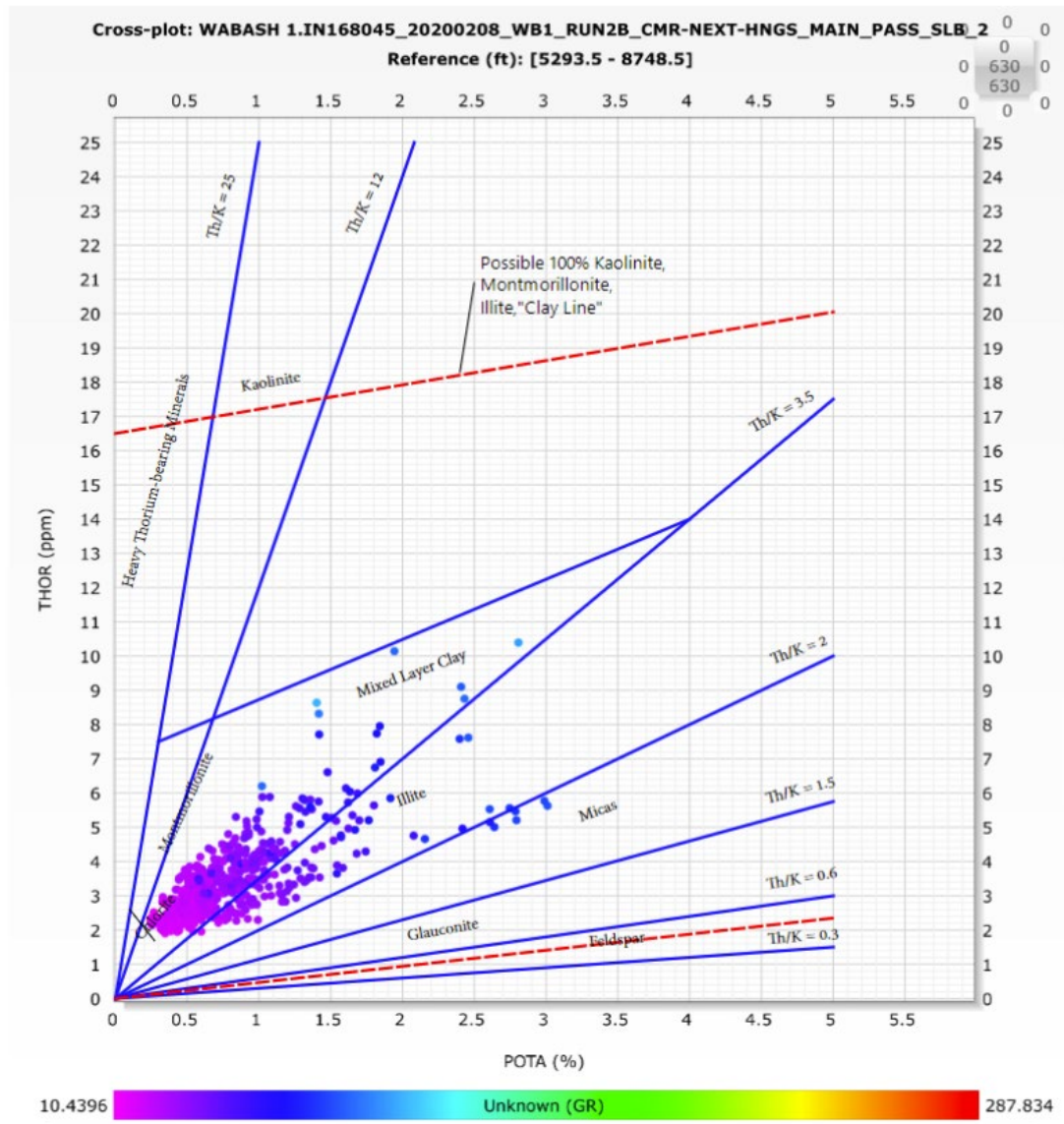
Figure 29*: Potassium/Thorium cross plot for the Lower Mt. Simon from spectral gamma ray log. Data points are colored by GR value.*
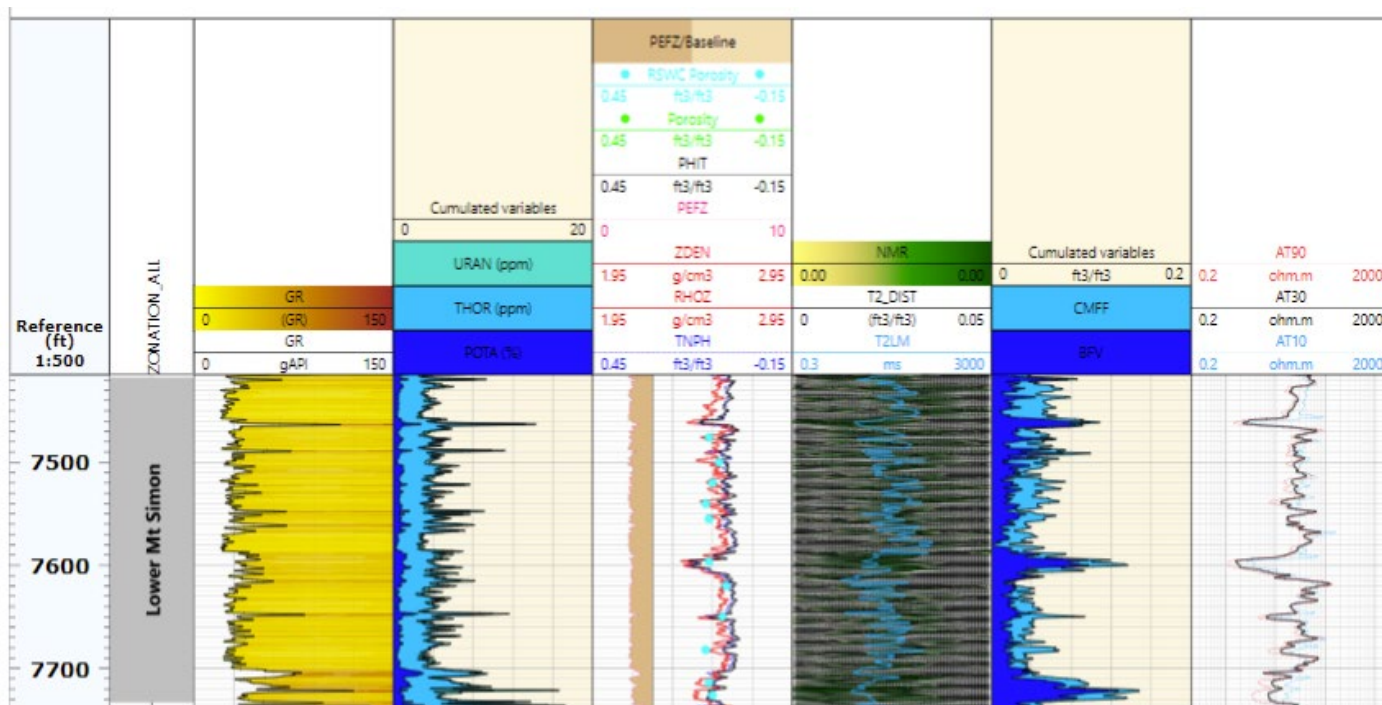
Figure 30: *Geophysical logs vs. depth for the Lower Mt. Simon.*

Arkose

The Arkose unit consists of fine- to medium-grained sandstone and mudstone with massive and large cross-stratification (see Delpomdor, Chapter 1). The natural GR log shows a range of 60 to 150 API for the entire interval (Figure 13). The potassium contents of SGR log have a range of 1.6 to 7%, which is an indication of feldspar-rich sandstone. The sandstones of the Arkose unit can be categorized into two classes: 1) quartz sandstone with Pe values between 2 to 2.5 b/e; 2) feldspar sandstone with Pe values between 2.5 to 3.0 b/e. The cross plot of Pe against RHOZ shows that the unit is a sandstone interbedded with thin layers of muddy sandstone and mudstone (Figure 14). The cross plot of thorium against potassium shows the clay contents are mainly illite and mica (Figure 15). Interpretation of the T2 distribution, CMFF, and BFV logs shows intervals of feldspar sandstone (7,922 to 8,002 ft and 8,042 to 8,075 ft) contain larger pore sizes and more free water relative to the other parts of the Arkose unit (Figure 13).
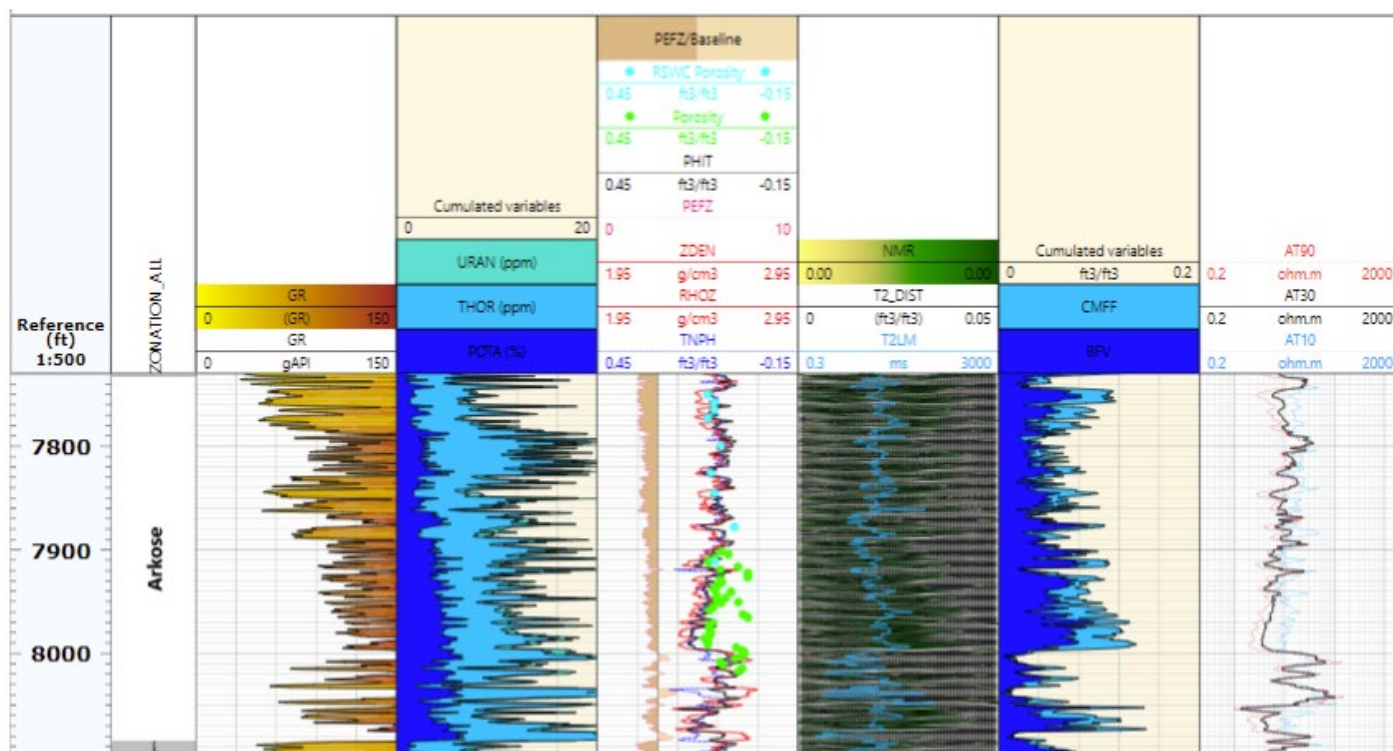
Figure 31: *Geophysical logs vs. depth for the Arkose interval.*
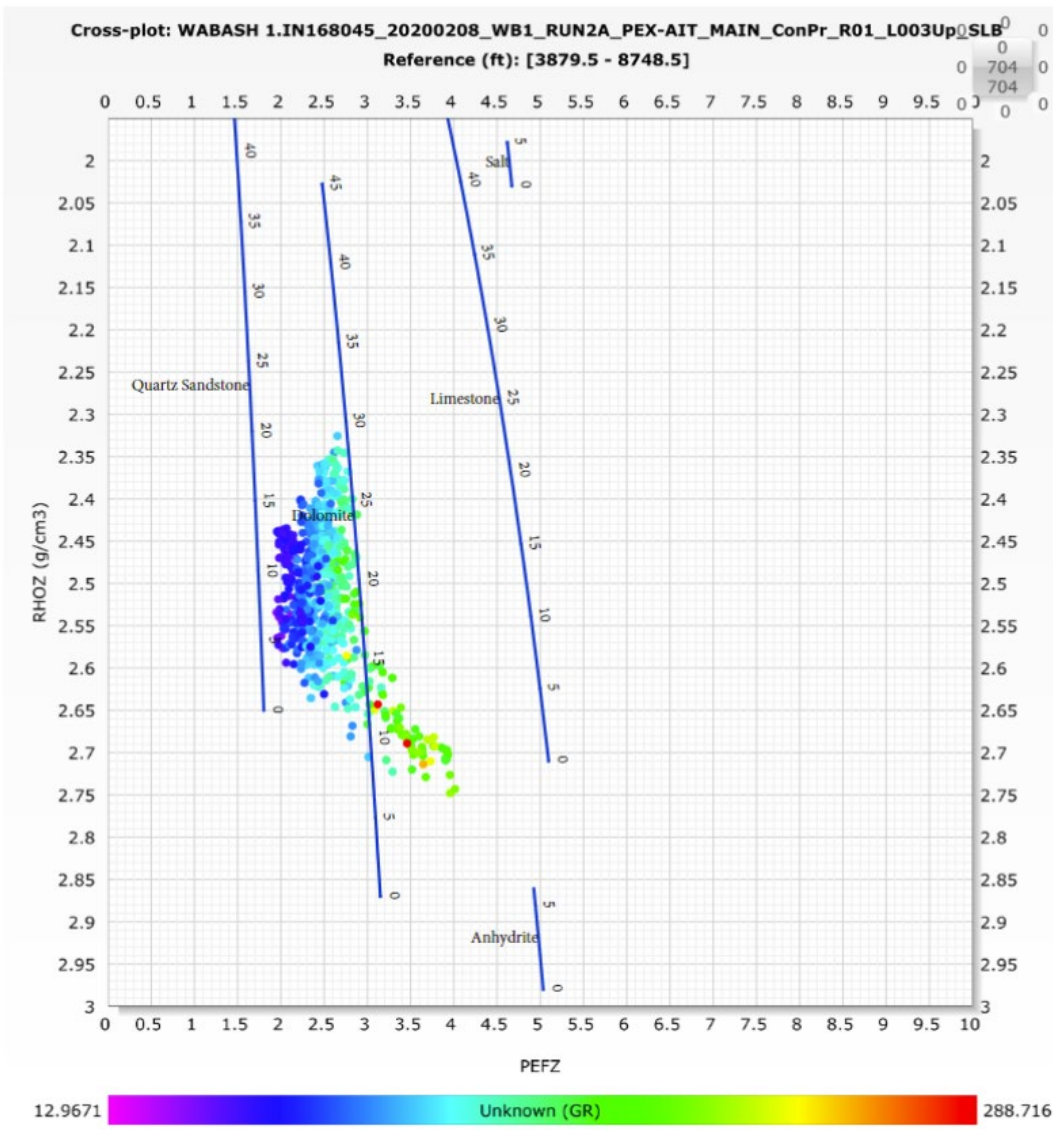
Figure 32: *Cross plot of the Pe and RHOZ data from the Arkose. Points are colored by GR value.*
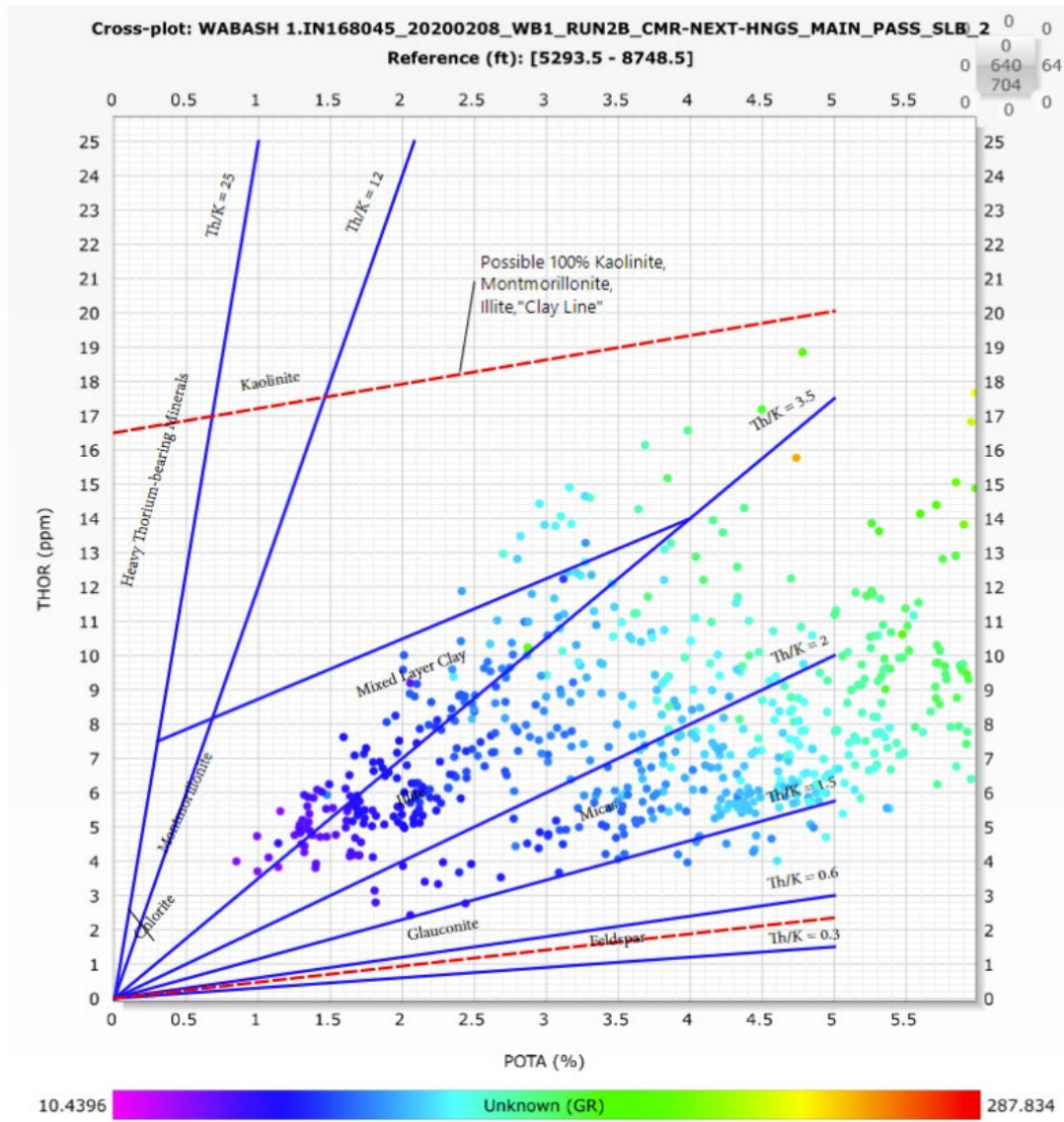
Figure 33: *Potassium/Thorium cross plot for the Arkose interval from spectral gamma ray log. Data points are colored by GR value.*

Argenta Sandstone

The Argenta sandstone primarily consists of fine- to very coarse-grained, locally interbedded with shaly sandstone, shale, and clay (see Delpomdor, Chapter 1). The cross plot of Pe and RHOZ (Figure 16) shows that the main lithology of the Argenta is sandstone, but shaly fine grained-sandstone and shale intervals are also present.

The uppermost part of the Argenta, between 8,085 to 8,210 ft, contains planar layers of medium- to coarse-grained sandstones based on interpretation of image logs (see Delpomdor, Chapter 1). The GR responses in this interval are between 40 to 70 API, less than lower units of the formation (Figure 17). The SGR displays a low concentration of potassium (0.6 to 2.4%), indicating the presence of fine-grained quartz sandstones. The thorium against potassium cross plot shows clay contents are mainly montmorillonite, chlorite, and mixed layer clays (Figure 18). Despite low GR

and PHIT around 10%, the T2 distribution, CMFF, and BFV logs display the pore sizes are small and concentration of clay-bound water is high.

The interval from 8,210 to 8,328 ft has GR values from 40 to 140 API with Pe between 2.4 to 3.7b/e and pronounced TNPH/DPHI log separation, indicating the interval consists of shale and shaly sandstone (Figure 17). The high thorium and low potassium concentrations reveal that the clay mainly consists of kaolinite (Figure 18). PHIT is between 10 and 20%, but the low T2 times and associated high percentage of BFV indicate that the pore sizes are small, and the effective porosity is very low.

The interval from 8,328 to 8,505 ft contains more sands relative to overlying interval. The potassium concentration of the unit increases relative to the middle part, indicating more feldspar sandstone. The PHIT log shows a range of 10-15% total porosity, but the T2 distribution and BFV logs show that most of the porosities are not categorized as effective. The thorium against potassium cross plot shows the clay contents are mainly illite and mixed layer clays (Figure 18).

The lowest most unit of the Argenta between 8,505 to 8,515 ft is characterized by GR over 100 API, high neutron-porosity, and high BFV, indicating that the interval has a high proportion of clay. The presence of the shaly intervals increases the Pe measurements from 2.5 b/e to a range of 3.5 to 5 b/e. The cross plot of thorium against potassium indicates the clay minerals of the unit mostly consist of mica and illite, most likely developed from physical weathering of underlying igneous rocks.
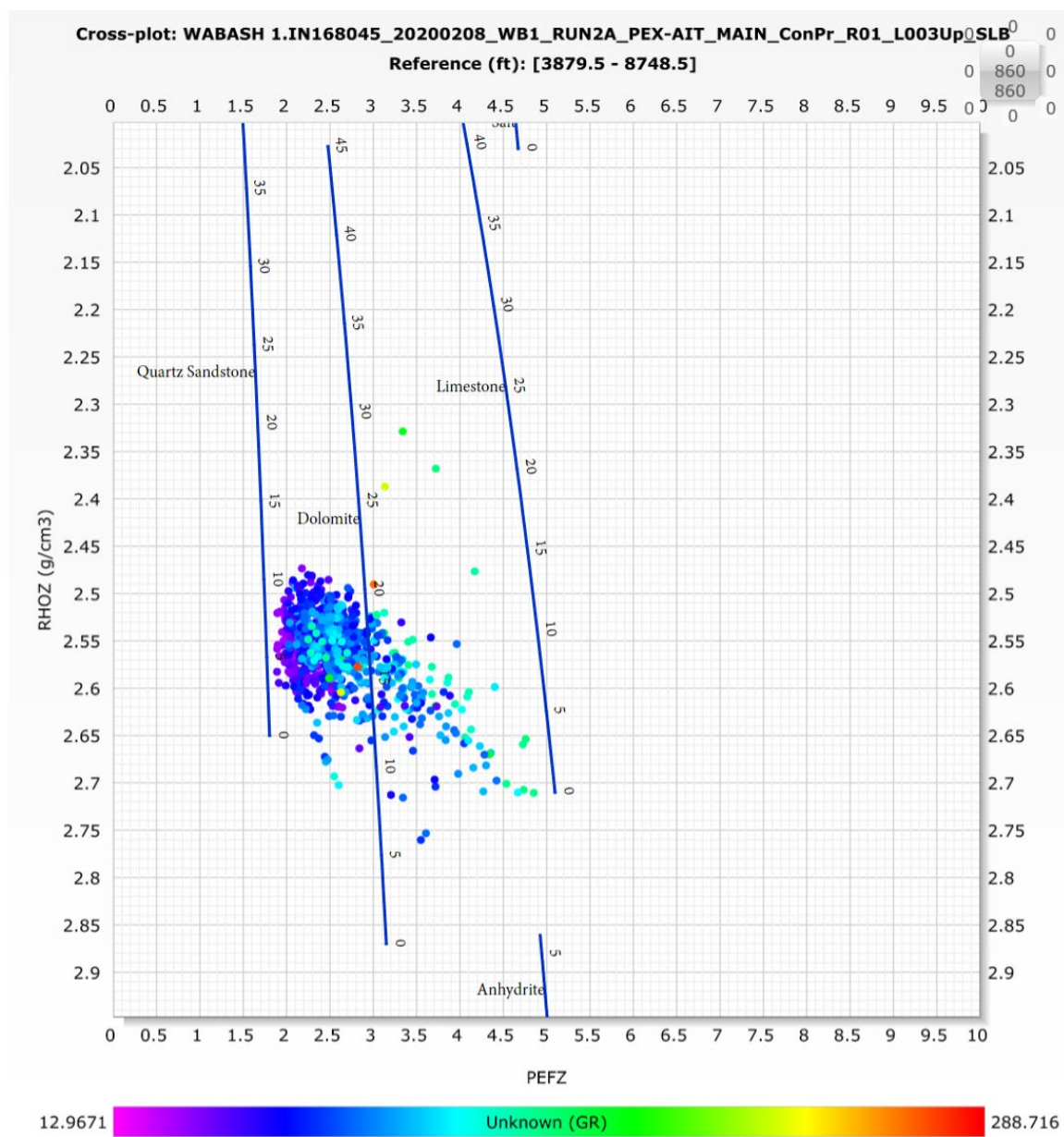
Figure 34: *Cross plot of the Pe and RHOZ data from the Argenta. Data is colored by GR value.*
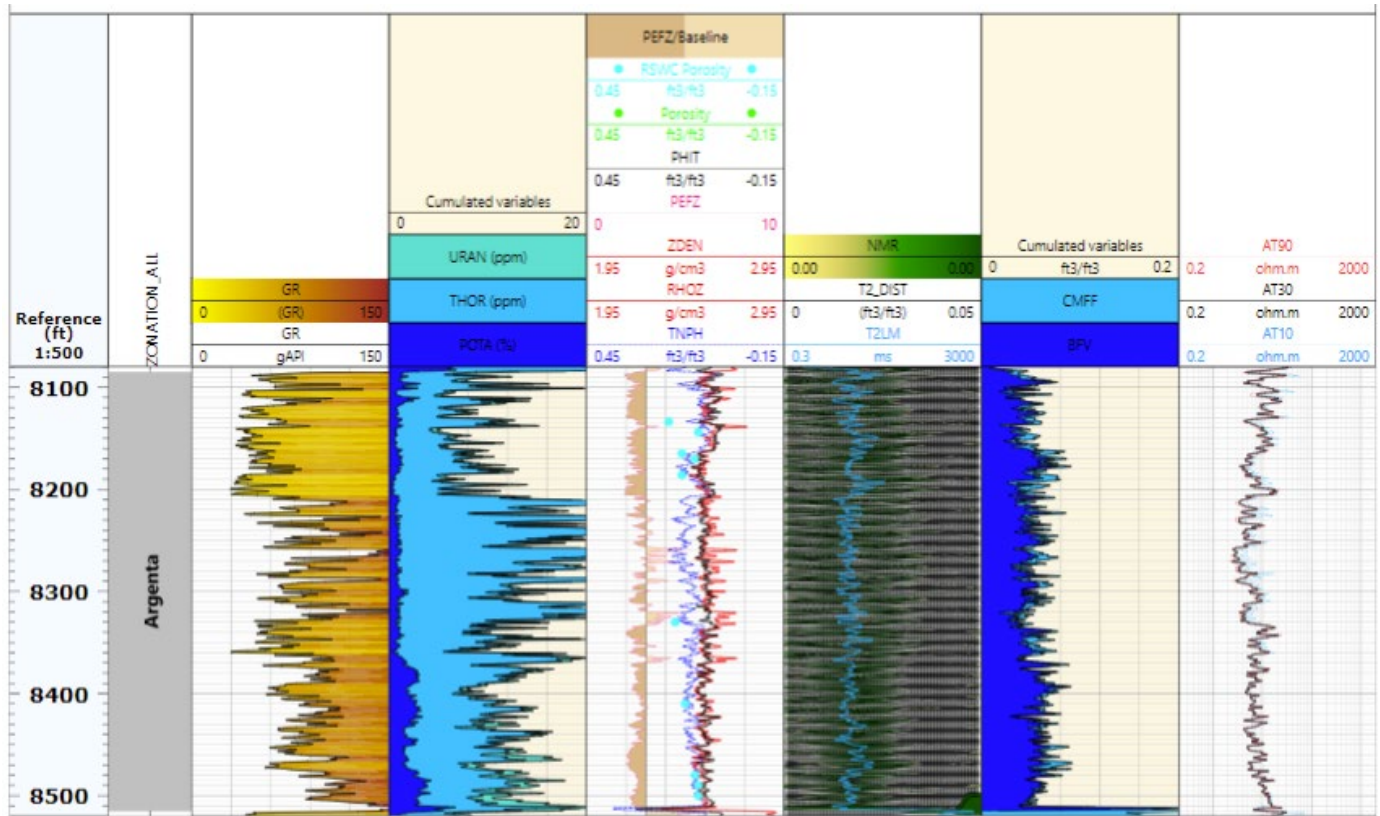
Figure 35: *Geophysical logs vs. depth for the Argenta.*
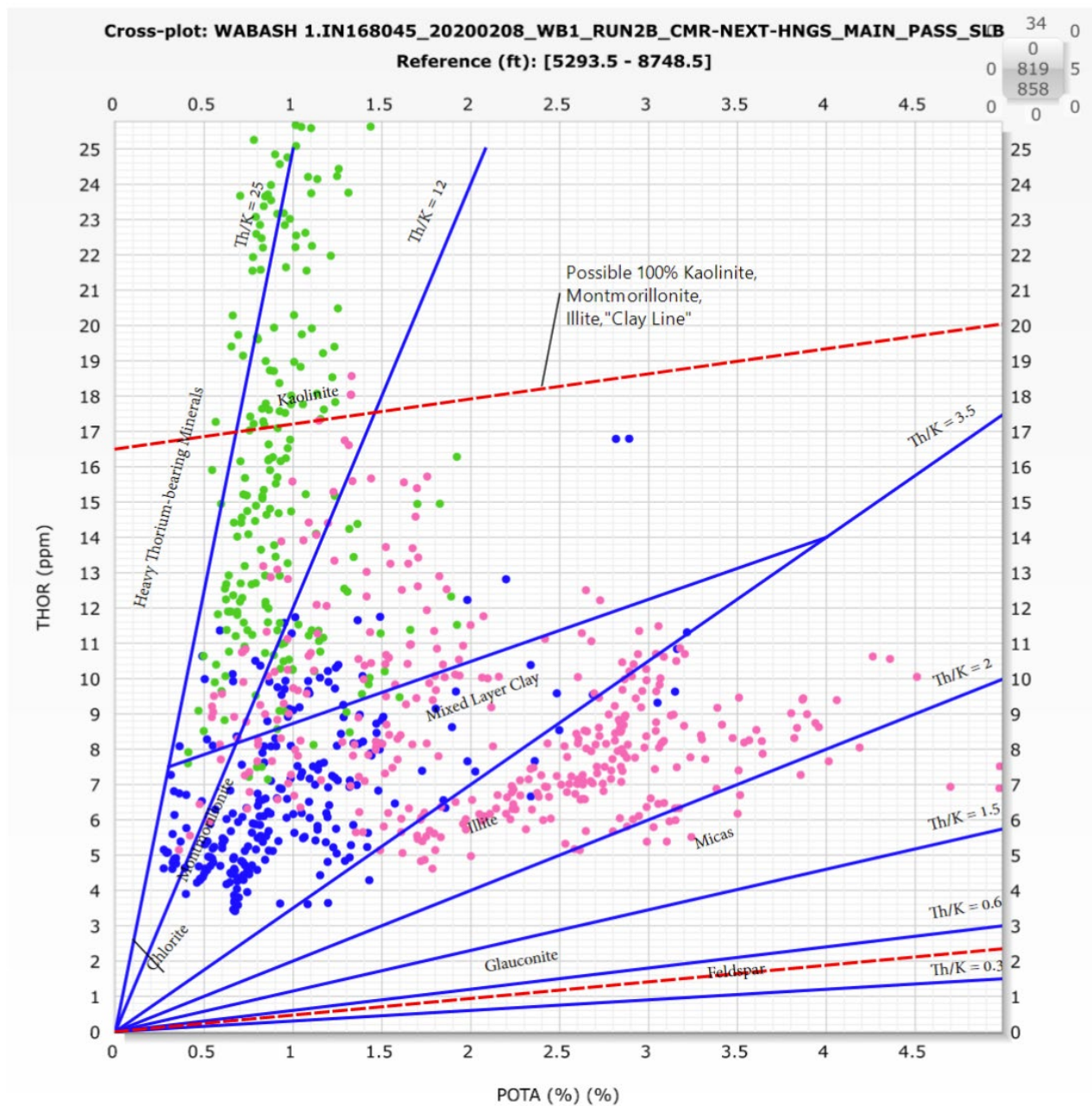
Figure 36: *Potassium/Thorium cross plot for the Argenta from spectral gamma ray log. Data are colored by interval; above 8,210 ft are colored blue and are a mixture of chlorite, montmorillonite, and mixed layer; data between 8,210-8,328 ft are colored green and are kaolinite; and data below 8,328 ft are colored pink and are primarily illite and mixed layer clays.*

Basalt interval

The basalt interval underlies the Argenta sandstone by a distinct unconformable boundary (see Delpomdor, Chapter 1; McBride et al., 2022). The basalt interval has 20 ft thickness with a total porosity range of 1-9%. The cross plot of Pe against RHOZ shows the interval has high density (2.8 to 2.94 g/cm^3) and Pe comparable with anhydrite (Figure 19).
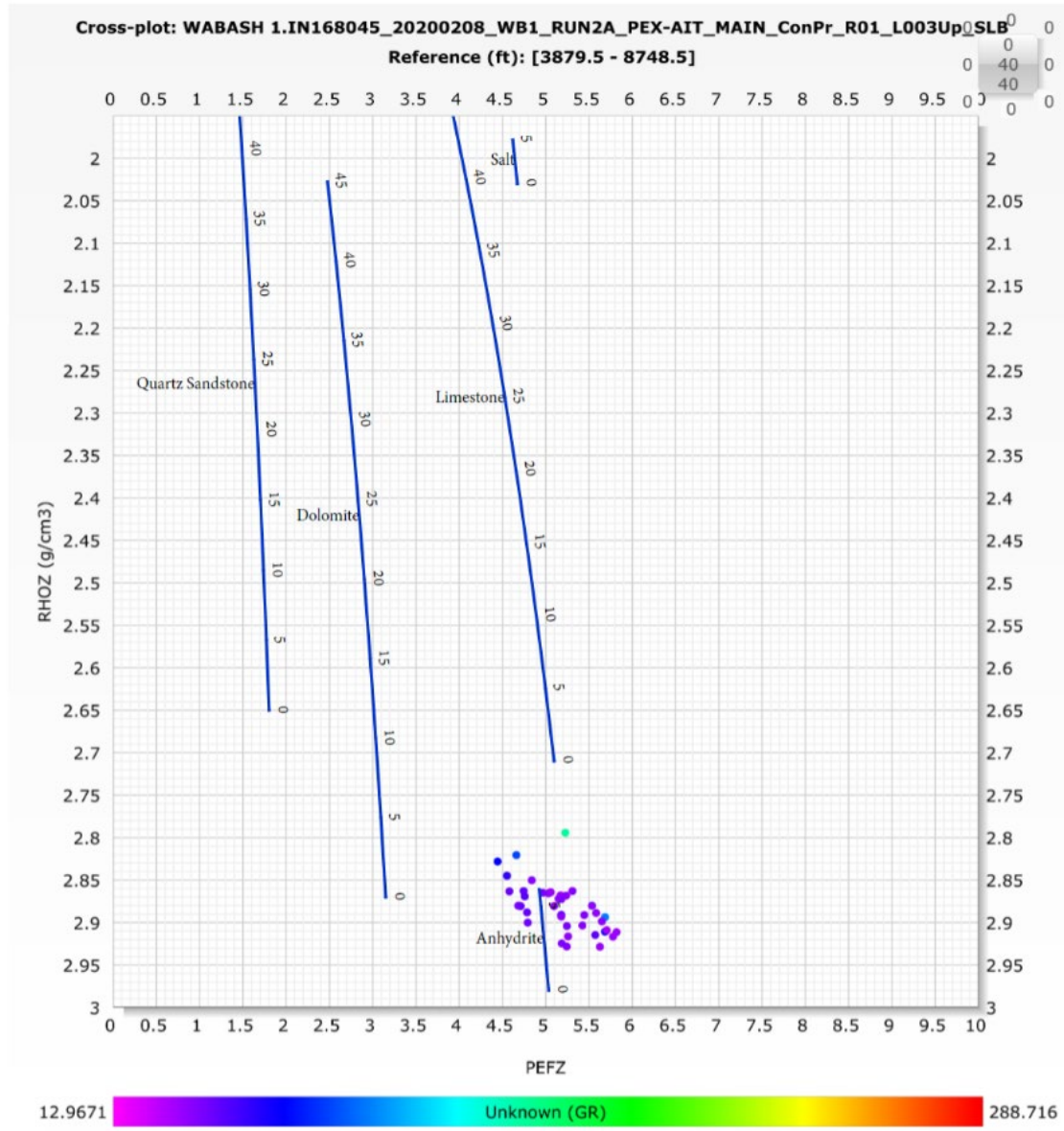
Figure 37: *Cross plot of the Pe and RHOZ data from the Basalt interval. Points are colored by GR value.*

Unidentified Sandstone

The FMI log and prepared plugs from unidentified sandstone indicated the unit is predominantly composed of fine- to coarse-grained sandstone (see Delpomdor, Chapter 1). The upper unit of the unidentified sandstone from 8,535 to 8,650 ft has high GR measurements (over 100 API; Figure 20). The spectral gamma ray shows that the potassium concentration is between 5-7%, indicating the presence of felspar sandstone. The Pe range of the upper unit (2.35-2.7 g/cm^3) is more than sandstone range because of the presence of the feldspar sandstones, shale, and clay contents. Two intervals from 8,540 to 8,551 ft and 8,563 to 8,589 ft show high porosity ranges between 22 to 42%, indicating the interval consists of porous unconsolidated sandstone. The T2 distribution and BFV logs display a high concentration of bounded water representing fine pore sizes between sandstone grains. The cross plot of potassium against thorium depicts that the clay contents are dominantly illite and mica.

Reservoir quality abruptly improves below 8,650 ft (Figure 20). Only 50 ft of this lowest interval were logged, but it has lower GR, less TNPH/DPHZ separation, and a higher proportion of NMR-derived free water.
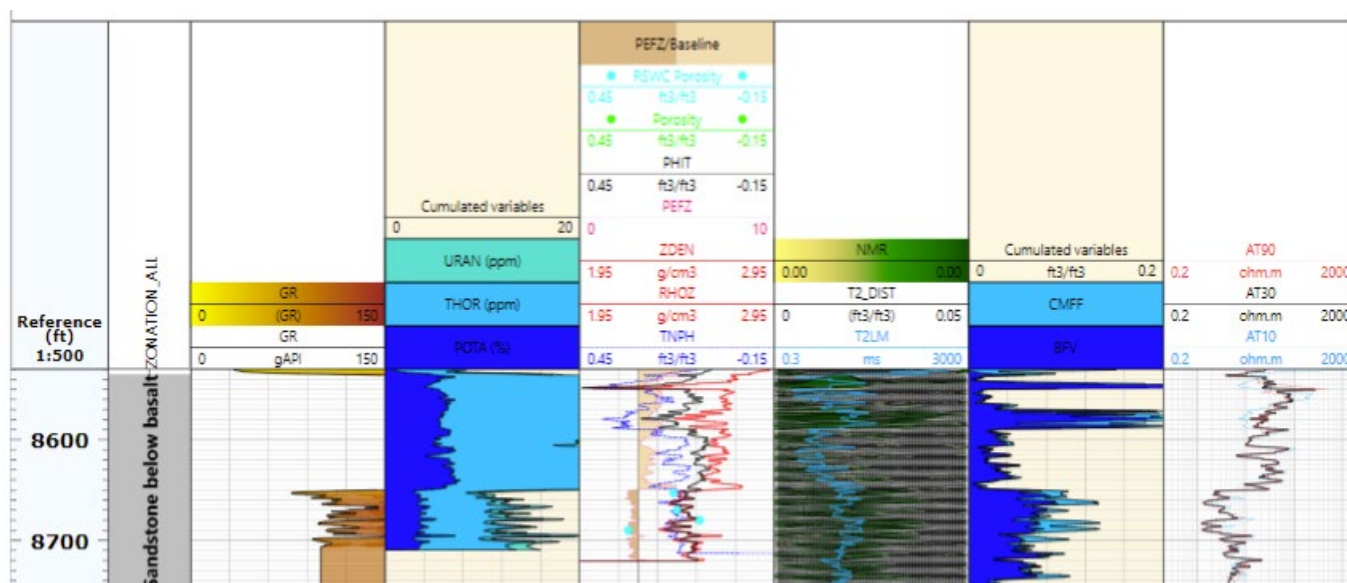
Figure 38: *Geophysical logs vs. depth for the unidentified sandstone.*

PERMEABILITY

Core Data

A total of 37 rotary sidewall core (RSWC) samples were taken and subjected to routine testing (Table 2). The average porosity and permeability of all the Mt. Simon samples is 9.85% and 3.09 mD, respectively, while the Arkose zone, which was expected to have the best reservoir properties, has an average porosity and permeability of 9.67% and 6.57 mD. The unidentified sandstone had the best petrophysical properties of all the intervals sampled with 17.25% average porosity and 27.95 mD average permeability.

Table 3: Rotary sidewall core porosity statistics for the reservoir.

Unit	Count	Porosity (%)			Permeability (mD)		
		Average	Minimum	Maximum	Average	Minimum	Maximum
Eau Claire	1	6.00	6.00	6.00	**0.09**	**0.09**	**0.09**
Upper	2	12.50	12.00	13.00	5.35	0.09	10.61
Middle	5	11.20	7.00	13.00	1.22	0.04	3.54
Lower	11	8.91	5.00	11.00	0.68	0.02	2.91
Arkose	9	9.67	4.00	12.00	6.57	0.02	27.93
Whole Mt Simon	**27**	**9.85**	**4.00**	**13.00**	**3.09**	**0.02**	**27.93**
Argenta	10	14.20	11.00	20.00	1.34	0.10	7.02
Unidentified	4	17.25	8.00	30.00	27.95	0.09	109.08
All Data	**42**	**11.50**	**4.00**	**30.00**	**5.09**	**0.02**	**109.08**

In addition to sidewall core, 120 ft of whole core was taken from the Arkose zone between the depths of 7,900 to 8,020 ft. The core was sampled at regular intervals, resulting in 40 total measurements (three samples were fractured and not included), which were subjected to routine testing (Table 3). These data were consistent with the data from the rotary sidewall cores (Figure 21) and confirm that the Arkose interval has lower porosity and permeability than expected.

Table 4: Whole core porosity and permeability statistics.

	Count	Average	St. Dev	Median	Minimum	Maximum
Porosity (%)	37	7.61	3.77	8.19	0.97	12.95
Permeability (mD)		2.19	2.76	1.00	0.09	10.90
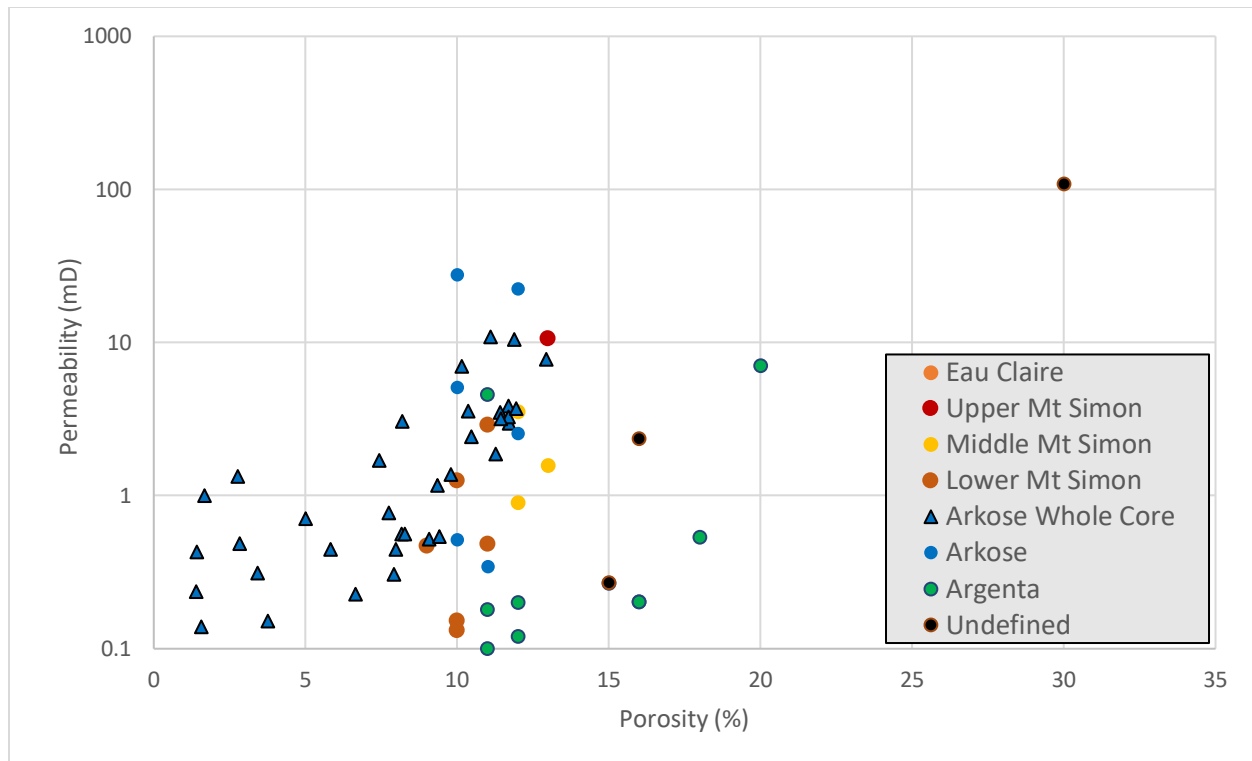
Figure 39*: Cross plot of porosity and permeability from core.*

Drill Stem Testing (DST)

During the drilling process, two drill stem tests, DST1 and DST2, were completed across two unique subintervals, 7,696-8,120 ft (424 ft; parts of Lower Mt. Simon/Arkose/Argenta) and 6,710-6,912 ft (202 ft; parts of Upper and Middle Mt. Simon), respectively. During each DST, two flow and two shut-in (SI) periods were planned, but DST1 had an atypical response, and 2nd flow and SI period failed. DST1's first flow period was 14 mins, and the SI period was 62 mins. DST2's flow periods were 21 and 23 mins, and the SI periods were 59 and 190 mins. Table 4 shows flow and SI durations, fluid produced, and initial and final flow and SI pressures. The SI period of each test was analyzed for permeability-thickness product. (To estimate permeability, it is necessary to estimate net thickness or assume the subinterval between the DST's packers is the net thickness.)

Table 5: *Results of the two DSTs conducted in different Mt. Simon Sandstone subintervals.*

Attribute	DST 1	DST 2	Comment
Name	Deeper MtS DST	Shallower MtS DST	
Subinterval, ft (KB)	7,696-8,120	6,710-6,912	
1st flow duration, mins	14	21	
1st SI duration, mins	62	23	
2nd flow duration, mins	-	59	DST1: 2nd SI failed
2nd SI duration, mins	-	190	DST1: 2nd SI failed
Fluid produced, bbl	101.04	71.03	
Test thickness, ft	424	202	
Perm-thickness, md-ft	1,260	980, 460	DST2 Two apparent radial flow periods (more confident in 980)
Initial pressure*, psia	3,828	3,227	
Initial pressure datum, ft (KB)	8,109	6,901	

* Pressure gauge was calibrated for psig; 14.79 psia was average atmospheric pressure in this area during this month.

Derivative and semilog (i.e., Horner or superposition) analyses were used to estimate permeability-thickness. (Only derivative plots are shown.) For DST1, qualitatively, the derivative plot (Figure 22) shows radial flow across the subinterval tested and no unique geologic features; the data between 0.1 and 1.0 hours was identified as radial flow (zero slope on derivative) and analyzed. This radial flow period gave 1,260 md-ft for the 424 ft test interval. For DST2, qualitatively, the derivative plot (Figure 23) shows two zero slopes between 0.015 and 0.05 hours and 1.5 and 3 hours identified as radial flow and analyzed. The first radial flow period starts and ends in less than 3 mins, and therefore not likely related to permeability of flow across the entire subinterval. Nevertheless, calculating permeability from each of these periods gives 980 and 460 md-ft for the 202 ft test interval.

Because the production period of DSTs are short, initial pressure is often measured directly and confirmed with semilog analyses. The initial pressure for DST1 and DST2 is 3,828 and 3,227 psia at datum depths of 8,109 ft and 6,901 ft (KB), respectively.
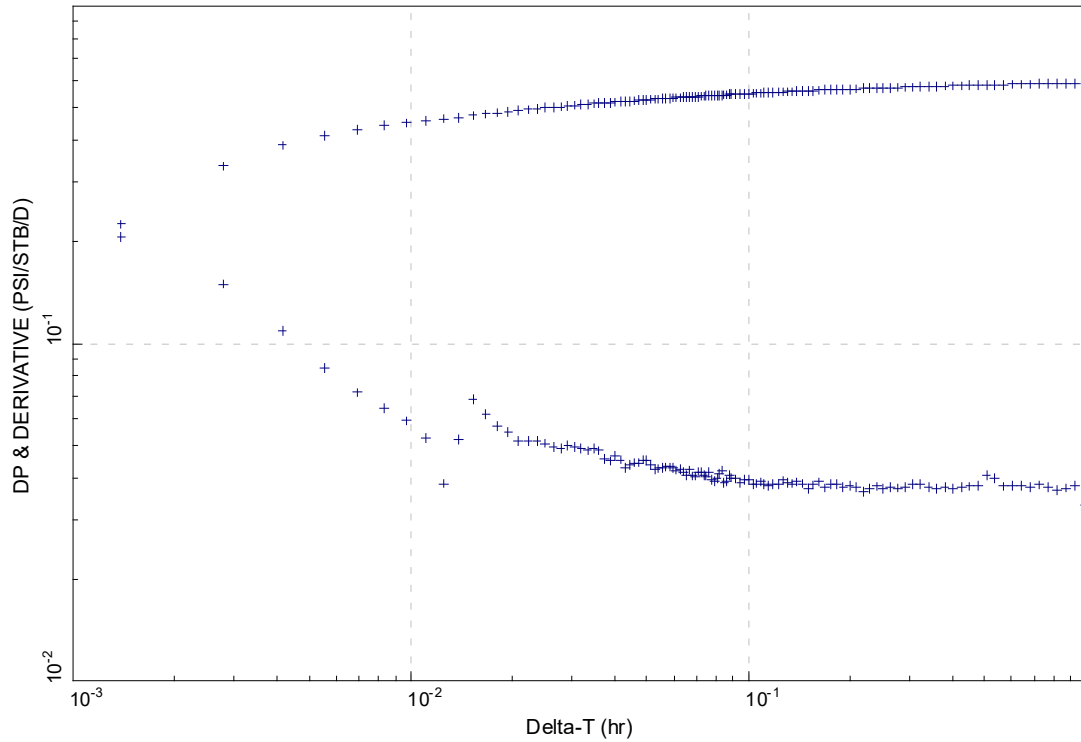
Figure 40: *Derivative plot of 1ˢᵗ SI period. 2ⁿᵈ SI was not analyzable due to failure during 2ⁿᵈ flow period over concerns the DST might be stuck in the well. Derivative shows radial flow from about 0.1 hrs to 1.0 hrs, which is analyzable for permeability.*
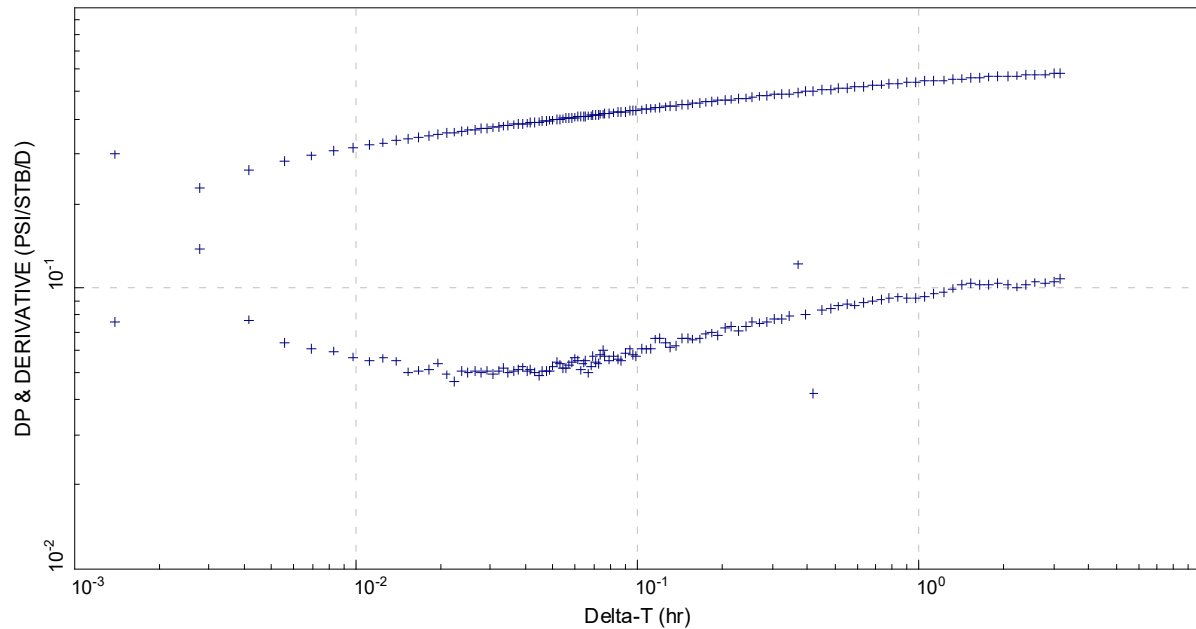
Figure 41: *Derivative plot of 1ˢᵗ SI period. 2ⁿᵈ SI was not analyzable due to failure during 2ⁿᵈ flow period over concerns the DST might be stuck in the well. Derivative shows two zero slope derivative between 0.015 and 0.05 hrs and 1.5 to 3.0 hrs, which are indicative of radial flow periods.*

112

INJECTION WELL TESTING

Wabash #1 drilled through the Mt. Simon Sandstone into a 20-ft thick basalt followed by a sedimentary unit that was tentatively correlated during drilling and well-testing as Precambrian. Later analyses identified the basalt, and unidentified sandstone below it, as Cambrian in age; note that to be consistent between well test interval names and related sample IDs/names, reports, etc., remnants of this preliminary "Precambrian" correlation exist in the injection well-testing data tables and discussion below.

The injection testing of the Mt. Simon Sandstone and "Precambrian" (PC) sediments (see Unidentified Sandstone in above sections of this report) followed placement and cementing of the production casing, which followed the Knox injection tests. While testing the Knox, the Mt. Simon Sandstone and PC sandstone were uncased and in contact with the drilling mud for nearly 5 months. The process of placing and cementing the production casing took much longer than projected and was more expensive than budgeted, which reduced the budget for Mt. Simon Sandstone and PC sandstone injection testing. Moreover, because the well log porosity and core permeability were very low, use of the Mt. Simon Sandstone and PC sandstone for CO_2 injection at this site was of much less interest. Consequently, the injection well-testing objectives were primarily short-term tests with emphasis on fracture pressure.

After the production casing was placed and cemented, two Mt. Simon Sandstone and two PC sandstone subintervals were perforated (MtS1 7,976-7,996 ft; MtS2 7,192-7,202 ft; PC1 8,681-8,691 ft; and PC2 8,661-8,671 ft) and injection tested. Due to suspected behind-pipe communication observed during swabbing, the two PC subintervals, PC12, were tested simultaneously. The injection tests were step rate tests (SRT), multirate tests (MRT), injection tests, and pressure falloff tests (PFO). Derivative and semilog analyses were attempted to estimate permeability-thickness for the short injection and PFO tests. Analyses of SRTs provided estimates of the fracture gradient. Initial pressure and temperature were primarily from analyses and interpretation of the swabbing procedures and early, pre-water pressure measurements of the memory gauge on injection test tubing and the surface readout memory gauge.

Derivative and semilog (i.e., Horner or superposition) analyses were used to estimate permeability-thickness. For PC12, qualitatively, the derivative plot (Figure 24) between 0.4 and 1.0 hours was identified as radial flow (zero slope on derivative) and analyzed; however, because of the short duration of the radial flow period, low confidence is placed on this value. This radial flow period gave 88.9 md-ft for the two 10-foot test intervals. For MtS1, qualitatively, the derivative plot (Figure 25) between 0.15 and 0.4 hrs and 30 to 100 hrs was identified as radial flow (zero slope on derivative) and analyzed. These radial flow periods gave 85 and 375 md-ft for the 20-ft test interval (Table 5). For MtS2, the derivative analysis was not possible due to short injection and shut periods. The MtS2 pre-fracture injection periods of the step rate tests were analyzed, but no pressure step response was recorded and could not provide an estimate for permeability-thickness product.
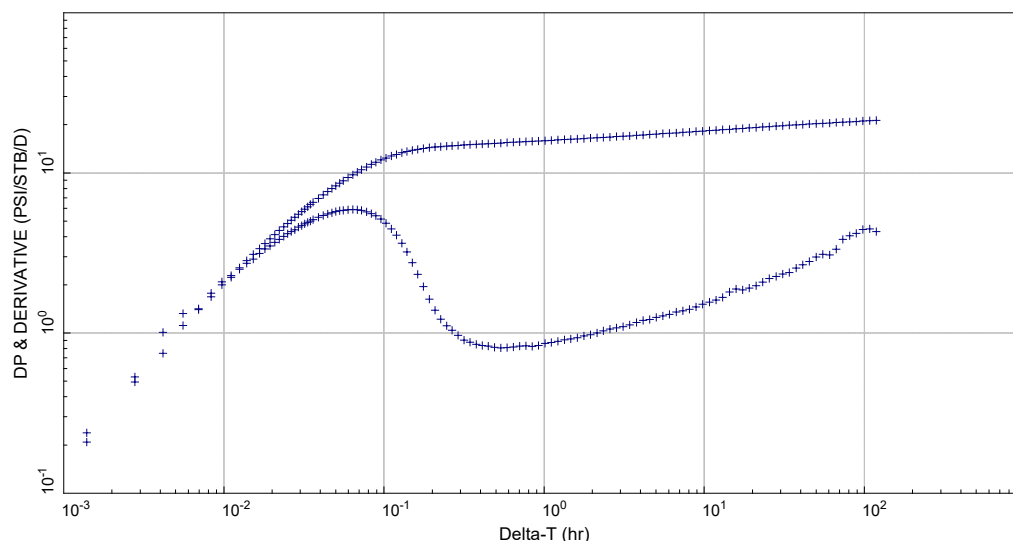
Figure 42: Simultaneous injection test of the PC12 intervals (8,681-8,691 and 8,661-8,671 ft). Derivative plot of final SI period of the PFO test. Derivative shows wellbore storage dominated data through 0.4 hrs. A single zero slope derivative is present between 0.4 and 1.0 hrs, which is indicative of radial flow period and used for estimating permeability-thickness product. However, this is a very short radial flow period and may be part of transition out of wellbore storage. The increase in derivative beyond 1.0 hrs is attributed to the relatively short injection period preceding this falloff test and the difference between the viscosity of the test water and the in-situ brine.
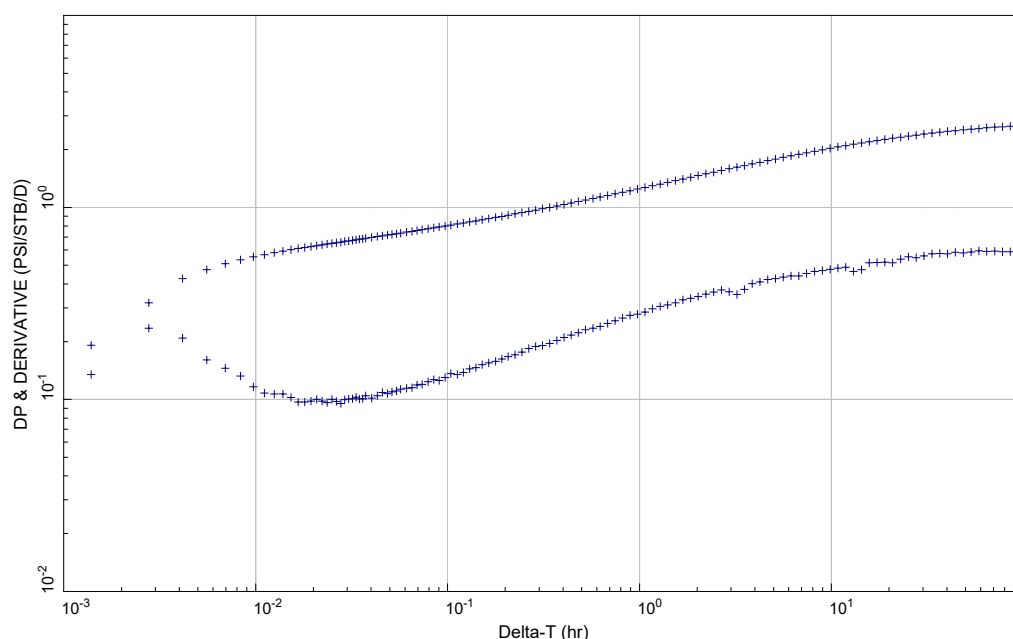
Figure 43: Injection test of the MtS1 interval (7,976-7,996 ft). Derivative plot of final SI period of the PFO test. Derivative shows two zero slope derivative between 0.15 and 0.4 hrs and 30 to 100 hrs, which are indicative of radial flow periods. At the time of this report, the transition between these two radial flow periods could not be uniquely identified. The difference in the viscosity of the test water and in situ brine and the relatively short injection period (compared to the SI period) are partially responsible for this transition. Consequently, both radial flow periods were used to estimate the permeability-thickness product.

114

PC12 and MtS1 gave typical SRT results after several attempts to find the combination of rate and duration that resulted in an analyzable SRT. The fracture pressure at the depth of the downhole pressure gauge was corrected to the top of the perforated interval tested using the freshwater gradient of the test fluid (0.433 psi/ft). The fracture gradients for PC12 and MtS1 were 0.665 and 0.574 psi/ft, respectively. Because of budget constraints, the injection test for the MtS2 interval was constrained to 8 hrs. Six SRT attempts failed during this time due to leaks and a valve that was left opened, which resulted in lack of step increase in pressure for each rate change. Consequently, no estimate of fracture pressure was possible.

Table 6: *Results of the well injection tests conducted in two Mt. Simon Sandstone and two "Precambrian" sandstone (see Unidentified Sandstone in above sections of this report) subintervals.*

Test interval	Depth interval (ft)	Permeability thickness (md-ft)	Fracture gradient (psi/ft)
MtS1	7,976-7,996	85-375	0.574
MtS2	7,192-7,202	-	-
PC12	8,681-8,691 8,661-8,671	88.9	0.665

POROSITY TO PERMEABILITY TRANSFORM

The five porosity-permeability transforms developed for IBDP were used for the Wabash #1 well using unique cementation exponent (m) ranges for each transform. The range of m was iteratively changed to get the best match of permeability from the transforms to the core, DST and/or well test permeability on a semilog plot with porosity (Figure 26) and Cartesian plot with depth (Figure 27). Using Archie's equation (Archie, 1942), the AT90 resistivity log and PHIT were used as-is with water resistivity (R_W) to calculate m for each 0.5 ft well log value. There was disagreement between well test and core-derived permeability, so two permeability curves were developed and used for geocellular models, one matched to the core data and another matched to the DST data.

Water resistivity for the core matched permeability was calculated by correcting the R_W observed at the IBDP well to a temperature log (MTEM) by using the following equation:

$$R_{Wcore}=0.0275 \text{ ohm-m}*(144F+6.77)/(MTEM+6.77)$$

Water resistivity for the DST-matched permeability was calculated by extrapolating the R_{WS} observed in the DSTs. The average depth and R_W for both tests were plotted against each other,

and a linear line was regressed through both data points. The equation defining the line was used to calculate R$_W$ at all other depths using the following equation:

$$R_{WDST}=(depth-41,658)/-493,070$$

The log of estimated permeability (i.e., via the transform) was compared to the core, DST, and/or well test permeability (Figure 27). The range of m for each transform was adjusted to best fit the core, DST, and/or well test permeability. Figure 27 (blue and grey curves) shows the estimated permeability used for the basis for the geocellular model.
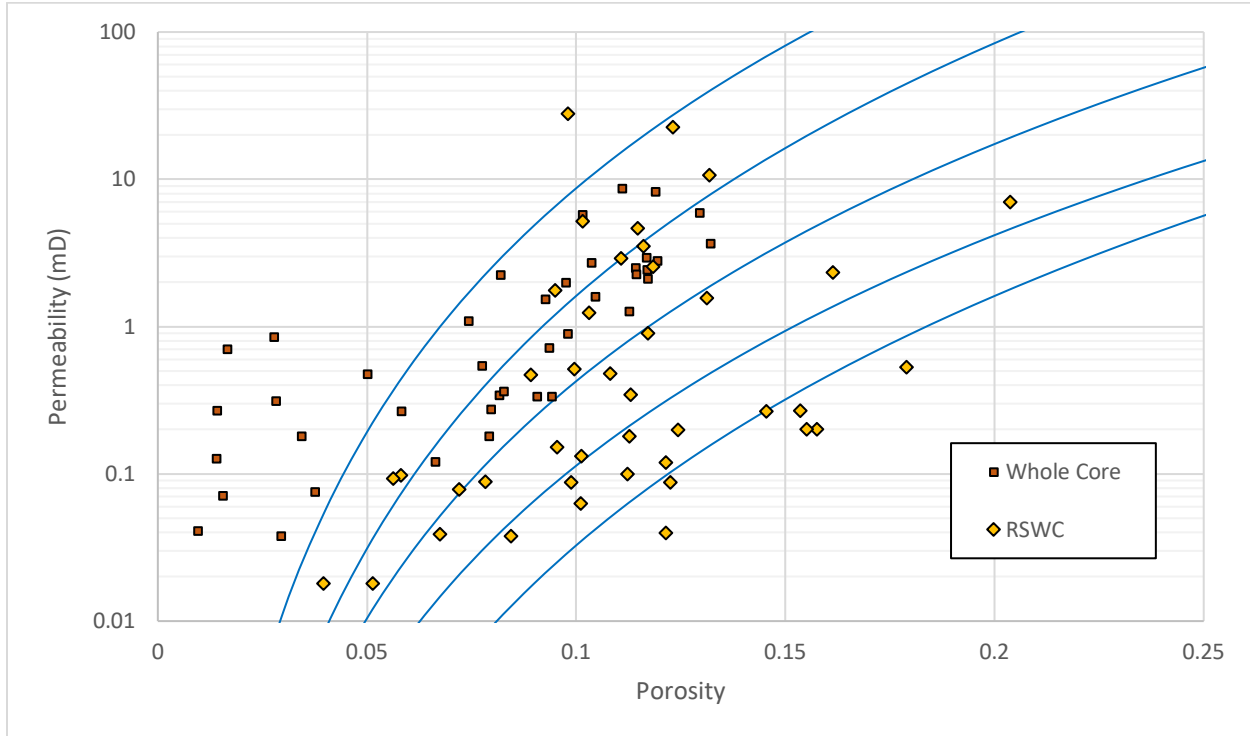
Figure 44: *Semilog plot of porosity vs. permeability. Whole core data shown with brown squares, RSWC data shown with yellow diamonds, and porosity to permeability transforms shown with blue lines.*
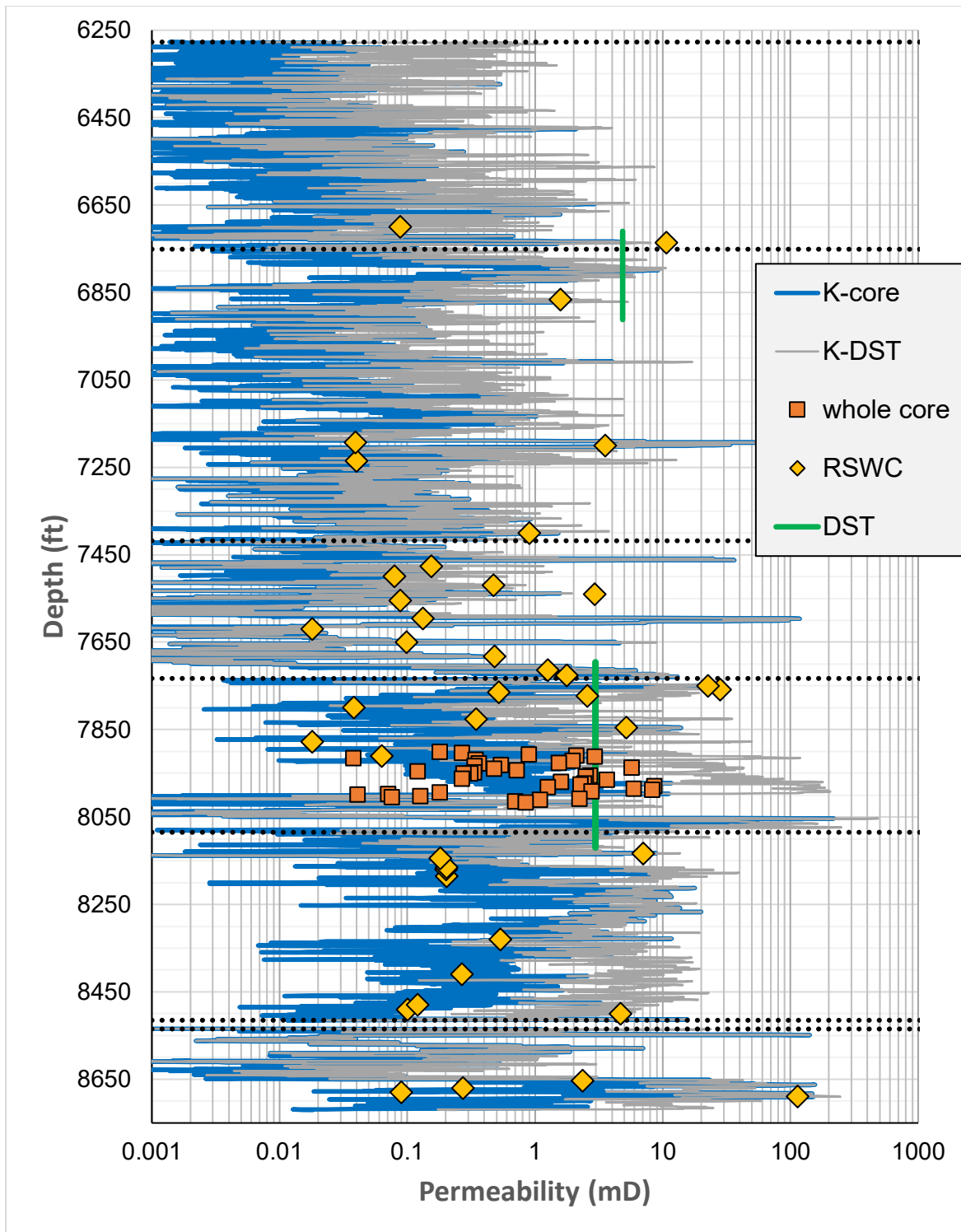
Figure 45: *Permeability vs. depth. The boundaries of the intervals evaluated are shown with dashed black lines. Data from whole cores shown with orange squares, data from RSWC shown with yellow diamonds. Permeability determined by DSTs shown with vertical green lines. Permeability derived from the transform matched to the core data is shown in blue line, and permeability derived from the transform matched to the DST is shown in grey line.*

CONCLUSIONS

Statistics of the logs for each of the intervals were compiled and analyzed. The average log responses for each of the Mt. Simon intervals are similar (Table 6), but the Upper Mt. Simon has the highest clay content and lowest reservoir quality, as illustrated by the GR, Pe, and TNPH/DPHZ separation (which are all higher than in the Middle and Lower intervals). Statistics for the GR log can be used as a crude indicator for reservoir quality (Figure 28) for each of the Mt. Simon intervals (low GR suggests low clay content and higher reservoir quality).

The Arkose was expected to be the best candidate for CO_2 storage, but while it does have some permeable feldspar rich units (as determined by the correlation between elevated Pe/GR and effective porosities from the NMR and SPHI logs), these units are thinner than anticipated. The permeability observed in core, both RSWC and whole core, was also lower than anticipated. The DST in the Arkose interval does suggest that the core data underrepresented the permeability, but the average permeability of the interval is still less than 100 mD.

The SGR suggests that the Argenta has four intervals with different clay constituents, so the raw statistics for the whole interval can be misleading, but the NMR log suggests that none of it has very good reservoir quality.

The Unidentified Sandstone has the highest average PHIT of all the sandstone units evaluated, but high GR, Pe, pronounced TNPH/DPHZ separation, and NMR-derived bound water show that the upper half of the interval has a high proportion of clay and ineffective porosity.

Table 7: *Average log values for each of the intervals evaluated.*

Formation	PHIT	DPHZ	TNPH	SPHI	GR	Pe
Upper Eau Claire	-20.82%	-53.51%	11.86%	2.16%	28.86	4.92
Eau Claire shale	23.02%	17.91%	28.14%	16.10%	123.05	2.95
Upper Mt. Simon	6.11%	4.90%	7.32%	7.45%	66.62	2.12
Middle Mt. Simon	6.10%	5.71%	6.49%	7.54%	43.66	1.97
Lower Mt. Simon	5.24%	5.03%	5.45%	7.08%	35.07	1.93
Arkose	9.70%	8.24%	11.15%	10.53%	114.15	2.53
Argenta	9.08%	5.38%	12.78%	11.11%	80.65	2.62
Basalt	-1.71%	-14.21%	10.80%	1.98%	45.95	5.18
Unidentified Sandstone	11.27%	3.59%	19.14%	14.75%	191.26	3.37
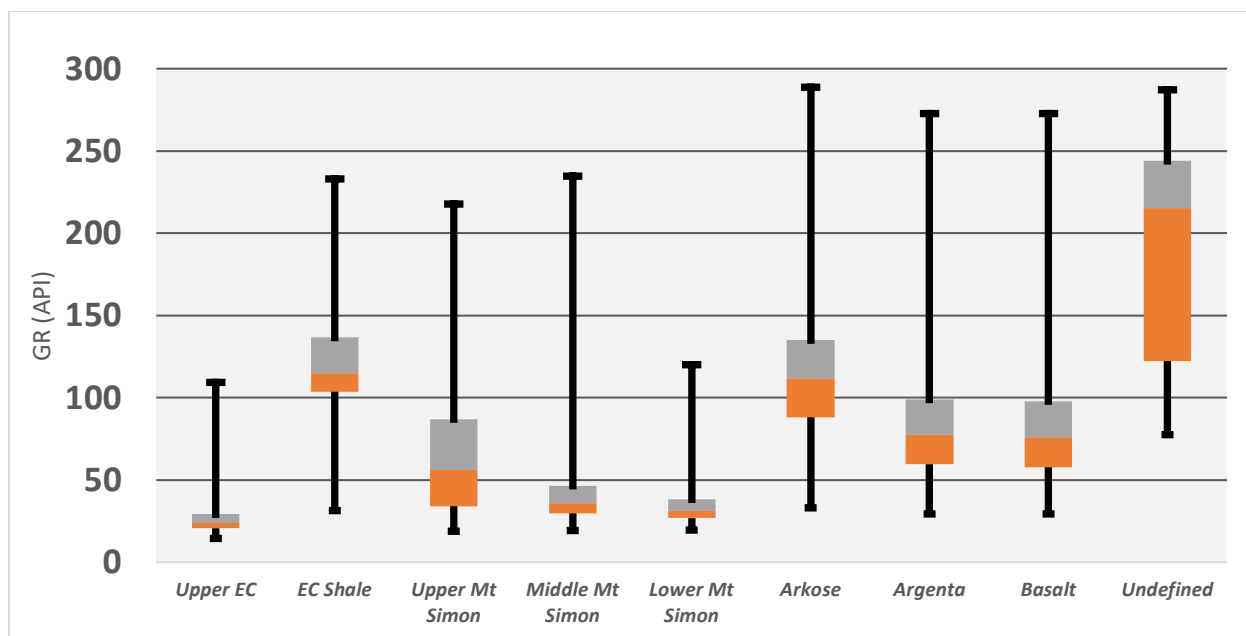
Figure 46*: Box and whisker plot of the GR values for each of the intervals evaluated.*

REFERENCES

Archie, G. E., 1942. The Electrical Resistivity Log as an Aid in Determining Some Reservoir Characteristics, Petroleum Transactions of the AIME, *Transactions of AIME 146*, 54-62.

Asquith, G., and D. Krygowski, 2004, Basic well log analysis, 2nd ed.: Tulsa, Oklahoma, AAPG Methods in Exploration 16, 244 p.

Freiburg, J.T., Morse, D.G., Leetaru, H.E., Hoss, R.P., and Yan, Q., 2014. A Depositional and diagenetic characterization of the Mt. Simon Sandstone at the Illinois Basin - Decatur Project Carbon Capture and Storage Site, Decatur, Illinois, USA, *Illinois State Geological Survey Circular 583*, p. 65.

Timur, A., 1968. An Investigation of Permeability, Porosity, & Residual Water Saturation Relationships For Sandstone Reservoirs, *The Log Analyst 9*, 8-17.

Schlumberger, 1998, Log Interpretation Charts: Sugar Land, Texas, Schlumberger Wireline and Testing, SMP-7006.

Wyllie, M.R.J. and Rose, W.D., 1950. Some Theoretical Considerations Related to the Quantitative Evaluation of the Physical Characteristics of Reservoir Rock From Electrical Log Data*, Journal of Petroleum Technology 189*, 105-110. SPE-950105-G, doi:10.2118/950105-G.

Chapter 5
Mt. Simon Sandstone Regional Mapping

By: Charles Monson and Zohreh Askari

Illinois State Geological Survey, Prairie Research Institute, University of Illinois at Urbana-Champaign

The suitability of a given site for geological carbon storage (GCS) is determined by factors that include not only thickness and quality of reservoir but also depth to reservoir and salinity of groundwater within the reservoir (i.e., potential potability of the groundwater). The Mt. Simon Sandstone in the Illinois Basin, while regarded as a major potential CO_2 storage reservoir (NETL, 2015), exhibits trends in groundwater salinity, depth to reservoir, and thickness of reservoir that render it unsuitable for GCS in some parts of the basin. As part of ongoing CarbonSAFE work, the need for a single map that captures some of these key elements—both for internal use and for distribution to external partners and stakeholders—was recognized. Figure 1 presents a map with superimposed elements of a top-Mt. Simon structural contour map with Mt. Simon (including Argenta strata) isopach contours and 10,000 mg/L total dissolved solids (TDS) formation water salinity.
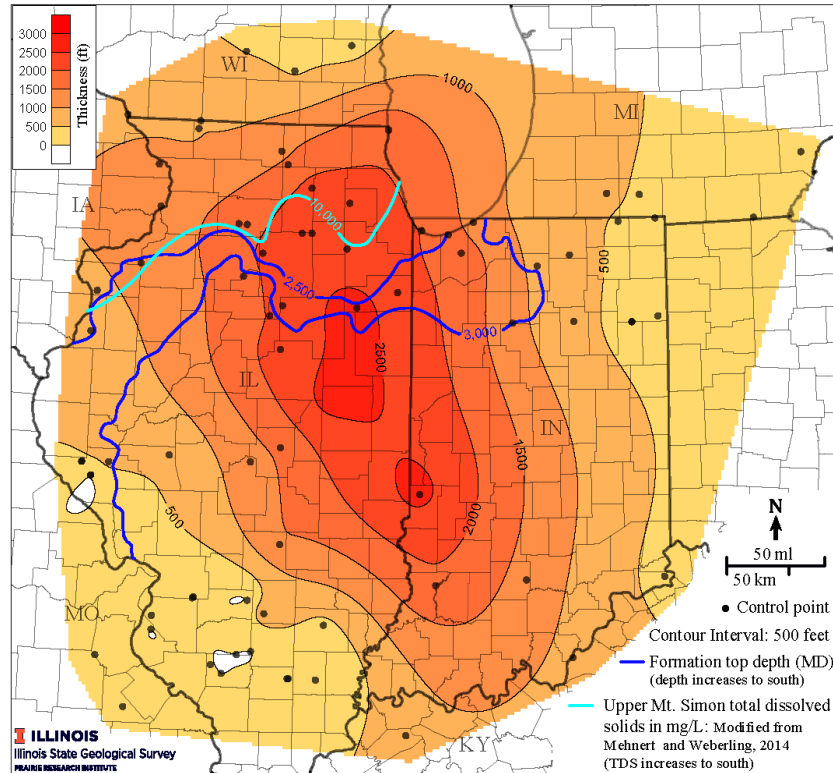
Figure 47*: Combined map of Mt. Simon-Argenta thickness (closed contours); selected values of measured depth (in feet) to top of Mt. Simon (dark blue lines), and USDW cutoff for Mt. Simon groundwater salinity (light blue line). Black dots = well control for Mt. Simon-Argenta thickness.*

TOP-MT. SIMON STRUCTURAL CONTOURS

Data coverage of the Mt. Simon in the Illinois Basin is insufficient to create high-resolution regional maps of the formation. Shallower sedimentary units, such as the Ordovician Galena Group, are penetrated by far more wells and can therefore be mapped with much greater resolution. These higher-resolution maps can then be used to add greater detail to maps of deeper formations via conformable mapping, since many of the large-scale structural features that heavily influence subsurface topography—e.g., the La Salle Anticlinorium—extend through much of the sedimentary column and therefore exert similar structural influence on both shallow and deep formations.

For this study, an isopach map of the thickness from the top of the Galena (8,754 well penetrations) to the top of the Mt. Simon (1,141 well penetrations) was created and was then subtracted from the Galena Group structure map to provide a realistic, data-constrained estimate of depth to Mt. Simon in areas of little to no deep well data coverage. The structure and isopach maps were created with IHS Petra software, using the Kingdom Flex Gridding method and an 8,000 x 8,000 grid size, with no faulting or manual adjustment of contours. The resulting Mt. Simon structure map is shown in Figure 2.
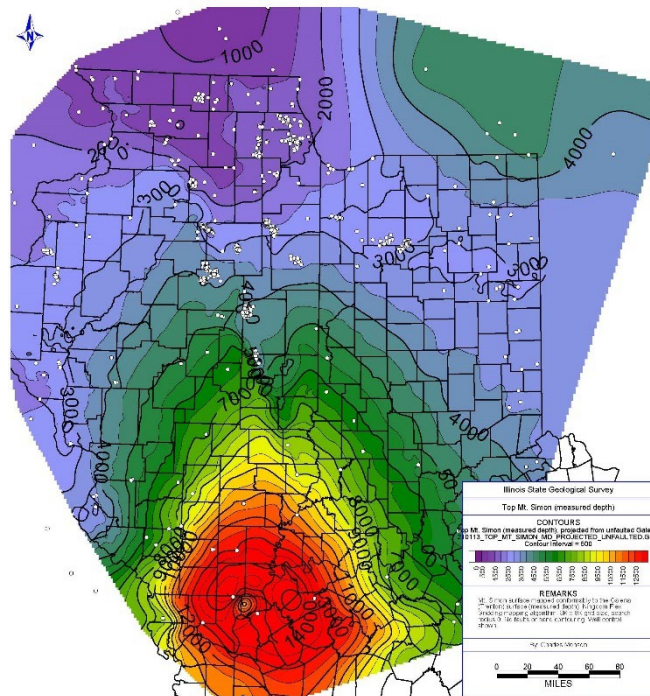
Figure 48: *Measured depth contour map of the top surface of the Mt. Simon Sandstone, mapped conformably to the Galena (Trenton) surface. Well control shown as white dots.*

Measured depth to the top of the Mt. Simon increases from roughly 1,100 ft (340 m) in the northernmost part of the state to >14,000 ft (4,300 m) in southernmost Illinois. A depth of 2,500-3,000 ft (760-910 m) measured depth (MD) below ground surface is necessary for CO_2 to be stored as supercritical fluid, meaning that areas of northern Illinois with relatively shallow Mt. Simon are unsuitable for CO_2 sequestration. The structure map for this work therefore shows the top of the Mt. Simon in MD, mapped conformably to the Galena Group as described above, as opposed to the more typical subsea-depth map. The 2,500 ft (760 m) and 3,000 ft (910 m) MD contour lines were captured as shapefiles and added to the larger map to function as a quick-look indicator of which parts of the Basin had Mt. Simon deposits that were too shallow to be targeted for GCS. Typically it is the Lower Mt. Simon Sandstone that is targeted for storage and, in particular, an arkosic zone that is usually some 1,000-2,000 ft (305-610 m) below the top of the formation; however, the Upper Mt. Simon serves as a gas storage target in parts of the Illinois Basin and is therefore a plausible target for CO_2 storage in some cases.

"MT. SIMON" ISOPACH

The second component of Figure 1 is a combined isopach map of the "Mt. Simon" system, which includes both the Mt. Simon Sandstone and the Argenta sandstone. The Argenta is a recently identified sedimentary unit (Freiburg et al., 2014, 2015) which underlies the Mt. Simon in the central Illinois Basin; it has yet to be formally named or described but is provisionally considered to be a discrete formation, as opposed to a subunit of the Mt. Simon. The Argenta was first

identified at the Illinois Basin-Decatur Project site (Freiburg et al., 2014), and subsequent reassessment of samples and geophysical logs from other deep Illinois Basin wells indicated that the deepest "Mt. Simon" beds at those locations were actually Argenta as well. However, the relatively low number and uneven distribution of wells deep enough to penetrate the Argenta creates difficulties in mapping the two units separately. As a result, the Mt. Simon and Argenta are often still treated as a single unit for isopach mapping, as was done here.

Carbon storage viability of the Mt. Simon at any given location is a function of several characteristics, including thickness and petrographic qualities of the arkosic zone generally targeted as the key injection zone, and of the Upper Mt. Simon deposits that might serve as a secondary target. Gross thickness of the total Mt. Simon-Argenta system does not directly correspond to GCS reservoir quality or capacity, but it can serve as a first-look proxy for GCS suitability; thicker Mt. Simon-Argenta deposits are broadly correlated with thicker Upper Mt. Simon and arkosic deposits, and areas of thinner Mt. Simon (such as southwestern Illinois) lack arkosic zone deposits entirely.

The combined Mt. Simon-Argenta isopach was based on 83 data points (Figure 1; Table 1) from wells that reach igneous basement. A first-draft isopach generated from this data yielded thickness estimates that were too small to accommodate known or projected sedimentary thicknesses at three locations. Consequently, three extrapolated "false" data points were used to help constrain contours:

A. The Hinton #7 well (Champaign County, Illinois, 10-digit API 1201923996) has the thickest known interval of Mt. Simon-Argenta in the Illinois Basin (2,620 ft [799 m], including 584 ft [178 m] of Argenta). The well bottoms out in Argenta, but total depth of the well is thought to be not far above Precambrian basement, so the well total depth of 6,550 ft (1,996 m) is often used as a Precambrian basement data point for mapping; the same was done here.

B. The Schwark #7 well (Kankakee County, Illinois, 10-digit API 1209100080) reaches neither Argenta nor basement but penetrates 113 ft (34 m) of Lower Mt. Simon arkosic zone before achieving total depth at 5,003 ft (1,525 m) MD. Regional isopach mapping (ISGS, unpublished data) projects approximately 135 ft (41 m) of arkose and approximately 160 ft (49 m) of Argenta at the Schwark location. Assuming the base of the arkosic zone corresponds to the top of the Argenta, as is typically the case, this would yield a total Mt. Simon-Argenta thickness of 2,620 ft (799 m) and a Precambrian basement depth of 5,185 ft (1,580 m). Mapping without a Precambrian basement value at Schwark #7 yielded a projected Precambrian value that was too shallow to accommodate the expected arkosic zone and Argenta thicknesses, so the 5,185 ft (1,580 m) Precambrian estimate was used as a control point for mapping.

C. The Wabash #1 well (Vigo County, Indiana) reached total depth at 8,740 ft (2,660 m) in an unidentified sandstone that underlies thin basaltic layers higher in the sedimentary column. This is several hundred feet below the projected Precambrian depth of ~8,350 ft

derived from older structure maps. A semi-arbitrary Precambrian basement depth of 8,900 ft (2,713 m) MD was used for mapping at this location to ensure that the mapping algorithm did not return a projected basement depth above known sedimentary deposits. This number yields a Mt.-Simon-to-basement thickness of approximately 2,623 ft (799 m), which is comparable to inferred values in the thickest part of the succession (Hinton and Schwark, as described above), in keeping with the general model of deposition in a previously unrecognized arm of the Reelfoot Rift (Freiburg et al., 2020).

The combined Mt. Simon-Argenta thickness map was created with IHS Petra software, using the Kingdom Flex Gridding method and a 10,000 x 10,000 grid size, with no faulting or manual adjustment of contours. It is represented by the concentric closed contours in Figure 1, with well control shown as black dots.

SALINITY
Regional Map

Reservoirs containing formation fluids having less than 10,000 mg/L TDS are designated as Underground Sources of Drinking Water (USDW) and considered unsuitable for carbon storage. In the Illinois Basin, formation water salinity decreases to the north. Mehnert and Weberling (2014) constructed maps of TDS concentrations in several Illinois Basin formations based on a combination of new data and data from ISGS files. They found that salinity in Mt. Simon formation waters transitions to potential USDW levels along a line that runs through Kankakee, Grundy, La Salle, and Bureau counties in north-central Illinois before deflecting southwards towards Adams County (Mehnert and Weberling, 2014; our Figure 3). Because salinity increases to the south in the Illinois Basin, areas north of this line would be considered potential USDWs. A slightly simplified version of the 10,000 mg/L TDS line from Mehnert and Weberling (2014) was adapted into a shapefile that was added to the Mt. Simon thickness and burial depth map.

Mehnert and Weberling caution, however, that creation of a salinity isopach obscures TDS variability caused by "temporal and vertical variability in when and where the groundwater samples were collected" (2014, p. 11); their data set spanned 100 years, and changes due to factors such as heavy groundwater withdrawal in northeastern Illinois are likely. The authors note (p. 9) that "limited data indicates that TDS increases with depth at a given location," which raises the possibility that the deep arkosic zone could have suitably high salinity even at locations where uppermost Mt. Simon formation waters are USDWs, although site-specific data would be needed to evaluate this.
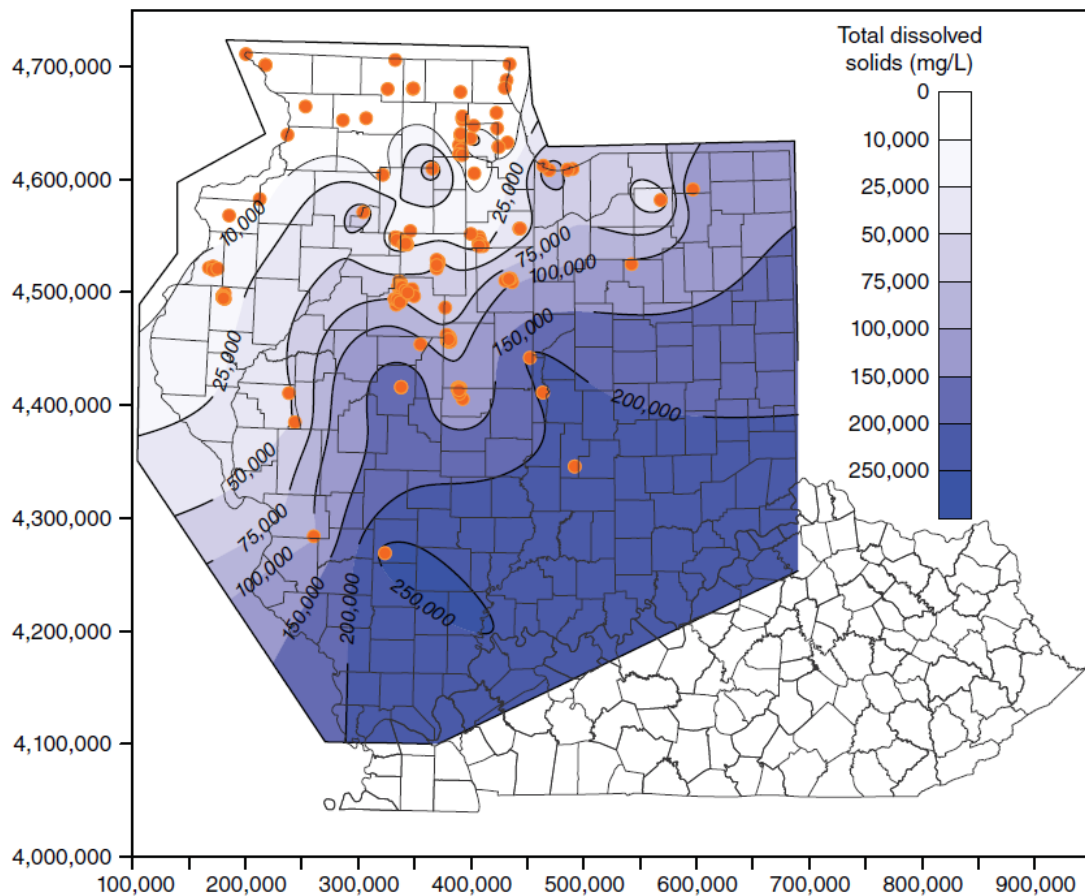
Figure 49: *Contour map of Mt. Simon Sandstone formation water salinity, from Mehnert and Weberling (2014; their Figure 8). The 10,000 mg/L TDS line from this map was adapted to a shapefile that was added to Figure 1 of this study.*

Fluid Samples from Wabash #1

Swab and Drill Stem Test (DST) samples were obtained from the Mt. Simon Sandstone in the Wabash #1 well during well testing operations. The sample analyses confirm the vertical variability of TDS concentrations as well as the high TDS concentration trends in the Mt. Simon Sandstone shown in the regional map (Figure 3) for the Vigo County, Indiana, area. The Wabash #1 fluid samples were analyzed for major, minor, and trace element composition using Ion Chromatography (IC) and Inductively Coupled Plasma-atomic Emission Spectrometry (ICP-ES) by the Illinois State Water Survey. TDS and pH values are presented below in Tables 2 and 3.

A DST performed in the Upper and Middle Mt. Simon (sample interval from 6,710 – 6,912 ft in depth) resulted in a TDS concentration of 154,460 mg/L. For the Lower Mt. Simon, TDS concentrations of 150,540 mg/L (swab sample from 7,976 – 7,996 ft) along with 169,700 mg/L and 168,490 mg/L (one DST sample from 7,696 – 8,121 ft, analyzed twice) were recorded. The deepest swab sample from beneath the basalt, obtained in the Mt. Simon/Argenta from 8,661 – 8,671 ft, yielded a TDS concentration of 270,890 mg/L.

OVERALL TRENDS

Figure 1 provides a quick-look evaluation of areas within the Illinois Basin in which the Mt. Simon Sandstone is potentially prospective for GCS as based on burial depth, overall thickness and salinity. This map does not necessarily address reservoir quality, and it must be noted that depositional and diagenetic features in the Mt. Simon Sandstone may be different across parts of the Basin (see Chapter 1).

The thickest Mt. Simon-Argenta deposits, which broadly correlate with thicker arkosic zone deposits, are found in east-central Illinois and west-central to southwestern Indiana. The thinnest deposits are found primarily in southwestern and far southern Illinois, where the Mt. Simon is less than 500 ft thick and is entirely absent locally due to nondeposition or erosion on buried Precambrian topographic highs; eastern Indiana also contains relatively thin deposits.

Formation depths of at least 2,500 to 3,000 ft (760-910 m) are necessary for subsurface storage of CO_2 in a supercritical state. Burial depth of the Mt. Simon becomes progressively shallower to the north, and in a large swath of northern Illinois and northwestern Indiana counties it is too shallow to retain CO_2 in a supercritical state, indicating GCS in the Mt. Simon in those areas is not favorable.

Salinity of less than 10,000 mg/L TDS in formation waters qualifies them as potential USDWs and therefore disqualifies them for GCS. Salinity within the Mt. Simon increases southward in the Illinois Basin and is well above 10,000 mg/L TDS in most of Illinois. Counties north of the light blue 10,000 mg/L TDS line in Figure 1 are unsuited for GCS based on salinity alone. This includes the six northernmost counties in the state, and partially or entirely excludes eight additional counties slightly farther south. It should also be noted that the exact placement of the 10,000 mg/L line contains uncertainty as it is based on relatively limited data but is representative of overall basin trends.

REFERENCES

Freiburg, J.T., Morse, D.G., Leetaru, H.E., Hoss, R.P., and Yan, Q. 2014. A Depositional and Diagenetic Characterization of the Mount Simon Sandstone at the Illinois Basin–Decatur Project Carbon Capture and Storage Site, Decatur, Illinois, USA. Illinois State Geological Survey, Prairie Research Institute, University of Illinois, *Circular 583*, 59 p.

Freiburg, J.T., Leetaru, H.E., and Monson, C.C. 2015. The Argenta Formation: a newly recognized Cambrian stratigraphic unit in the Illinois Basin. Geological Society of America, *Abstracts with Programs 47*, 86.

Mehnert, E., and Weberling, P.H., 2014. Groundwater Salinity Within the Mt. Simon Sandstone in Illinois and Indiana. *Illinois State Geological Survey Circular 582*, 23 p.

National Energy Technology Laboratory (NETL), 2015. *Carbon Storage Atlas*, 5th edition. Washington, D.C., 113 p.

TABLES

Table 1: *Well control data used for the combined Mt. Simon-Argenta thickness map, Figure 1.*

UWI/API	STATE	COUNTY	WELL NAME AND NUMBER	MT SIMON TOP (MD)	PRECAMBRIAN TOP (MD)	MS-PC THICKNESS (FT)	WELL TD (FT)	NOTES
120070027100	IL	Boone	E. Taylor 1	1325	2925	1600	2998	
120192399601	IL	Champaign	Hinton 7	3930	6550	2620	6550	PC top projected
120212565000	IL	Christian	T.R. McMillen 2	5130	6386	1256	7085	
120272454800	IL	Clinton	Hemminghaus Comm 1	6879	6883	4	7038	
120370067600	IL	De Kalb	E. Wyman 1	1720	3845	2125	4484	
120430101300	IL	Du Page	Rare Earth/Lindsay 1	1824	4021	2197	4043	
120510157200	IL	Fayette	Weaber-Horn Unit 1	6892	8314	1422	8616	
120552523100	IL	Franklin	Sugar Camp UIC 2	CONFIDENTIAL	CONFIDENTIAL	CONF.	CONF.	
120552523200	IL	Franklin	Sugar Camp UIC 1	CONFIDENTIAL	CONFIDENTIAL	CONF.	CONF.	
120650345000	IL	Hamilton	E. Cuppy 1	13012	13015	3	13051	
120710031700	IL	Henderson	Lillard 1	2420	3158	738	3138	TD=plugged back
120730036000	IL	Henry	E.A. South 1	2610	3855	1245	3863	
120910008000	IL	Kankakee	Schwark 7	2565	5185	2620	5003	PC top projected
120910040000	IL	Kankakee	Parish 1	2780	5045	2265	5045	
120973414200	IL	Lake	IL Beach State Park 1	1640	3460	1820	3500	
120990030000	IL	La Salle	A. Miller 1	1046	3469	2423	3659	
120990102600	IL	La Salle	Swensen 1	1152	3641	2489	3725	
120990103700	IL	La Salle	Mathesius 1	1421	3534	2113	3556	
120992317300	IL	La Salle	R. Goodwin 1	3584	5617	2033	5800	
121030018000	IL	Lee	J. McElroy 1	2070	3760	1690	3772	
121030027700	IL	Lee	Vedovell 1	1700	3465	1765	3653	
121052235900	IL	Livingston	Cullen 12	2200	4425	2225	4550	
121132294201	IL	Mc Lean	Furrow 11	3596	5792	2196	5938	
121152341500	IL	Macon	CCS 1	5544	7165	1621	7236	

121152346000	IL	Macon	VW 1	5522	7058	1536	7290	
121152355200	IL	Macon	VW 2	5529	7110	1581	7225	
121152371300	IL	Macon	CCS 2	5552	7164	1612	7193	
121190087601	IL	Madison	Kircheis 1-S	4991	5014	23	5019	
121190087702	IL	Madison	Klein S-2	5144	5205	58	5213	
121210519800	IL	Marion	Johnson 1	8450	9170	720	9210	
121310017200	IL	Mercer	Fullerton 1	2366	3250	884	3411	
121330002800	IL	Monroe	Theobald A-15	Absent	2750	0	2768	
121372213200	IL	Morgan	FutureGen 2.0	3854	4439	585	4830	
121452323400	IL	Perry	Poiter 1	Absent	6950	0	7057	
121452888200	IL	Perry	Shaglee 1	6007	6010	3	6062	
121490018900	IL	Pike	Campbell 1	2747	3205	458	3206	
121490020500	IL	Pike	Mumford	Absent	2221	0	2226	
121492102000	IL	Pike	Sleight 1	2986	3570	584	3602	
121550010400	IL	Putnam	Waste Disposal 1	3086	4842	1756	4877	
121632673500	IL	St Clair	Haas 1	3578	3915	337	4085	
121772131500	IL	Stephens	UPH-1	1166	1998	832	2096	
121772131600	IL	Stephens	UPH-2	1306	2173	867	5442	
121772131700	IL	Stephens	UPH-3	1230	2182	952	5272	
121892329000	IL	Washington	Bochantin Community 1	Absent	7296	0	7338	
121892433300	IL	Washington	Borowiak, Paul	8698	8704	6	9222	
121910773100	IL	Wayne	Cisne Comm	11156	11513	357	11614	
121970130300	IL	Will	McCoy	1913	4244	2331	4300	
122010064600	IL	Winnebago	Seele	1251	2656	1405	3385	
107208	IN	Lawrence	Brown	5491	6794	1303	6728	
126873	IN	Switzerland	Collins	3637	3974	337	4000	
133540	IN	Allen	Leuenberger	3127	3484	357	3672	
136060	IN	Fulton	Pfeil	2771	3912	1141	4056	
142098	IN	Lake	Inland Steel	2345	4333	1988	4363	
143816	IN	Marshall	Ames	3004	3900	896	4082	
144409	IN	Porter	WD-1	2762	4533	1771	4548	
144410	IN	Porter	Pfizer	2766	4480	1714	4528	
144458	IN	Porter	Bethlehem Steel WD-2C	2518	4265	1747	4301	

144461	IN	Porter	Midwest Steel	2486	4259	1773	4308	
147749	IN	Wabash	Hudson	2994	3654	660	3685	
159241	IN	Lake	Inland Steel	2352	4330	1978	4385	
133529	IN	Allen	Gibson	3132	3485	353	3517	
135895	IN	Elkhart	Hoskin Mfg.	3430	4109	679	4132	
144456	IN	Porter	Bethlehem Steel	2536	4263	1727	4304	
146918	IN	Steuben	Swager	4556	4895	339	6866	
159232	IN	Lagrange	L & R Inc.	4218	4670	452	4737	
159265	IN	Laporte	Criterion	2878	4164	1286	4300	
164778	IN	Knox	IGGC	7974	9877	1903	10050	
WABASH	IN	Vigo	Wabash	6277	8900	2623	8740	PC top projected
121	IA	Dubuque	City of Dubuque	950	1800	850	1810	
2603	IA	Clinton	DuPont	1875	3204	1329	3216	
26115	IA	Jackson	Green Island Strat	1440	2667	1227	2673	
16111000010000	KY	Jefferson	DuPont	5098	5993	895	6011	
1623329845	KY	Webster	Bell	13471	14280	809	14340	
21023380450000	MI	Branch	Arco & Gaglio	4764	5210	446	5378	
21091104480000	MI	Lenawee	H. Taylor 1	3611	3877	266	3902	
21149313350000	MI	St Joseph	L. Cupp	4466	5074	608	5283	
21163556620000	MI	Wayne	Sunoco	4170	4458	288	4579	
24028366	MO	Jefferson	Desoto	885	1295	410	1300	
2424236	MO	St Francois	Farmington Correctional	325	775	450	790	
488MC404	WI	Jefferson	Ft. Atkinson City Well	595	1060	465	1067	
48BF523	WI	Dane	City of Madison	230	725	495	729	
48BH424	WI	Waukesha	Village of Sussex	975	1285	310	1298	

Table 2: pH and TDS concentration ranges in Mt. Simon Sandstone swab samples taken from the Wabash #1 well. Sample interval range is based on measured depths, in feet. Analyses performed by the Illinois State Water Survey.

UWI	Sample ID	Sample Interval	Lab ID	Analyte	Value	Units	Analysis Date	Method
168045	S19 (WCP7 Lower Mt.Simon)	7976 - 7996	ISWS	pH	6.7	SU	7/10/2020	EPA150.1
				TDS	150540	mg/L	7/21/2020	SM2540
168045	S26 (WCP6 Mt.Simon/Argenta)	8661 - 8671	ISWS	pH	6.556	SU	7/10/2020	EPA150.1
				TDS	270890	mg/L	7/21/2020	SM2540

Table 3: pH and TDS concentration ranges in Mt.Simon Sandstone drill stem test (DST) samples taken from the Wabash #1 well. Sample interval range is based on measured depths, in feet. Analyses performed by the Illinois State Water Survey.

UWI	Sample ID	Sample Interval	Lab_ID	Analyte	Value	Units	Analysis Date	Method
168045	DST02A (WCP4 Upper-Middle Mt. Simon)	6710 - 6912	ISWS	pH	5.971	SU	2/17/2020	EPA150.1
				TDS	154460	mg/L	2/18/2020	SM2540
168045	DST01A (WCP1 Lower Mt.Simon)	7696 - 8121	ISWS	pH	6.161	SU	2/17/2020	EPA150.1
				TDS	169700	mg/L	2/18/2020	SM2540
168045	DST01B (WCP2 Lower Mt.Simon)	7696 - 8121	ISWS	pH	6.146	SU	2/17/2020	EPA150.1
				TDS	168490	mg/L	2/18/2020	SM2540

Chapter 6

Characterization of the Eau Claire Formation in Illinois and Southwest Indiana

By: Yaghoob Lasemi and Zohreh Askari

Illinois State Geological Survey, Prairie Research Institute, University of Illinois at Urbana-Champaign

STRATIGRAPHY AND FACIES

The Upper Cambrian Eau Claire Formation conformably overlies the Mt. Simon Sandstone; it underlies, with a transitional contact, the Galesvile Sandstone in the northern half of Illinois and the Davis Shale Member of the Franconia Formation in the southern part of the state (Figure 1). In Indiana, the Eau Claire is generally overlain conformably by the Galesville Sandstone or the Davis Formation, but in the southwestern part of the state it grades upward into the Potosi Dolomite (Shaver et al., 1986). In northern and western Illinois, the Eau Claire Formation consists mainly of dolomitic sandstone that is intercalated with siltstone, silty shale, and sandy/silty Dolomite and is subdivided (Buschbach, 1975) into Elmhurst Sandstone, Lombard Dolomite, and Proviso Siltstone Members (Figure 1).

The Eau Claire ranges in thickness from approximately less than 300 ft (90 m) in western Illinois to nearly 700 ft (213 m) in southwestern Indiana (Figure 2). It is more than 1,200 ft (300 m) in southern Illinois, reaching a maximum thickness of nearly 3,000 ft (914 m) in the Rough Creek Graben of western Kentucky (Sargent 1990; Lasemi and Askari, 2014a). The Eau Claire in the Wabash #1 well is around 900 ft (274 m) thick (Figure 3).

In central and eastern Illinois and in southwestern Indiana, however, the Eau Claire is predominantly dolomitic shale interbedded with siltstone, sandstone, oolitic limestone, and dolomite in which planar bedding with internal lamination and bioturbation are common (Figures 4 through 6). Similar lithology and sedimentary structures were also recognized in the Eau Claire Formation at the ADM Illinois Basin-Decatur Project area, Macon County, Illinois. The Eau Claire in southern Illinois and in southwestern Indiana consists mainly of dolomite and oolitic/fossiliferous limestone and includes a bed of shale, siltstone, and sandstone (Buschbach, 1975; Shaver et al., 1986). Fossiliferous lime mudstone-wackestone and packstone-grainstone facies have been recognized in the Eau Claire carbonates (Lasemi and Askari 2014a, b; Palkovic, 2015). These facies contain bioclasts, ooids, peloids, and intraclasts representing a carbonate platform, and the adjacent deeper marine settings are recognized (Lasemi and Askari, 2014a).

Figure 1*: Stratigraphic column of the Cambro-Ordovician Succession in southern Illinois (from Kolata, 2005) and southwestern Indiana (from Thompson et. al., 2016).*
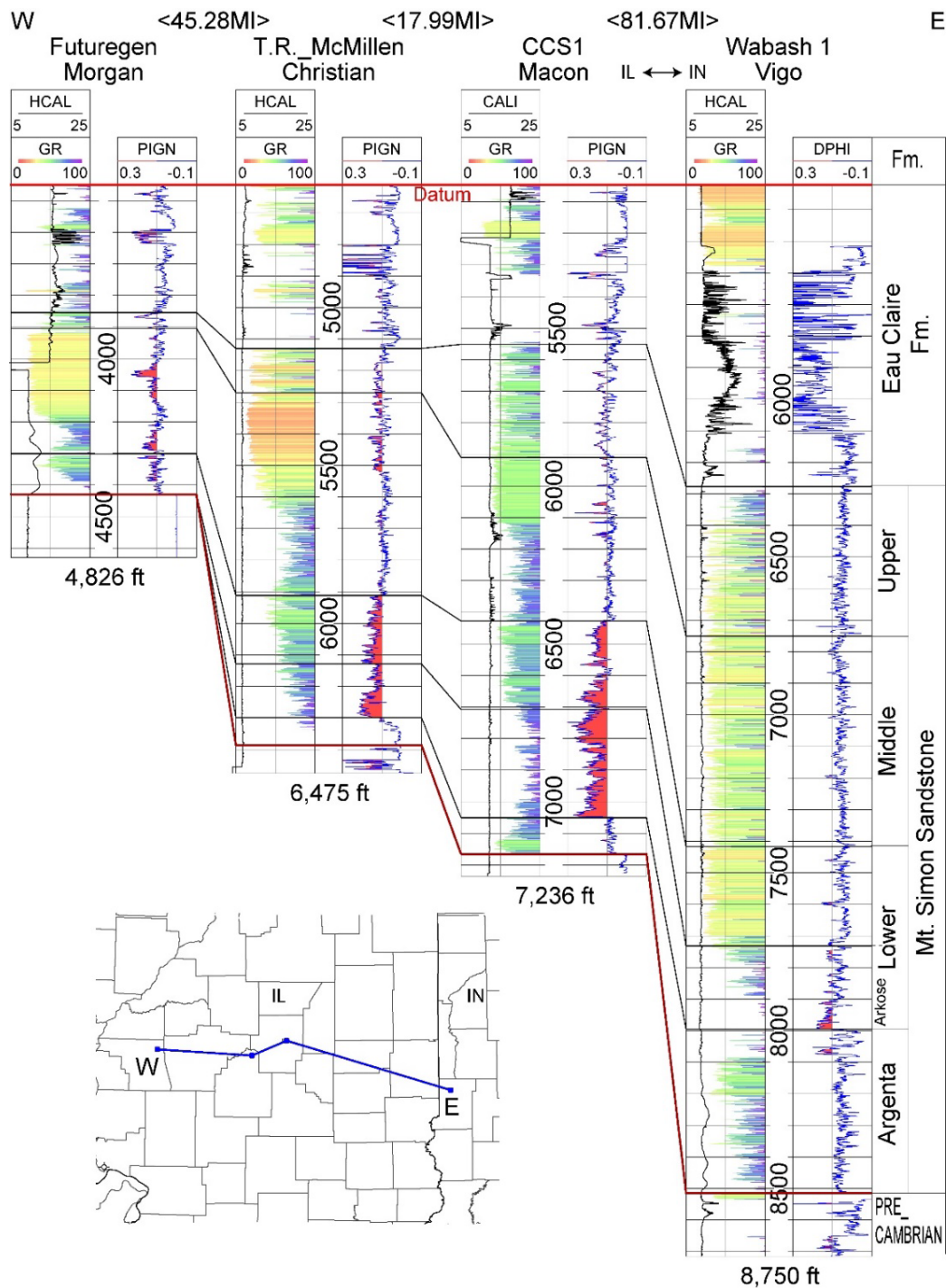
Figure 2: *Stratigraphic variability of the Eau Claire Formation and Mt. Simon Sandstone in a west-east transect from the FutureGen site in Morgan County, Illinois, to the Wabash #1 well in Vigo County, Indiana, showing the thickness variation of these units across the region.*
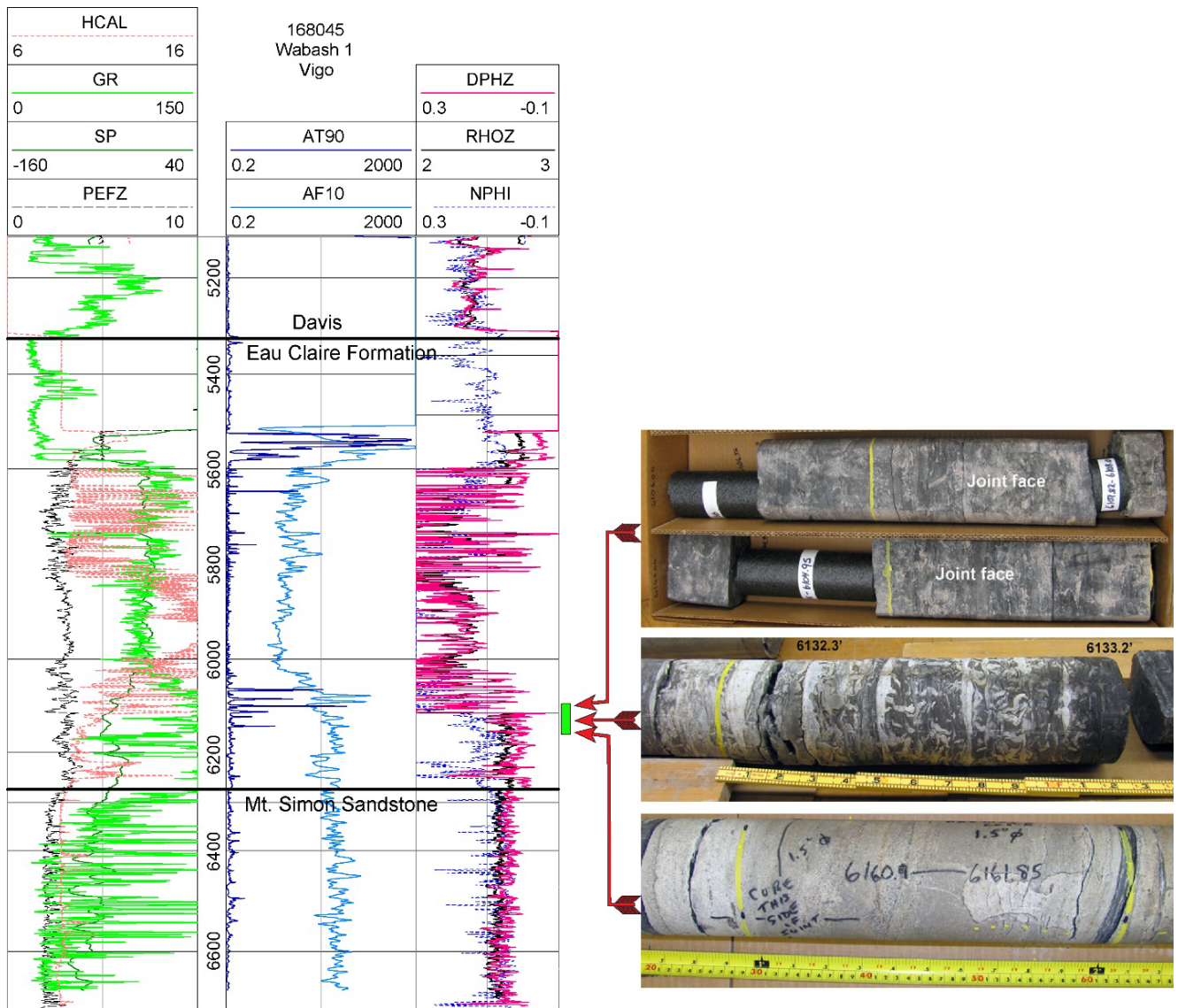
Figure 3: *Geophysical log signatures and photographs of the Eau Claire Formation in the Wabash #1 Well, Vigo County, Indiana. Note the interbedded sandstone, shale, and heavily bioturbated shale/siltstone in the lower part of the formation.*
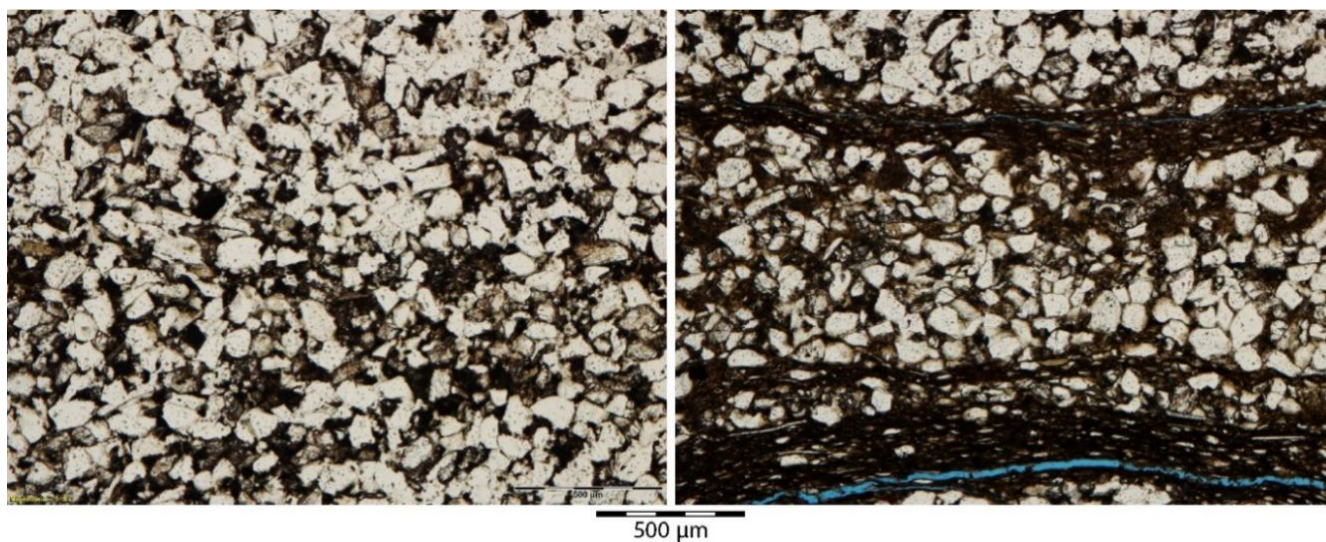
Figure 4: Thin section photographs of the lower part of the Eau Claire in the Wabash #1 well, Vigo County, Indiana. Note angular and sub-angular fine-grained sandstone (left) and interlaminated sandstone and shale in the right photograph (depth 6,186-6,187 ft).
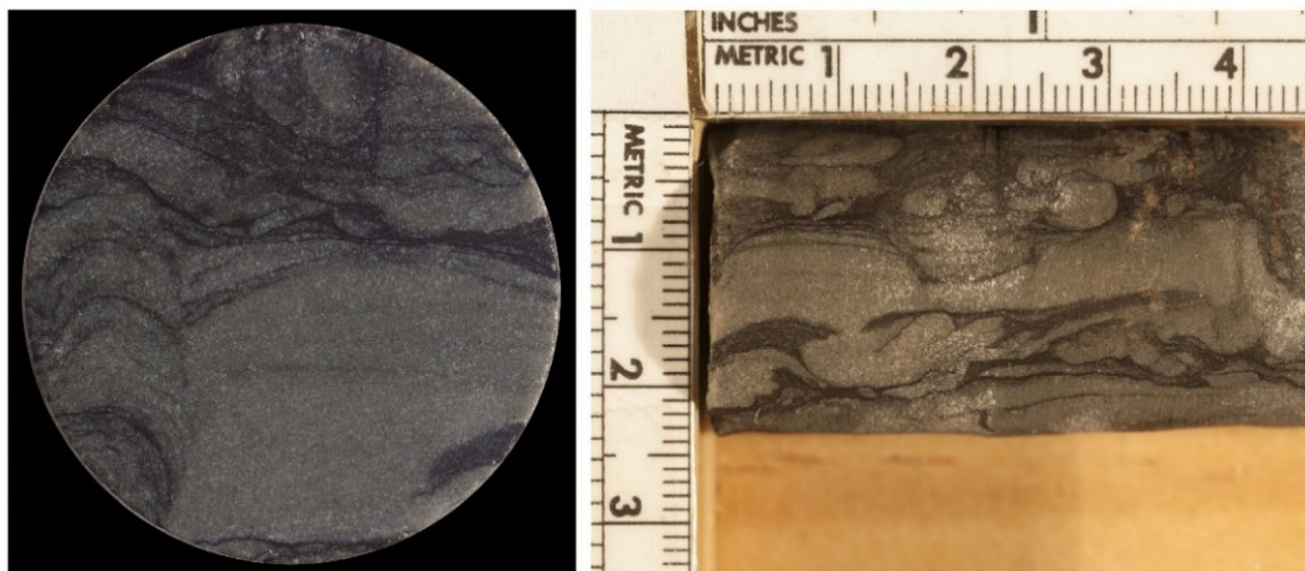
Figure 5: Core photographs of the Eau Claire Formation (depth 6,186 ft-6,187 ft) in the Wabash #1 well, Vigo County, Indiana, displaying a heavily bioturbated laminated siltstone.
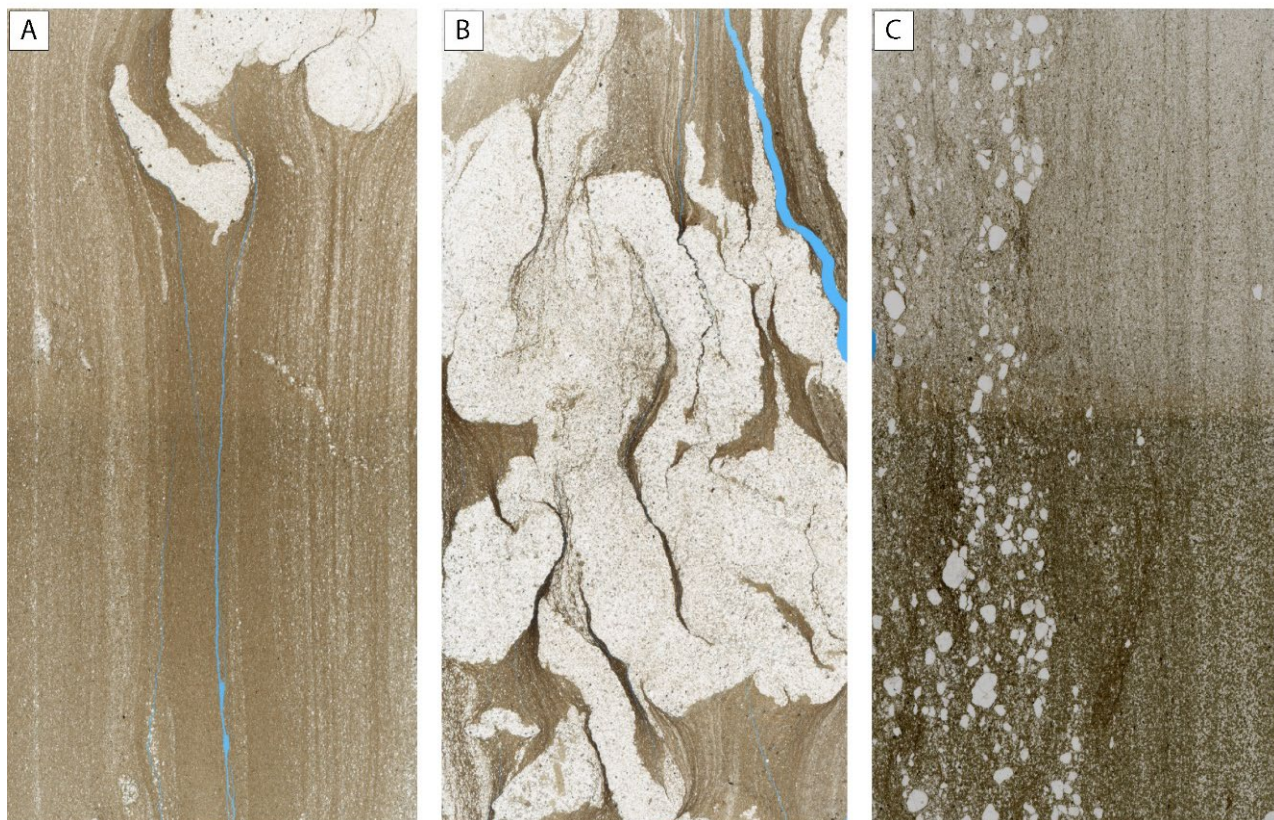
Figure 6*: Thin section photographs of dolomitic siltstone/shale from the core in the basal part of the Eau Claire Formation in Wabash #1 well, Vigo County, Indiana. (A) Heavily bioturbated dolomitic shale (depth 6,112 ft). (B) Laminated heavily bioturbated siltstone and dolomitic shale (depth 6,143 ft). (C) Interlaminated sandy and silty dolomitic shale (depth 6,159 ft).*

EAU CLAIRE SHALE

Shale constitutes the main part of the Eau Claire Formation and is very extensive in central and eastern parts of Illinois and in western Indiana (Figure 7). It is the primary seal and prevents upward migration of CO_2 and other fluids injected into the Mt. Simon Sandstone (e.g., Carroll et al., 2013). The integrity of the seal is an essential component of a storage system; therefore, investigating the characteristics of this stratigraphic unit is an essential step in determining the effective confinement of injected fluids (Lahamn, 2014). The thickness of shale and siltstone is important in determining the reliability of the seal for the underlying Mt. Simon Sandstone reservoir. To demonstrate the thickness of the shale in the Eau Claire Formation in Illinois and western Indiana, subsurface data, specifically borehole wireline logs and regional analyses from selected wells were used. Gamma ray log data signatures and the gamma ray log values of greater than 90 API were used to define the shaly intervals and to prepare the shale thickness map (Figure 7). This map suggests the eastward thickening of shale to more than 600 ft (182 m) in Wabash Well #1 and the surrounding areas.
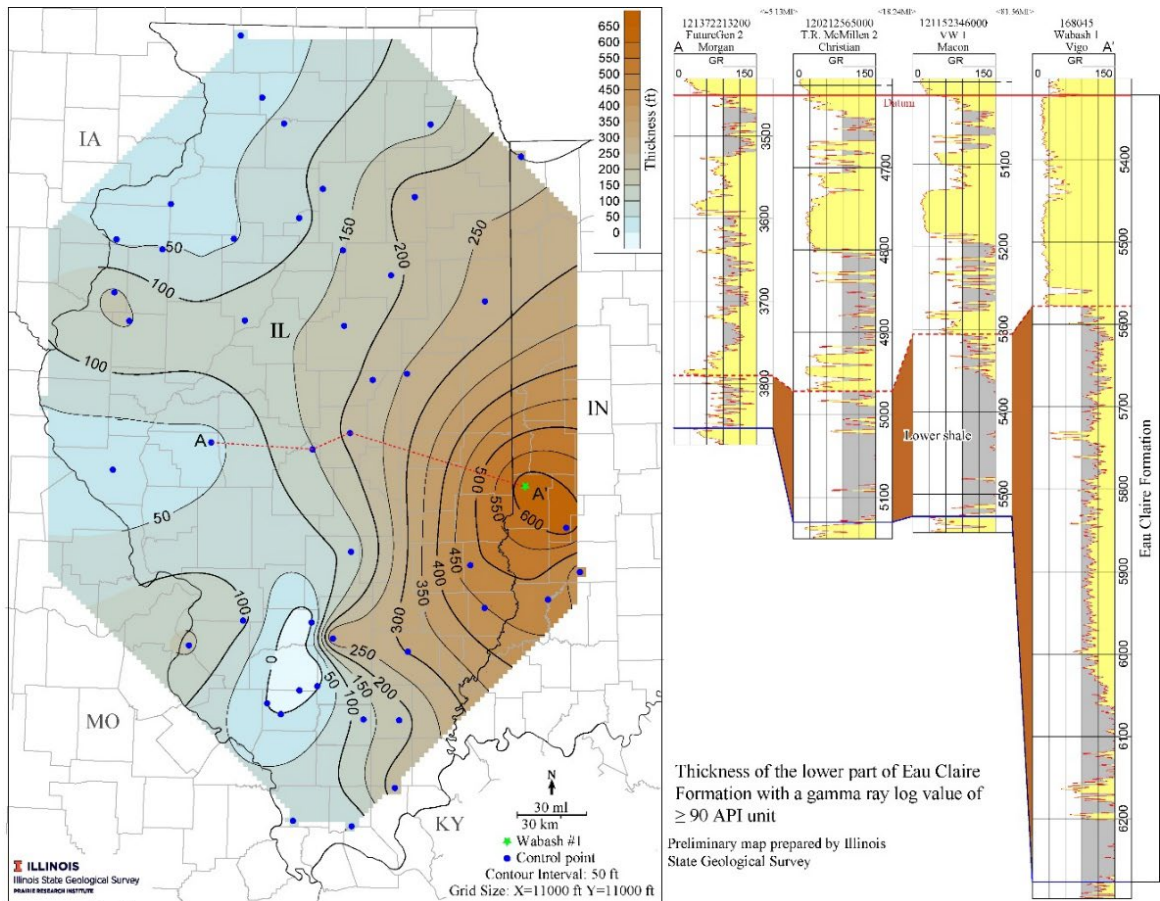
Figure 7: Thickness of the lower part of Eau Claire Formation with a gamma ray log value of ≥ 90 API unit. The index stratigraphic cross section from FutureGen #2, Morgan County, Illinois, to Wabash #1, Vigo County, Indiana, is shown to correlate the Eau Claire and the mapped interval.

REFERENCES

Carroll, S. A., McNab, W.W., Dai, Z., and Torres, S.C., 2013, Reactivity of Mount Simon Sandstone and the Eau Claire Shale under CO_2 storage conditions: *Environmental Science & Technology 47*, 252–261.

Buschbach, T. C., 1975, Cambrian system, in H. B. Willman, E. Atherton, T. C. Buschbach, C. Collinson, J. G. Frye, M. E. Hopkins, J. A. Lineback, and J. A. Simon, eds., Handbook of Illinois stratigraphy: *Illinois State Geological Survey Bulletin 95*, 34-46.

Kolata, D. R., 2005. Bedrock geology of Illinois. IGGS Illinois Map 14, 1:500,000.

Lahann, R., Rupp, J., and Medina, C., 2014. An evaluation of the seal capacity and CO_2 retention properties of the Eau Claire Formation (Cambrian). *Environmental Geosciences 21*, 83-106.

Lasemi, Y. and Askari, Z., 2014a. Sequence stratigraphy of the Cambrian Bonneterre Formation in the Illinois Basin: Implications for carbonate platform development and its evolution in southern Illinois and the adjacent Reelfoot-Rough Creek rift. *Geological Society of America North-Central Section Abstracts with Programs, 46*(4), 59.

Lasemi, Y., Askari, Z., 2014b. Stratigraphy of the Cambo-Ordovician Knox succession in Illinois. US DOE Knox Project Cooperative Agreement No. DE-FE0002068, Topical Report No. FE0002068-12, 43 p.

Palkovic, M. J., 2015. Depositional characterization of the Eau Claire Formation at the Illinois Basin – Decatur project: facies, mineralogy, and geochemistry. MS thesis, Department of Geology, University of Illinois at Urbana-Champaign, 84 p.

Sargent, M. L., 1990, Sauk Sequence: Cambrian System through Lower Ordovician Series. In M.W. Leighton, D.R. Kolata, D.F. Oltz, and J.J. Eidel, eds., Interior Cratonic Basins; Tulsa, Oklahoma, *AAPG Memoir 51*, 75-86.

Shaver, R. H., Ault, C. H., Burger, A. M., Carr, D. D., and others, 1986, Compendium of Paleozoic rock-unit stratigraphy in Indiana—a revision: *Indiana Geological Survey Bulletin 59*, 203 p.

Thompson, T. A., Sowder, K. H., and Johnson, M. R., 2016. Generalized stratigraphic column of Indiana bedrock. Indiana Geological Survey, Bloomington, Indiana.

Chapter 7

Seal Capacity

By: Donna Willette

Illinois State Geological Survey, Prairie Research Institute, University of Illinois at Urbana-Champaign

Mudstones and shale within the Eau Claire Formation and Maquoketa Group are considered caprocks to vertical CO_2 migration from the Mt. Simon Sandstone and Potosi Dolomite potential storage reservoirs at the Wabash CarbonSAFE project location. The Maquoketa is evaluated as a regional, secondary seal for the potential case of injection into the Mt. Simon sandstone; however, for potential injection into the Potosi Dolomite it would be considered a primary seal. The Wabash #1 well was drilled as a stratigraphic test to characterize and evaluate the Cambrian Mt. Simon Sandstone as a CO_2 storage reservoir, assess potential caprocks, and evaluate other prospective storage intervals. Similar to sandstones, the mineralogy and diagenetic alteration of shales can vary both vertically and horizontally within centimeters in the subsurface. This will induce rock properties such as porosity and permeability to fluctuate, sometimes by a couple orders of magnitude.

Recent characterization of the Maquoketa Shale as a regional seal interval uses a lithofacies model to define three main zones (upper, middle, and lower) consisting of five distinct lithologies (Medina et al., 2020).The upper zone of the Maquoketa is dominated by dolomitic, calcareous, and silty shale; the middle zone is dominated by limestone and argillaceous limestone; and the lower zone is dominated by dolomitic and calcareous shale, and occasionally contains minor amounts of argillaceous limestone and silty shale. In the Wabash #1 well, the Maquoketa Group is 314 ft (96 m) thick and is composed of dominantly interbedded shale with thin argillaceous layers in the upper zone with increasing limestone and argillaceous limestone in the middle–lower interval. Core taken in the Maquoketa Shale from the Wabash #1 well indicates a thinly laminated shale lithology with mm-scale carbonate laminations present in the lower section. In contrast, core recovered from the Eau Claire consists of alternating beds of shale and fine-grained sandstone, with thin interlaminated and deformed siltstone/shale, and thinly bedded carbonate. The Eau Claire Formation has been described in detail earlier in this report.

Depending upon where samples are taken in the Eau Claire (and portions of the Maquoketa), the analytical results will only characterize a limited portion of a heterogenous caprock. Prior to interpreting the mercury injection capillary-pressure (MICP) results, it is beneficial to calculate a relative range of seal capacity (column heights) as this may reflect the lithology range within the caprock. A first approximation of the sealing capacity (column height of supercritical (sc) CO_2 that the caprocks can retain before leakage occurs) of these caprocks can be evaluated using permeability estimates, which span the range of values calculated from petrophysical analyses. This evaluation is determined from previous experimental research in which statistically

significant relationships between air permeability (md) and air threshold pressure (psi) are evident (Li, et al., 2005; Dewhurst et al., 2002).

The correlation between $scCO_2$ threshold pressure (psi) and N_2 threshold pressure (psi) is key to approximating the sealing capacity to $scCO_2$. Mean pressure given in relation to $scCO_2$ is 42.7% of that measured in relation to air or N_2. Using Equation (1), the relation is:

(1) $P_{tscCO2} = [(0.427 \text{ x } (e^{3.02} \text{ x } k_{seal}^{-0.434})]$

      where P_{tscCO2} is the threshold pressure in psi and k_{seal} is permeability in millidarcys (md).

Substitution of Equation (1) into the standard evaluation of column height (2), or the height of a hydrocarbon or $scCO_2$ column the seal can hold before breakthrough, is as follows (Daniel and Kaldi, 2008):

(2) $h_{scCO2} \text{ max} = \dfrac{[0.427 \text{ x } (e^{3.02} \text{ x } k_{seal}^{-0.434})] - [(e^{3.02} \text{ x } k_{res}^{-0.434})]}{[(\rho_f - \rho_{scCO2}) \text{ x } 0.433]}$

      where $\underline{k_{seal}}$ is seal permeability (md), $\underline{k_{res}}$ is reservoir permeability (md), ρ_f is density of the reservoir brine, and ρ_{scCO2} is density of $scCO_2$ at reservoir temperature and pressure.

A range of permeability values for each caprock interval was calculated using temperature, pressure, and density values determined from the Wabash #1 well data. Table 1 lists the calculated brine density (ρ_f) and $scCO_2$ density (ρ_{scCO2}): Maquoketa Shale ($\rho_f = 1.03$ g/cc and $\rho_{scCO2} = 0.72$ g/cc) and Eau Claire Shale ($\rho_f = 1.10$ g/cc and $\rho_{scCO2} = 0.75$ g/cc).

Theoretical $scCO_2$ column heights across a range of permeabilities were determined for the Maquoketa and Eau Claire Shales (Figure 1). In the case of the Maquoketa Shale, a comparison with data derived from a Phase 2 CO_2 Injection well located in central Kentucky (Blan #1) was used to further assess the potential sealing capacity. For this comparison, the density ($\rho_f = 1.05$ g/cc and $\rho_{scCO2} = 0.80$ g/cc) values were input to the formulation (Bowersox, 2013). Column heights derived for the Wabash and Blan wells are very similar and range between 185 ft–4,400 ft for permeability values between 10^{-2} and 10^{-4} md. Primarily based upon the difference in reservoir fluid and CO_2 densities, this first approximation indicates that seal capacity of the Eau Claire Shale is less than the Maquoketa Shale relative to the same range of caprock permeabilities (10^{-2} to 10^{-4}). Derived seal capacity estimates for the Eau Claire Shale (161 ft–3,140 ft) indicate a reduced capacity to hold a CO_2 column relative to the Maquoketa Shale. However, these theoretical sealing capacity estimates shown in Figure 1 also indicate that both primary caprocks in the Wabash #1 well will hold $scCO_2$ column heights greater than the projected reservoir thicknesses in the Mt. Simon and Potosi storage intervals. These are theoretical estimates that will be compared to point-source MICP analyses. It is important to note that MICP analytical results only constrain a snapshot of a limited lithological representation of the caprock interval.

Detailed MICP data was used to create a range of minimum to maximum $scCO_2$ column heights based upon a distribution of CO_2 contact angles and Hg/air threshold pressures. This will provide insight into seal capacity and leakage potential. Generally, prior to 2006, $scCO_2$/water/rock

interface in the sub-surface was assumed to have a contact angle (θ) of 0°, as water was thought to be the wetting phase (Daniel and Kaldi, 2008). More recent experimental studies using quartz, mica, and clay substrates with scCO$_2$ immersed in brine indicate that these substrates become less water-wet in the presence of scCO$_2$, i.e., contact angles (CA) varying from 0° to 40° (Sarmadivaleh, et al., 2015). An increase in contact angle becomes more pronounced at higher pressures up to 20 mPa, ranging from 30° to 60°. Various researchers only use a CA of 60° for scCO$_2$ evaluation purposes of membrane capillary behavior as this produces the most conservative estimate of sealing capacity and column height. For the purposes of this study, a range of column heights was calculated using a contact angle of 0°, 20°, 40°, and 60° to bracket the wettability uncertainty. In addition, based upon the sample MICP entry pressure (Hg/air), the threshold pressure of the CO$_2$/brine system was modified by 20% (either low or high) to capture some of the variability in pore volume and permeability of changing caprock composition and resultant diagenesis. This allowed a maximum/minimum comparison of column heights relative to the data derived from the sample. Variability of capillary pressure using a range of contact angles follows the wettability transformation from an air/mercury system to brine equation (after Schowalter 1979):

(1) $P_{b/CO2} = P_{a/m} (\sigma_{b/CO2} \cos\theta_{b/CO2}) / (\sigma_{a/m} \cos\theta_{a/m})$

Where $P_{b/CO2}$ is the capillary pressure in the brine/CO$_2$ system, $P_{a/m}$ is the capillary pressure in the air/mercury system, $\sigma_{b/CO2}$ and $\sigma_{a/m}$ are the interfacial tensions of the brine/CO$_2$ and the air/mercury systems respectively, $\theta_{b/CO2}$ and $\theta_{a/m}$ are the contact angles of the brine/CO$_2$/substrate and air/mercury/substrate systems respectively.

Calculation of the column height uses the standard equation:

(2) h_{scCO2} max $= (Pth_s - Pth_r) / (\rho_f - \rho_{scCO2})*0.433$

where Pth_s is the entry pressure of the seal in the scCO$_2$/brine system, Pth_r is the entry pressure of the reservoir in the scCO$_2$/brine system, $\rho_f - \rho_{scCO2}$ is the density difference of the brine and scCO$_2$, 0.433 is the normal hydrostatic gradient of water in psi/ft, and h_{scCO2} max is the maximum column height or caprock capacity (Daniel and Kaldi, 2008).

The interfacial tension (IFT) used in the Hg/air to brine/CO$_2$ conversion for each sample is listed in Table 1 and is based upon studies indicating that it typically ranges between 21–27 dynes/cm under scCO$_2$ conditions (Espinoza, et al., 2010).

Column height calculations from point-specific MICP analyses are at least an order of magnitude less than the theoretical calculations spanning ranges of permeability values. Table 2 lists the ranges for column heights calculated for all caprock samples in which MICP analyses were run. Similar to the first approximation results, the seal capacity of the Maquoketa Shale is significantly higher than the Eau Claire Shale caprock. The Maquoketa Shale may support columns ranging between 1,891 ft–2,844 ft (576–867m) using a contact angle of 0°, which is approximately three times larger than column heights calculated for the Eau Clair Shale. As the table indicates, larger contact angles of the scCO$_2$/water/rock interface result in diminished caprock column capacity. In general, as the contact

angle increases to 60°, the amount of column the caprock can seal before breakthrough is reduced by approximately one-half. Since the pressure at sample depth for the Eau Claire is approximately 2,671.15 psi (18.42 mPa), it is likely that estimates derived from CA between 40°–60° is reasonable. Therefore, the calculated minimum seal capacity for the Eau Claire would range between 342 ft–525 ft (104 m–160 m) relative to the underlying Mt. Simon Formation (Table 2). However, Wabash CarbonSAFE reservoir characterization (discussed earlier in this report) and modeling (discussed in Dessenberger et al., 2022) concluded that due to diminished storage rock properties (porosity and permeability), the Mt. Simon is unlikely to be utilized as the primary $scCO_2$ storage interval. While the Eau Claire is a viable caprock at the Wabash CarbonSAFE project location, it is expected that it will not be utilized as a caprock for an underlying reservoir at this location.

Petrophysical/lithological characterization and reservoir modeling indicate that the Cambrian Potosi Dolomite is a viable $scCO_2$ storage reservoir at the Wabash CarbonSAFE project location (discussed in Khosravi et al., 2022 and Dessenberger et al., 2022). Therefore, the Maquoketa Shale is the primary caprock to vertical/lateral migration of $scCO_2$ given a significant thickness of carbonate separates the Maquoketa Shale from the Potosi Dolomite. As formation pressure of the Maquoketa Shale is 1,080 psi (7.45 mPa) at the Wabash #1 well, which is approximately half the formation pressure of the Eau Claire Shale, it is reasonable to assume a CA range between 0° and 40°. Given that range, the minimum sealing capacity based upon membrane capillary behavior is between 1,449 ft–1891 ft (442 m–576 m) and indicates that the Maquoketa is an effective caprock to $scCO_2$ migration (Table 2).

The efficacy of the caprock to prevent CO_2 vertical movement depends not only on capillary behavior, but also seal integrity which is a function of geomechanical properties and the degree of fracturing present in the rock. Geological characterization and geomechanical testing of Maquoketa Shale samples from the Wabash #1 well highlight the Maquoketa's sealing characteristics (discussed in Khosravi et al., 2022). The Formation Micro Imager (FMI) log and Maquoketa core from the Wabash #1 well show little to no natural fractures within the Maquoketa interval. Triaxial test results (Table 3) show the Maquoketa to have a high Young's modulus (suggesting very stiff rock and not easily deformable), and that it has high cohesive and uniaxial compressive strength (UCS), suggesting it will require very high injection pressures to induce a failure in the formation. The Eau Claire shale sample from Wabash #1 has UCS (Table 3) comparable to the Eau Claire shale that was tested from the Illinois Basin – Decatur Project (IBDP) well; the Eau Claire has been used as a primary seal for CO_2 injection at the IBDP project site and at natural gas storage fields in central Illinois Basin. While geomechanical characteristics indicate a viable caprock at this location, heterogeneity in the Wabash #1 silty-shale sample produces a range of Young's modulus values. The maximum recorded value is ~102 MPa, suggesting the Eau Claire is likely stiffer and less ductile in some layers compared to the Maquoketa. In summary, the core test results from the Wabash #1 well indicate the Maquoketa exhibits geomechanical characteristics of a good seal, and both the theoretical approximations and detailed MICP data indicate that the Maquoketa Shale is an effective caprock to $scCO_2$ migration. While the seal capacity of the Eau Claire Shale is lower than the Maquoketa Shale, it is also a viable caprock at this location.

REFERENCES

Bowersox, J.R., 2013. Evaluation of Phase 2 CO_2 Injection Testing in the Deep Saline Gunter Sandstone Reservoir (Cambrian-Ordovician Knox Group), Marvin Blan No.1 Well, Hancock County, Kentucky. Contract Report 53, Series XII. Kentucky Geological Survey, University of Kentucky, Lexington.

Daniel, R.F., and J.G., Kaldi, 2008. Evaluating seal capacity of caprocks and intraformational barriers for the geosequestration of CO_2. Paper-PESA Eastern Australian Basin Symposium III, Sydney, 14-17.

Dessenberger, Richard, Roland Okwen, Mansour Khosravi, Scott Frailey, James Damico, and Carl Carman, 2022, Wabash CarbonSAFE Static and Dynamic Modeling – Task 9.0, Technical Report: DOE-FE0031626-8. U.S Department of Energy.

Dewhurst, D.N., Jones, R.M., and M.D. Raven, 2002. Microstructural and petrophysical characterization of Muderong Shale: Application to top seal risking: *Petroleum GeoScience 8*, 371-383.

Espinoza, D.N. and Santamarina, J.C., 2010. Water-CO_2 mineral systems – Interfacial tension, contact angle, and diffusion. Implications to CO_2 geological storage. *Water Resources Research 46*, WO7537.

Khosravi, M., Yaghoob L., Askari Z., Leetaru, H., Frailey, S., Babarinde, O., Willette, D., Blakley, C., Monson, C., Carman, C., Whittaker, S., and Korose, C. 2022 (antic.), Wabash CarbonSAFE, Geologic Analysis of the Potosi Dolomite Reservoir Interval and Potential Confining Units – Subtask 7.2, Technical Report for DOE-FE0031626. U.S Department of Energy.

Li, S., Dong, M., Li, Z., Huang, H., Qing, H., and E. Nickel, 2005. Gas break-through pressure for hydrocarbon reservoir seal rocks: Implications for the security of long-term CO_2 storage in the Weyburn Field: *Geofluids 5*, 326-334.

Liu, F., Lu, P., Griffith, C., Hedges, S. W., Soong, Y., Hellevang, H., and Zhu, C., 2012. CO_2–brine–caprock interaction: reactivity experiments on Eau Claire shale and a review of relevant literature. *International Journal of Greenhouse Gas Control 7*, 153-167.

Medina, C., Mastalerz, M., Lahann, R., and Rupp, J., 2020. A novel multi-technique approach used in the petrophysical characterization of the Maquoketa Group (Ordovician) in the southeastern portion of the Illinois Basin: Implications for seal efficiency for the geologic

sequestration of CO_2. *International Journal of Greenhouse Gas Control 93*. 10.1016/j.ijggc.2019.102883.

Sarmadivaleh, A., Al-Yaseri, Z, and Iglauer, S., 2015. Influence of Temperature and Pressure on quartz=water-CO_2 contact angle and CO_2-water interfacial tension. *Journal of Colloid and Interface Science 441*, 59-64.

Schowalter, T.T., 1979. Mechanics of secondary hydrocarbon migration and entrapment. AAPG Bulletin, 63, pp. 723-760.

FIGURES AND TABLES

Table 1: *Rock and fluid properties for caprock samples taken at Wabash #1. Includes pressure, temperature, and salinity data for the selected samples, threshold pressures measured from MICP analyses, and calculated brine and CO_2 densities. Also lists interfacial tension and contact angles used in seal capacity calculations.*

Formation Name (sample)	Depth of sample (m) TVDSS	Pressure at sample depth (psi) (mPa)	Temp. at sample depth (°F) (°C)	Salinity at sample depth (ppm) (mg/l)	CO_2 density (g/cm^3)	Brine density (g/cm^3)	Interfacial tension (mN/m or dynes/cm)	Contact angle (°)	Seal threshold pressure (air-Hg) psia	Reservoir threshold pressure (air-Hg) psia
Maquoketa	760.0	1,080.0 7.45	83.0 28.33	35,000[1]	0.72	1.03	25	0- 60	10,824	30
Eau Claire Shale	1,880.2	2,671.15 18.42	120.0 48.89	150,000[2]	0.75	1.10	26	0 - 60	4,252	30

1. Salinity constrained by swab fluid collected from the Potosi Dolomite
2. Salinity constrained by regional salinity trends in the Mt. Simon
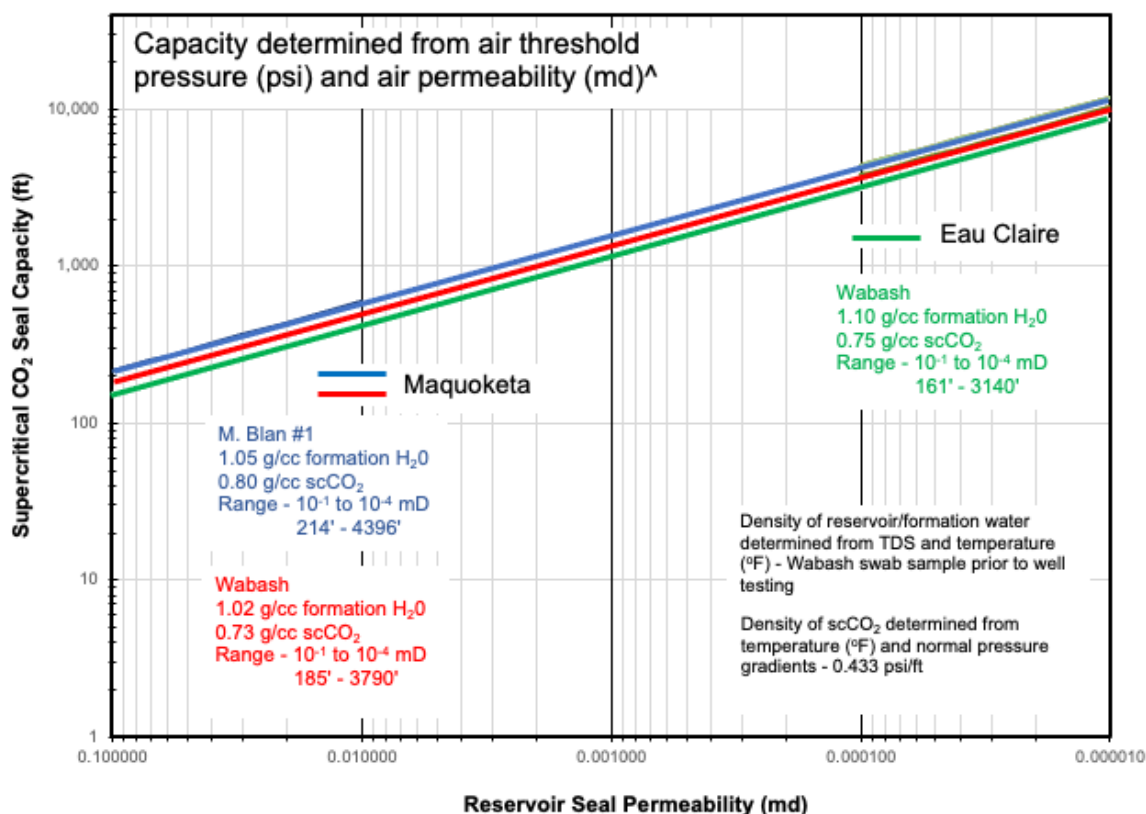
Figure 1: *An approximation of seal capacity (column heights) based upon a range of permeability values constrained by petrophysical analyses for the Maquoketa Shale and Eau Claire Shale (after Li et al., 2005).*

Table 2: *Calculated minimum, sample value, and maximum scCO₂ column heights relative to caprock capacity based upon MICP analyses of one sample from the Maquoketa Shale and Eau Claire Shale. The variability in the column heights was calculated using a range of contact angles (CA) and threshold pressures (20% variability relative to sample value).*

Formation	CO₂ Column Height ft. (m) @ CA 0º	CO₂ Column Height ft. (m) @ CA 20º	CO₂ Column Height ft. (m) @ CA 40º	CO₂ Column Height ft. (m) @ CA 60º
	min – sample - max	min – sample - max	min – sample - max	min – sample - max
Maquoketa	1,891(576) – 2,365 (721) – 2,844 (867)	1,777 (542) – 2,223 (678) – 2,673 (815)	1,449 (442) – 1,812 (552) – 2,179 (664)	946(288) – 1,183 (361) – 1,422 (433)
Eau Claire Shale	685 (209) – 856 (261) – 1,028 (313)	643 (196) – 805 (245) – 966 (294)	525 (160) – 656 (200) – 787 (240)	342 (104) – 428 (130) – 514 (157)

Table 3: *Measured parameters from triaxial tests and ultrasonic measurements in the Maquoketa Group, Wabash #1 well.*

Formation	Petrophysical properties	Static elastic properties				
Seal	ρ (g/cc)	E (GPa)	υ	UCS (MPa)	C_0 (Mpa)	φ (°)
Maquoketa	2.61-2.71	42-46	0.23-0.3	180	51.8	30
Eau Claire	2.59-2.7	5-102	0.03-0.62	76	22	30

(ρ) = Density, (ϕ) = angle of internal friction, (C_0) = cohesive or shear strength, (E) = static Young's modulus, (υ) = static Poisson's ratio, (UCS) = uniaxial or unconfined compressive rock strength.

Geomechanical Testing and Analysis of the Maquoketa Group, Eau Claire Formation, and Mt. Simon Sandstone

By: Oladipupo Babarinde and Chris Korose

Illinois State Geological Survey, Prairie Research Institute, University of Illinois at Urbana-Champaign

GEOMECHANICAL TESTING AND ANALYSIS

Sample Collection and Preparation

Geomechanical testing of the Maquoketa Group, Eau Claire Formation, and Mt. Simon Sandstone samples was performed in September 2020 on wax-preserved core samples obtained from the Wabash #1 well.

At the Wabash #1 well, the Maquoketa Group is ~315 ft (96 m) thick and occurs from 2,386 to 2,700 ft (727 to 823 m) in depth. A 61 ft (18.6 m) interval was cored (3-1/2 inch [9 cm] diameter) from 2,435 to 2,496 ft (742 to 761 m) in depth. A 2 ft (0.6 m) section of core from 2,446.92 to 2,448.45 ft (745.82 to 746.29 m) was preserved in wax.

The Eau Claire Formation is 955 ft (291 m) thick in Wabash #1 and is present from 5,322 to 6,277 ft (1,622 to 1,913 m) in depth. A 66.4 ft (20.2 m) interval was cored (4 inch [10 cm] diameter) in the lower silty-shale portion of the Eau Claire, and a 0.94 ft (0.29 m) wax-preserved sample from 6,132.25 to 6,133.19 ft (1,869.11 to 1,869.396 m) best representative of the entire cored interval was used for geomechanical testing.

The Mt. Simon Sandstone occurs at depths below 6,277 to 8,085 ft (1,319 to 2,464 m), with the Argenta sandstone and/or unidentified sandstone occurring from approximately 8,085 ft (1,319 m) to the well's total depth (TD) of 8,739 ft (2,664 m)—exclusive of a 20 ft (6 m) basalt layer encountered from 8,515 to 8,535 (2,595 to 2,601 m). A 118.9 ft (36.2 m) Mt. Simon interval was cored (4 inch [10 cm] diameter) in the arkose unit from 7,900 to 8,018.9 (2,408 to 2,444.2 m); wax-preserved samples from 7,913 to 7,913.75 ft (2,411.9 to 2,412.11 m), and from 7,913.75 to 7,914.45 ft (2,412.11 to 2,412.32 m), with lengths of 0.75 ft and 0.70 ft (0.23 and 0.21 m), respectively, were used for geomechanical testing.

Identification of Fractures

As described separately in Khosravi et al. (2022), drilling- and handling-induced fractures have been observed in the Maquoketa Group core obtained from Wabash #1, although examination of the intermediate-section Formation Micro Imager (FMI) log shows the Maquoketa Group interval overall to have no significant natural fractures, drilling-induced tensile fractures (DITFs), or wellbore breakouts (WBOs).

Prominent subvertical jointing was observed in Eau Claire Formation core in the Wabash #1 well by Bauer (2020), and the joints were found to be intact or separated, and mostly unfilled, along

much of the core. Mt. Simon Sandstone core from Wabash #1 described by Freiburg (2020) noted occasional near-vertical to high-angle natural fractures, some open but mostly mineral-filled with non-calcareous white cement or, less commonly, calcite. Table 1 shows that examination of the Wabash #1 TD-section FMI log corroborates natural fractures observed in Eau Claire and Mt. Simon core, and beyond the cored intervals from the lower Eau Claire shale below 5,575 ft (1,699 m) through the Mt. Simon and underlying basalt through 8,535 ft (2,601 m).

Table 1: *Summary of observed sedimentary and structural (joints/natural fractures) features observed on formation micro-imaging log*

Formation unit (Depth, ft)	Sedimentary structures and natural joints/fractures observed on FMI
Eau Claire shale (5,575–6,277)	• Presence of lithobound natural fractures around 5,590' • Presence of fractured zone/deformed slump around 5,733'; 5,738'; 5,800'; 6,014 – 6,100'; 6,100 – 6,200' • Bedding direction is generally multi-directional. However, stronger WSW and ESE bed boundary and cross-bedding orientation is observed within the Eau Claire shale interval
Mt. Simon Sandstone (6,277–8,515)	• Cross bedding feature observed around 6,324'; 6,362'; 6,380'; 6,418'; 6,466'; 6,483'; 6,517'; 6,583'; 6,606'; 6,952'; 7,109'; 7,176'; 7,207'. Low dip < 25 degrees • Presence of possible lithobound natural fractures/ditfs around 6,300 – 6,325' • Strong indication of lithobound natural fractures around 6,418'; 6,453'; 6,466'; 6,558'; 6,993'; 7,208'; 7,836' • Presence of continuous natural fractures around 6,474'; 6,490'; 6,515'; 6,527'; 6,597'; 6,612'; 6,619'; 6,626'; 6,727'; 6,739'; 6,757 – 6,906'; 6,964'; 7,055'; 7,146'; 7,236'; 7,364 – 7,592'; 7,617 – 7,693'; 7,928' • Bedding direction is generally multi-directional. However, stronger WNW, WSW, and ESE orientation of bed boundary and cross-bedding is observed within the Mt. Simon Sandstone interval
Basalt, Cambrian (8,515–8,535)	• Presence of continuous natural fractures around 8,516 – 8,533'
Mt. Simon Sandstone/Argenta (8,535-8,739)	• Indication of cross-beddings

Testing Procedure

For geomechanical testing, the waxed-preserved core samples detailed above were sent to Schlumberger's Reservoir Laboratory (SRL), where three vertical core plugs, one horizontal plug, and one inclined plug (oriented 45-degrees to horizontal) were prepared. Triaxial compressive strength tests and ultrasonic velocity measurements were conducted on the Maquoketa Group, Eau Claire Formation, and Mt. Simon Sandstone core plug samples to determine elastic (dynamic and static) and petrophysical characteristics. The tests were conducted on the Maquoketa under confining pressures of S3 = 675; 1,350; and 2,025 psi (Table 5; ~4.6, ~9.3, and ~14.0 MPa), and on the Eau Claire shale and Mt. Simon Sandstone under confining pressures of S3 = 2,000; 4,000; and 6,000 psi (Table 2; ~14, ~28, and ~41 MPa). Results from the tests were interpreted based on Mohr-Coulomb failure criteria.

Table 8: *Confining pressures used for testing at Schlumberger Reservoir Laboratory.*

Formation	Sample depth (ft)	TZSG (psi/ft)	TXSG_ANISO (psi/ft)	PPG (psi/ft)	MES (psi)	MES x 0.5 (psi)	MES x 1.5 (psi)
Maquoketa	~2,447.25	1.100	0.743	0.430	1,350	675	2,025
Eau Claire shale	~6,132	1.100	0.757	0.462	4,000	2,000	6,000
Mt. Simon Sandstone	~7,913	1.100	0.632	0.468	4,000	2,000	6,000

* TZSG = vertical stress gradient; TXSG = horizontal stress gradient; PPG = Pore pressure gradient; MES = Mean effective stress.

Rock Strength of the Maquoketa Group

Uniaxial or unconfined compressive rock strength (UCS) of ~26,000 psi (~180 MPa) for the Maquoketa Group was extrapolated (based on triaxial testing of five cores) from the best-fit line to the relationship between σ3 and resulting yield strength (Figure 1; Zoback, 2007). The slope (i.e., m = 3) of the best-fit line is used to determine a coefficient of internal friction (μ_i) of ~0.58, an angle of internal friction (ϕ) of 30° and a cohesive or shear strength (C_0) of ~7,514 psi (~52 MPa). Measurements of compressional velocities (V_p), shear velocities (V_s), dynamic and static Young's modulus (E), and dynamic and static Poisson's ratio (υ) are presented in Table 3. Elastic properties which typically correlate with UCS show nearly consistent values at this depth (Figures 2 and 3).

The triaxial test results show the Maquoketa to have a high Young's modulus (~42 – 46 GPa), suggesting very stiff rock. In addition, it has high UCS (~180 MPa) compared to the Eau Claire shale UCS value (~76 MPa) observed at this location (Figure 3; Table 4) and at the Illinois Basin – Decatur Project (IBDP) site in the central IL Basin (Bauer et al., 2016; Babarinde et al., 2021). Shale within the Eau Claire Formation forms the primary seal at the IBDP (Leetaru and Freiburg, 2014). The high strength values in the Wabash #1 Maquoketa Group results suggest that a sufficiently high pore pressure change will be required (depending on the in situ stress field) to induce a tensile failure in any layer of the Maquoketa with similar strength values.
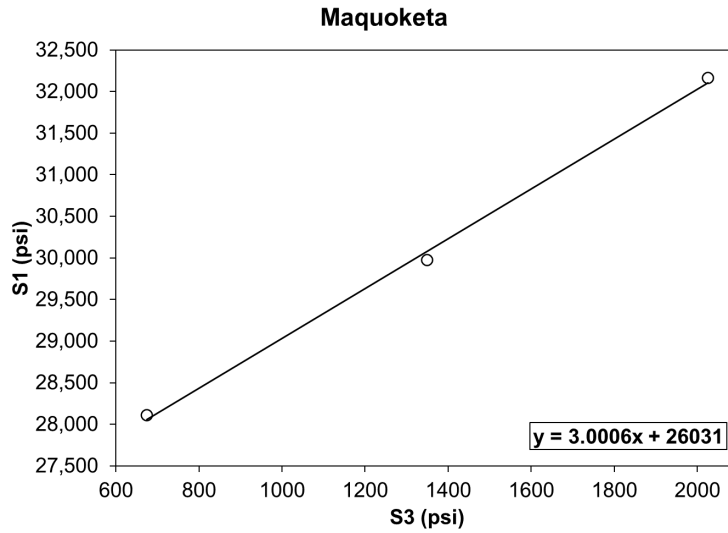
Figure 50: *Plot of confining stress versus the resulting yield strength. Note that three measurements on Maquoketa shale were used to create a best-fit line.*

Table 9: *Measured parameters from the triaxial tests and ultrasonic measurements on the Maquoketa core samples. These parameters are also plotted on the cross section in Figures 2, 3, and 4.*

Sample orientation	Petrophysical properties	Ultrasonic velocities		Dynamic elastic properties		Static elastic properties				
	ρ (g/cc)	Vp (km/s)	Vs (km/s)	E (GPa)	υ	E (GPa)	υ	UCS (MPa)	C_0 (Mpa)	φ (°)
Vertical	2.61-2.71	4.9-5.5	2.6-3.0	45-62	0.30	42-46	0.23-0.3	180	51.8	30
45 degrees	2.71	5.5	2.9-3.0	60-62	0.30					
Horizontal	2.63-2.70	5.2-5.7	2.6-3.0	48-63	0.30-0.32					

* (ρ) = Density, (ϕ) = angle of internal friction, (C_0) = cohesive or shear strength, (V_p) = compressional velocities, (V_s) = shear velocities, (E) = dynamic and static Young's modulus, (υ) = dynamic and static Poisson's ratio, (UCS) = uniaxial or unconfined compressive rock strength.
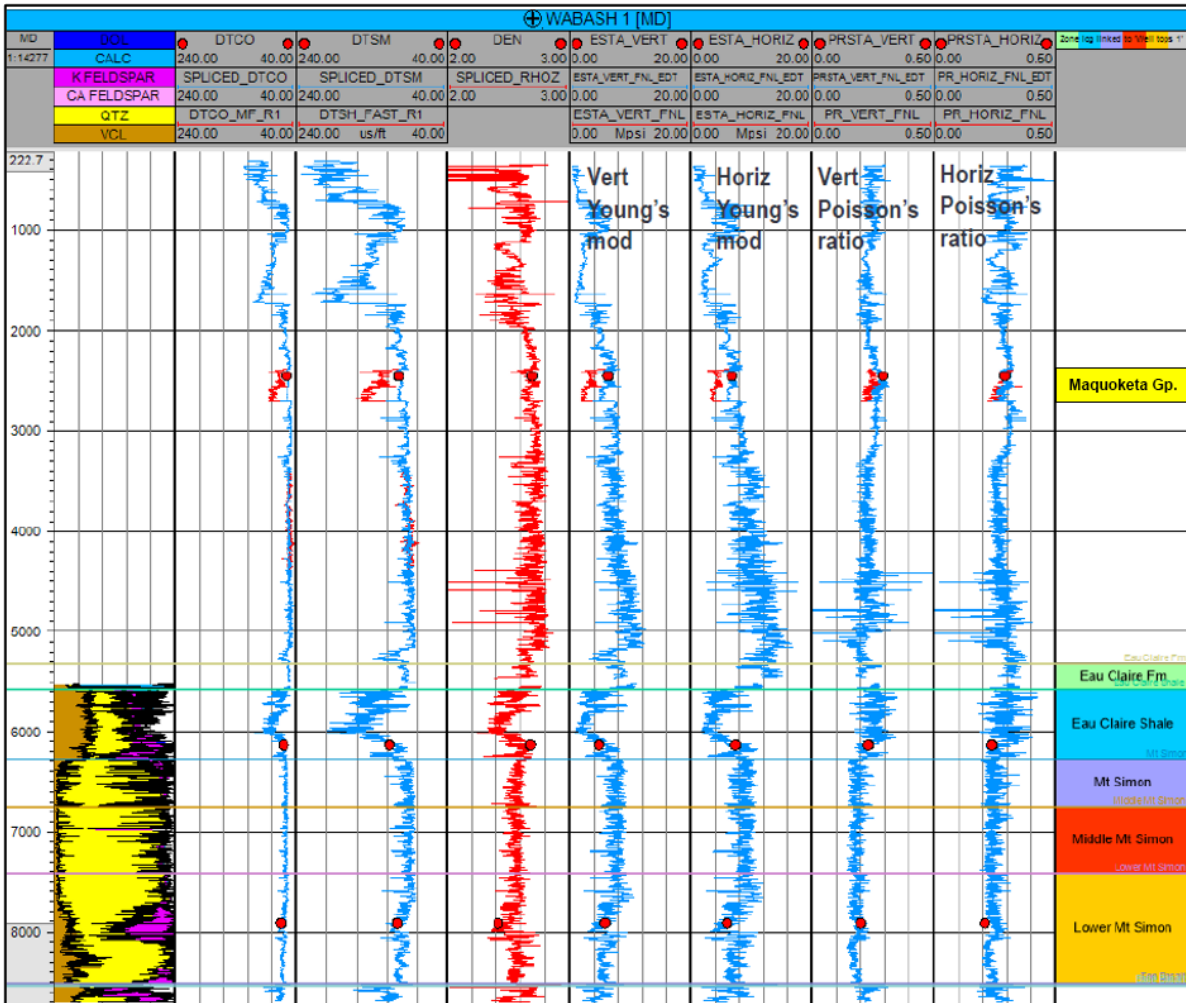
Figure 2: *Cross section shows core calibrated elastic properties (in blue) estimated from well log data. Laboratory measurement of static elastic properties (red dots) are also shown on the section. (Modified from Mohamed, 2021).*
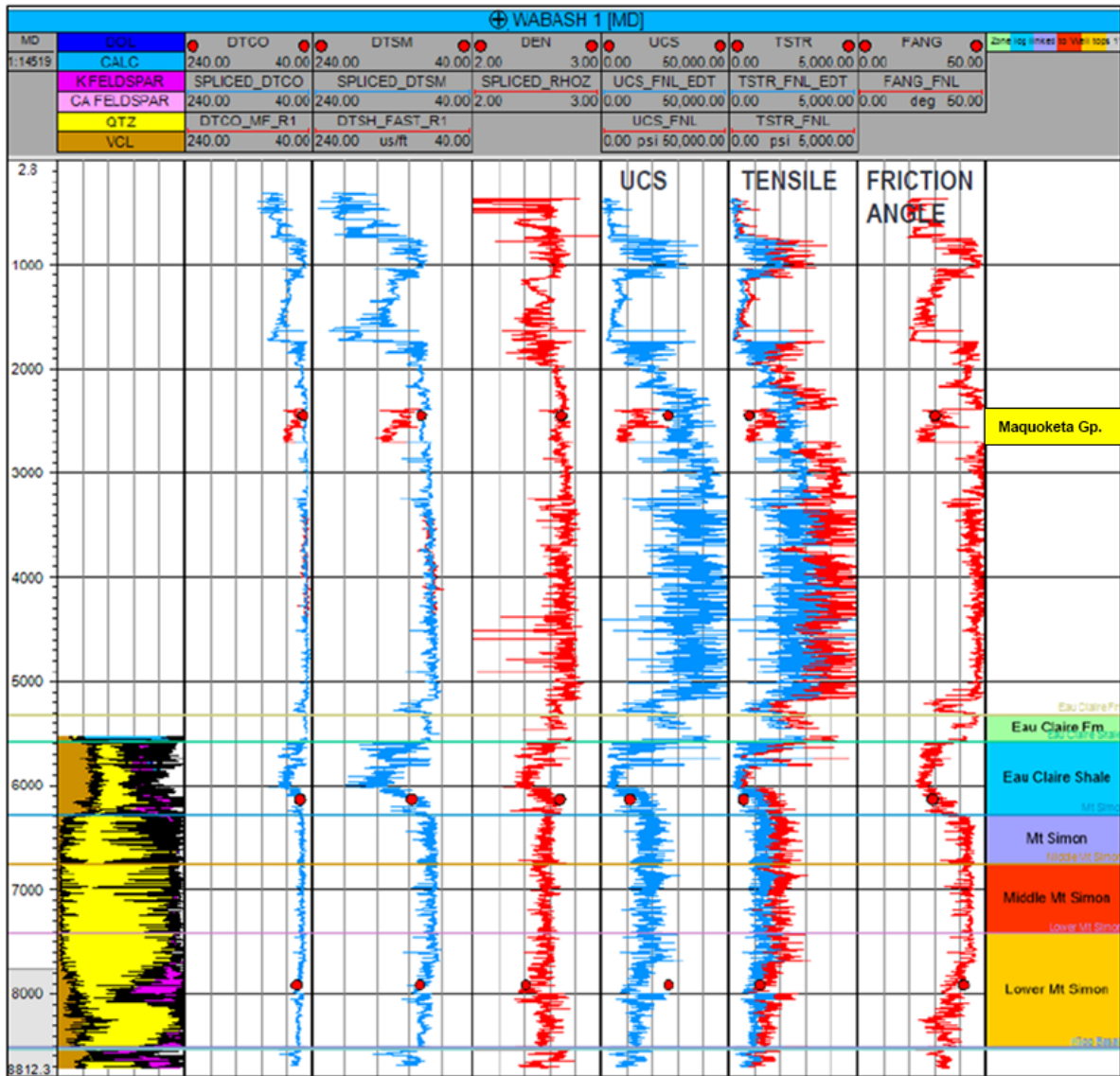
Figure 3: *Cross section shows core calibrated rock strength properties (in blue) estimated from well log data. Laboratory measurement of rock strength (red dots) are also shown on the section. (Modified from Mohamed, 2021).*
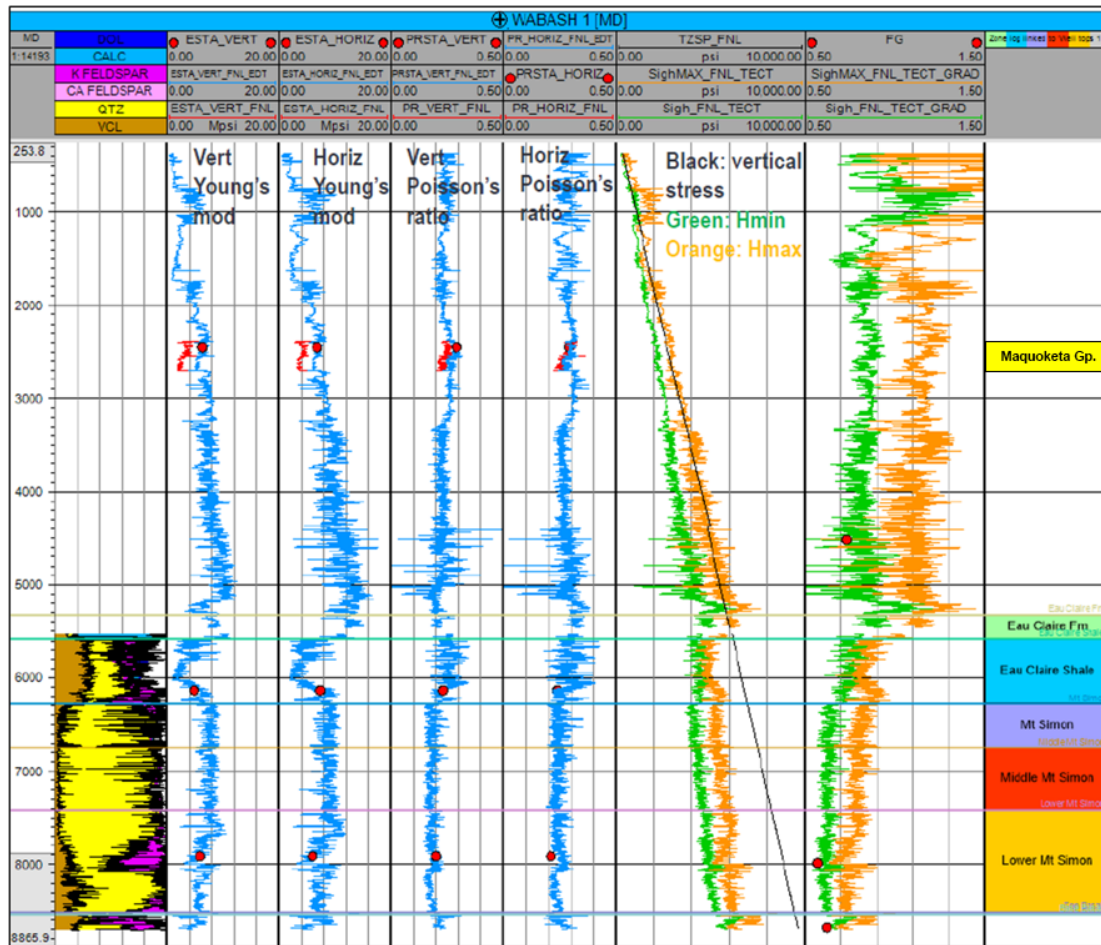
Figure 4: Cross section shows calculated stresses from well log data. Field estimates of minimum horizontal stress (i.e., fracture gradient) are also shown on the section.(Modified from Mohamed, 2021).

Rock Strength of the Eau Claire shale

For the Eau Claire shale, UCS of ~11,020 psi (~76 MPa) was extrapolated (based on triaxial testing of five cores) from the best-fit line to the relationship between σ3 and resulting yield strength (Figure 5). The slope (i.e., m = ~2.8) of the best-fit line is used to determine a coefficient of internal friction (μ_i) of ~0.58, an angle of internal friction (ϕ) of 30°, and a cohesive or shear strength (C_0) of ~3,190 psi (~22 MPa). Measurements of compressional velocities (V_p), shear velocities (V_s), dynamic and static Young's modulus (E), and dynamic and static Poisson's ratio (υ) are presented in Table 4.

As mentioned earlier in this report, the triaxial test results show that the Eau Claire shale sample from Wabash #1 has UCS (~76 MPa) comparable to the Eau Claire shale that was tested from the IBDP well. In addition, due to the heterogeneity of the Wabash #1 silty-shale sample, it has a range of Young's modulus values. The maximum recorded value is ~102 MPa, thus suggesting it is likely stiffer compared to the Maquoketa in some layers. The recorded elastic properties of the Eau Claire shale suggest it would be a good seal (if planned to be used as a sealing unit), as it has been used as a primary seal at the IBDP project site and natural gas storage fields in the central Illinois Basin.
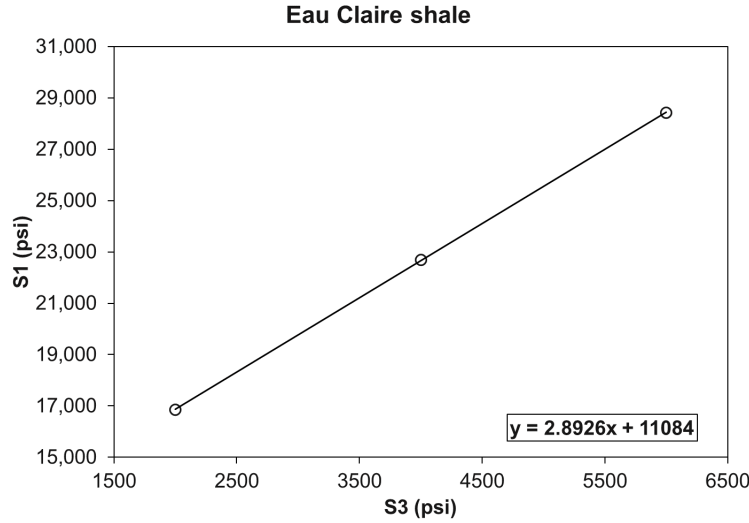
Figure 5: *Plot of confining stress versus the resulting yield strength. Note that three measurements on Eau Claire shale were used to create a best-fit line.*

Table 10: *Measured parameters from the triaxial tests and ultrasonic measurements on the Eau Claire shale core samples. These parameters are also plotted on the cross section in Figures 2, 3, and 4.*

	Petrophysical properties	Ultrasonic velocities		Dynamic elastic properties		Static elastic properties				
Sample orientation	ρ (g/cc)	Vp (km/s)	Vs (km/s)	E (GPa)	υ	E (GPa)	υ	UCS (MPa)	C_0 (Mpa)	φ (°)
Vertical	2.59-2.69	4.4-5.21	2.59-3.06	46-61	0.2-0.32	5-102	0.03-0.62	76	22	30
45 degrees	2.69-2.7	4.97-5.03	2.73-2.85	52-55	0.26-0.29					
Horizontal	2.68-2.7	5.2-5.53	2.91-3.33	58-73	0.21-0.27					

* (ρ) = Density, (ϕ) = angle of internal friction, (C_0) = cohesive or shear strength, (V_p) = compressional velocities, (V_s) = shear velocities, (E) = dynamic and static Young's modulus, (υ) = dynamic and static Poisson's ratio, (UCS) = uniaxial or unconfined compressive rock strength.

Rock Strength of the Mt. Simon Sandstone

For the Mt. Simon Sandstone, UCS of ~26,245 psi (~181 MPa) was extrapolated (based on triaxial testing of three cores) from the best-fit line to the relationship between σ3 and resulting yield strength (Figure 6). The slope (i.e., m = ~4.9) of the best-fit line is used to determine a coefficient of internal friction (μ_i) of ~0.86, an angle of internal friction (ϕ) of 41°, and a cohesive or shear strength (C_0) of ~5,945 psi (~41 MPa). Measurements of compressional velocities (V_p), shear velocities (V_s), dynamic and static Young's modulus (E), and dynamic and static Poisson's ratio (υ) are presented in Table 5.

The triaxial test results show the Mt. Simon Sandstone has relatively similar Young's modulus (up to ~43 GPa) compared to Mt. Simon Sandstone at the IBDP site (Table 5; Bauer et al., 2016; Babarinde et al., 2021). The measured UCS and C_0 for the Wabash #1 sample is over six times greater

than the tested Mt. Simon Sandstone at the IBDP; this difference in value is presumably a function of petrophysical properties. The tested lower Mt. Simon Sandstone from the IBDP site has density of ~1.9 g/cc and porosity up to 28%, while the tested Mt. Simon Sandstone from Wabash #1 has a density of ~2.42 and whole core samples over the entire cored interval had an average porosity of 7.61% (with a maximum of 12.95%). The measured UCS and C_0 for the Wabash #1 Mt. Simon Sandstone sample suggest a very stiff rock, and it will require a sufficiently high pore pressure change to induce a tensile failure in any layer of the Mt. Simon Sandstone with similar strength values.

Mt. Simon Sandstone

$y = 4.854x + 26250$
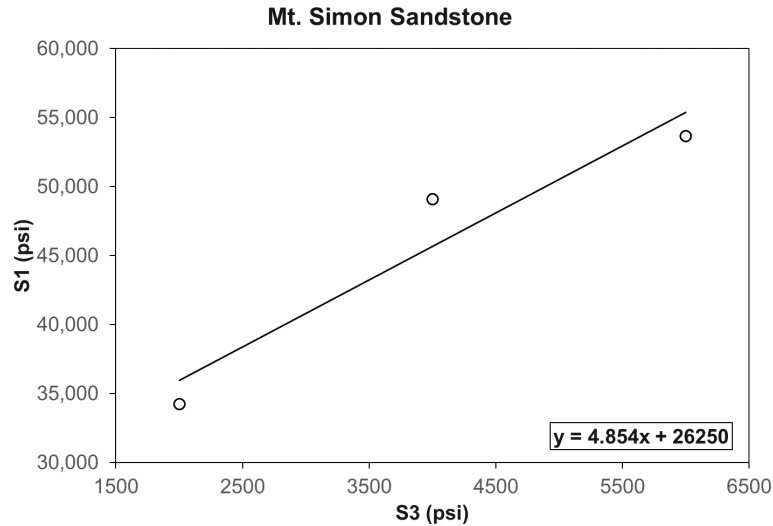
Figure 6: *Plot of confining stress versus the resulting yield strength. Note that three measurements on Mt. Simon Sandstone were used to create a best-fit line.*

Table 11: *Measured parameters from the triaxial tests and ultrasonic measurements on the Mt. Simon Sandstone core samples. These parameters are also plotted on the cross section in Figures 2, 3, and 4.*

	Petrophysical properties	Ultrasonic velocities		Dynamic elastic properties		Static elastic properties				
Sample orientation	ρ (g/cc)	Vp (km/s)	Vs (km/s)	E (GPa)	υ	E (GPa)	υ	UCS (MPa)	C_0 (Mpa)	φ (°)
Vertical	2.39-2.45	4.2-4.82	2.31-2.99	33-52	0.19-0.31	0.28-43	0.06-0.53	181	41	41
45 degrees	2.42-2.42	4.63-4.83	2.87-2.95	47-51	0.19-0.21					
Horizontal	2.42-2.44	4.73-4.92	2.66-2.97	43-52	0.2-0.27					

* (ρ) = Density, (ϕ) = angle of internal friction, (C_0) = cohesive or shear strength, (V_p) = compressional velocities, (V_s) = shear velocities, (E) = dynamic and static Young's modulus, (υ) = dynamic and static Poisson's ratio, (UCS) = uniaxial or unconfined compressive rock strength.

REFERENCES

Babarinde, O., Okwen, R., Frailey, S., Yang, F., Whittaker, S, Sweet, D., 2021. A workflow to assess the efficacy of brine extraction for managing injection-induced seismicity potential using data from a CO2 injection site near Decatur, Illinois. Int. J. Greenh. Gas Control (2021), https://doi.org/10.1016/j.ijggc.2021.103393

Bauer, R.A., et al., Overview of microseismic response to CO2 injection into the Mt. Simon saline reservoir at the Illinois Basin-Decatur Project. Int. J. Greenhouse Gas Control (2016), http://dx.doi.org/10.1016/j.ijggc.2015.12.015 .

Bauer, R., January 17, 2020, Wabash #1 Eau Claire Core Fracture Logging, unpublished core description notes for Wabash CarbonSAFE, 3 p with photos.

Freiburg, J. T., July, 2020, IN168045 Wabash #1 Full Diameter Core Descriptions – Mt. Simon Sandstone, unpublished core description notes for Wabash CarbonSAFE, 1 p.

Khosravi, Mansour, Yaghoob Lasemi, Zohreh Askari, Hannes Leetaru, Scott Frailey, Oladipupo Babarinde, Donna Willette, Curt Blakley, Charles Monson, Carl Carman, Steve Whittaker, Chris Korose, 2022 (antic.), Wabash CarbonSAFE, Geologic Analysis of the Potosi Dolomite Reservoir Interval and Potential Confining Units – Subtask 7.2, Technical Report for DOE-FE0031626. U.S Department of Energy.

Leetaru, H.E. and J. T. Freiburg, 2014. Litho-facies and reservoir characterization of the Mt. Simon Sandstone at the Illinois Basin–Decatur Project. Greenh. Gases: Sci. Technol. 4 (5), 580–595. https://doi.org/10.1002/ghg.1453.

Mohamed, Farid Reza, January 2021, 1D Mechanical Earth Model for Wabash #1, Core calibration update, unpublished work for Wabash CarbonSAFE, Schlumberger, 5 p. with figures.

Zoback, M.D., 2007, Reservoir Geomechanics: Cambridge University Press, Cambridge, UK, 505 pp.

Chapter 9
Petrographic Characterization

By: Mingyue Yu and Lauren Gardiner

Illinois State Geological Survey, Prairie Research Institute, University of Illinois at Urbana-Champaign

INTRODUCTION

The Wabash #1 well was drilled to a depth of 8,739 ft through Maquoketa Formation and into the Mt. Simon Formation. In total, 60 thin section samples from whole cores and 57 from rotary sidewall cores (RSWC) were taken for this report.

This report details the core analysis completed, specifically thin section point count analysis that includes mineralogical and pore space quantification, including grain size analysis annotated thin section photomicrographs, scanning electron microscopy (SEM) with energy dispersive X-ray spectroscopy (EDS), and routine analysis of full diameter core and rotary sidewall core for porosity and permeability calculations.

MAQUOKETA GROUP
2,386 – 2,700 ft
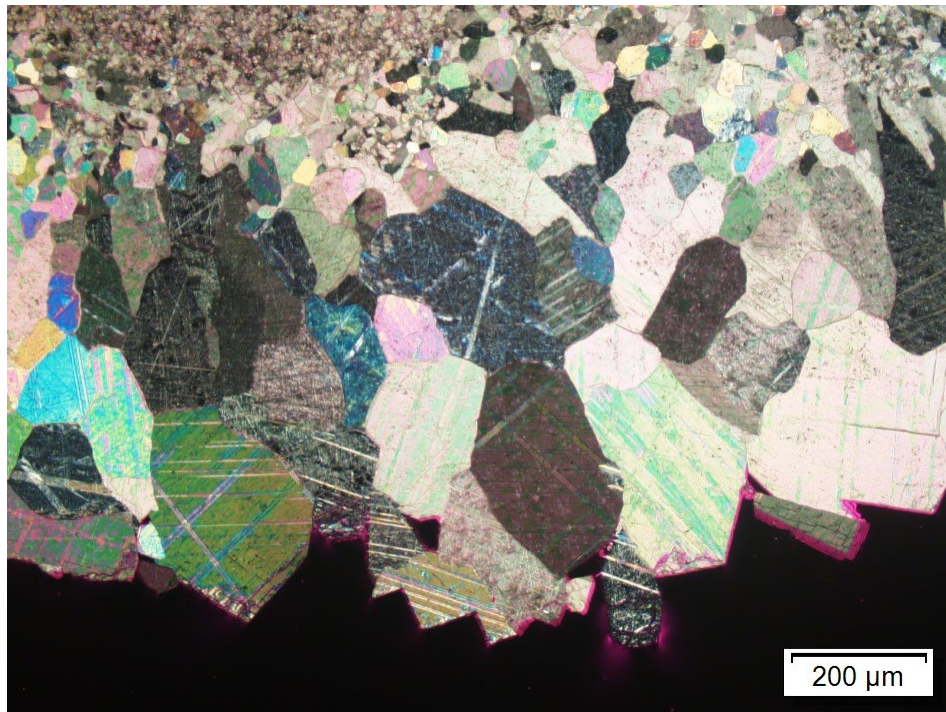
Figure 1: *Thin section photomicrograph of the Maquoketa Group at depth 2,435.8 ft under cross polarized light (XPL). Coarse-grained crystalline calcite microfacies were only found at this depth amongst all thin section samples collected.*
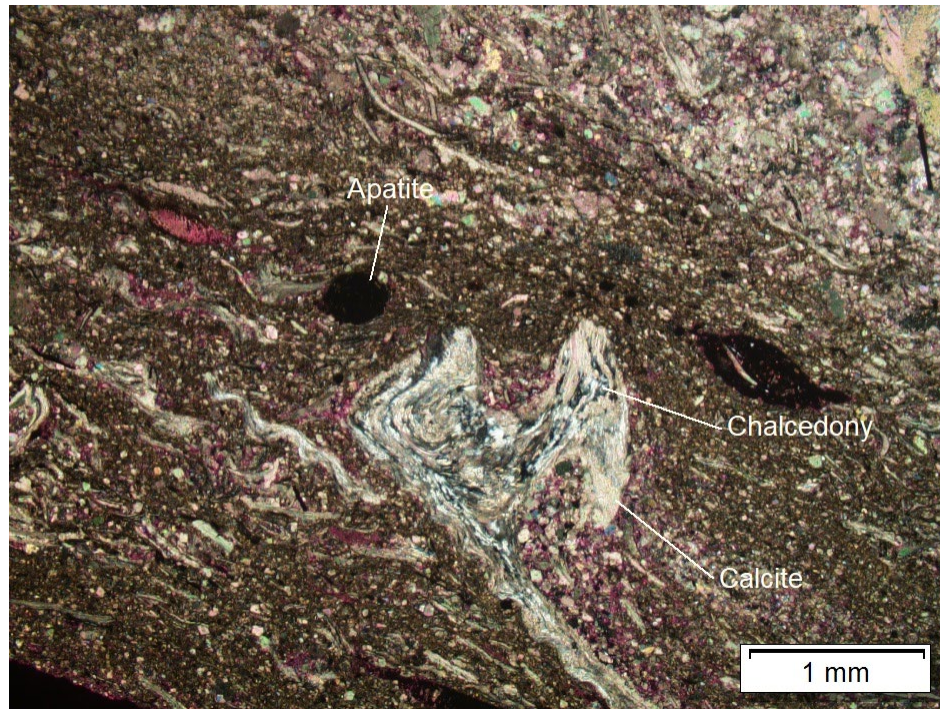
Figure 2*: Thin section photomicrograph of the Maquoketa Group at depth 2,435.8 ft. Shell fragments have been altered to chalcedony and fibrous calcite and a rounded apatized skeletal grain.*
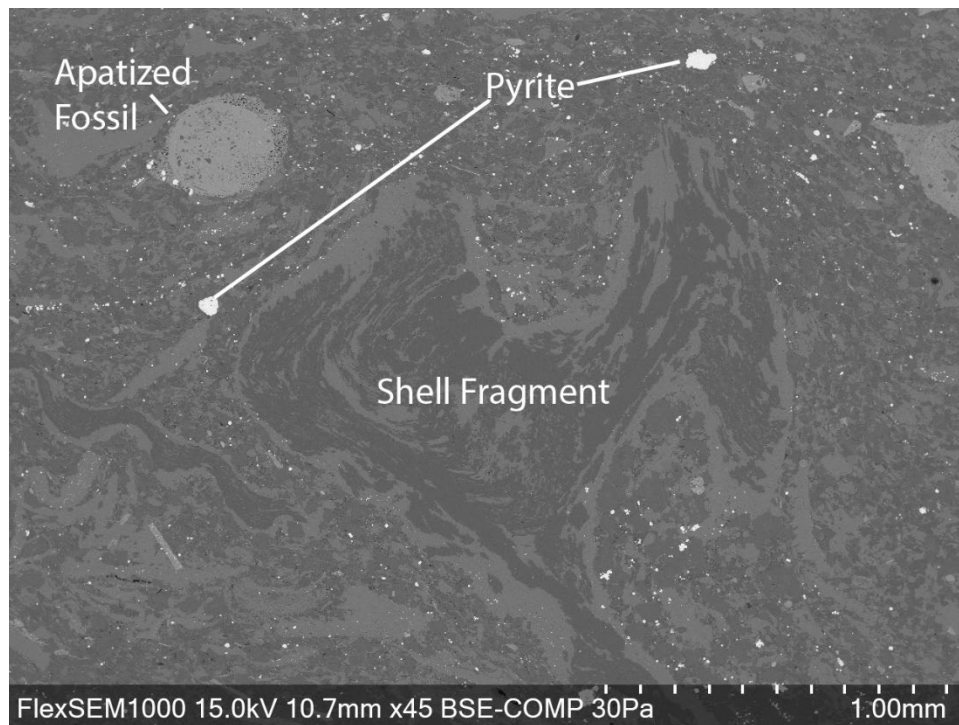
Figure 3*: SEM backscattered electron (BSE) thin section photomicrograph of the Maquoketa Group at depth 2,435.8 ft (same area as Figure 2), featuring rounded apatized (phosphatized) grain and the shell fragment. Also note tiny pyrite grains throughout the sample.*
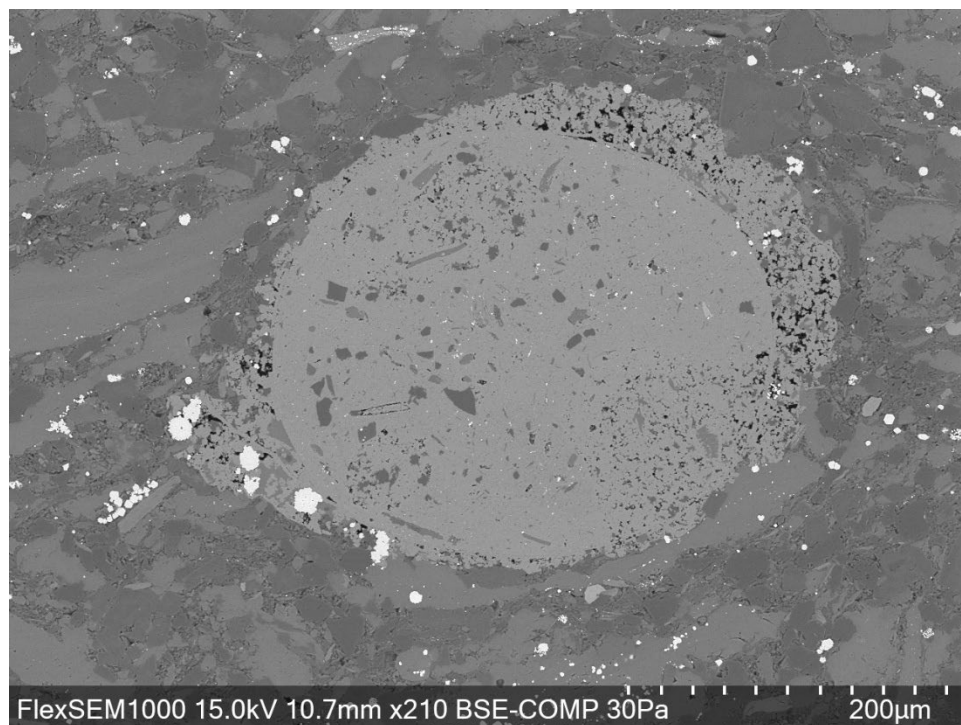
Figure 4: SEM BSE thin section photomicrograph of the Maquoketa Group at depth 2,435.8 ft showing the apatized fossil. Note internal core and overgrowth.
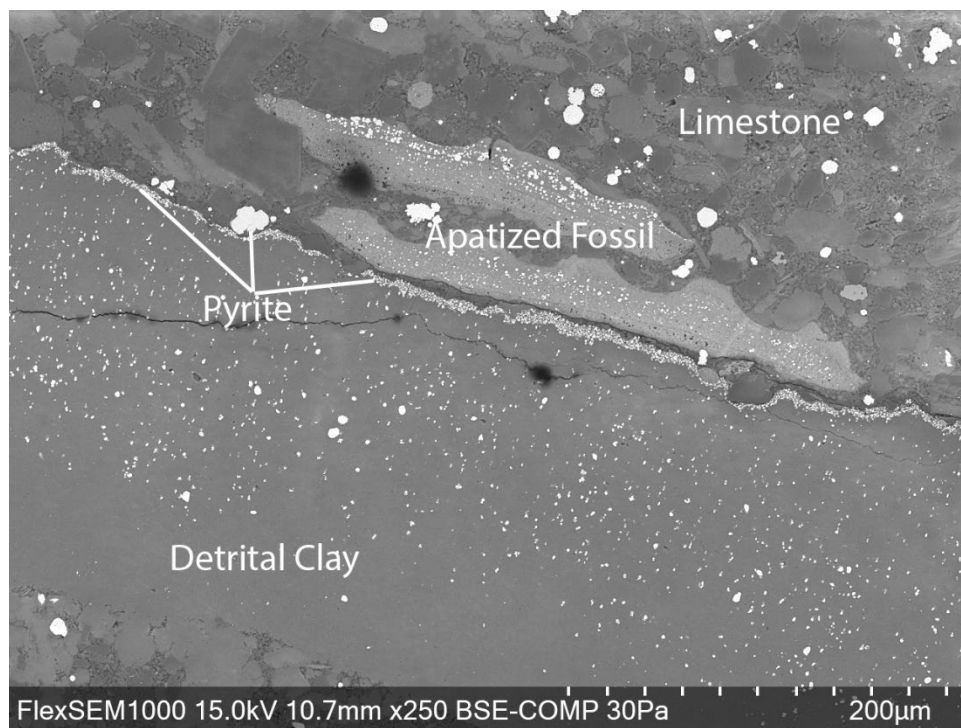
Figure 5: SEM BSE thin section photomicrograph of the Maquoketa Group at depth 2,435.8 ft showing the apatized fossil and detrital clay with a layer of pyrite on top.
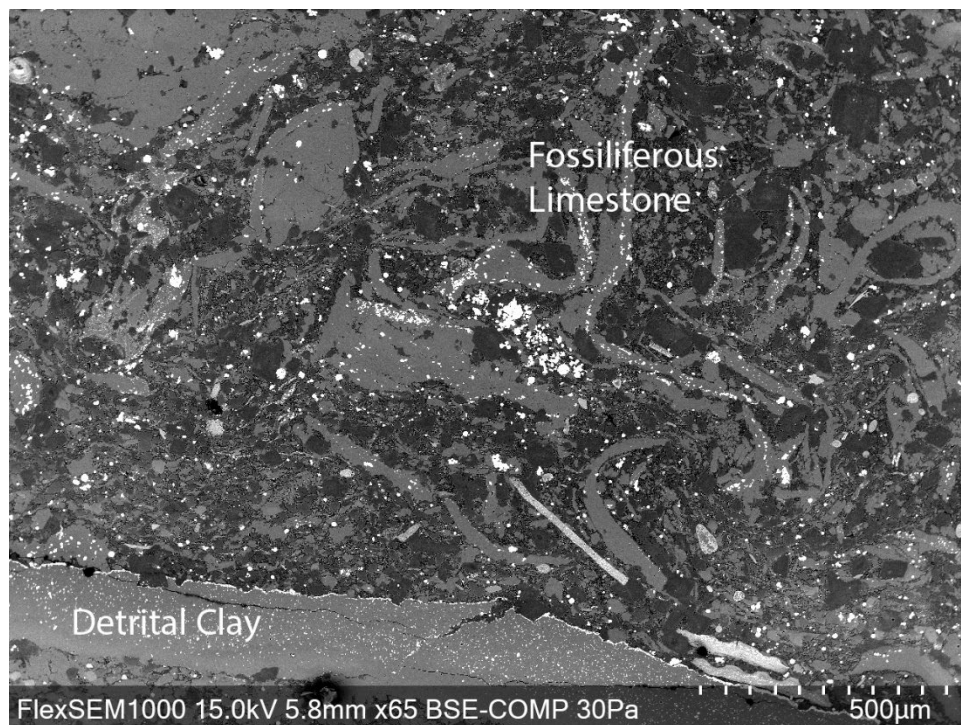
Figure 6: SEM BSE thin section photomicrograph of the Maquoketa Group at depth 2,435.8 ft. Fossiliferous packstone with micrite matrix and the skeletal fragment (bottom right), as imaged in Figure 5.
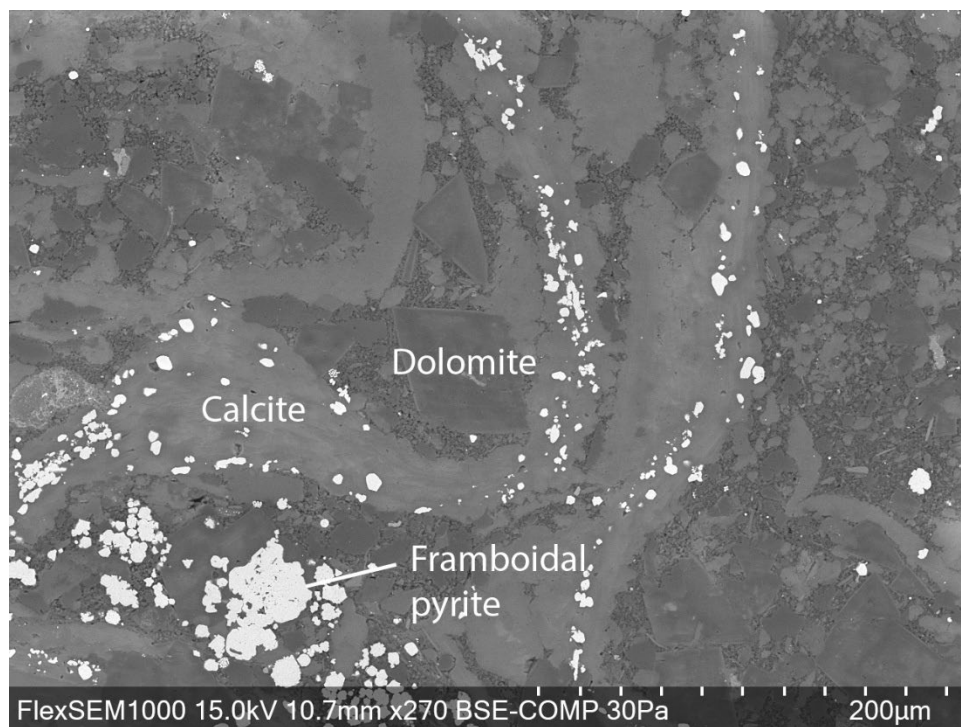
Figure 7: SEM BSE thin section photomicrograph of the Maquoketa Group at depth 2,435.8 ft. Note the repeating layers of calcite and dolomite, with an authigenic rhombohedral dolomite in the center. The pyrite seems to form within the calcite layers.
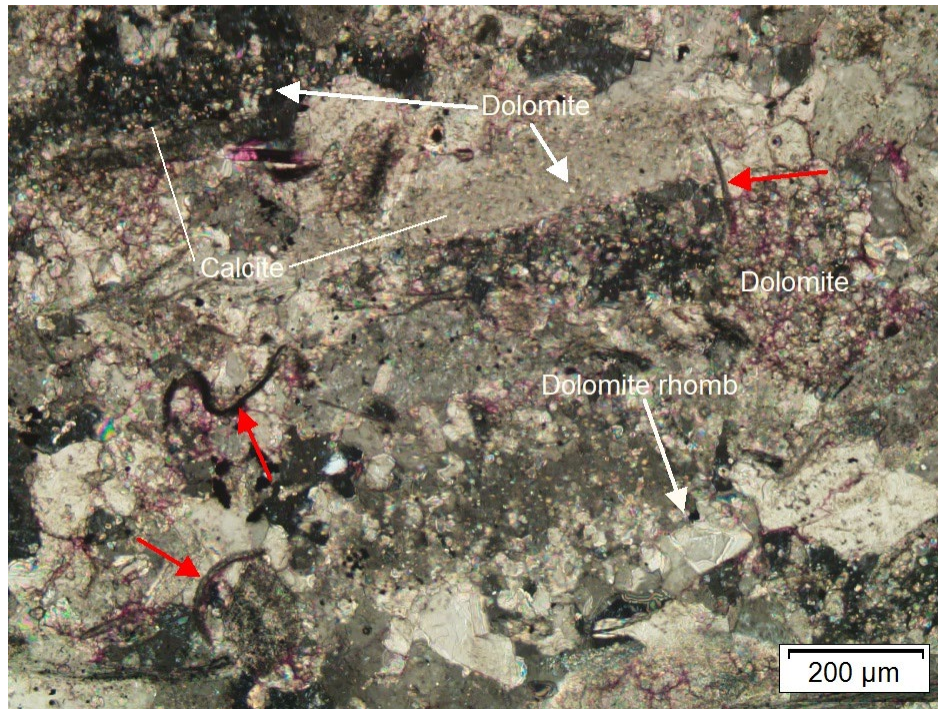
Figure 8: *Thin section photomicrograph of the Maquoketa Group at depth 2,435.8 ft. Regions of calcite containing microcrystalline dolomite, as well as coarser-grained dolomite. Red arrows point at high birefringence grains that are likely to be fossil fragments.*
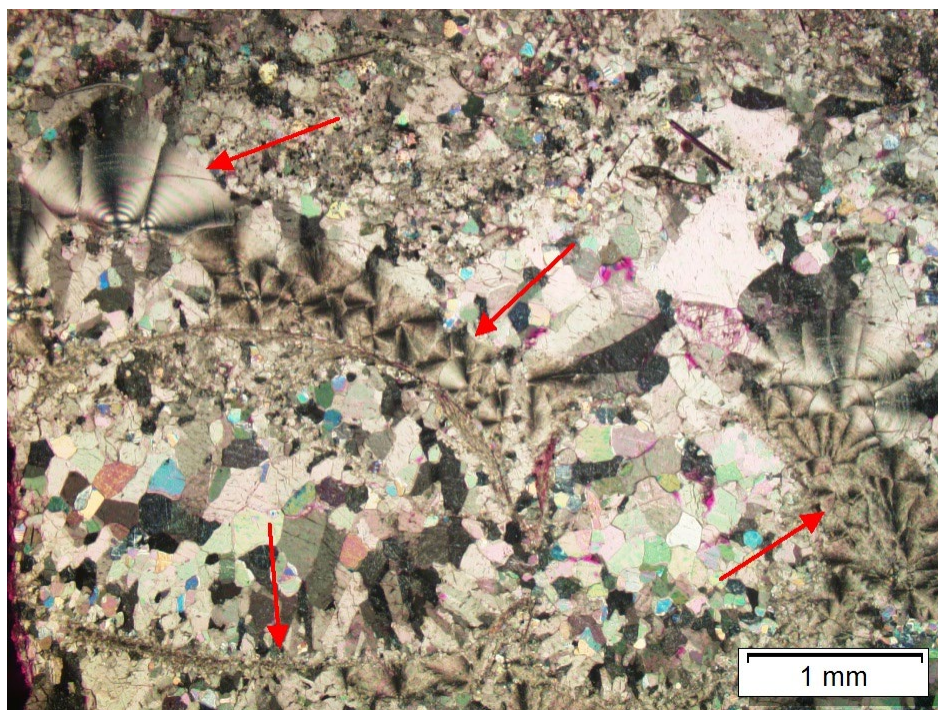
Figure 9: *Thin section photomicrograph of the Maquoketa Group at depth 2,435.8 ft. Red arrows show chalcedony veins that formed around and inside of the shell fragments. Crystalline calcite is present between fragment outlines. Note false interference figures from top left chalcedony grains.*
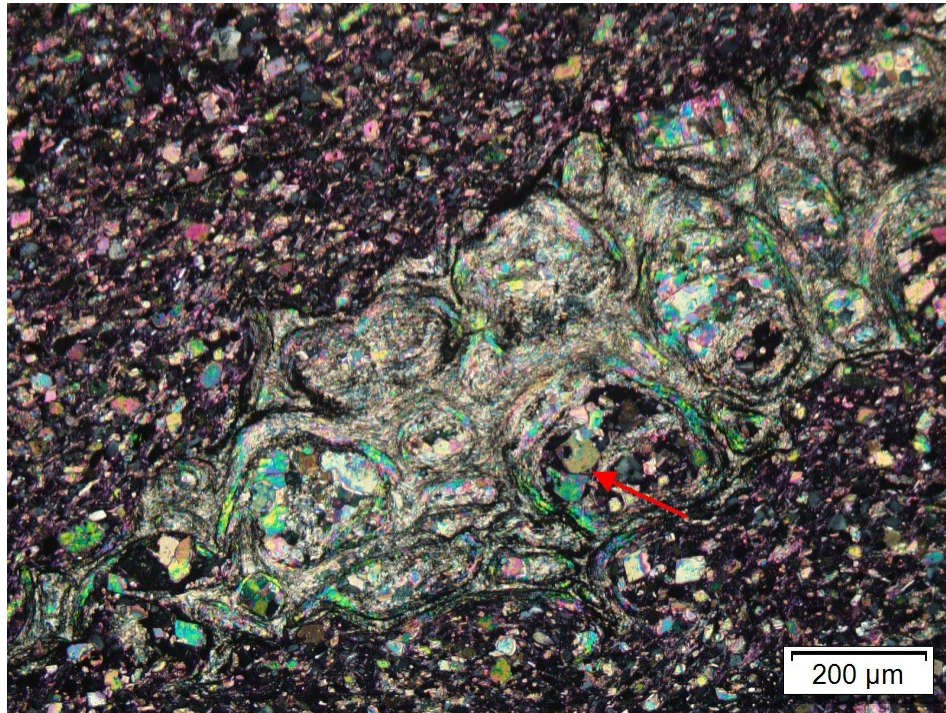
Figure 10: *Thin section photomicrograph of the Maquoketa Group at depth 2,446.5 ft. Red arrow shows dolomite grains growing inside the fossil fragment.*
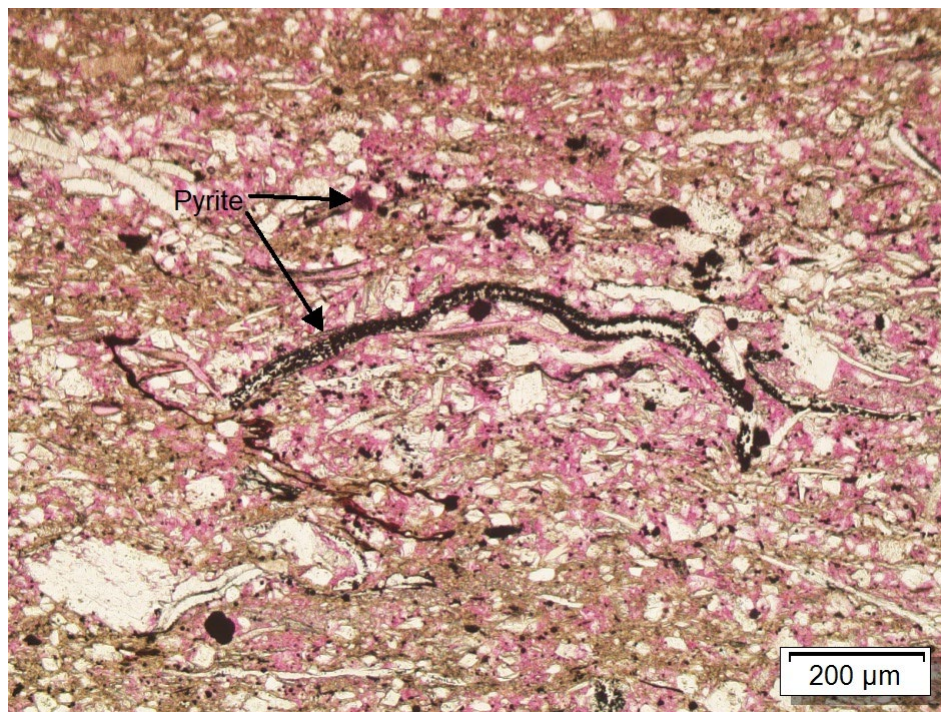
Figure 11: *Thin section photomicrograph of the Maquoketa Group at depth 2,467.1 ft. Authigenic pyrite forming preferentially along the borders of a shell fragment. Note visible microporosity, denoted by pink epoxy.*
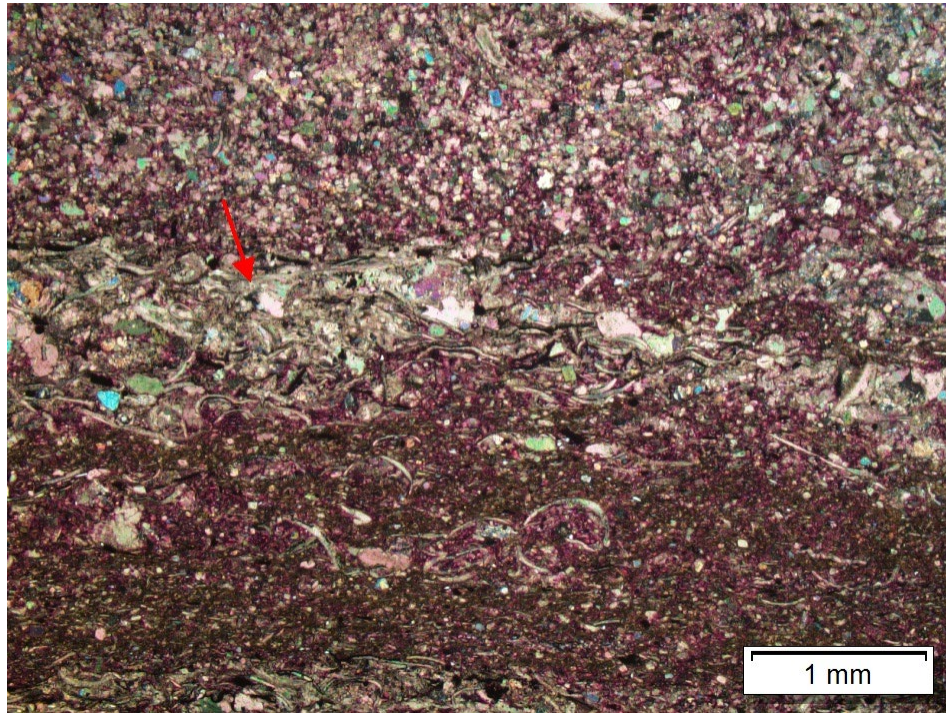
Figure 12*: Thin section photomicrograph of the Maquoketa Group at depth 2,467.1 ft. Red arrow shows fossiliferous packstone bed between a poorly washed biosparite (top) and a biomicrite (bottom).*
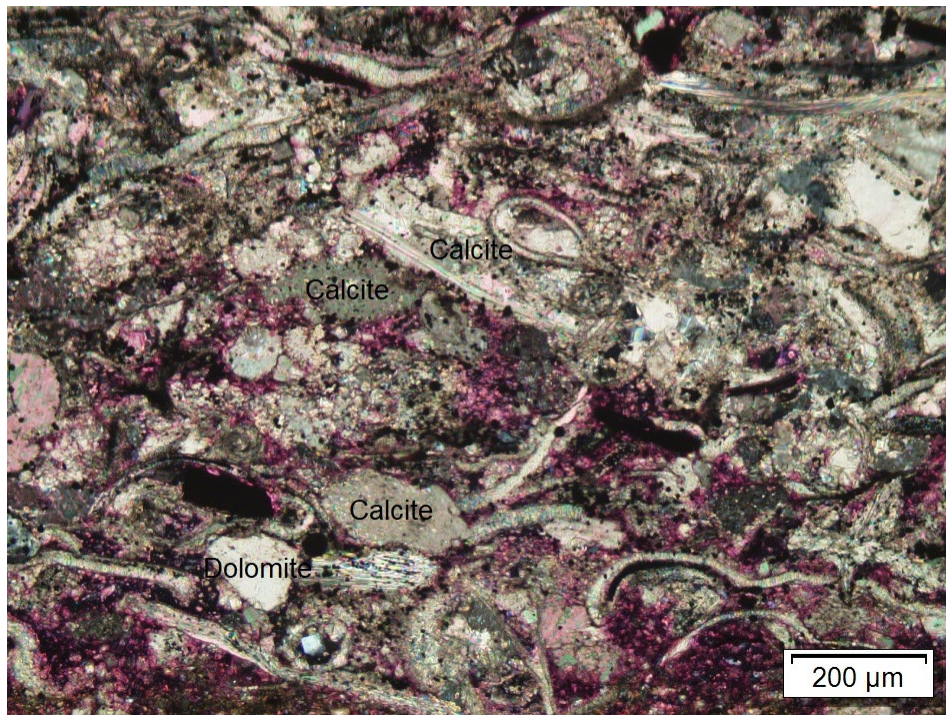
Figure 13*: Thin section photomicrograph of the Maquoketa Group at depth 2,467.1 ft. This is a 10X magnification of the packstone bed imaged in Figure 12.*
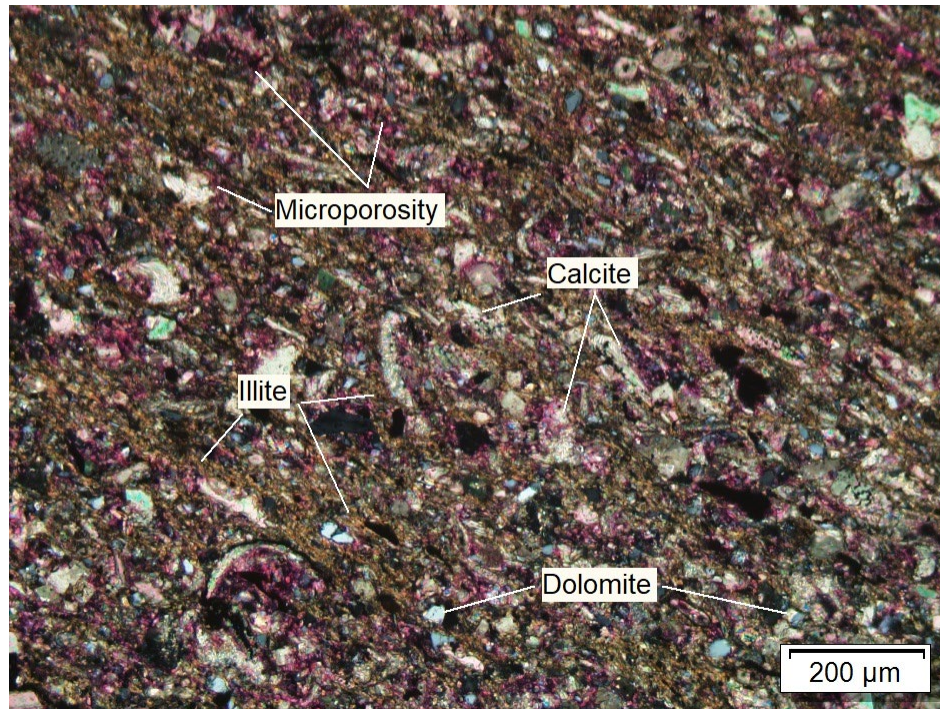
Figure 14*: Thin section photomicrograph of the Maquoketa Group at depth 2,467.1 ft. This is a 10X magnification of the biomicrite bed imaged in Figure 12.*
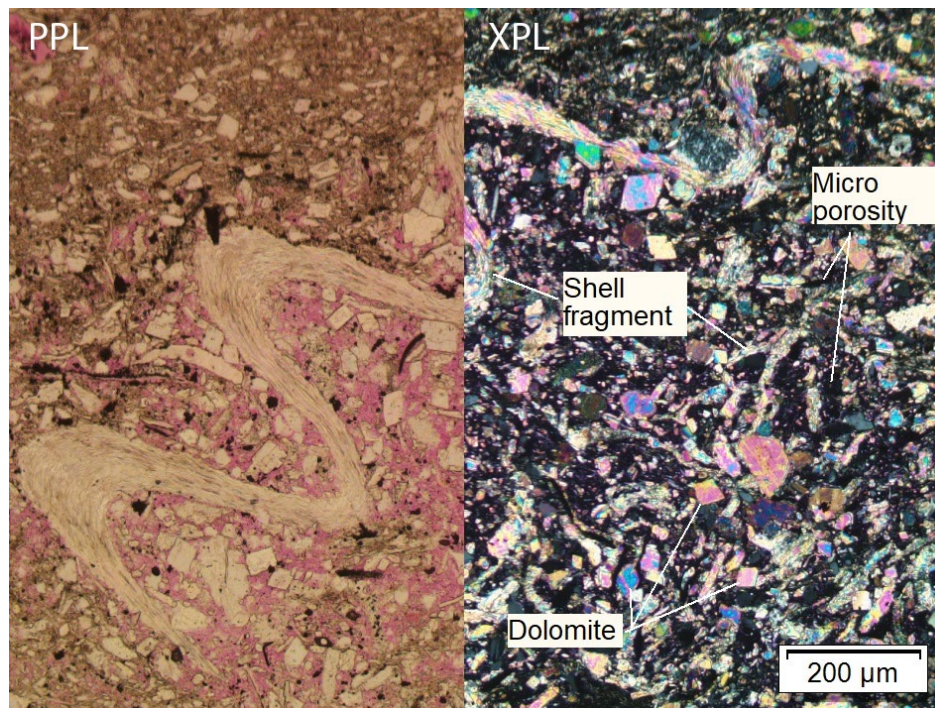
Figure 15*: Conjunct thin section photomicrograph of the Maquoketa Group at depth 2,473.15 ft. A calcite-altered bivalve shell fragment adjacent to a higher relative percentage of microporosity. Well-developed dolomite rhombs are visible within the matrix.*
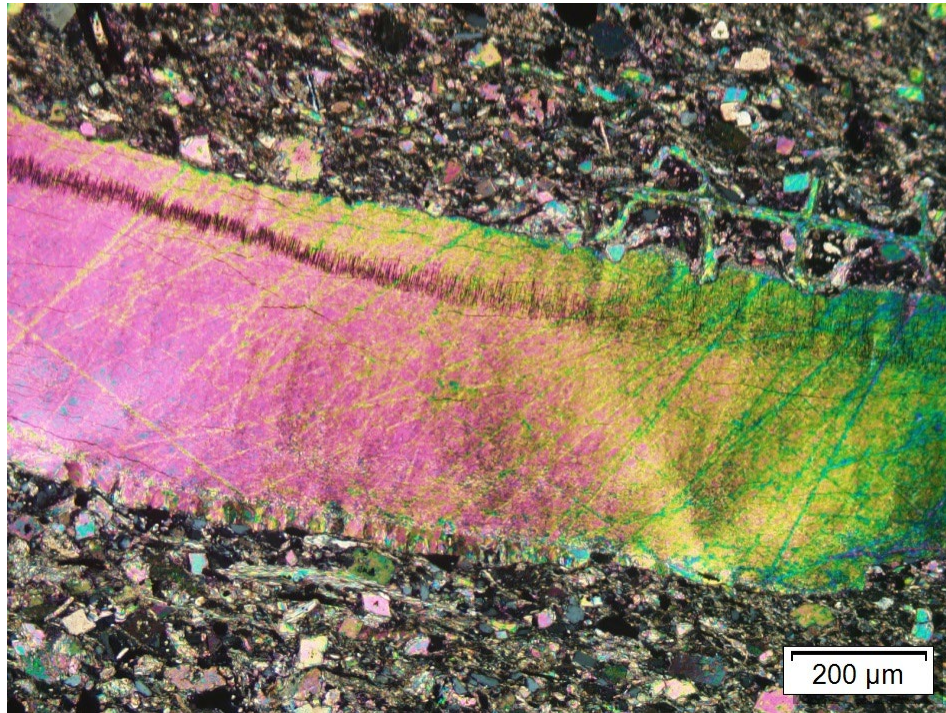
Figure 16: *Thin section photomicrograph of the Maquoketa Group at depth 2,473.15 ft. The calcite vein appears to be a piece of a fossil. Note the uniformity in texture of the calcite as well as the unparalleled laminae.*
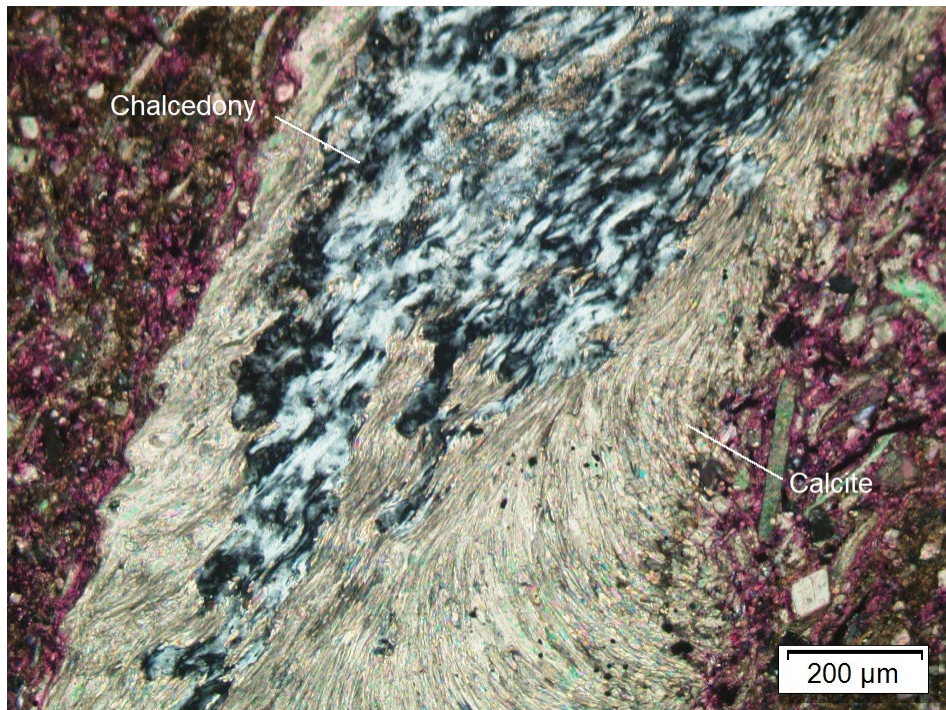
Figure 17*: Thin section photomicrograph of the Maquoketa Group at depth 2,473.15 ft. A skeletal fragment replaced by a core of crystalline quartz and fibrous calcite is along its borders.*
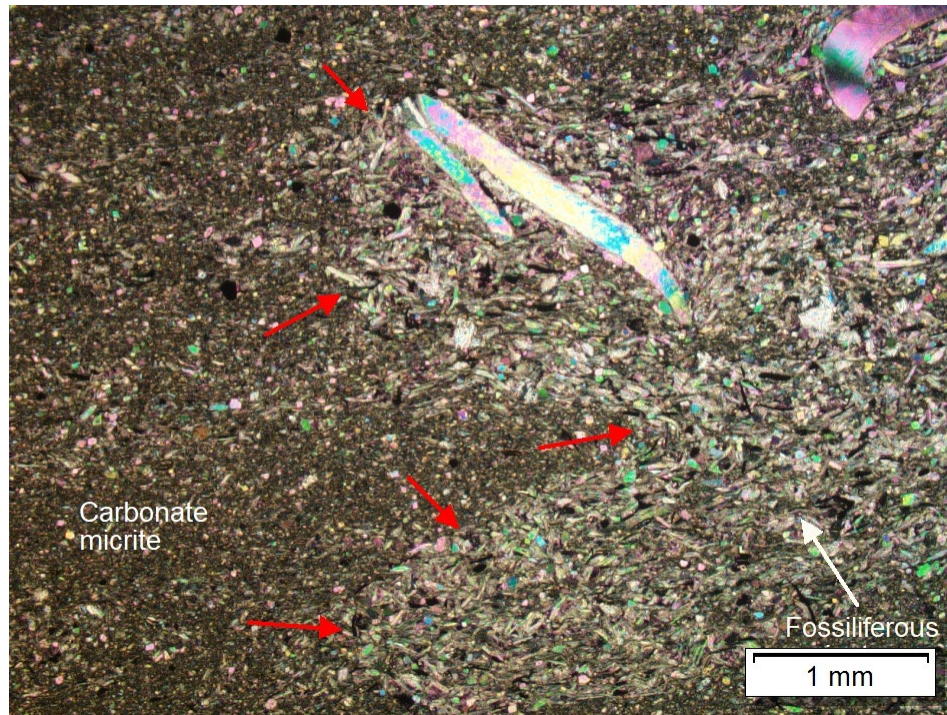
Figure 18: Thin section photomicrograph of the Maquoketa Group at depth 2,477.6 ft. Red arrows denote the boundary between the two facies present in this set of samples. Biomicrite on the left and fossiliferous packstone on the right.
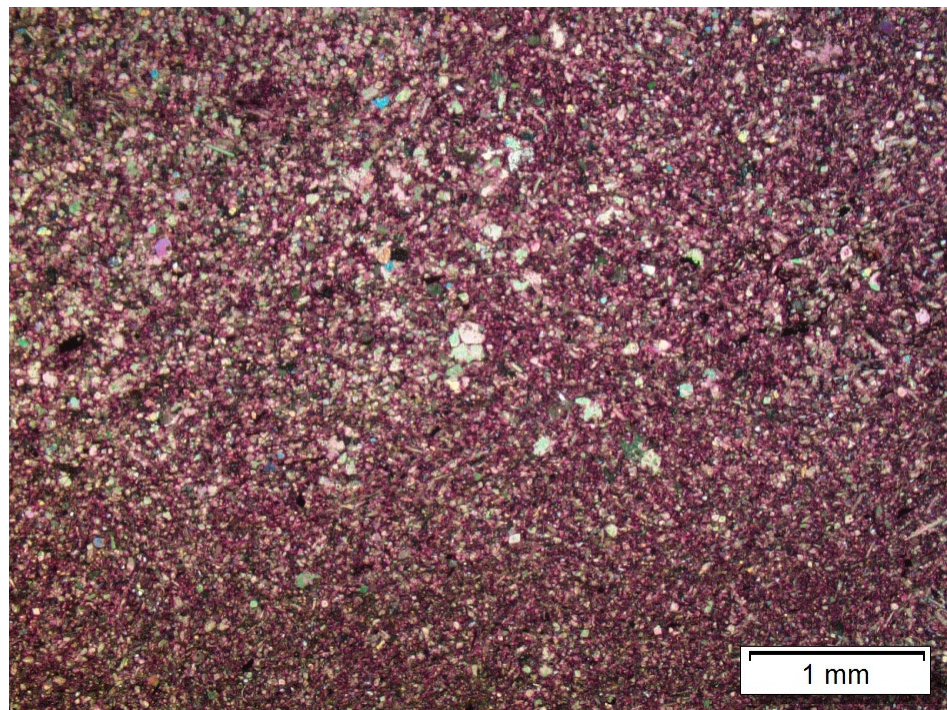
Figure 19: Thin section photomicrograph of the Maquoketa Group at depth 2,493 ft. A region of biomicrite; the pink, fluorescent epoxy showing microporosity is prominent in this region.
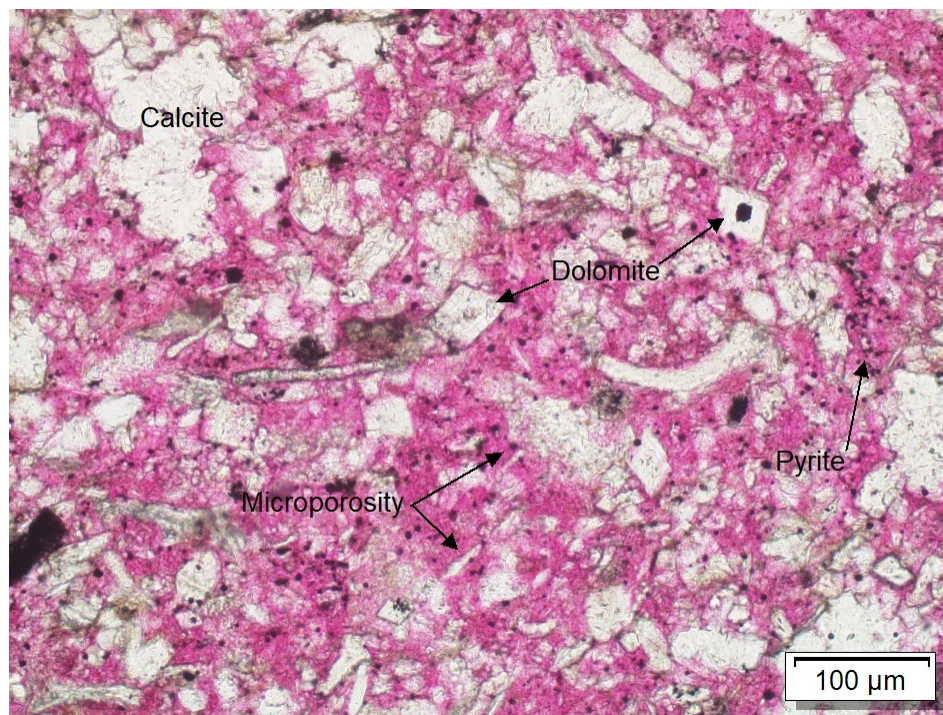
Figure 20*: Thin section photomicrograph of the Maquoketa Group at depth 2,493 ft. Microcrystalline calcite are found within microporosity, which appears to be high birefringence under XPL.*
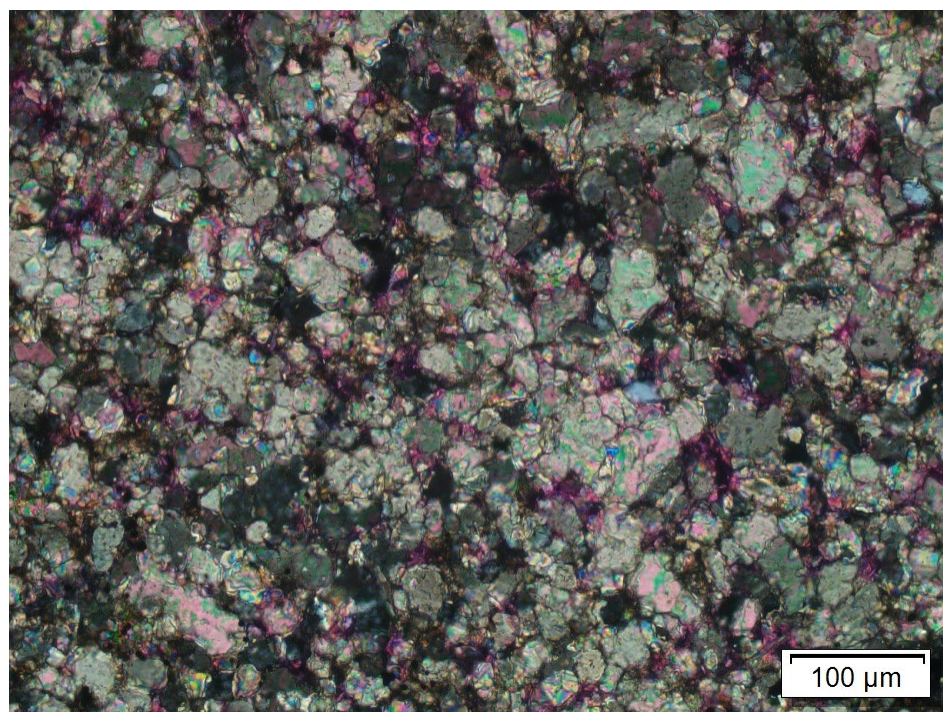
Figure 21*: Thin section photomicrograph of the Maquoketa Group at depth 2,493 ft. An XPL view of a crystalline region of the previous sample. Each sample features several different facies, as demonstrated by varying degrees of crystallinity and micrite.*

EAU CLAIRE FORMATION
5,322 – 6,277 ft

Table 1*: (From top to bottom) Petrographic point count analysis from thin sections prepared from whole cores cut in the Eau Claire Formation, including detrital grains, authigenic cements, and porosity analysis.*

| Whole Core | Detrital | | | | | | | | | | | |
| | Lithics | | | | | Matrix | Feldspar | | Quartz | | Mica | |
Depth	Granitic	Rhyolite	Sedimentary	Zircon	Oxides	Illitic	Plagioclase	Orthoclase	Monocrystalline	Polycrystalline	Muscovite	Biotite
6112.4	0.00%	0.00%	0.00%	0.00%	1.00%	47.86%	1.79%	22.93%	7.28%	0.00%	5.98%	3.29%
6131.4	0.00%	0.00%	0.00%	0.00%	1.00%	31.67%	1.29%	32.37%	7.47%	0.30%	7.27%	1.79%
6143	0.00%	0.00%	0.31%	0.00%	0.31%	15.79%	3.92%	32.51%	30.75%	0.00%	1.34%	0.00%
6147	1.02%	0.31%	0.82%	0.31%	0.31%	3.37%	0.31%	34.15%	35.58%	0.82%	3.07%	0.82%
6152.2	0.00%	0.00%	0.30%	0.00%	0.80%	5.57%	2.99%	39.60%	32.14%	1.00%	1.99%	0.00%
6159.6	0.70%	0.00%	0.70%	0.20%	2.51%	5.72%	3.51%	28.08%	22.37%	0.00%	3.71%	0.50%
6167	0.00%	0.30%	0.00%	0.00%	0.00%	4.46%	4.46%	12.90%	44.64%	0.00%	0.00%	0.99%
6167.1	0.00%	0.00%	0.00%	0.00%	0.00%	56.63%	0.00%	23.73%	7.48%	0.00%	9.27%	2.29%
6168.3	0.00%	0.00%	0.00%	0.00%	0.80%	36.39%	1.50%	25.92%	19.74%	0.30%	3.99%	2.49%
6169.9	0.00%	0.00%	0.00%	0.30%	0.80%	14.71%	1.29%	30.62%	30.82%	0.30%	2.78%	3.78%
6170.6	0.00%	0.00%	0.00%	0.79%	0.30%	28.26%	1.28%	26.48%	23.52%	0.30%	2.77%	0.99%
6171.3	0.50%	0.30%	0.00%	0.00%	0.00%	4.98%	1.29%	9.96%	55.58%	0.80%	0.00%	0.00%

| Whole Core | Authigenic Mineral | | | | | | |
| | Carbonate | | Illite | | | | |
Depth	Dolomite	Calcite	Pore Filling	Clay lining	Kaolinite	Feldspar	Quartz
6112.4	0.00%	0.00%	8.77%	0.80%	0.00%	0.00%	0.00%
6131.4	0.50%	0.00%	11.75%	3.78%	0.00%	0.80%	0.00%
6143	0.00%	1.86%	6.19%	4.64%	0.00%	0.00%	2.37%
6147	0.00%	0.00%	11.76%	2.15%	0.00%	1.53%	3.68%
6152.2	0.80%	0.30%	8.46%	3.28%	0.00%	0.00%	2.29%
6159.6	1.00%	1.50%	20.06%	3.51%	0.50%	3.71%	1.71%
6167	0.30%	0.50%	6.25%	5.75%	0.00%	0.99%	14.88%
6167.1	0.00%	0.00%	0.30%	0.30%	0.00%	0.00%	0.00%
6168.3	0.00%	0.00%	2.29%	6.28%	0.00%	0.30%	0.00%
6169.9	0.30%	0.30%	5.47%	7.46%	0.00%	0.30%	0.80%
6170.6	0.49%	0.30%	6.42%	5.73%	0.00%	0.79%	0.99%
6171.3	0.00%	0.00%	7.07%	2.49%	0.00%	0.00%	6.47%

| Whole Core | Porosity | |
Depth	Intergranular	Intragranular
6112.4	0.30%	0.00%
6131.4	0.00%	0.00%
6143	0.00%	0.00%
6147	0.00%	0.00%
6152.2	0.50%	0.00%
6159.6	0.00%	0.00%
6167	1.79%	1.79%
6167.1	0.00%	0.00%
6168.3	0.00%	0.00%
6169.9	0.00%	0.00%
6170.6	0.59%	0.00%
6171.3	10.26%	0.30%
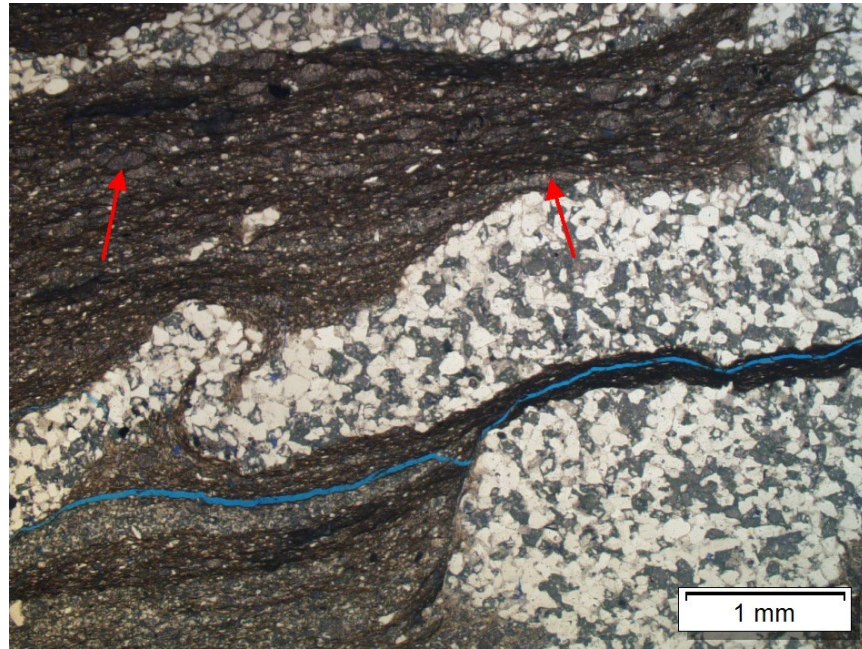
Figure 22: *Thin section photomicrograph of the Eau Claire Formation at depth 6,143 ft. This depth is characterized mostly by alternating beds of clay and sand. Note ptygmatic folding of the sand bed, center left. Red arrows show prominent calcite regions within the mudstone lamina. The small fracture in this location is likely artificial.*
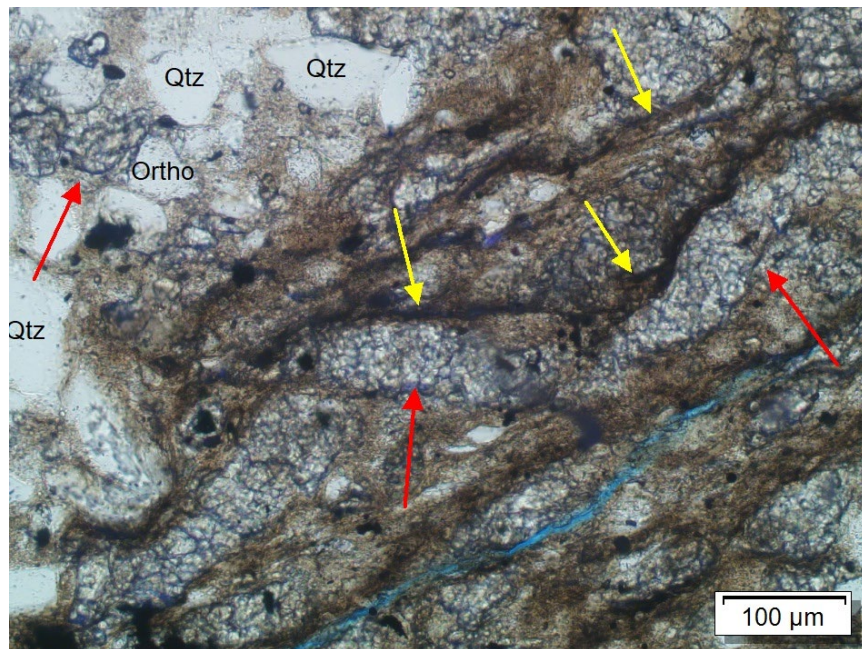
Figure 23: Thin section photomicrograph of the Eau Claire Formation at depth 6,143 ft. The yellow arrows denote detrital clay and red arrows denote authigenic calcite. Note the small fracture through the clay region, which shows minute signs of authigenic illite infill.
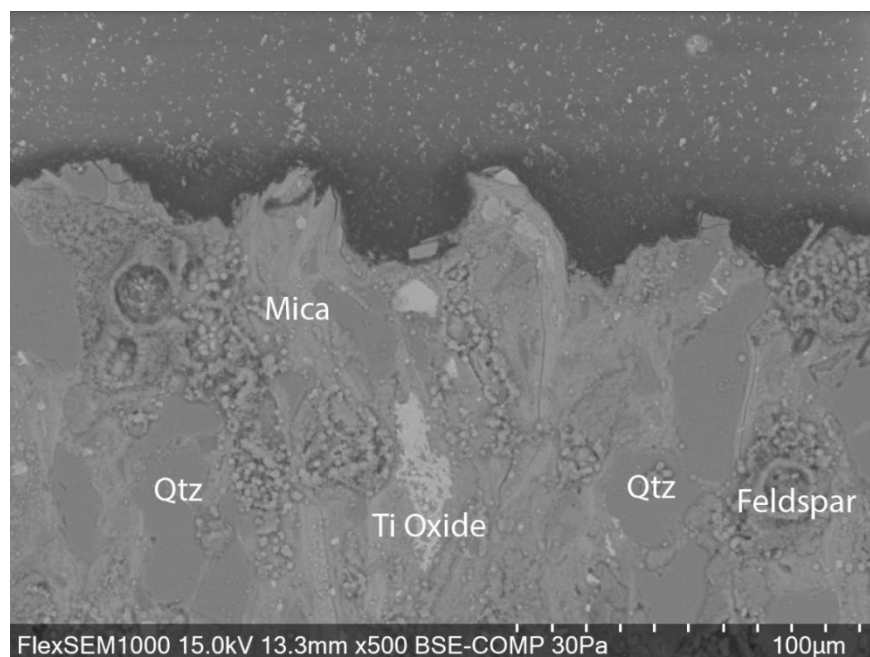
Figure 24: SEM BSE thin section photomicrograph of the Eau Claire Formation at depth 6,147 ft. Some opaque mineral in the thin section was later found to be titanium oxide (rutile or ilmenite), using SEM-EDS analysis. The granular speckles on top of the feldspar grains are cobalt staining, as is the bubble, an artificial feature from the staining procedure from thin section preparation.
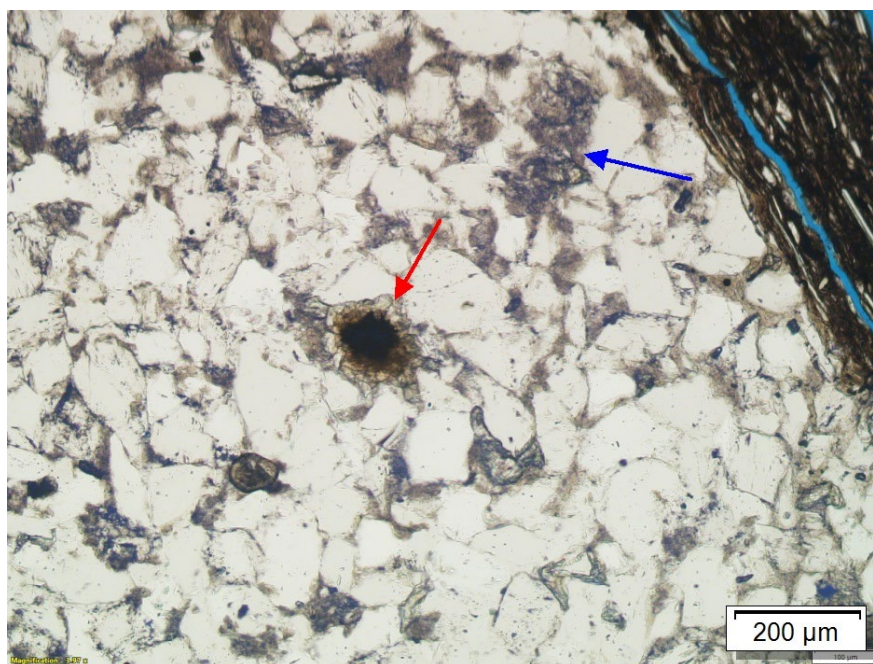
Figure 25: Thin section photomicrograph of the Eau Claire Formation at depth 6,152.2 ft. The red arrow denotes a region of authigenic siderite growing radially on a core of magnesite. The blue arrow shows authigenic illite alongside calcite. Note the accessory zircon in the lower left to the magnesite.
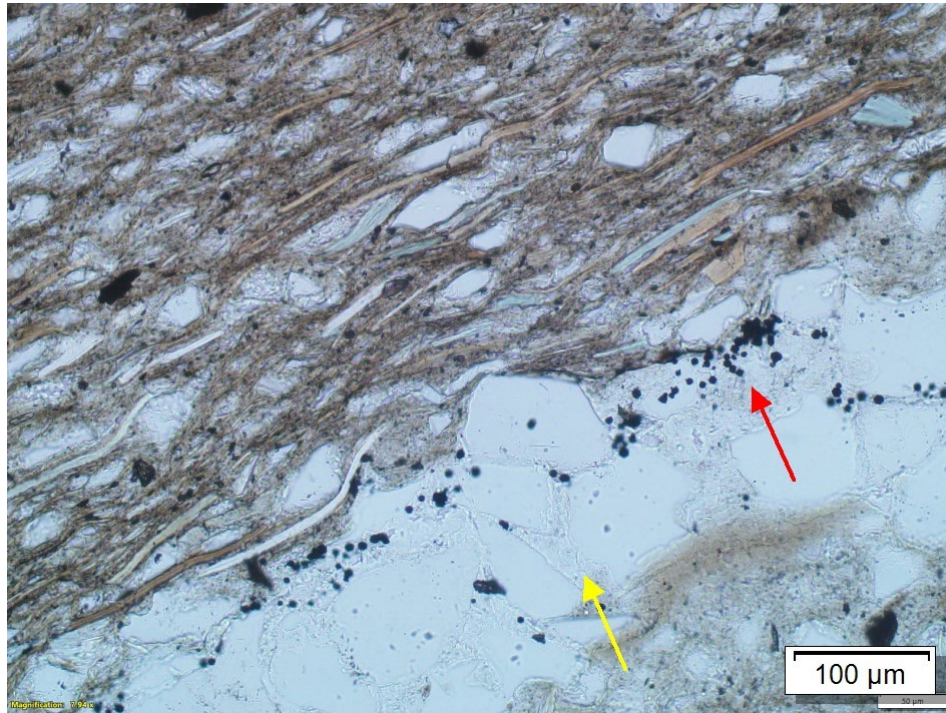
Figure 26*: Thin section photomicrograph of the Eau Claire Formation at depth 6,167 ft. The highly micaceous authigenic illite lamina in this sample also contains siliceous grains. The yellow arrow shows feldspar (orthoclase) cement, and the red arrow denotes authigenic framboidal pyrite.*
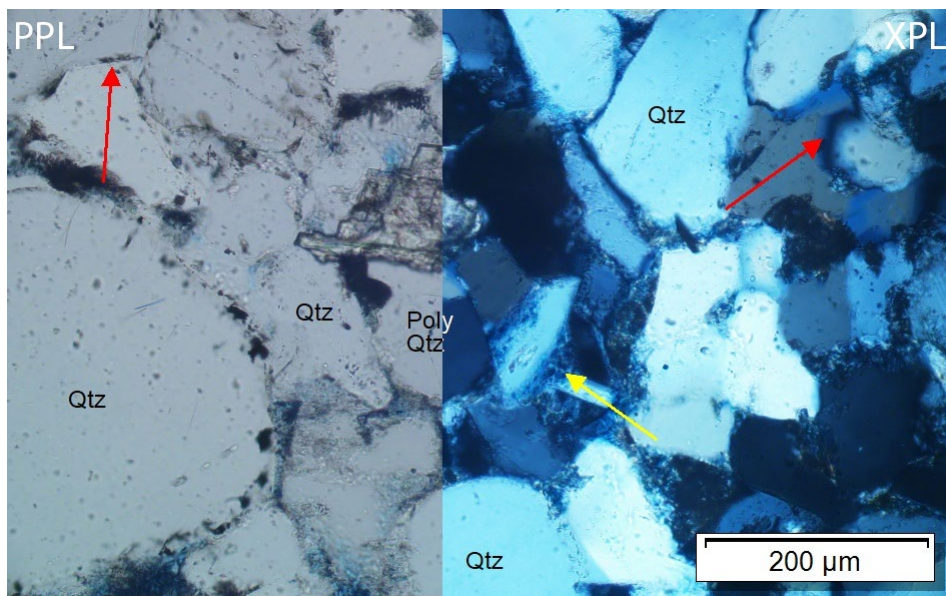
Figure 27*: Conjunct thin section photomicrograph in the Upper Mt. Simon at depth 6,171.3 ft. Red arrows point out quartz cement that dominates this region as well as the overgrowth sutures two grains on the right side. Yellow arrow shows illite cement filling pore space. Note the high relief calcite grain at the center of the image.*

MT. SIMON SANDSTONE
6,277 – 8,515 ft

Table 2: *(From top to bottom) Petrographic point count analysis from thin sections prepared from whole cores cut in the Mt. Simon Sandstone, including detrital grains, authigenic cements, and porosity analysis.*

Whole Core	Authigenic Mineral						
	Carbonate		Illite				
Depth	Dolomite	Calcite	Pore Filling	Clay lining	Kaolinite	Feldspar	Quartz
7902.2	0.00%	0.00%	1.80%	2.80%	0.00%	5.79%	19.28%
7904.4	0.00%	0.00%	4.75%	2.08%	0.99%	0.30%	20.30%
7905.3	0.00%	0.00%	15.02%	0.80%	0.00%	31.03%	4.80%
7906	0.00%	0.00%	6.80%	7.00%	0.00%	8.30%	15.80%
7911	0.00%	0.00%	9.36%	5.84%	0.00%	11.17%	9.86%
7912	0.00%	0.00%	7.31%	4.31%	0.00%	8.12%	20.54%
7912.55	0.00%	1.49%	3.27%	2.48%	0.99%	0.30%	9.23%
7914.9	0.00%	0.00%	6.07%	1.57%	0.52%	17.07%	11.83%
7916	0.00%	0.00%	3.99%	1.79%	0.00%	2.59%	8.97%
7917	0.00%	0.00%	9.30%	5.80%	0.00%	9.50%	23.50%
7917.6	0.00%	1.96%	1.27%	0.00%	0.00%	39.20%	11.05%
7918.3	0.00%	0.00%	1.79%	0.80%	0.50%	5.58%	17.73%
7920	0.00%	0.00%	4.15%	6.53%	0.00%	5.49%	21.24%
7922.2	0.00%	0.00%	7.02%	3.81%	0.00%	9.83%	18.05%
7923	0.00%	0.00%	2.50%	5.99%	0.00%	3.50%	15.98%
7925	0.00%	0.00%	4.33%	2.01%	0.50%	11.87%	20.62%
7926	0.00%	0.00%	3.83%	4.33%	0.00%	6.05%	18.65%
7929	0.00%	0.00%	12.94%	10.41%	0.30%	7.18%	10.62%
7930.5	0.00%	0.00%	5.56%	4.55%	0.81%	11.63%	15.98%
7931.2	0.00%	0.30%	0.30%	0.30%	0.30%	1.79%	10.25%
7932.3	0.00%	0.00%	7.50%	4.27%	0.00%	13.97%	15.91%
7933.55	0.00%	0.00%	6.57%	2.83%	0.00%	13.43%	14.44%
7934.9	0.00%	0.00%	5.59%	1.68%	0.00%	6.26%	12.86%
7937.5	0.00%	0.00%	0.00%	0.80%	0.00%	0.50%	16.97%
7940.5	0.00%	0.00%	22.66%	9.74%	0.00%	0.00%	0.00%
7942.7	0.00%	0.00%	1.50%	17.95%	0.00%	4.09%	11.27%
7944.3	0.00%	0.00%	0.50%	0.50%	3.81%	14.63%	9.82%
7947.4	0.00%	0.00%	3.02%	3.02%	0.30%	10.36%	18.11%
7955.2	0.00%	0.00%	4.81%	5.52%	0.00%	7.82%	8.83%
7958.5	0.00%	0.00%	3.50%	4.80%	0.30%	7.10%	13.50%
7959	0.00%	0.00%	0.00%	7.28%	0.00%	0.50%	18.94%
7960.3	0.00%	0.00%	1.00%	1.79%	1.50%	8.28%	9.47%
7963	0.00%	0.00%	4.98%	4.48%	0.00%	1.29%	18.43%
7964	0.00%	0.00%	2.79%	11.75%	0.00%	7.77%	19.22%
7965	0.00%	0.00%	3.02%	4.83%	0.30%	11.87%	13.08%
7969.7	0.00%	0.00%	7.81%	1.27%	0.00%	1.27%	12.99%
7973.5	0.00%	0.00%	3.79%	1.00%	0.00%	0.00%	17.47%
7977.5	0.00%	0.00%	3.49%	6.77%	0.00%	3.78%	3.98%
7978.2	0.00%	0.00%	1.00%	3.98%	0.00%	3.29%	10.26%
7986	0.00%	0.00%	1.99%	3.28%	0.00%	2.09%	9.75%
7991.3	0.00%	0.00%	3.29%	3.98%	0.00%	1.29%	9.26%
7996.5	1.99%	0.00%	11.47%	5.48%	0.00%	1.00%	7.98%
8001.8	41.92%	0.00%	0.50%	0.00%	0.00%	0.00%	0.00%
8002.7	43.51%	0.00%	0.00%	0.00%	0.00%	0.00%	0.30%
8003.35	23.43%	0.00%	0.80%	0.00%	0.00%	0.80%	0.30%
8009	0.00%	0.00%	0.80%	1.49%	0.00%	2.29%	13.23%
8011.7	0.00%	0.00%	1.51%	0.50%	0.00%	3.33%	15.12%
8016.6	19.96%	0.00%	0.30%	0.00%	0.00%	0.30%	0.30%

| Whole Core | Detrital | | | | | | | | | | | |
| | Lithics | | | | | Matrix | Feldspar | | Quartz | | Mica | |
Depth	Granitic	Rhyolite	Sedimentary	Zircon	Oxides	Illitic	Plagioclase	Orthoclase	Monocrystalline	Polycrystalline	Muscovite	Biotite
7902.2	0.00%	0.00%	0.00%	0.00%	0.00%	0.00%	5.99%	15.48%	41.26%	0.30%	0.00%	0.00%
7904.4	0.79%	0.00%	0.99%	0.50%	1.58%	0.00%	0.99%	25.74%	33.47%	0.79%	0.30%	0.00%
7905.3	0.00%	0.00%	0.00%	0.00%	0.00%	0.00%	4.50%	22.02%	21.82%	0.00%	0.00%	0.00%
7906	0.00%	0.00%	0.00%	0.00%	0.00%	0.00%	4.50%	15.00%	32.30%	0.00%	0.00%	0.00%
7911	0.00%	0.00%	0.00%	0.00%	0.00%	0.00%	3.02%	20.42%	30.99%	0.00%	0.00%	0.00%
7912	0.00%	0.00%	0.00%	0.00%	0.00%	0.00%	5.81%	13.03%	31.06%	0.00%	0.00%	0.00%
7912.55	0.50%	0.00%	0.50%	0.30%	1.79%	0.00%	0.99%	27.58%	34.52%	2.78%	0.00%	0.00%
7914.9	0.00%	0.00%	0.00%	0.00%	0.00%	0.00%	7.12%	18.64%	28.27%	0.00%	0.00%	0.00%
7916	0.00%	0.00%	0.00%	0.00%	0.00%	40.88%	2.79%	13.26%	25.42%	0.00%	0.00%	0.00%
7917	0.00%	0.00%	0.00%	0.00%	0.00%	0.00%	3.00%	16.30%	31.30%	0.00%	0.00%	0.00%
7917.6	0.00%	0.00%	0.00%	0.00%	0.00%	0.00%	4.30%	30.60%	11.05%	0.00%	0.00%	0.00%
7918.3	0.00%	0.00%	0.00%	0.00%	0.00%	2.79%	3.29%	16.93%	47.81%	0.00%	0.00%	0.00%
7920	0.00%	0.00%	0.00%	0.00%	0.00%	0.00%	1.35%	10.16%	49.22%	0.00%	0.00%	0.00%
7922.2	0.00%	0.00%	0.00%	0.00%	0.00%	0.00%	3.31%	11.53%	38.11%	0.00%	0.00%	0.00%
7923	0.00%	0.00%	0.00%	0.00%	0.00%	0.00%	4.00%	11.79%	43.76%	0.00%	0.00%	0.00%
7925	0.00%	0.00%	0.00%	0.00%	0.00%	0.00%	3.02%	13.58%	35.71%	0.00%	0.00%	0.00%
7926	0.00%	0.00%	0.00%	0.00%	0.00%	0.00%	6.55%	12.40%	38.10%	0.00%	0.00%	0.00%
7929	0.00%	0.00%	0.00%	0.00%	0.00%	0.00%	2.53%	11.93%	39.23%	0.00%	0.00%	0.00%
7930.5	0.00%	0.00%	0.00%	0.00%	0.00%	0.00%	4.35%	10.11%	40.95%	0.00%	0.00%	0.00%
7931.2	1.00%	1.99%	0.00%	0.00%	2.29%	0.00%	2.79%	30.85%	42.59%	0.50%	0.00%	0.00%
7932.3	0.00%	0.00%	0.00%	0.00%	0.00%	0.00%	6.21%	23.29%	27.17%	0.00%	0.00%	0.00%
7933.55	0.00%	0.00%	0.00%	0.00%	0.00%	0.00%	2.32%	15.66%	32.63%	0.00%	0.00%	0.00%
7934.9	0.00%	0.00%	0.00%	0.00%	0.00%	0.00%	6.71%	22.37%	39.71%	0.00%	0.00%	0.00%
7937.5	1.30%	1.00%	0.50%	0.00%	0.00%	0.00%	1.50%	27.74%	36.93%	3.99%	0.00%	0.00%
7940.5	0.00%	0.00%	1.29%	0.00%	1.29%	0.00%	1.99%	60.14%	0.00%	0.00%	2.29%	0.60%
7942.7	0.00%	0.00%	0.00%	0.00%	0.00%	0.00%	2.29%	17.75%	39.38%	0.00%	0.00%	0.00%
7944.3	0.00%	0.00%	0.00%	0.00%	0.00%	0.00%	8.82%	27.05%	31.56%	0.00%	0.00%	0.00%
7947.4	0.00%	0.00%	0.00%	0.00%	0.00%	0.00%	3.52%	10.36%	45.77%	0.00%	0.00%	0.00%
7955.2	0.00%	0.00%	0.00%	0.00%	0.00%	0.00%	3.01%	16.55%	41.42%	0.00%	0.00%	0.00%
7958.5	0.00%	0.00%	0.00%	0.00%	0.00%	0.00%	1.00%	14.00%	44.50%	0.00%	0.00%	0.00%
7959	5.48%	0.30%	0.00%	0.00%	0.50%	0.00%	2.99%	14.96%	35.19%	0.30%	0.30%	0.00%
7960.3	0.00%	0.00%	0.00%	0.00%	0.00%	0.00%	5.78%	18.25%	40.68%	0.00%	0.00%	0.00%
7963	4.78%	1.00%	0.00%	0.30%	0.30%	0.00%	0.50%	17.73%	36.85%	0.30%	0.00%	0.00%
7964	0.00%	0.50%	0.00%	0.00%	0.00%	0.00%	1.29%	15.24%	30.68%	0.30%	0.00%	0.00%
7965	0.00%	0.00%	0.00%	0.00%	0.00%	0.00%	3.02%	18.61%	34.21%	0.00%	0.00%	0.00%
7969.7	2.93%	1.76%	0.00%	0.29%	0.00%	0.29%	0.29%	30.27%	21.00%	12.70%	0.49%	0.00%
7973.5	4.29%	0.50%	0.00%	0.00%	0.50%	0.50%	0.50%	26.95%	31.74%	0.30%	0.00%	0.00%
7977.5	1.99%	0.00%	0.00%	0.00%	0.30%	0.00%	0.00%	27.69%	41.14%	0.30%	0.00%	0.00%
7978.2	1.29%	0.00%	0.00%	0.30%	0.30%	0.00%	0.00%	32.67%	33.86%	0.80%	0.00%	0.00%
7986	2.79%	0.00%	0.80%	0.50%	0.00%	0.00%	0.00%	23.68%	34.13%	11.74%	0.00%	0.00%
7991.3	2.29%	0.00%	0.30%	0.00%	0.50%	0.00%	0.00%	36.35%	34.36%	0.80%	0.30%	0.00%
7996.5	0.50%	0.00%	0.00%	0.50%	0.50%	17.75%	0.30%	27.22%	21.73%	1.50%	1.79%	0.00%
8001.8	0.00%	0.00%	0.00%	0.00%	0.80%	30.44%	0.00%	14.27%	11.78%	0.00%	0.30%	0.00%
8002.7	4.49%	0.00%	0.00%	0.00%	0.00%	0.00%	1.00%	19.76%	29.44%	1.50%	0.00%	0.00%
8003.35	8.28%	0.00%	2.49%	0.00%	0.00%	0.00%	2.29%	20.44%	36.69%	3.99%	0.00%	0.00%
8009	5.77%	0.30%	9.55%	0.00%	0.00%	0.00%	1.99%	13.93%	42.59%	1.99%	0.00%	0.00%
8011.7	4.54%	0.00%	2.02%	0.00%	0.30%	0.00%	0.30%	10.08%	54.74%	4.03%	0.00%	0.00%
8016.6	0.50%	0.79%	1.59%	0.30%	0.30%	0.30%	1.99%	36.74%	35.05%	1.29%	0.30%	0.00%

| Whole Core	Porosity	
Depth	Intergranular	Intragranular
7902.2	7.29%	0.00%
7904.4	3.47%	2.97%
7905.3	0.00%	0.00%
7906	10.30%	0.00%
7911	9.36%	0.00%
7912	9.82%	0.00%
7912.55	10.71%	2.58%
7914.9	8.90%	0.00%
7916	0.30%	0.00%
7917	1.30%	0.00%
7917.6	0.59%	0.00%
7918.3	2.79%	0.00%
7920	1.87%	0.00%
7922.2	8.32%	0.00%
7923	12.49%	0.00%
7925	8.35%	0.00%
7926	10.08%	0.00%
7929	4.85%	0.00%
7930.5	6.07%	0.00%
7931.2	1.79%	2.99%
7932.3	1.68%	0.00%
7933.55	12.12%	0.00%
7934.9	4.81%	0.00%
7937.5	5.99%	2.79%
7940.5	0.00%	0.00%
7942.7	5.78%	0.00%
7944.3	3.31%	0.00%
7947.4	5.53%	0.00%
7955.2	12.04%	0.00%
7958.5	11.30%	0.00%
7959	8.77%	4.49%
7960.3	13.26%	0.00%
7963	2.79%	6.27%
7964	10.46%	0.00%
7965	11.07%	0.00%
7969.7	4.20%	2.44%
7973.5	9.98%	2.50%
7977.5	7.27%	3.29%
7978.2	8.47%	3.78%
7986	7.96%	1.29%
7991.3	5.48%	1.79%
7996.5	0.30%	0.00%
8001.8	0.00%	0.00%
8002.7	0.00%	0.00%
8003.35	0.00%	0.50%
8009	3.78%	2.29%
8011.7	1.51%	2.02%
8016.6	0.00%	0.00%

Table 3: (From top to bottom) Petrographic point count analysis from thin sections prepared from rotary sidewall cores cut in the Mt. Simon Sandstone, including detrital grains, authigenic cements, and porosity analysis.

| Rotary Side-wall Core | Detrital | | | | | |
| | Lithics | Matrix | Feldspar | | Quartz | |
Depth	Rhyolite	Illitic	Anorthite2	Orthoclase2	Monocrystalli	Polycrystal
6300.93	0.00%	0.00%	18.50%	0.80%	51.80%	0.80%
6479.94	0.00%	0.00%	9.30%	0.80%	58.50%	1.00%
6564.11	0.00%	0.00%	2.00%	0.50%	79.80%	0.00%
6699.94	0.00%	0.00%	3.30%	0.30%	65.30%	1.00%
6736	0.00%	0.00%	2.00%	0.30%	70.50%	0.00%
6776.06	0.00%	0.00%	2.30%	0.00%	72.80%	0.00%
6799.97	0.00%	0.00%	1.50%	0.00%	72.30%	1.50%
6866.02	0.00%	0.00%	3.80%	0.50%	66.30%	0.00%
7193.09	0.00%	0.00%	1.80%	0.00%	75.30%	0.00%
7200.01	0.00%	0.00%	3.30%	0.80%	68.00%	0.50%
7234.98	0.00%	0.00%	3.50%	0.80%	75.00%	0.30%
7400.06	0.00%	0.00%	2.00%	0.50%	67.00%	0.00%
7460.04	0.00%	0.00%	0.50%	0.00%	78.00%	0.00%
7476.6	0.00%	0.00%	1.50%	0.30%	73.50%	0.00%
7499.91	0.00%	0.00%	0.80%	0.00%	80.30%	0.50%
7519.98	0.00%	0.00%	4.80%	1.80%	73.00%	0.00%
7539.93	0.00%	0.00%	3.30%	0.50%	76.00%	0.30%
7554.94	0.00%	0.00%	0.80%	0.00%	82.30%	0.30%
7596.08	0.00%	0.00%	3.50%	0.80%	76.00%	0.00%
7599.95	0.00%	0.00%	7.50%	8.80%	65.50%	0.80%
7619.97	0.00%	0.00%	2.00%	0.50%	77.80%	0.50%
7649.95	0.00%	0.00%	5.80%	0.50%	75.50%	0.80%
7682.02	0.00%	0.00%	2.80%	1.50%	77.50%	0.30%
7705.05	0.00%	0.00%	0.00%	0.00%	0.00%	0.00%
7714.02	0.00%	0.00%	5.50%	0.80%	64.50%	0.00%
7725.98	0.00%	0.00%	3.30%	4.00%	67.50%	0.00%
7750	0.30%	0.00%	4.00%	6.80%	58.80%	2.00%
7757.97	0.00%	0.00%	2.80%	3.30%	74.00%	1.80%
7765.05	0.30%	0.00%	3.50%	11.00%	54.00%	0.80%
7772.92	0.00%	0.00%	0.80%	6.30%	58.30%	0.30%
7800.06	0.00%	0.00%	1.00%	4.80%	52.30%	11.00%
7825.9	0.00%	0.00%	3.50%	17.50%	44.00%	0.30%
7845.08	0.00%	0.00%	1.80%	6.00%	66.30%	0.00%
7877.96	0.00%	0.00%	1.70%	6.50%	16.40%	0.00%
7911.07	0.00%	0.00%	0.30%	10.80%	49.80%	0.00%
8133.97	0.00%	0.00%	5.30%	3.50%	67.00%	3.80%
8134.06	0.00%	0.00%	3.80%	3.00%	62.00%	2.30%
8144	0.00%	0.00%	2.00%	2.50%	69.80%	3.00%
8164.98	0.00%	0.00%	2.00%	0.80%	69.00%	0.80%
8170.08	0.00%	0.00%	0.50%	2.00%	74.50%	0.30%
8178.07	0.00%	0.00%	1.00%	2.00%	77.80%	0.80%
8324.03	0.00%	0.00%	0.30%	0.80%	49.50%	13.30%
8330.07	0.00%	0.00%	0.50%	0.30%	62.00%	0.50%
8339.95	0.00%	0.00%	0.30%	1.00%	72.80%	3.00%
8360	0.00%	0.00%	0.00%	0.30%	67.30%	10.50%
8410.1	0.80%	0.00%	4.30%	4.30%	51.00%	10.00%
8435.95	0.00%	0.00%	0.80%	1.50%	60.30%	2.50%
8460.09	0.30%	0.00%	0.50%	1.80%	72.30%	0.50%

Rotary Side-wall Core Depth	Authigenic Mineral						
	Carbonates	Illite		Kaolinite	Anorthite	Orthoclase	Quartz
		Pore Filling	clay lining				
6300.93	0.00%	0.00%	1.80%	0.00%	0.00%	20.80%	18.50%
6479.94	0.00%	0.00%	2.00%	0.00%	0.00%	18.00%	9.30%
6564.11	0.00%	0.00%	1.00%	0.00%	0.00%	8.00%	2.00%
6699.94	0.00%	0.00%	1.00%	0.00%	0.00%	17.80%	3.30%
6736	0.00%	0.00%	1.80%	0.00%	0.00%	13.80%	2.00%
6776.06	0.00%	0.00%	1.30%	0.00%	0.00%	13.80%	2.30%
6799.97	0.00%	0.00%	0.80%	0.00%	0.00%	16.00%	1.50%
6866.02	0.00%	0.00%	0.80%	0.00%	0.00%	14.00%	3.80%
7193.09	0.00%	0.00%	1.80%	0.00%	0.00%	16.80%	1.80%
7200.01	0.00%	0.00%	2.50%	0.00%	0.00%	11.50%	3.30%
7234.98	0.00%	0.00%	3.30%	0.00%	0.00%	4.80%	3.50%
7400.06	0.00%	0.00%	2.30%	0.00%	0.00%	15.50%	2.00%
7460.04	0.00%	0.00%	0.80%	0.00%	0.00%	5.80%	0.50%
7476.6	0.00%	0.00%	4.00%	0.00%	0.00%	15.50%	1.50%
7499.91	0.00%	0.00%	1.80%	0.00%	0.00%	11.00%	0.80%
7519.98	0.00%	0.00%	1.80%	0.00%	0.00%	11.00%	4.80%
7539.93	0.00%	0.00%	1.80%	0.00%	0.00%	10.30%	3.30%
7554.94	0.00%	0.00%	1.80%	0.00%	0.00%	9.00%	0.80%
7596.08	0.00%	0.00%	5.80%	0.00%	0.00%	6.80%	3.50%
7599.95	0.00%	0.00%	3.80%	0.00%	0.00%	6.30%	7.50%
7619.97	0.00%	0.00%	2.80%	0.00%	0.00%	16.50%	2.00%
7649.95	0.00%	0.00%	5.50%	0.00%	0.00%	11.30%	5.80%
7682.02	0.00%	0.00%	0.80%	0.00%	0.00%	9.80%	2.80%
7705.05	0.00%	0.00%	0.00%	0.00%	0.00%	0.00%	0.00%
7714.02	0.00%	0.00%	4.50%	0.00%	0.00%	14.50%	5.50%
7725.98	0.00%	1.50%	2.30%	0.00%	0.00%	12.00%	3.30%
7750	0.00%	0.80%	0.30%	0.00%	0.00%	13.30%	4.00%
7757.97	0.00%	0.30%	0.30%	0.00%	0.00%	10.30%	2.80%
7765.05	0.00%	1.30%	2.80%	0.00%	0.00%	18.00%	3.50%
7772.92	0.00%	2.00%	3.50%	0.00%	0.00%	14.80%	0.80%
7800.06	0.00%	0.00%	1.50%	0.00%	0.00%	26.30%	1.00%
7825.9	0.00%	1.00%	3.30%	0.00%	0.00%	18.30%	3.50%
7845.08	0.00%	1.00%	1.50%	0.00%	0.00%	15.80%	1.80%
7877.96	70.10%	0.00%	2.70%	0.00%	70.10%	0.50%	1.70%
7911.07	0.00%	0.00%	17.50%	0.00%	0.00%	11.30%	0.30%
8133.97	0.00%	0.00%	13.30%	0.00%	0.00%	2.30%	5.30%
8134.06	0.00%	0.00%	23.80%	0.00%	0.00%	4.50%	3.80%
8144	0.00%	0.00%	12.50%	0.00%	0.00%	7.00%	2.00%
8164.98	0.00%	0.50%	4.30%	0.00%	0.00%	3.80%	2.00%
8170.08	0.00%	0.00%	5.00%	0.00%	0.00%	6.50%	0.50%
8178.07	0.00%	0.00%	2.50%	0.00%	0.00%	5.50%	1.00%
8324.03	0.00%	0.00%	31.30%	0.00%	0.00%	1.50%	0.30%
8330.07	0.00%	0.00%	25.50%	0.00%	0.00%	4.80%	0.50%
8339.95	0.00%	0.00%	8.50%	0.00%	0.00%	7.50%	0.30%
8360	0.00%	0.30%	5.50%	0.00%	0.00%	6.00%	0.00%
8410.1	0.00%	0.00%	4.50%	0.00%	0.00%	8.50%	4.30%
8435.95	0.00%	0.00%	28.50%	0.00%	0.00%	2.80%	0.80%
8460.09	0.00%	0.00%	1.80%	0.00%	0.00%	10.50%	0.50%

Rotary Side-wall Core Depth	Porosity Undifferentiated
6300.93	5.30%
6479.94	10.50%
6564.11	8.00%
6699.94	11.50%
6736	11.80%
6776.06	9.80%
6799.97	8.00%
6866.02	14.80%
7193.09	4.50%
7200.01	13.50%
7234.98	12.50%
7400.06	12.80%
7460.04	15.00%
7476.6	5.30%
7499.91	5.80%
7519.98	7.80%
7539.93	8.00%
7554.94	6.00%
7596.08	7.30%
7599.95	7.50%
7619.97	0.00%
7649.95	0.80%
7682.02	7.50%
7705.05	0.00%
7714.02	9.80%
7725.98	9.30%
7750	13.00%
7757.97	7.30%
7765.05	7.00%
7772.92	11.00%
7800.06	2.80%
7825.9	8.50%
7845.08	6.80%
7877.96	0.00%
7911.07	5.30%
8133.97	5.00%
8134.06	0.80%
8144	3.30%
8164.98	19.00%
8170.08	11.30%
8178.07	10.50%
8324.03	3.30%
8330.07	6.30%
8339.95	6.50%
8360	9.30%
8410.1	12.50%
8435.95	3.50%
8460.09	12.00%
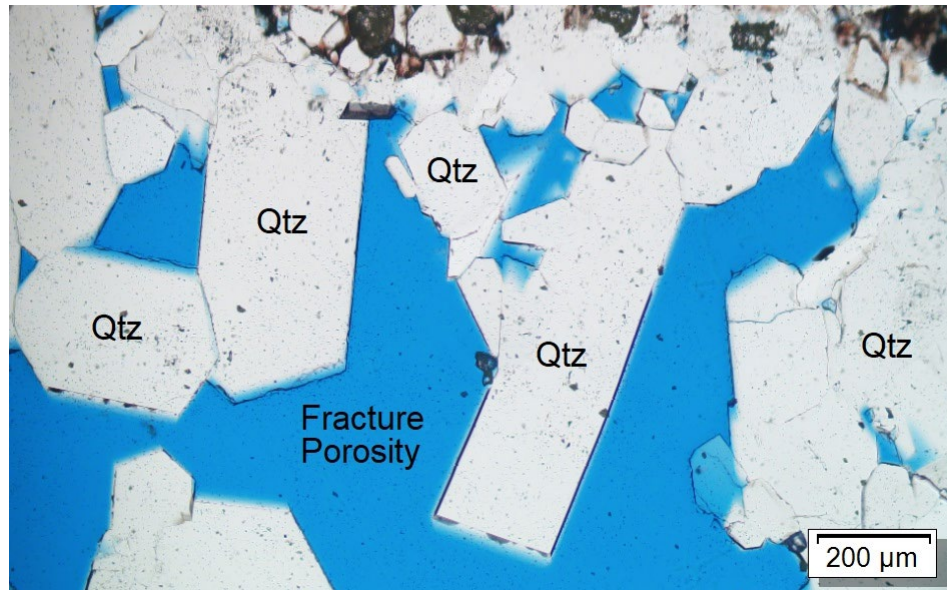
Figure 28: *Thin section photomicrograph of the Mt. Simon Sandstone at depth 7,904.4 ft. A prominent fracture has allowed for large quartz overgrowths to form into the void. Other small fractures are present at 7,931.2 ft depth. Note the hematite staining on grain boundaries near the top of the image, which predates quartz cement.*
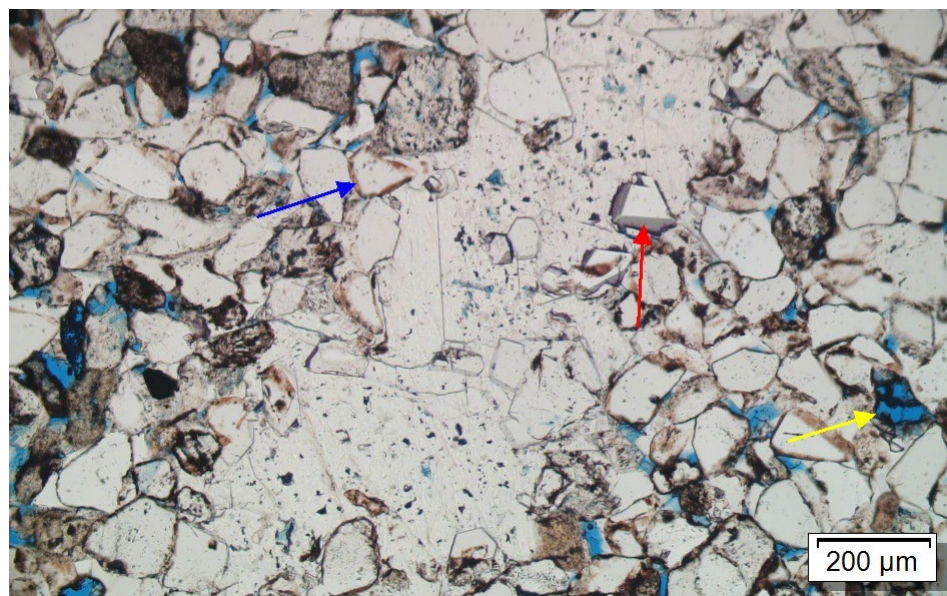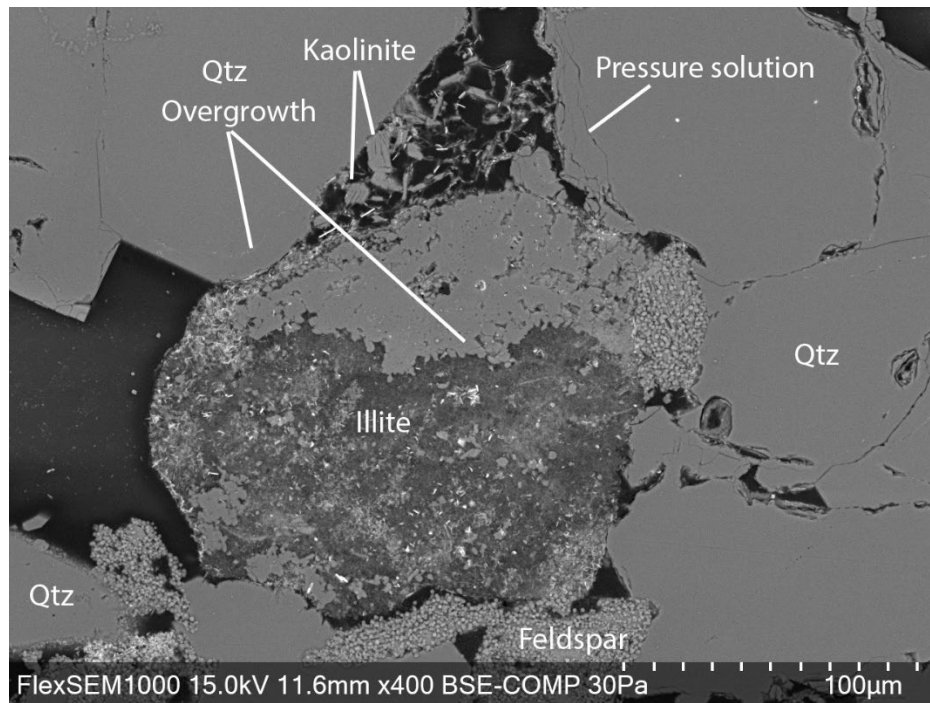

Figure 29: *Thin section photomicrograph of the Mt. Simon Sandstone at depth 7,912.55 ft. A vein of carbonaceous minerals (discussed in Figure 30) features crystalline calcite grains with compositional zoning (red arrow). Blue arrow shows hematite coating; yellow arrow shows a dissolved grain's remnant titanium oxide crust.*
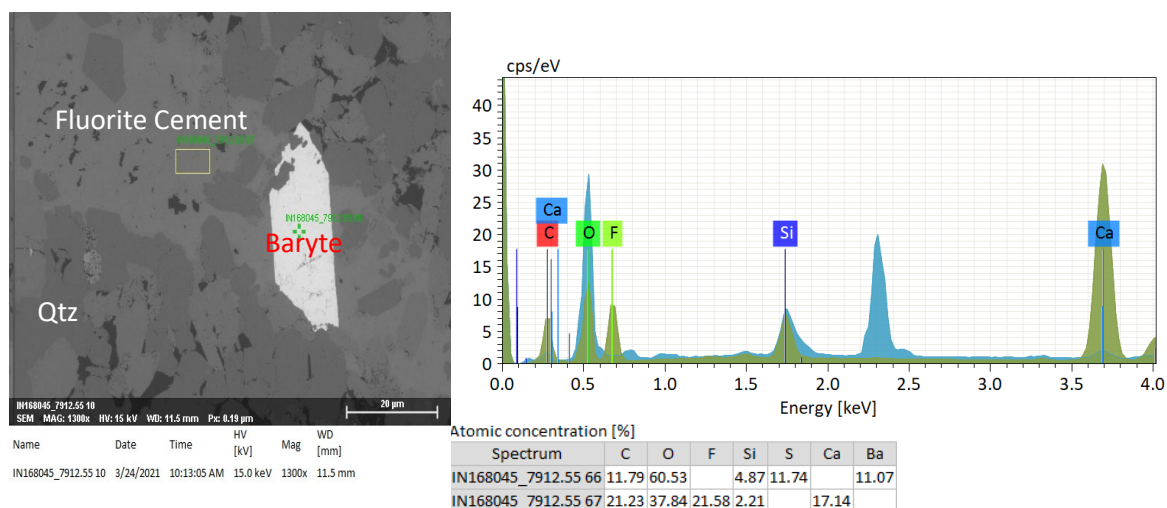
Figure 30: *SEM BSE thin section photomicrograph with Energy Dispersive Spectroscopy (EDS) analysis of the Mt. Simon Sandstone at depth 7,912.55 ft. Spot 66 shows the Barium sulfate peaks for the baryte, and spot 67 shows the carbonaceous cement that is also rich in fluorine. The EDS analysis shows that there is carbonate in the cement in addition to the fluorite.*
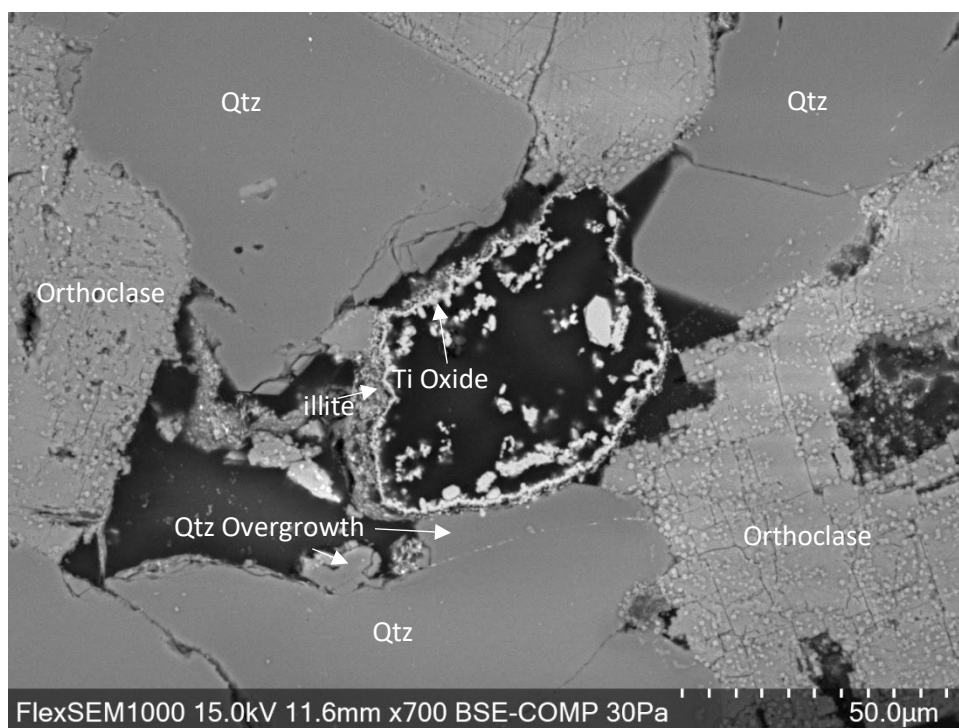
Figure 31: *SEM BSE thin section photomicrograph of the Mt. Simon Sandstone at depth 7,912.55 ft. Note the titanium oxide crust, as seen in Figure 29, and illite forming on the rim of the titanium oxide. Quartz and feldspar overgrowth are also common at this depth.*

Figure 31: *SEM BSE thin section photomicrograph of the Mt. Simon Sandstone at depth 7,912.55 ft. The highly altered grain in the center was likely an igneous fragment or a feldspar grain that is illitized and sericitized. The kaolinite and webby illite to the top of that grain helped to retain some pore space from being taken by the quartz overgrowth.*
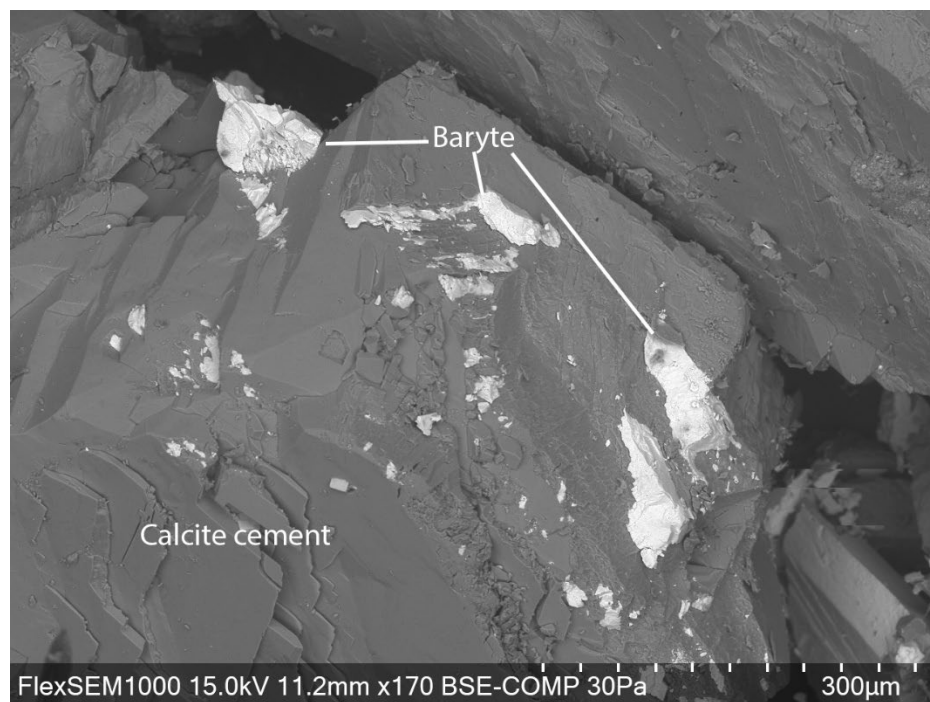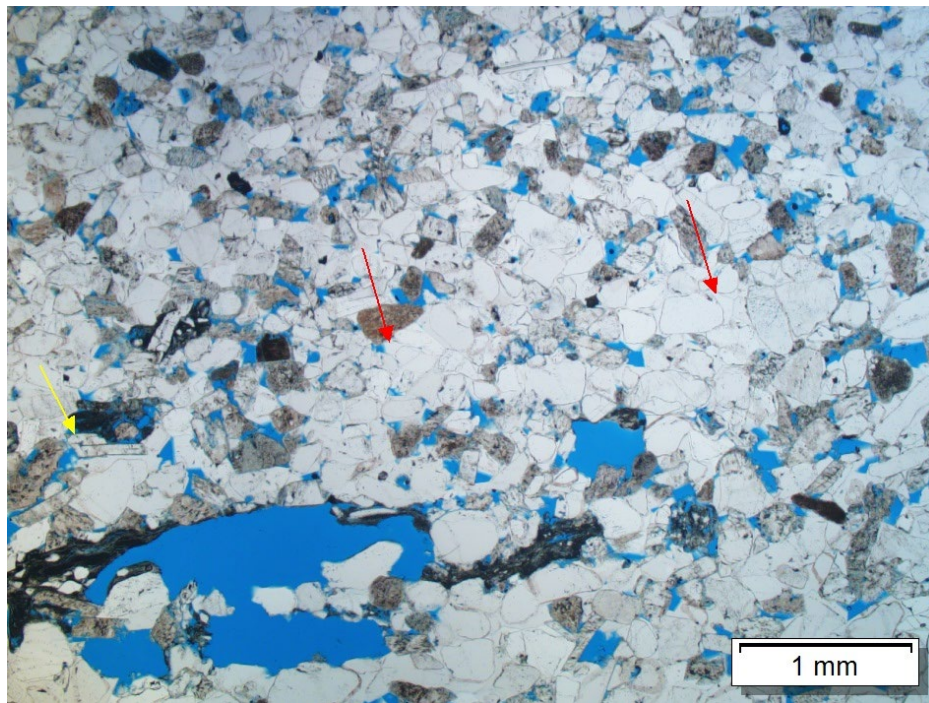

Figure 32: *SEM BSE photomicrograph of the Mt. Simon Sandstone at depth 7,926 ft. Baryte growing in the calcite cement was taken from a micro-fault/fracture that were effervescence with acid testing.*
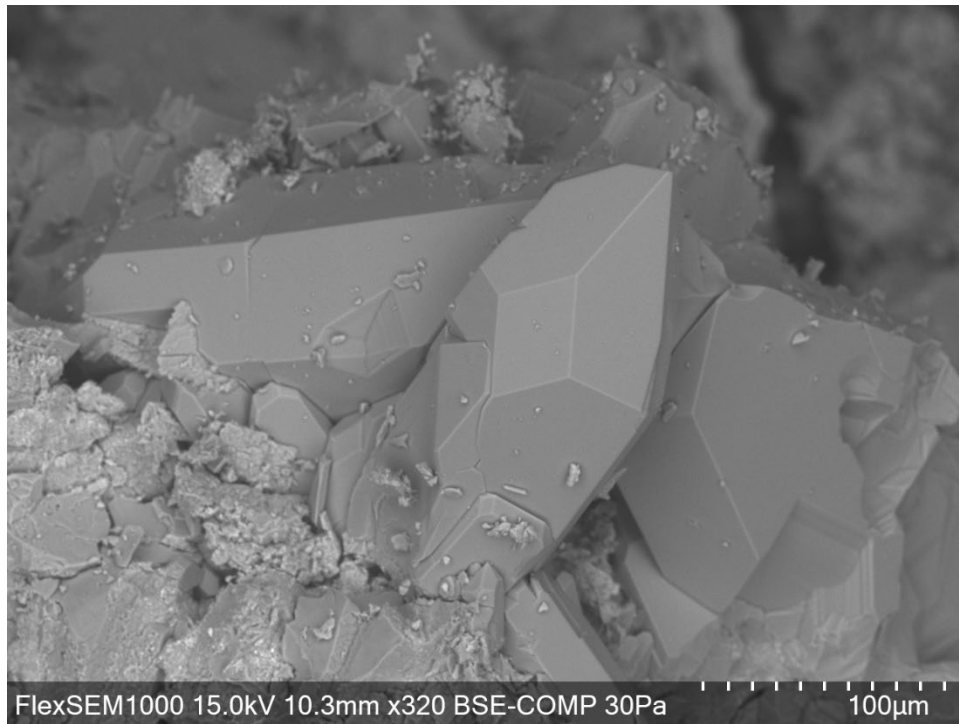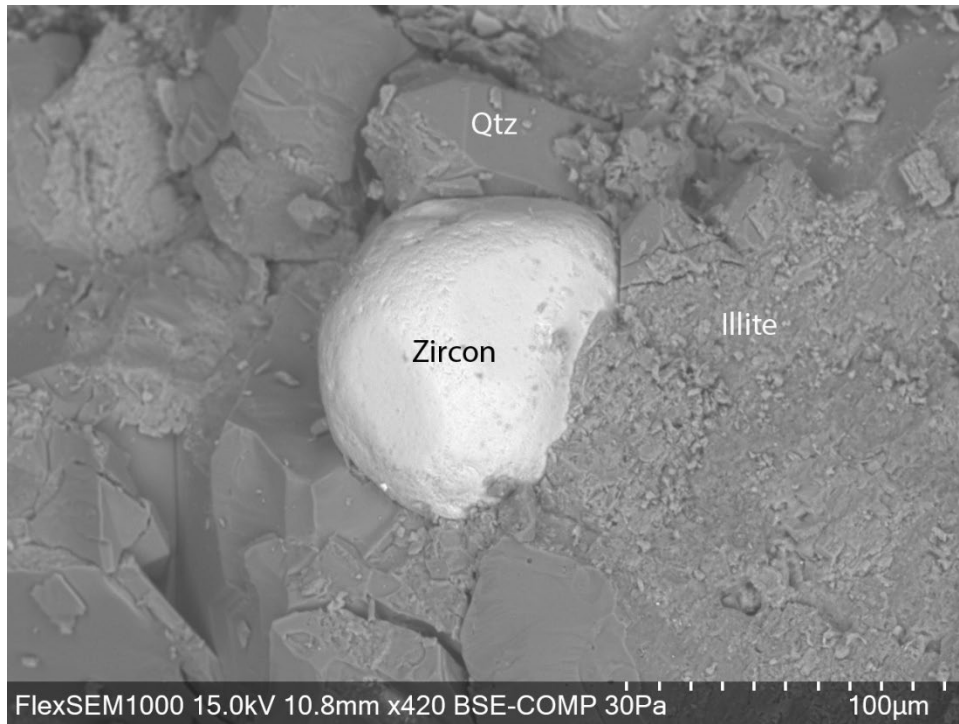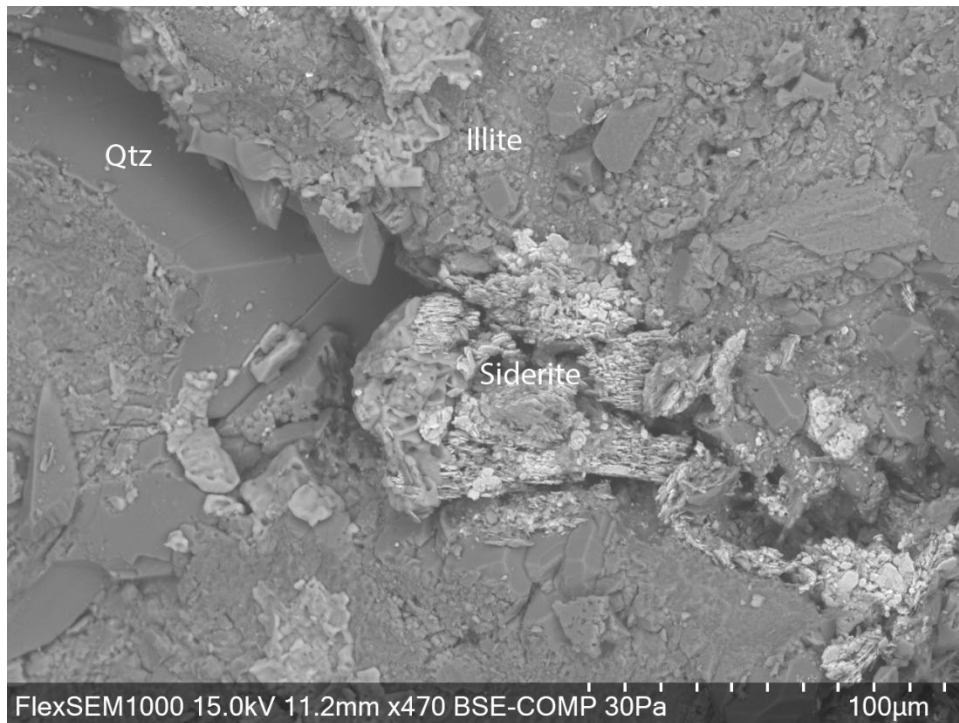
Figure 33: SEM BSE photomicrograph of the Mt. Simon Sandstone at depth 7,931.2 ft. A euhedral quartz overgrowth is surrounded by authigenic illite.

Figure 34: Thin section photomicrograph of the Mt. Simon Sandstone at depth 7,937.5 ft. Red arrows show quartz cement; yellow arrow shows feldspar overgrowth. Note the vugular porosity at lower left.
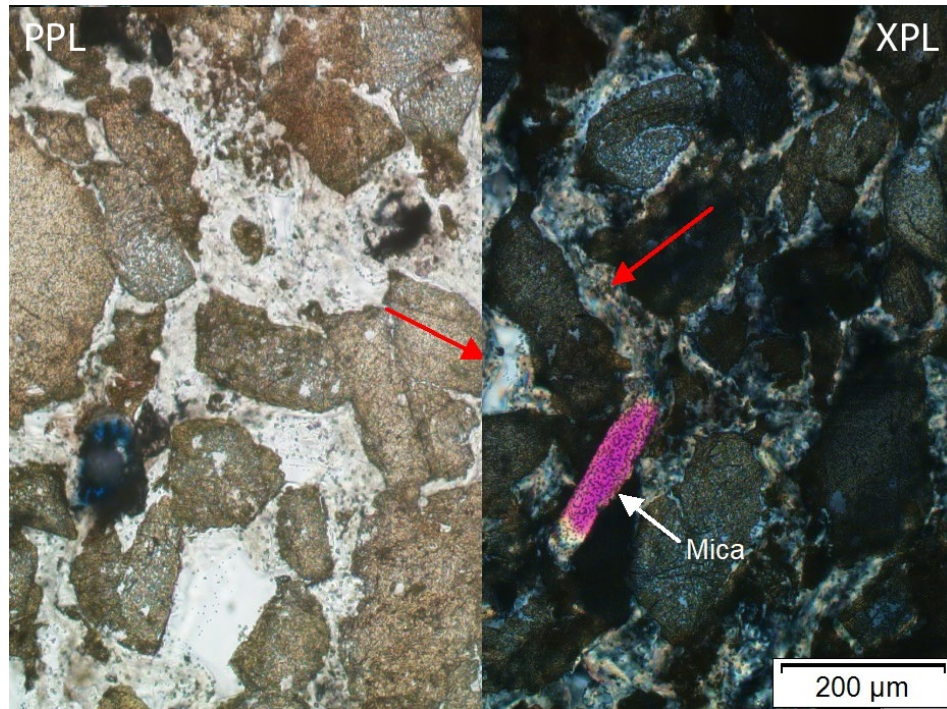
Figure 35*: SEM BSE section photomicrograph of the Upper Mt. Simon at depth 7,937.5 ft. A zircon grain is in-between quartz and authigenic illite.*
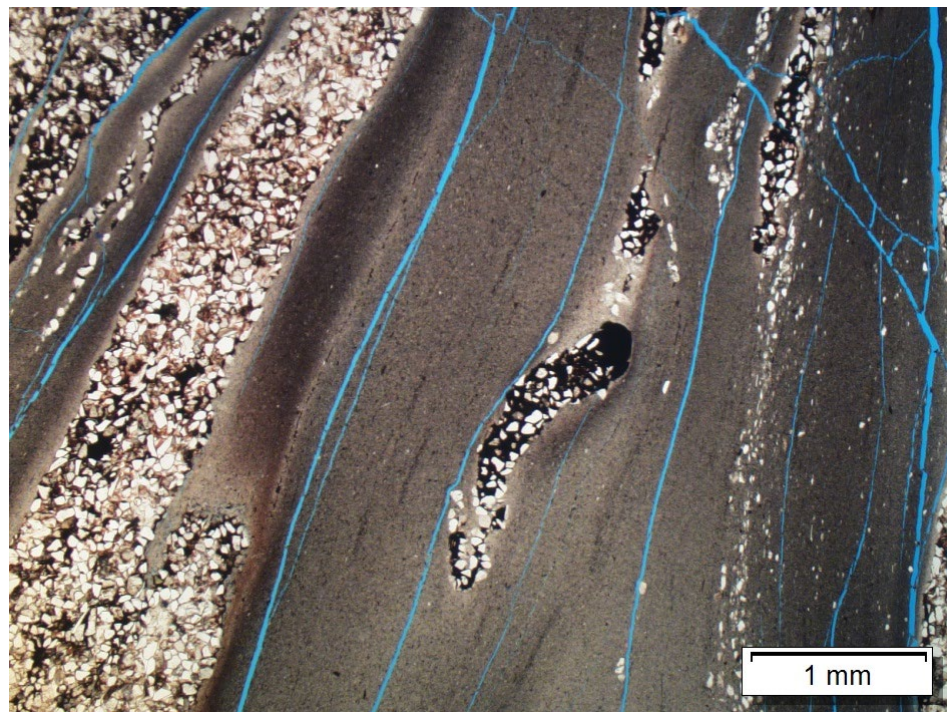

Figure 36*: SEM BSE section photomicrograph of the Upper Mt. Simon at depth 7,937.5 ft. A siderite clast is in-between quartz and authigenic illite.*
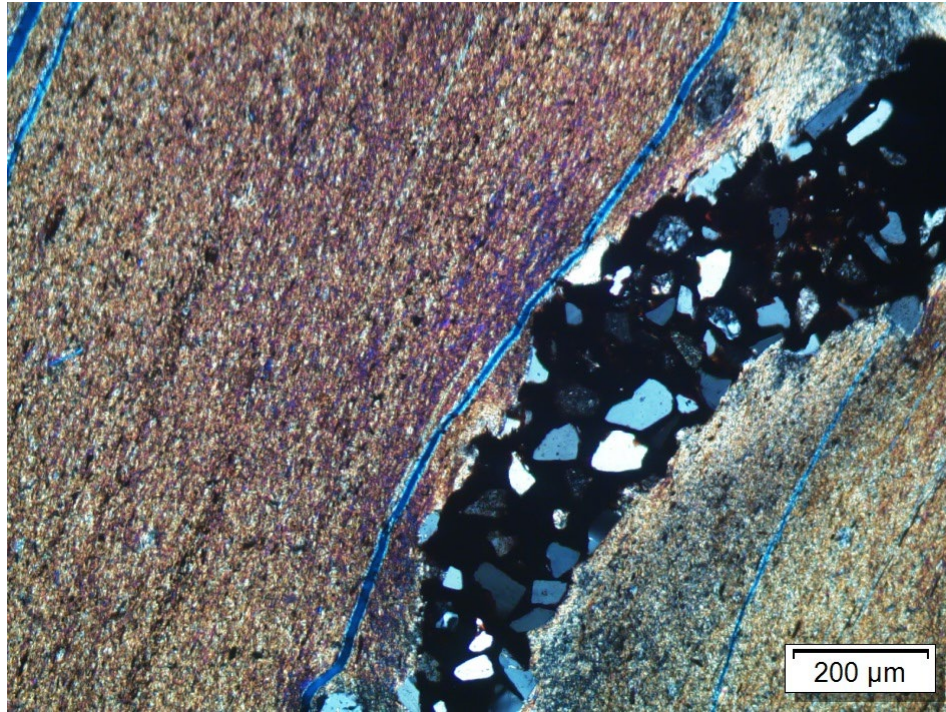
Figure 37*: Conjunct thin section photomicrograph of the Mt. Simon Sandstone at depth 7,940.5 ft. Red arrows show an arkose cemented by authigenic illite. Mica is denoted by the white arrow.*
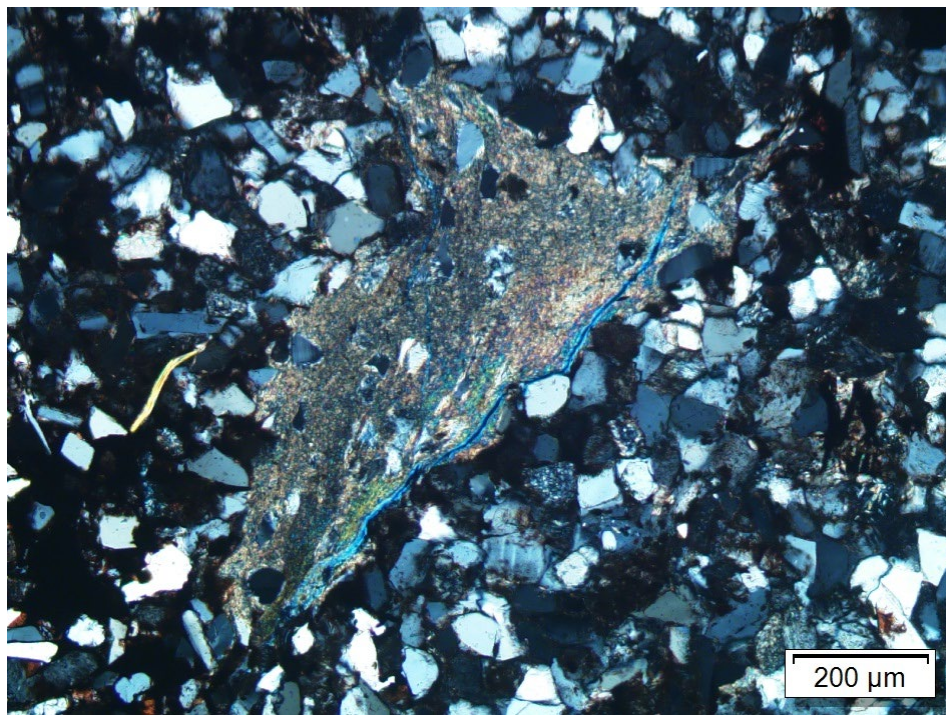

Figure 38*: Thin section photomicrograph of the Mt. Simon Sandstone at depth 7,996.5 ft. Thick clay laminations are interspersed between fine sand. Illite is heavily stained by hematite, as shown by the clast in the center of the image.*
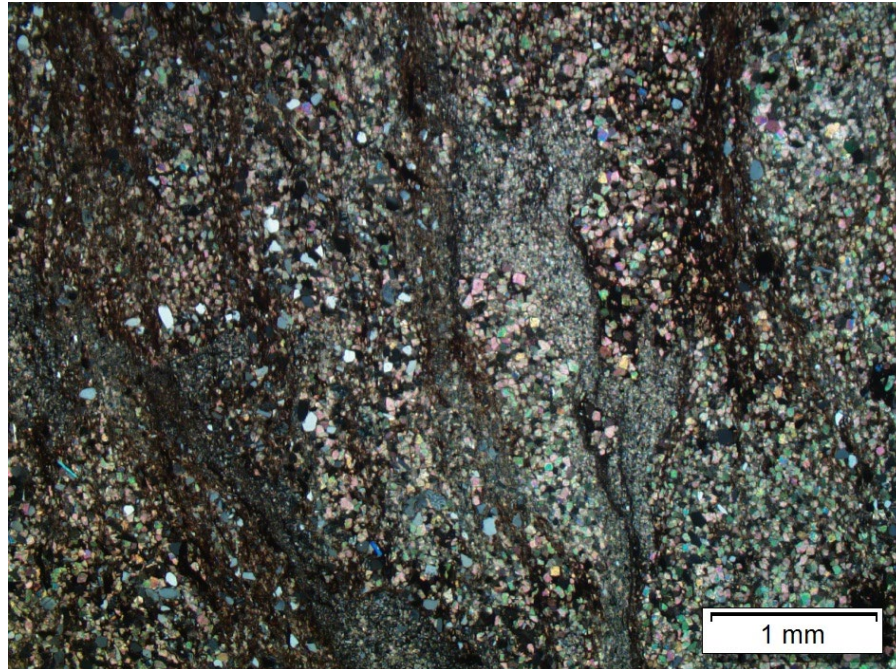
Figure 39*: Thin section photomicrograph of the Mt. Simon Sandstone at depth 7,996.5 ft. The high birefringence clay lamina shows some level of sericitization and alteration at this depth.*
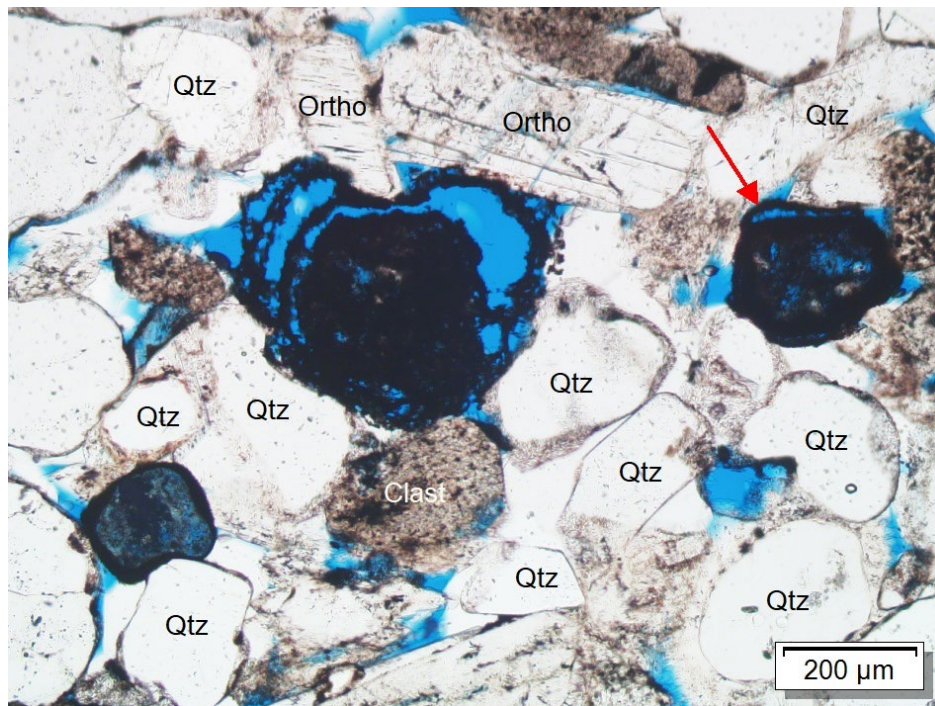

Figure 40*: Thin section photomicrograph of the Mt. Simon Sandstone at depth 7,996.5 ft. Figure shows an isolated pocket of detrital clay where some quartz grain migrated into the matrix with compaction.*

Figure 41: Thin section photomicrograph of the Mt. Simon Sandstone at depth 8,001.8 ft. A wider view shows soft sediment deformation with a heavily dolomitezed zone. Note two distinct dolomite grain sizes, as well as a microcrystalline dolomite presence within clay lamina.

Figure 42: Thin section photomicrograph of the Mt. Simon Sandstone at depth 8,009 ft. Stained illite crust deliniate the original grain after multiple rounds of dissolution. Red arrow shows a similar process occurring on a smaller grain.
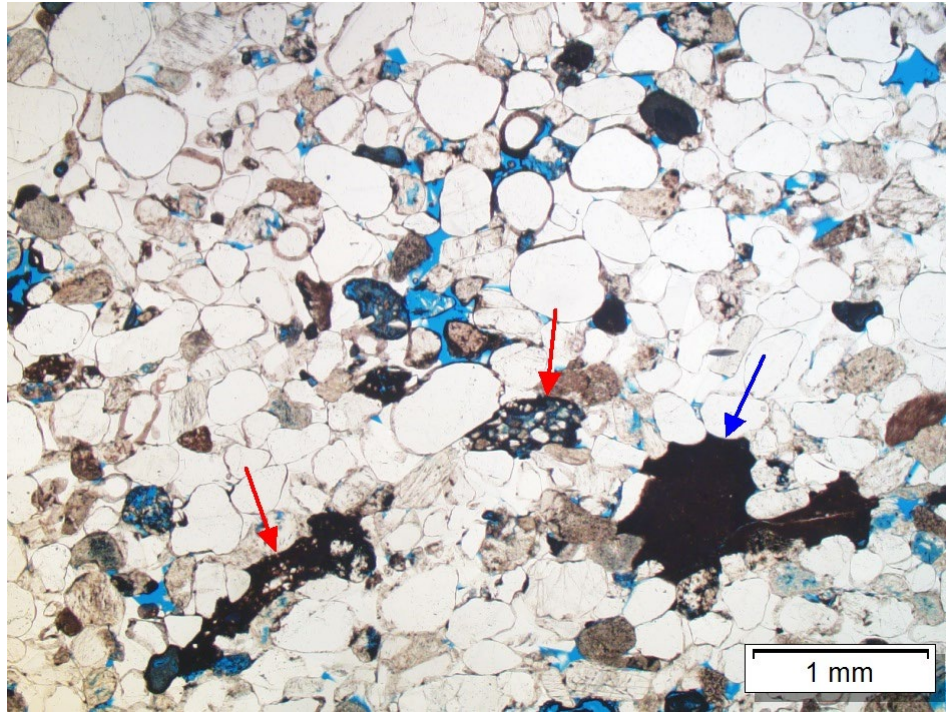
Figure 43: *Thin section photomicrograph of the Mt. Simon Sandstone at depth 8,009 ft. Figure shows quartz-cemented grain fabric with hematite-stained mudstone clasts. Red arrows denote clasts that are more siliceous than clasts that are matrix-rich (denoted by the blue arrow).*

Table 4: *Lower Mt. Simon full diameter sample analysis of sorting ranking, average grain size, initial porosity, intergranular volume (IGV), compaction porosity loss (COPL), cementation porosity loss (CEPL), and index of compaction all based on methodology from Freiburg et al. (2016).*

| Depth	Sorting	Grain size	Pi (initial prosity)	IGV	C (total Cement)	COPL	CEPL	Icomp
6167	Moderately well	Lower medium	36.7	32.24	33.13	6.5792	30.9549	0.1753
6168.3	Very well	Upper very fine	41.2	8.87	45.26	35.4744	29.2070	0.5484
6169.9	Very poorly	upper medium	25.8	14.61	29.32	13.1022	25.4820	0.3396
6171.3	well sorted	lower medium	38.8	26.59	21.02	16.6285	17.5213	0.4869
7904.4	very well	lower very fine	41.8	34.85	28.42	10.6657	25.3851	0.2959
7912.55	well sorted	lower fine	39.70	31.05	17.76	12.5433	15.5305	0.4468
7931.2	well sorted	upper very fine	40.2	18.01	13.23	27.0643	9.6522	0.7371
7937.5	well sorted	lower fine	39.7	27.05	18.26	17.3453	15.0956	0.5347
7959	very well sorted	lower fine	40.8	39.98	26.72	1.3661	26.3548	0.0493
7963	well sorted	upper very fine	40.2	38.25	29.18	3.1626	28.2603	0.1006
7969.7	very well sorted	lower fine	40.8	29.98	23.63	15.4522	19.9810	0.4361
7973.5	very well sorted	lower fine	40.8	34.73	22.75	9.2991	20.6385	0.3106
7977.5	extremely well	lower fine	43.5	28.59	18.03	20.8842	14.2629	0.5942
7978.2	extremely well	upper very fine	42.3	30.78	18.53	16.6463	15.4420	0.5188
7986	very well	lower fine	43.5	26.37	17.11	23.2669	13.1324	0.6392
7991.3	well sorted	upper fine	39.1	25.10	17.83	18.6920	14.4961	0.5632
8003.35	very well sorted	lower medium	40.2	25.82	25.32	19.3825	20.4156	0.4870
8009	well sorted	upper medium	38.1	23.88	17.81	18.6804	14.4838	0.5633
8011.7	very well sorted	lower coarse	41.5	23.99	20.46	23.0345	15.7500	0.5939
8016.6	very poorly	lower medium	23.4	20.85	21.15	3.2168	20.4715	0.1358

*Samples in red are carbonate rich

XRD ANALYSIS

Table 5: *(From top to bottom) XRD bulk mineralogy and clay mineral results from rotary sidewall core samples.*
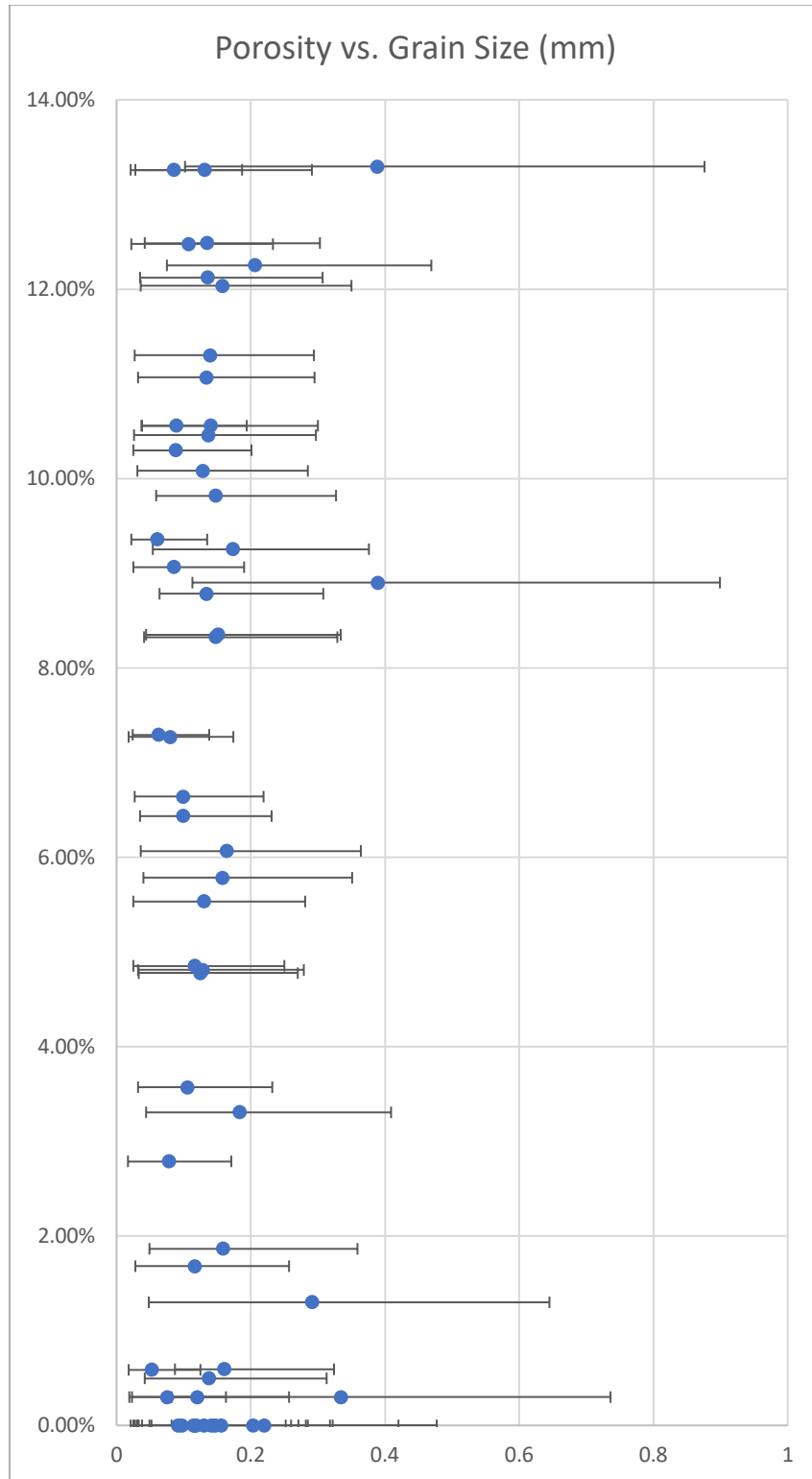
Depth	Results: Semi-Quantitative X-Ray Powder Diffraction Analysis, MBP									
	Bulk mineral data									
	%clay	%Quartz	%K-feldspar	%P-feldspar	%Calcite	%Dolomite	%Siderite	%Pyrite/Marcasite	%Magnetite	Total %
7937.3	3%	69%	18%	1%	1%	2%	1%	1%	4%	100%
8009.2	3%	82%	7%	1%	2%	1%	2%	1%	1%	100%
7993.9	14%	32%	23%	4%	3%	3%	8%	6%	8%	100%
7931.2	4%	75%	14%	1%	1%	2%	2%	1%	2%	100%
6112.4	23%	37%	13%	4%	2%	2%	10%	1%	7%	100%
2467.1	9%	22%	4%	3%	45%	6%	5%	4%	2%	100%
6170.7	11%	53%	16%	2%	2%	3%	7%	2%	4%	100%
2492.8	10%	35%	5%	4%	34%	4%	3%	3%	2%	100%

Depth	Results: Semi-Quantitative X-Ray Diffraction Analysis, < 2 CLAY				
	Clay mineral percentages				
	%Smectite	%Illite	%Kaolinite	%Chlorite	Total %
7937.3	12%	78%	5%	5%	100%
8009.2	22%	64%	6%	8%	100%
7993.9	10%	80%	3%	7%	100%
7931.2	9%	78%	6%	7%	100%
6112.4	3%	32%	43%	23%	100%
2467.1	7%	78%	4%	11%	100%
6170.7	3%	67%	11%	20%	100%
2492.8	5%	81%	5%	9%	100%
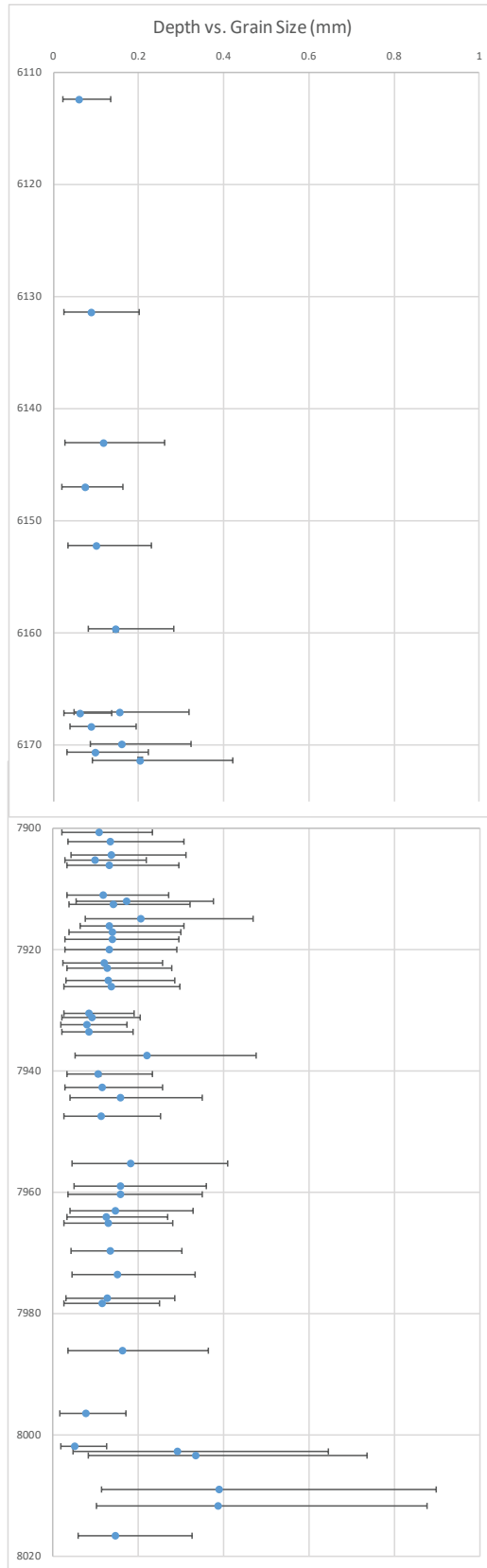
Figure 44: *Graph of textural data with the average grain size (blue point) and range of grain size.*

Figure 45*: Graph showing porosity and grain size (average and range). Note there is little correlation between grain size and total porosity.*